

Structure and Dynamics of the Mantle Beneath Western Canada

by

Tai-Chieh Yu

A thesis submitted in partial fulfillment of the requirements for the degree of

Doctor of Philosophy

in

Geophysics

Department of Physics  
University of Alberta

© Tai-Chieh Yu, 2022

## Abstract

The Canadian Cordillera (mountain belts) in western Canada has a high elevation (~1.5 km above sea level), thin crust (~35 km) and thin lithosphere (50-70 km). In contrast, the Laurentian Craton to the east has a low elevation (near sea level) and thicker crust and lithosphere (~40 km and >200 km, respectively). However, the structure and dynamics of the uppermost mantle beneath the cordillera and craton are unclear.

The first part of my research investigates the mantle structure of southwestern Canada using seismic tomography and magnetotelluric data for the Cascadia subduction zone backarc and adjacent Craton. Both shear wave velocity ( $V_s$ ) and electrical resistivity are sensitive to the temperature and olivine water content of the mantle. I developed a joint analysis of  $V_s$  and resistivity to quantify the temperature and olivine water content at 75-150 km depth. These depths correspond to the sublithospheric mantle for the cordillera and the lithospheric mantle for the craton. I found that the cordilleran mantle is either hydrated (~1600 ppm H/Si) and warm (~1240 °C) or drier (~600 ppm H/Si) and hot (~1370 °C); in contrast, the craton mantle is relatively dry (<500 ppm H/Si) and cool (~960 °C). These conditions imply that the cordillera sublithospheric mantle viscosity is in the range  $10^{19}$  of  $10^{21}$  Pa s, whereas the craton mantle lithosphere viscosity is in the range  $10^{22}$  of  $10^{24}$  Pa s. At present-day, there is a sub-vertical boundary between the cordilleran and craton mantle. My results indicate that the cordillera sublithospheric mantle is weak enough to undergo small-scale and edge-driven convection, and that the cordillera-craton boundary may be unstable, as the craton mantle lithosphere is susceptible to deformation.

The second part of my research investigates the mantle dynamics in the Northern Canadian Cordillera (NCC) to test the hypothesis that the thin NCC lithosphere developed recently through

gravitational thinning via delamination. I developed 2D thermal-mechanical models to investigate the consequences of delamination. Removal was triggered by a combination of (1) weak zone in the mantle lithosphere and (2) an eclogite layer in the lowermost crust, assumed to have formed due to shear zone or previous arc volcanism at the western edge of the NCC and an earlier episode of crustal thickening, respectively. The weak zone created a low viscosity conduit that enabled the dense eclogite layer to decouple from the crust. Delamination resulted in the formation of a high-elevation region with a thin crust, thin lithosphere and high heat flow, in good agreement with present-day NCC observations. The models predict that removal was accompanied by widespread mantle melting and changes in crustal stress. Hence, a delamination event at 15 Ma provides a new explanation for the enigmatic Northern Cordilleran Volcanic Province and crustal earthquakes in the Mackenzie Mountains.

The last part of my research uses generic models to study the dynamics and surface expressions of delamination. The models investigate an area with earlier crustal thickening, where there is an eclogite layer in the lowermost crust. The density and strength of this layer play a crucial role in triggering delamination. Three styles of delamination are identified: (1) slab-like removal occurs for strong (cool) lithosphere and creates a migrating wave of surface subsidence followed by uplift, (2) stringy delamination occurs for a weaker (hotter) lithosphere, and (3) delamination with drips occurs for the weakest (hottest) lithosphere. For Styles 2 and 3, delamination causes surface uplift but minimal subsidence. All three styles result in a wide region of thin, hot lithosphere and mantle decompression melting. The models also show that delamination induces stresses in the overlying crust, creating areas of extension/compression and crustal thickening. These results suggest that the wide range of surface observations for areas with delamination may reflect differences in lithospheric rheology and temperature.

## Preface

The research in this thesis is an original work by myself, Tai-Chieh Yu. My work was carried out under the supervision of Dr. Claire Currie at the University of Alberta.

**Chapter 2** is a manuscript that is under revision for *Journal of Geophysical Research: Solid Earth*, with the title “The structure and dynamics of the uppermost mantle of southwestern Canada from a joint analysis of geophysical observations” (authors: Yu, T.C., C.A. Currie, and M.J. Unsworth). I developed the computer codes for the joint analysis and carried out the calculations and interpretation. Dr. Currie was the supervisory author. I wrote the first draft of the manuscript and drafted the figures. All coauthors were involved in manuscript revision.

**Chapter 4** has been submitted to *Geology* under the title “Recent delamination below the Northern Canadian Cordillera?” (authors: Yu, T.C., C.A. Currie, P. Audet, A.J. Schaeffer, and Z. Wang). I designed the models and conducted the model experiments, data analysis, and interpretation. Zhirui Wang contributed to the initial models. Dr. Currie was the supervisory author. I wrote the first draft of the manuscript and drafted the figures. All coauthors were involved in manuscript revision.

**Chapter 5** is an original work that has been written as a manuscript, in preparation for submission to *Journal of Geophysical Research* (authors: Yu, T.C. and C.A. Currie). I designed the models and conducted the model experiments and data analysis, and interpretation. I wrote the first draft of the manuscript and drafted the figures. Dr. Currie was the supervisory author. We both contributed to revisions of the manuscript.

## Acknowledgments

I would like to thank my supervisor, Dr. Claire Currie, for her support, guidance, patience, and all the help over these years. I appreciate having opportunities to work on different research topics and attend several conferences. I am grateful to learn how to do solid research in science.

In addition, thank my committee members: Dr. Martyn Unsworth, Dr. Yu J. Gu, Dr. Stephen Johnston, and Dr. David Eaton, for spending some time reviewing my research work and giving me insightful thoughts for this thesis.

I also want to thank my friends for providing good friendships.

Finally, thank my family for everything that you have done. I'm blessed to have such a wonderful family.

This research was supported by funding from the Natural Sciences and Engineering Research Council of Canada (NSERC). The computational resources from Compute Canada are appreciated. 2D numerical models (using the SOPALE code) are developed by Dr. Christopher Beaumont (Dalhousie University, Halifax, Canada).

# Contents

## Chapter 1

Introduction.....	1
1.1 Tectonic setting of western Canada .....	2
1.2 Geophysical observations .....	4
1.3 Thin cordilleran lithosphere.....	6
1.4 Thesis objectives.....	9
1.5 Organization of the thesis .....	10

## Chapter 2

The structure and dynamics of the uppermost mantle of southwestern Canada from a joint analysis of geophysical observations .....	11
Abstract.....	12
2.1 Introduction.....	13
2.2 Data and analysis methods.....	17
2.2.1 Seismic shear wave velocity .....	17
2.2.2 Electrical resistivity .....	19
2.2.3 Joint analysis of Vs and resistivity.....	21
2.3 Results.....	24
2.3.1 Example calculations .....	24
2.3.2 Mantle structure along the ABC_S profile .....	28
2.3.3 Mantle structure along the ABC_N profile.....	31
2.3.4 Effect of parameter variations.....	34
2.4 Discussion.....	38
2.4.1 Cordilleran mantle structure .....	38
2.4.2 Craton mantle structure.....	42
2.4.3 Regional Q values .....	45
2.4.4 Mantle viscosities below western Canada .....	47

2.4.5 The cordillera-craton boundary and implication for mantle dynamics.....	48
2.5 Conclusions.....	50
2.6 Appendix.....	51
2.6.1 Calculation of shear wave velocity and resistivity .....	51
2.6.2 Calculation of the mantle solidus.....	54
2.6.3 Calculation of effective viscosity.....	54
Chapter 3	
Numerical model methodology.....	60
3.1 Governing equations .....	61
3.2 Material properties .....	63
Chapter 4	
Recent delamination below the Northern Canadian Cordillera? .....	66
Abstract.....	67
4.1 Introduction.....	67
4.2 Numerical model of delamination .....	70
4.3 Surface expressions of delamination .....	73
4.4 Implications for magmatism .....	75
4.5 Crustal deformation induced by delamination .....	77
4.6 Conclusions.....	78
4.7 Appendix.....	78
4.7.1 Numerical model set-up and material properties .....	78
4.7.2 Additional results from the preferred model.....	81
4.7.3 Additional models.....	86
4.7.4 Observed surface topography and heat flow .....	89
Chapter 5	
Styles and surface expressions of lithosphere delamination.....	90

Abstract .....	91
5.1 Introduction .....	91
5.2 Method .....	93
5.2.1 Numerical model setup .....	93
5.2.2 Material properties .....	95
5.2.3 Model initiation and boundary conditions .....	99
5.2.4 Numerical model experiments .....	100
5.2.5 Surface observables .....	101
5.3 Results: Dynamics of delamination .....	102
5.3.1 Reference model (Model A1) .....	102
5.3.2 Style, initiation, and duration of delamination .....	108
5.4 Results: Surface effects of delamination .....	114
5.4.1 Reference model with a lower crust eclogitization (Model B1) .....	115
5.4.2 Comparison between Model A1 and B1 .....	118
5.4.3 Effect of eclogite layer rheology .....	119
5.4.4 Variations in crustal rheology .....	119
5.4.5 Lithosphere thermal structure (Models B6 and B7) .....	126
5.5 Discussion .....	131
5.5.1 Dynamics of lithosphere delamination .....	131
5.5.2 Surface expressions of delamination .....	133
5.5.3 Implication for surface expressions of delamination in the western United States ...	135
5.6 Conclusions .....	136
Chapter 6	
Conclusions and future work .....	139
6.1 Main conclusions .....	140
6.2 Future work .....	145
6.3 Concluding remarks .....	148

References..... 149

## List of Figures

- Figure 1.1 (a) Topography in western Canada. The Canadian Cordillera can be divided in the Northern Canadian Cordillera (NCC) and the Southern Canadian Cordillera (SCC). CDF is the Cordilleran Deformation Front; JdF is the Juan de Fuca Plate; EP is the Explorer Plate. Red triangles indicate Neogene to Holocene volcanoes (Edwards & Russell, 2000; Gabrielse & Yorath, 1991). (b) S wave velocity at 100 km depth is provided by the seismic tomography model SL2013NA (Schaeffer & Lebedev, 2014). ..... 4
- Figure 1.2 Temperatures estimated from the joint inversion of gravity data and seismic tomography model NA07 at 100 km depth. White dashed lines indicate the tectonic boundaries (modified from Tesauro et al., 2015). ..... 8
- Figure 1.3 Hypotheses for lithosphere evolution in western Canada. (a) For the Southern Canadian Cordillera, the thin, hot cordilleran lithosphere is proposed to be a long-lived feature that is maintained by small-scale convection of a hydrated mantle wedge (after Hyndman et al., 2005). (b) For the Northern Canadian Cordillera, it is proposed that there was a lithospheric removal event at 5-25 Ma and the present-day cordilleran mantle lithosphere formed by cooling (after Audet et al., 2019). ..... 8
- Figure 2.1 Topography of western Canada, showing the cordillera and craton geological regions. The black dotted lines indicate the Cordilleran Deformation Front (CDF), Tintina Fault, Rocky Mountain Trench, and boundaries between the Foreland Belt (FB), Omineca Belt (OB), Intermontane Belt (IB), Coast Belt (CB), and Insular Belt (IS). Blue dashed lines are profiles ABC\_N and ABC\_S analyzed in this study. The red triangles denote Holocene volcanoes. Locations of lavas with mantle-derived xenoliths are shown as dark purple triangles (eruption age  $\geq 5$  Ma) and pink triangles (eruption age  $< 5$  Ma) (Canil et al., 2021; Francis et al., 2010). JdF is the Juan de Fuca plate, which subducts below North America at the plate margin (yellow dashed line). ..... 16
- Figure 2.2 Geophysical observations along the ABC\_S profile (a, b, d) and ABC\_N profile (c, e): (a) surface heat flow after correction for variations in crustal radiogenic heat (Currie & Hyndman, 2006) (b, c) shear wave velocity (Schaeffer & Lebedev, 2014), and (d, e) electrical resistivity

(Rippe et al., 2013). Points A and B are used in the analysis in Section 2.3.1. Red triangles are locations of volcanoes erupted since 28 Ma within 50 km of each profile..... 17

Figure 2.3 (a) Predicted  $V_S$  at 100 km depth as a function of temperature (T) for a pyrolite mantle with 10 mm grain size and 0.03 Hz frequency.  $V_{anh}$  is the anharmonic velocity (black line). The blue lines show the  $Q_F$ -corrected  $V_S$  for different olivine water contents ( $C_{OH}$ ): 50 ppm H/Si (dry; solid line), 1000 ppm H/Si (damp; dashed line), 5000 ppm H/Si (wet; dotted line). The dashed red line is  $Q_K$ -corrected  $V_S$ ; dotted purple line is  $Q_S$ -corrected  $V_S$ ; dotted green line is  $Q_Y$ -corrected  $V_S$ . Gray lines are average  $V_S$  for the cordillera and craton; gray areas are standard deviation. (b) Contour plot of  $V_S$  as a function of T and  $C_{OH}$  for the  $Q_F$  attenuation correction at 100 km depth with contours every 0.2 km/s. (c) Predicted electrical resistivity as a function of temperature for different olivine water contents, based on Gardés et al. (2014) (G, black) and Wang et al., (2006) (W, blue). (d) Contour plot of resistivity as a function of T and  $C_{OH}$  for Gardés et al. (2014) on a logarithmic scale. The white dashed line in (b;d) is the mantle solidus temperature for different  $C_{OH}$  (Hirschmann et al., 2009). ..... 24

Figure 2.4 Example analysis for  $V_S$  and resistivity ( $\rho$ ) for two points at 100 km depth along the ABC\_S profile (locations on Figure 2.2). The contour plots show the misfit between the observed and predicted values of  $V_S$  (left column) and  $\rho$  (middle column) and the summed misfit (right column, Equation 2.3) for: (a) cordilleran point and  $Q_F$  attenuation model, (b) cordilleran point and  $Q_K$  attenuation model, (c) craton point and  $Q_F$  attenuation model, and (d) craton point and  $Q_K$  attenuation model. All analyses use the Gardés et al. (2014) resistivity model. Green star shows the global minimum on the joint misfit plot, and magenta contour indicates where the misfit is ten times the global minimum. The white line is the mantle solidus temperature, as plotted in Figure 2.3b..... 27

Figure 2.5 Results of the joint analysis for the ABC\_S profile for the Gardés et al. (2014) resistivity model and  $Q_F$  attenuation model (a, c, e) and  $Q_K$  attenuation model (b, d, f). In (a) and (b), the plots from top to bottom are: best-fit T, best-fit  $C_{OH}$ , temperature uncertainty ( $\delta T$ ), water content uncertainty ( $\delta C_{OH}$ ) and global minimum misfit. Gray boxes indicate where the temperature is above the solidus based on the best-fit  $C_{OH}$ . Histograms of best-fit values at each depth for (c) temperature and (e) water content using the  $Q_F$ -corrected  $V_S$ , and (d) temperature and (f) water

content for the  $Q_K$ -corrected  $V_s$ . Red indicates cordilleran points (west of RMT) and blue is craton (east of RMT). The average and standard deviation for the cordillera and craton are given at each depth (units  $^{\circ}\text{C}$  for temperature and ppm H/Si for water content)..... 30

Figure 2.6 Results of the joint analysis of the ABC\_N profile for the Gardés et al. (2014) resistivity model and the  $Q_F$  attenuation model (a, c, e) and the  $Q_K$  attenuation model (b, d, f), with the format used in Figure 2.5..... 33

Figure 2.7 (a) Observed  $V_s$  (left) and resistivity (right) at 100 km depth for profiles ABC\_S (black line) and ABC\_N (dashed blue line), with the RMT.S and RMT.N labels indicating where the RMT crosses the ABC\_S and ABC\_N profiles, respectively and shown as a vertical line with the same line style. (b) The results of the joint analysis showing the best-fit temperatures (left) and water contents (right) and their uncertainties using the  $Q_F$  correction for each profile. (c) Best-fit temperatures (left) and water contents (right) their uncertainties using the  $Q_K$  correction. Volcanoes on the ABC\_N profile note as blue triangles. The triangle with black outline is the oldest volcano (6 Ma) that sites between the two profiles (location in Figure 2.1)..... 37

Figure 2.8 Effect of parameter variations for the joint analysis for the ABC\_S profile at 100 km depth. (a) Best fit temperatures (left) and water content (right) for different Q corrections ( $Q_K$  solid black line,  $Q_F$  dashed black line;  $Q_S$  dotted red line), using a grain size of 10 mm, seismic frequency of 0.03 Hz, pyrolite composition, and the Gardés et al. (2014) resistivity model. The dotted black line (W06) shows the results using the reference  $Q_K$  attenuation correction and Wang et al. (2006) resistivity model. The lower plots show the difference in temperature (left) and water content (right) relative to the reference  $Q_K$  values for variations in: (b) seismic wave frequency, (c) mantle composition. M.H. is Modified Harzburgite..... 38

Figure 2.9 (a) Vertical temperature profile for the cordillera from the joint analysis using the  $Q_F$  correction (blue) and  $Q_K$  correction (magenta) based on the average and standard deviation for ABC\_S. Gray shaded regions show temperatures from Hyndman et al. (2009; H09) based on surface heat flow (crust) and  $V_s$  (mantle). Symbols show temperatures from mantle xenoliths from Greenfield et al. (2013; black pluses), Saruwatari et al. (2001; light turquoise), and Ross (1983; light gray) and mantle-derived magmas from Canil et al. (2021; red circles). Dark gray line is the dry solidus (Hirschmann et al., 2009). (b) Vertical profile of olivine water content from this study

( $Q_F$  in blue;  $Q_K$  in magenta), with experimental measurements (Kovács et al., 2012, black crosses) and the value inferred by Canil et al. (2021; C21) at 45-100 km depth. .... 41

Figure 2.10 (a) Vertical profile of the craton mantle temperature ( $Q_F$  in blue;  $Q_K$  in magenta) based on ABC\_S, with temperatures from Hyndman et al. (2009; H09 in gray) based on surface heat flow (crust) and  $V_S$  (mantle), and mantle xenoliths from Slave Craton, Buffalo Hills kimberlites, and Sask Craton, respectively (Kopylova & Russell, 2000, squares; Aulbach et al. 2004, crosses; Czas et al., 2020, circles). (b) Vertical profile of olivine water content ( $Q_F$  in blue;  $Q_K$  in magenta), with olivine water content of mantle xenoliths from kimberlite pipes in Kaapvaal, Siberian, and Slave Cratons, respectively (Baptiste et al., 2012, diamonds; Doucet et al., 2014, pluses; Kilgore et al., 2020, squares). (c)  $V_S$  from SL2013NA (black line and grey shaded area; Schaeffer & Lebedev, 2014) and SEMUCB\_WM1 (blue line :  $V_{SISO}$ ; blue dashed line :  $V_{SH}$ ; blue dotted line :  $V_{SV}$ ; French & Romanowicz, 2014). .... 44

Figure 2.11 Observed average and standard deviations of  $V_S$  (left), resistivity (center), and seismic  $Q$  (right) along (a) ABC\_N and (b) ABC\_S from Schaeffer & Lebedev (2014), Rippe et al. (2013), and Dalton et al. (2008), respectively, for the cordillera (red line) and craton (blue line). The predicted  $Q$  from the joint analysis is also shown. .... 46

Figure 2.12 Effective viscosity for the mantle based on the best-fit temperature and olivine  $C_{OH}$  along (a, b) ABC\_N and (c, d) ABC\_S. Left column is from the  $Q_F$  attenuation function and right column is from the  $Q_K$  attenuation function; both use the Gardés et al. (2014) resistivity model. Areas are shown in black have large misfit values (shown in Figure 2.5b and Figure 2.6b). .... 48

Figure 2.13 Effect of uncertainties in  $V_S$  and resistivity for the  $Q_K$  analysis for point A (cordillera). (a) Fitting of the observed  $V_S$  and resistivity shows a global minimum at 1400 °C and 253 ppm H/Si with a misfit of 0.08 %. (b) Increase in  $V_S$  by 0.1 km/s and increase in resistivity by a factor of 2 relative to the observed values. The global minimum lies at 1338 °C and 1 ppm H/Si with a misfit of 2.02 %. (c) Decrease in  $V_S$  by 0.1 km/s and decrease in resistivity by a factor of 2 relative to the observed values. The global minimum lies at 1415 °C and 1109 ppm H/Si with a misfit at 0.02 %. .... 57

Figure 2.14 Effect of uncertainties in  $V_S$  and resistivity for the  $Q_K$  analysis on point B (craton). (a) Fitting of the observed  $V_S$  and resistivity shows a global minimum at 928 °C and 385 ppm H/Si

with a misfit of 0.02 %. (b) Increase in  $V_s$  by 0.1 km/s and increase in resistivity by a factor of 2 relative to the observed values. The global minimum lies at 651 °C and 1833 ppm H/Si with a misfit of 0.01 %. (c) Decrease in  $V_s$  by 0.1 km/s and decrease in resistivity by a factor of 2 relative to the observed values. The global minimum is at 1121 °C and 5 ppm H/Si with a misfit of 0.35 %.

Figure 4.1 Geological setting of northwest Canada, with model profile A-A'. Triangles are Northern Cordilleran Volcanic Province (NCVP) volcanoes (ages from Edwards & Russell, 2000; Abraham et al., 2005, and references therein), including Level Mountain (LM) and Mount Edziza (ME). Earthquakes (depth  $\leq 30$  km,  $M \geq 3$ ) are from the Geological Survey of Canada National Earthquakes Database. Focal mechanisms ( $M \geq 4.5$ ) are from the Global Harvard CMT catalog for the Mackenzie Mountains (MM). Barbed line is the Cordilleran Deformation Front (CDF); black lines are Denali fault (DF) and Tintina fault (TF).

Figure 4.2 Numerical model of delamination. Surface observations are (A) heat flow, (B) elevation relative to the craton, and (C) crustal thickness. Grey-shaded area shows present-day observations (see text). (D) Evolution of model. LC=lower crust, ML=mantle lithosphere.

Figure 4.3 Temporal variations in (A) relative elevation, (B) surface heat flow, and (C) Moho temperature at  $x=700$  km (solid line) and 900 km (dotted line). Grey shows observed values (see text). (D) Effective viscosity and Lagrangian mesh at given model times. Arrows indicate upper crust deformation.

Figure 4.4 Time-distance plot showing the distribution of horizontal strain rate in the upper 3 km of the crust (positive values are extension) and mantle melting (gray circles). The plot on the right shows the calculated melt volume across the width of the model (per km perpendicular to the model plane). Also shown are total magma volumes at Level Mountain (green,  $\sim 860$  km<sup>3</sup>) and Mount Edziza (yellow,  $\sim 665$  km<sup>3</sup>); line length indicates duration of magmatism (Edwards & Russell, 2000).

Figure 4.5 Initial model geometry and boundary conditions. Colours denote materials in the model domain (as in Figure 4.2). The weak zone has a viscosity of  $5 \times 10^{19}$  Pa s and its reference density is equal to that of the adjacent mantle lithosphere (3250 kg/m<sup>3</sup>). The MM block is a region with weak sediments with  $\phi = 1^\circ$  and reference density of 2700 kg/m<sup>3</sup>. The reference density of the

eclogitized lower crust is  $3450 \text{ kg/m}^3$ . The initial thermal structures of the cordillera and craton are also shown. To clearly show each material in the model, vertical and horizontal scales are not equal. .... 79

Figure 4.6 Temperature-depth profiles over time at  $x=700 \text{ km}$  (solid black line) and  $x=900 \text{ km}$  (dotted line) for the preferred model. The red line is the damp peridotite solidus (see text). The blue line is the dry granite solidus (Elkins-Tanton, 2005). The gray solid line is the average Moho depth in the models between 700 and 900 km at each time. .... 82

Figure 4.7 Spatiotemporal evolution of (A) surface topography and (B) rate of vertical displacement for the reference model, where positive values indicate uplift. .... 83

Figure 4.8 Effect of delamination on the maximum shear strain rate field at the given model times for the preferred model. .... 84

Figure 4.9 Evolution of Model 2 in which reference density of the eclogitized lower crust is  $3400 \text{ kg/m}^3$  and extends beneath the Mackenzie Mountains (MM) where its thickness decreased from 3 km at the Tintina Fault (TF) to 0 km at the Cordilleran Deformation Front (CDF). (A) Surface heat flow, (B) elevation relative to the craton, and (C) crustal thickness at 13 m.y. (dotted yellow line), 15 m.y. (short-dashed orange line), 20 m.y. (long-dashed blue line), and 29 m.y. (solid black line). The observations are in grey. (D) The model geometry and temperature field at the given times. (E) The spatial and temporal distribution of the modeled mantle melt (grey) and surface horizontal strain rate, as well as the total melt volume over time (right side). .... 87

Figure 4.10 Evolution of Model 3 in which there is no weak Mackenzie Mountains block. (A) Surface heat flow, (B) elevations relative to craton, (C) crustal thickness, and (D) model geometry and thermal structure at the given model times, using the same format as in Figure 4.9. (E) The spatial and temporal distribution of the modeled mantle melt (grey) and surface horizontal strain rate, as well as the total melt volume over time (right side). .... 88

Figure 4.11 (A) Map of ETOPO1 surface topography (Amante & Eakins, 2009) and heat flow measurements (Lewis et al., 2003). A-A' is the model profile and the black dashed line shows region over which heat flow and topography are extracted. (B) Surface heat flow along A-A'. The dashed lines show the mean values for the cordilleran and craton regions. (C) Surface elevation

(relative to sea level) along A-A'. Blue lines are minimum, maximum, and mean values of observed topography; labels give the mean and standard deviation (in m above sea level). ..... 89

Figure 5.1 (a) Initial model geometry and thermal-mechanical boundary conditions; the initial geotherm is also shown. The upper crust rheology is wet quartzite (WQ). Lower crust is mafic granulite (MG). Mantle lithosphere and sublithospheric mantle are wet olivine (WO). The dashed rectangle is the area of the plots shown in later figures. (b) Lithosphere viscosity profile based on the initial thermal structure and strain rate of  $10^{-15} \text{ s}^{-1}$ . Thick lines show the effective viscosity for the reference crust and mantle lithosphere (Models A1 and B1). Dashed lines indicate the range of crustal rheologies tested in the Type B models (see text for details). Red lines show the effective viscosity of eclogite (EC) based on two experimental studies: EC1 (Jin et al., 2001) and EC2 (Zhang & Green, 2007). Blue lines are frictional-plastic yield stress for unsoftened ( $\phi = 15^\circ$ ) and softened ( $\phi = 1^\circ$ ;  $\phi = 2^\circ$ ) materials. .... 95

Figure 5.2 (a) Density profile and (b) profile of the density difference relative to the adiabatic mantle, based on the initial model geotherm. The densities include the effects of composition and temperature. Within the eclogite layer, the lines correspond to compositional density contrasts of -118, -68, -18, +32, +82 and +132  $\text{kg/m}^3$  (from left to right), where the density contrast is relative to mantle at the same temperature. UC=upper crust, LC=lower crust, EC=eclogite layer, ML=mantle lithosphere, EL=bottom of the eclogite layer, LAB=lithosphere-asthenosphere boundary. .... 99

Figure 5.3 Evolution of Model A1 in which the eclogite layer has a viscosity is  $5 \times 10^{19} \text{ Pa s}$  and a density contrast of  $-68 \text{ kg/m}^3$ . This model exhibits stringy delamination (see text for information). Plots show: (a) surface topography (numbers denote the model time in Myr), (b-g) model structure, and (h-m) viscosity structure at the given times after the start of the model. The black lines are isotherms every  $300 \text{ }^\circ\text{C}$ . LC=lower crust; EC = eclogite; SLM = sublithospheric mantle..... 104

Figure 5.4 Time-distance plots for Model A1 with the upward direction on the y-axis corresponding to an increase in model time. These show the evolution of: (a) crustal thickness, (b) surface elevation, (c) Moho depth, (d) surface heat flow, (e) Moho temperature, and (f) distribution of mantle melting (dark grey circles) and horizontal strain rate at the surface (positive indicates extension). Delamination begins at  $\sim 38.5 \text{ Myr}$  and proceeds in an unsteady manner. The temporal

changes in surface elevation and horizontal strain rate are associated with slab break-offs at ~40 Myr, ~45 Myr, and ~49 Myr. Open circles show the location of the lithosphere detachment point.

..... 107

Figure 5.5 Effects of variations in the eclogite layer viscosity and density contrast on the (a) initiation time for delamination and (b) duration of the delamination; the symbols indicate the style of delamination. The initiation time is given by the time of first mantle melting and the duration is the time between initiation and removal of 90% of the mantle lithosphere below the eclogite layer. Blue outlines are Type B models that used mafic granulite rheology, and red outlines are eclogite rheology (Ec1, Jin et al., 2001; Ec2, Zhang & Green, 2007); see text for discussion. The position of the Type B models is based on the dynamics of delamination; the effective viscosity of the eclogite layer in these models varies with time, depending on the temperature and strain rate. 109

Figure 5.6 Evolution of Model A2, in which the eclogite layer has a viscosity is  $10^{22}$  Pa s and a density contrast of  $-68 \text{ kg/m}^3$ . Delamination does not occur in this model. Plots show: (a) surface topography, (b-d) model structure, and (e-g) viscosity structure at the given times after the start of the model. The black lines are isotherms every  $300 \text{ }^\circ\text{C}$ . LC=lower crust; EC = eclogite; SLM = sublithospheric mantle. .... 110

Figure 5.7 Evolution of Model A3, in which the eclogite layer has a viscosity is  $10^{23}$  Pa s and a density contrast of  $+132 \text{ kg/m}^3$ . This model exhibits slab-like delamination. Plots show: (a) surface topography, (b-g) model structure, and (h-m) viscosity structure at the given times after the start of the model. The black lines are isotherms every  $300 \text{ }^\circ\text{C}$ . LC = lower crust; EC = eclogite; SLM = sublithospheric mantle. .... 112

Figure 5.8 Evolution of Model A4, in which the eclogite layer has a viscosity is  $10^{19}$  Pa s and a density contrast of  $+82 \text{ kg/m}^3$ . This model exhibits delamination with drips. Plots show: (a) surface topography, (b-g) model structure, and (h-m) viscosity structure at the given times after the start of the model. The black lines are isotherms every  $300 \text{ }^\circ\text{C}$ . LC = lower crust; EC = eclogite; SLM = sublithospheric mantle. .... 113

Figure 5.9 Evolution of Model B1. The eclogite layer uses the rheology of mafic granulite and has a density contrast of  $+ 82 \text{ kg/m}^3$ . Plots show: (a) surface topography, (b-g) model structure, and

(h-m) viscosity structure at the given times after the start of the model. The black lines are isotherms every 300 °C. LC = lower crust; EC = eclogite; SLM = sublithospheric mantle..... 116

Figure 5.10 Time-distance plots for Model B1 showing the evolution of: (a) crustal thickness, (b) surface elevation, (c) Moho depth, (d) surface heat flow, (e) Moho temperature, and (f) distribution of mantle melting (dark grey circles) and horizontal strain rate at the surface (positive indicates extension). Delamination begins at ~2.5 Myr and lithospheric removal occurs through stringy delamination with frequent slab necking and breakoffs. Open circles show the location of the lithosphere detachment point. .... 117

Figure 5.11 Evolution of the surface topography (top plot) and model geometry at the given model times for: (a) Model B2 and (b) Model B3, in which the upper and lower crust are 10 times weaker and 10 times stronger than in Model B1, respectively. The black lines are isotherms every 300 °C. LC = lower crust; EC = eclogite; SLM = sublithospheric mantle. .... 121

Figure 5.12 Temporal distributions of crustal thickness and surface elevation in: Model B2 (a and b) and Model B3 (c and d), respectively. Open circles show the location of the lithosphere detachment point. .... 123

Figure 5.13 Evolution of the surface topography (top plot) and model geometry at the given model times for: (a) Model B4 which uses the reference crustal viscous rheology. (b) Model B5 uses a crustal viscous rheology that is 10 times weaker. Both models use a weak frictional-plastic rheology (internal friction angle of 1°) for the upper and lower crust. The black lines are isotherms every 300 °C. LC = lower crust; EC = eclogite; SLM = sublithospheric mantle. .... 125

Figure 5.14 Evolution of the surface topography (top plot) and model geometry at the given model times for: (a) Model B6 with a cooler lithosphere (~600 °C Moho), and (b) Model B7 with a hotter lithosphere (~800 °C Moho). The black lines are isotherms every 300 °C. LC = lower crust; EC = eclogite; SLM = sublithospheric mantle. The Moho is taken as the top of the eclogite layer (i.e., base of uneclogitized lower crust). .... 128

Figure 5.15 Time-distance plots for Model B6 (~600 °C Moho) showing the evolution of: (a) crustal thickness, (b) surface elevation, (c) Moho depth, (d) surface heat flow, (e) Moho temperature, and (f) distribution of mantle melting (dark grey circles) and horizontal strain rate at

the surface (positive indicates extension). Open circles show the location of the lithosphere detachment point ..... 129

Figure 5.16 Time-distance plots for Model B7 (~800 °C Moho) showing the evolution of: (a) crustal thickness, (b) surface elevation, (c) Moho depth, (d) surface heat flow, (e) Moho temperature, and (f) distribution of mantle melting (dark grey circles) and horizontal strain rate at the surface (positive indicates extension). Open circles show the location of the lithosphere detachment point. Black dashed line indicates the style of removal changes from stringy delamination to local drips..... 130

Figure 5.17 Seismic tomography in (a) the southern Sierra Nevada from Saleeby et al. (2012) and (b) southwestern edge of Colorado Plateau from Karlstrom et al. (2008)..... 136

Figure 5.18 Surface expressions are associated with styles of delamination, including (a) stringy delamination (b) delamination with drips (c) slab-like delamination. Dashed lines show the profiles of the surface topography, distribution of the mantle melt, and base of lithosphere after delamination..... 138

Figure 6.1 Summary of the key results from this thesis for present-day western Canada. (a) For the Southern Canadian Cordillera, the cordilleran mantle is hydrated and hot, and the craton mantle is cool and partially dry; there is an increase in lithospheric thickness to the east of the Rocky Mountain Trench. These results support the hypothesis of small-scale convection for the cordilleran mantle and suggest that the cordillera-craton lithosphere step may be partially unstable. (b) Lithosphere delamination at 15 Ma for the Northern Canadian Cordillera can explain the present-day structure of this region, magmatism in the Northern Cordilleran Volcanic Province (NCVP), and earthquakes in the Mackenzie Mountains..... 143

Figure 6.2 Global locations of proposed lithosphere drips (Darold & Humphreys, 2013; Elkins-Tanton & Hager, 2000; Gorczyk et al., 2012; Gutiérrez-Alonso et al., 2011; Handy et al., 2015; Pinet et al., 2013, 2013; Pysklywec & Beaumont, 2004; Wang et al., 2021; West et al., 2009; Zhu et al., 2012) and delamination (Bao et al., 2014; Chung et al., 2005; Comeau et al., 2021; Göğüş et al., 2016; Göğüş & Pysklywec, 2008b; Karlstrom et al., 2008; Krystopowicz & Currie, 2013; Saleeby et al., 2012; Schurr et al., 2006; Stern et al., 2013; Valera et al., 2008; van Wijk et al., 2010). ..... 145

Figure 6.3 Schematic diagrams showing mantle flow directions in (a) 2D and (b) 3D models of lithosphere delamination. .... 147

## List of Tables

Table 2.1 Bulk oxide composition for the three mantle compositions considered in this study. .	51
Table 2.2 Parameters used in calculations of $V_S$ and $Q_F$ .....	52
Table 2.3 Hydrous olivine conductivity parameters .....	53
Table 2.4 Rheology parameters for diffusion creep (dif) and dislocation creep (dis) of olivine (Behn et al., 2009; Hirth & Kohlstedt, 2003). .....	56
Table 2.5 Average and one standard deviation of temperature and olivine water content for the cordillera and craton regions.....	59
Table 4.1 Material parameters used in the model shown in Figure 4.2 (the preferred model). MM=Mackenzie Mountains block, uc. = upper crust (0-9 km depth), mc. = mid-crust (9-21 km depth), ec. = eclogitized lower crust, cr. = craton mantle lithosphere. ....	85
Table 5.1 Materials parameters used in numerical models.....	97
Table 5.2 List of models discussed in text. EC=eclogite layer. ....	101

# **Chapter 1**

## **Introduction**

## 1.1 Tectonic setting of western Canada

This study addresses the structure and dynamics of the mantle below western Canada. It includes an assessment of the present-day mantle structure below western Canada, the origin of the thin lithosphere in the Northern Canadian Cordillera, and the surface expressions associated with lithosphere delamination. Figure 1.1 shows the topography of western Canada. This area can be divided into two main geological regions: the high-elevation Canadian Cordillera in the west and the low-elevation North American Craton in the east. The Cordilleran Deformation Front marks the topographic eastern limit of the cordillera, and as discussed below, the Rocky Mountain Trench and Tintina Fault are interpreted to delineate the geological boundary between the craton and cordillera (Hyndman & Lewis, 1999).

The craton is the ancient core of North America. It contains Archean and Proterozoic continental blocks (ages of ~1.8-2 billion years) that make up the crystalline crust and underlying rigid mantle lithospheric layer (Griffin et al., 2003; Hoffman, 1988). Today, the craton crust is covered by the Western Canadian Sedimentary Basin, an important area for oil and gas resources. The tectonic evolution of the western margin of craton dates back to ~750 Ma when the Rodinia supercontinent underwent rifting, creating an ocean basin to the west of the continent (Burchfiel & Davis, 1975; Stewart, 1972, 1976). This developed a continent-ocean boundary similar to the present-day setting in eastern North America and the Atlantic Ocean basin. At ~390 Ma, the tectonics changed to plate convergence. This created a series of subduction zones and magmatic arcs during the late Paleozoic and early Mesozoic (~355-185 Ma) (Monger & Price, 2002). The cordillera began forming at ~185 Ma as plate convergence lead to the accretion of exotic terranes to the western margin of the craton (Monger & Price, 2002). As a result, the North American Plate grew westward. The geological structure of the Canadian Cordillera is thus the result of a long history of plate convergence, as well as lateral (along-margin) translation of material along strike-slip faults (Price, 1994).

At present day, both the craton and cordillera are part of the North American Plate, and the western margin of the plate lies just offshore (Figure 1.1). The Cascadia subduction zone is found offshore Vancouver Island in southwestern Canada, where the Juan de Fuca and Explorer plates descend below the North American Plate. North of this, subduction terminated at ~42 Ma (Engebretson et al., 1985), and the plate boundary between the Pacific and North America Plates

is now predominantly a right-lateral strike-slip fault. The Canadian Cordillera can be divided into five main morphogeological belts. From east to west, these are Foreland belt, Omineca belt, Intermontane belt, Coast belt, and Insular belt (Monger & Price, 2002). The cordillera is also characterized by widespread magmatism, including volcanoes of the Cascade volcanic arc in southwest Canada and magmatism within the interior of the cordillera.

Although the cordilleran rocks were accreted through plate convergence, there are significant uncertainties about the details of accretion and the geological evolution of western North America. The accepted hypothesis suggests that the cordilleran terranes were added to the western side of the craton through a series of east-dipping subduction zones (i.e., the same orientation as the present-day Cascadia subduction zone, Figure 1.1) (Cook & Erdmer, 2005). There is debate about the mechanics of accretion, with one model suggesting that cordilleran upper crust material was emplaced above craton deep crust and mantle lithosphere (e.g., Cook et al., 2004) and another model suggesting that the entire cordilleran lithosphere is exotic (e.g., Johnston, 2008). Alternately, it has been proposed that plate convergence and accretion included periods of west-dipping subduction, whereby an oceanic plate outboard of the craton subducted below the cordilleran terranes and the final subduction of this oceanic plate resulted in a collision between the craton and cordillera. Johnston (2001, 2008) suggests that this may have involved multiple subduction and collision events. In addition, it appears that plate convergence was oblique, resulting in significant northward motion of cordilleran blocks during accretion, as shown by paleomagnetic studies of sedimentary and volcanic rocks (e.g., Enkin et al., 2006; Irving et al., 1995).

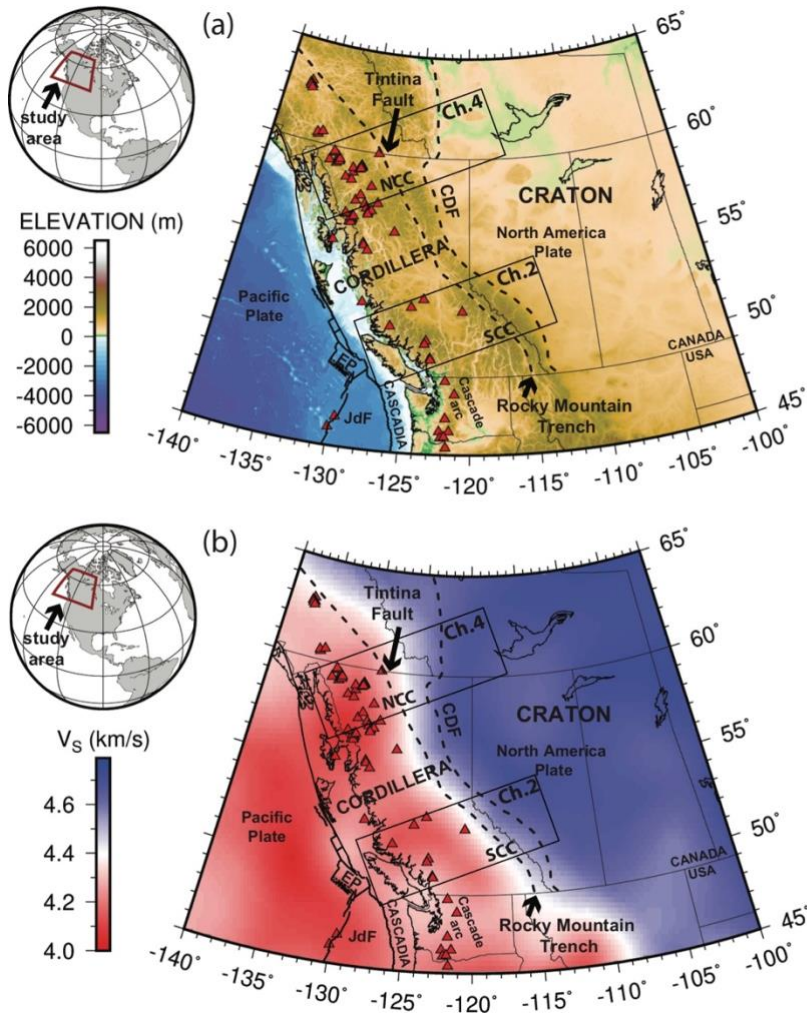


**Figure 1.1** (a) Topography in western Canada. The Canadian Cordillera can be divided in the Northern Canadian Cordillera (NCC) and the Southern Canadian Cordillera (SCC). CDF is the Cordilleran Deformation Front; JdF is the Juan de Fuca Plate; EP is the Explorer Plate. Red triangles indicate Neogene to Holocene volcanoes (Edwards & Russell, 2000; Gabrielse & Yorath, 1991). (b) S wave velocity at 100 km depth is provided by the seismic tomography model SL2013NA (Schaeffer & Lebedev, 2014).

## 1.2 Geophysical observations

As shown in Figure 1.1a, the average elevation of the cordillera is ~1.5-2 km above sea level, whereas the adjacent craton has an average elevation of ~0.5 km. Differences between the regions are also obvious in geophysical observations, including surface heat flow, crustal

thickness, seismic tomography and magnetotelluric observations. Note that this research defines the cordillera and craton based on geophysical observations that suggest the boundary occurs approximately below the RMT-TTN fault, as discussed below and in Chapter 2. The most well-studied region is the Southern Canadian Cordillera. Near  $\sim 50^{\circ}\text{N}$  latitude, the cordillera has a regionally high heat flow of  $\sim 75 \text{ mW/m}^2$ , whereas the craton exhibits a low heat flow of  $\sim 42 \text{ mW/m}^2$  (Hyndman & Lewis, 1999). To the north ( $59\text{-}64^{\circ}\text{N}$  latitude), the heat flow in cordillera is  $\sim 105 \text{ mW/m}^2$ , whereas the craton heat flow is  $\sim 90 \text{ mW/m}^2$ ; these higher values appear to be primarily due to increased crustal radiogenic heat for the cordillera and craton (Lewis et al., 2003). An intriguing observation is that the crustal thickness for the cordillera is relatively uniform, with a mean and standard deviation of  $\sim 33 \pm 3 \text{ km}$  (Audet et al., 2020; Hammer et al., 2000). In the craton, there is a greater lateral variation in crustal thickness, with values generally 40-50 km (Gu et al., 2011, 2018; Hyndman & Lewis, 1999). The cordillera and craton also have significantly different mantle seismic velocities. At 100 km depth, an S-wave velocity of  $\sim 4.4 \text{ km/s}$  nearly aligns with the Rocky Mountain Trench (RMT) (Figure 1.1b), based on the SL2013NA model (Schaeffer & Lebedev, 2014). Low S-wave velocities are found to the west of the RMT, whereas high values are to the east. Chen et al. (2019) show that both P-wave and S-wave velocities are low for the cordillera and high for the craton, with a sharp lateral gradient below the RMT. Additionally, the cordilleran mantle has a low electrical resistivity ( $\sim 100 \Omega\text{m}$ ), with an even lower resistivity below the Cascade volcanic arc ( $\sim 50 \Omega\text{m}$ ) (Rippe et al., 2013). To the east of the RMT, the electrical resistivity increases, with high resistivity ( $\sim 1000 \Omega\text{m}$ ) for the craton mantle at depths less than 150 km.

Previous studies have shown that these observations are consistent with different subsurface temperatures (e.g., Hyndman et al., 2009). The cordillera is interpreted to have a relatively hot mantle, with a temperature of  $\sim 800\text{-}900 \text{ }^{\circ}\text{C}$  at the base of the crust (the Moho). In contrast, the craton is cooler, with a Moho temperature of  $\sim 400\text{-}500 \text{ }^{\circ}\text{C}$ . The thermal differences are also demonstrated by xenoliths, which show that the cordillera is  $\sim 400 \text{ }^{\circ}\text{C}$  hotter than the craton at 100 km depth (Hyndman et al., 2009 and references therein). In addition, the cordillera has an effective elastic thickness of  $\sim 20 \text{ km}$ , compared to a thickness of  $\sim 100 \text{ km}$  for the craton (Flück et al., 2003). These are consistent with the cordillera having a hot, weak lithosphere, compared to the

cool and strong craton lithosphere (Hyndman et al., 2009). Further, Hyndman & Currie (2011) argued that the high cordilleran elevations are the result of the hot, low-density cordilleran mantle.

The thermal boundary between the cordillera and craton approximately coincides with the RMT–Tintina Fault system at the Earth’s surface (Hyndman & Lewis, 1999), as shown in Figure 1.1. From the geophysical observations, it is possible to determine the thickness of the lithosphere (e.g., Hyndman et al., 2009). The lithosphere is the rigid outer shell of the Earth; below the lithosphere, the mantle is undergoing convection. The lithospheric thickness depends on temperature because rock strength decreases with increasing temperature. It is inferred that the hot cordillera has a lithospheric thickness of 50-70 km and the cooler craton has a thickness of ~200-300 km (Hyndman & Lewis, 1999; Currie & Hyndman, 2006). As a result, there is a large subvertical step in the lithospheric thickness from the cordillera to the craton. Body wave tomography shows that the gradient in velocity occurs over a distance ~50 km west of RMT at depths of 150 km (Chen et al., 2019).

### **1.3 Thin cordilleran lithosphere**

Geophysical observations from western Canada show a hot and thin lithosphere for the cordillera compared to the adjacent cool, thick craton. As an example, Figure 1.2 shows the high temperatures estimated from the joint inversion of gravity data and seismic tomography model NA07 (Bedle & van der Lee, 2009) at 100 km depth (Tesauro et al., 2015). This raises the question: when did the present-day cordilleran lithosphere become thin? One possibility is that this is a long-lived feature inherited from the initial accretion of the cordilleran terranes (e.g., Lowe & Ranalli, 1993). Alternately, the cordillera may have thinned more recently. For example, Southern Canadian Cordillera has been suggested to have thinned in the last 50-60 Ma (Bao et al., 2014).

A long-lived thin cordilleran lithosphere requires a mechanism to keep the cordilleran mantle hot. Hyndman et al. (2005) propose that the high temperatures are maintained by active small-scale convection. They suggest that this region was extensively hydrated by the adjacent subduction zones owing to the long-term plate convergence, leading to low viscosities and vigorous convection (Figure 1.3a). However, this hypothesis does not address why the craton lithosphere is so much thicker, nor why there is a step in lithospheric thickness between the two

regions. Such a step will create edge-driven convection (EDC) (King & Anderson, 1998), and numerical models show that EDC causes the step to be smoothed over time (Currie & van Wijk, 2016). Models of western Canada predict that a subvertical step can only be maintained if the craton mantle is dry and compositionally depleted (Mallyon, 2017). This suggests that, in addition to a thermal difference between the cordillera and craton, there are also differences in composition and water content.

The other possibility is that the cordilleran lithosphere has thinned more recently through gravitational instabilities. Thermal calculations show that the present-day lithospheric structure in the Northern Canadian Cordillera is compatible with a thinning event that occurred 5-25 Myr ago (Audet et al., 2019). Gravitational instability is driven by high lithospheric densities owing to the cool temperatures (Poudjom Djomani et al., 2001), as well as the possible presence of dense materials, such as eclogite in the lower crust created by metamorphism (Kay and Kay, 1993). There are two end-member styles of lithospheric removal: (1) delamination involves the detachment of the dense mantle lithosphere along a weak interface at the Moho or in the deep crust, resulting in the wholesale removal of the deep lithosphere (Bird, 1979), as shown in Figure 1.3b, and (2) localized Rayleigh-Taylor type instability (RTI, “drips”) (Houseman & Molnar, 1997). Both styles of thinning have been proposed for the cordillera. Bao et al. (2014) suggest that the Southern Canadian Cordillera underwent a widespread delamination event at 55 Ma. Conversely, Currie et al. (2008) and Hardebol et al. (2012) suggest that the cordillera could have thinned more gradually through RTI induced by mantle shearing and EDC. However, to date, there has been little quantitative work to examine whether such episodes of thinning are compatible with surface observations. Both delamination and RTI should change the shallow thermal structure (e.g., Audet et al., 2019), and may lead to observable changes in surface elevation and the occurrence of magmatism (e.g., Göğüş & Pysklywec, 2008a; Wang & Currie, 2015).

Regardless of whether the thin cordilleran lithosphere is a long-lived or recent feature, it is well-documented that there is a significant change in lithospheric thickness at the Rocky Mountain Trench. The geometry of the cordillera-craton boundary (the lithosphere step) provides an important constraint that must be matched by any mechanisms proposed for creating and maintaining the thin cordilleran lithosphere. This step in lithospheric thickness may also evolve in response to complex mantle flow (e.g., Bao et al., 2016), as well as internal deformation of the

craton lithosphere (e.g., Mallyon, 2017). These along-strike effects may explain the north-south variations in the structure of the craton margin (e.g., Chen et al., 2019).

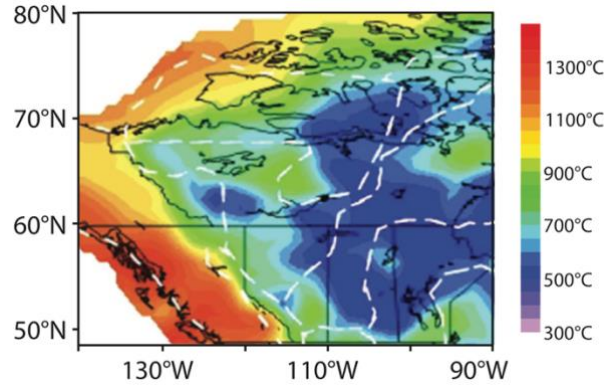


**Figure 1.2** Temperatures estimated from the joint inversion of gravity data and seismic tomography model NA07 at 100 km depth. White dashed lines indicate the tectonic boundaries (modified from Tesauro et al., 2015).

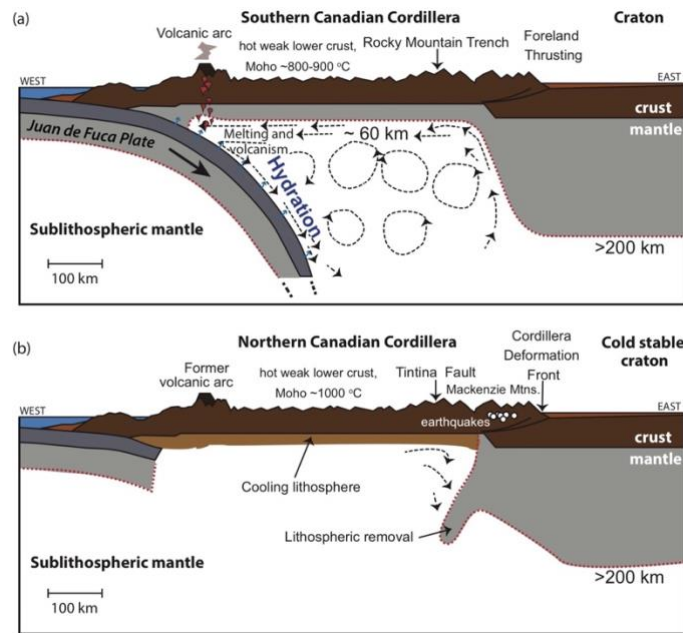


**Figure 1.3** Hypotheses for lithosphere evolution in western Canada. (a) For the Southern Canadian Cordillera, the thin, hot cordilleran lithosphere is proposed to be a long-lived feature that is maintained by small-scale convection of a hydrated mantle wedge (after Hyndman et al., 2005). (b) For the Northern Canadian Cordillera, it is proposed that there was a lithospheric removal event at 5-25 Ma and the present-day cordilleran mantle lithosphere formed by cooling (after Audet et al., 2019).

## 1.4 Thesis objectives

This research is motivated by recent geophysical observations that show that the cordilleran and craton lithosphere have different lithospheric thicknesses and thermal structures, which may reflect variations in composition and water content. Based on these observations, the thermal structure of the cordillera has been hypothesized to be related to either long-lived small-scale convection or recent lithospheric removal (Figure 1.3). These two hypothesis may lead to different surface expressions that allow them to be identified. This thesis addresses the nature of the cordilleran mantle using a combination of geophysical observations, geodynamic numerical models and surface observations (including topography and magmatism). The thesis is divided into three distinct projects. The objectives are:

(1) an updated assessment of the present-day mantle structure of the Southern Canadian Cordillera and adjacent craton. I use recent geophysical observations and mineral-physics-based relationships to determine the thermal and compositional structure of the mantle (at 75 to 150 km depth). One goal is to test the hypothesis that the cordilleran mantle is hot and extensively hydrated (Hyndman et al., 2005) and that the craton mantle is dry and depleted (Mallyon, 2017).

(2) an examination of the factors that can create thin cordilleran lithosphere through lithospheric removal, to test the hypothesis that the thin Northern Canadian Cordillera lithosphere is a recent feature (i.e., thinning occurred within the last 25 Ma; Audet et al., 2019). I use two-dimensional (2D) numerical models to study the factors needed to induce lithospheric removal through delamination and assess the timescales and surface expressions of thinning (e.g., surface heat flow, elevation, magmatism, crustal stress).

(3) an exploration of the dynamics and surface expressions of delamination. This work extends the Northern Canadian Cordillera models to investigate delamination in general, in order to explain observations from other orogens. 2D numerical models are used to evaluate the timing and styles of delamination and how delamination may cause temporal variations in surface uplift, crust and lithospheric structure, volcanic activity, and crustal extension or compression.

## 1.5 Organization of the thesis

The thesis is organized as follows:

*Chapter 2* investigates the mantle structure in southwestern Canada. Models of seismic shear wave velocity and electrical resistivity are used to constrain the temperature and hydration state of mantle at depths of 75 to 150 km. These results are then used to determine the effective viscosity and discuss the implications for the present-day mantle dynamics.

*Chapter 3* introduces the numerical methods used in the 2D geodynamic numerical model (SOPALE program), including the governing equations and material properties.

*Chapter 4* presents numerical models of lithosphere delamination for the Northern Canadian Cordillera. Model results are compared to existing observations for this area, including surface topography, magmatism and crustal deformation.

*Chapter 5* systematically examines how variations in the rheology and density of the eclogitized lower crust affect the dynamics of lithosphere delamination. Model results show the timing and styles of delamination and demonstrate their surface expressions.

*Chapter 6* summarizes the key results of the thesis research and gives suggestions for future work.

## **Chapter 2**

# **The structure and dynamics of the uppermost mantle of southwestern Canada from a joint analysis of geophysical observations**

A version of the manuscript submitted to *Journal of Geophysical Research: Solid Earth*

## **Abstract**

Geophysical imaging reveals significant lateral variations in the properties of the mantle across southwestern Canada. Here, the Southern Canadian Cordillera forms the backarc of the Cascadia subduction zone and is bounded on the east by the Laurentian Craton. We examine mantle structure using shear wave velocity ( $V_s$ ) from seismic tomography and an electrical resistivity model from magnetotellurics. Independent analyses of  $V_s$  and resistivity are poorly constrained because of the number of free parameters. To overcome these limitations, we conduct a joint analysis of the  $V_s$  and resistivity models to quantify temperature and water content across the cordillera-craton boundary at 75-150 km depth. Our analysis indicates that the cordillera mantle either has a warm and hydrated mantle ( $\sim 1240$  °C and olivine water content of  $\sim 1600$  ppm H/Si) with no widespread in-situ melt) or a hotter and less hydrated mantle ( $\sim 1370$  °C;  $\sim 600$  ppm H/Si) with some melt at 75 km depth. In contrast, the craton mantle lithosphere is  $\sim 350$  °C cooler and drier ( $< 500$  ppm H/Si). Temperatures depend strongly on the seismic attenuation model. If this is known, the temperature uncertainty is  $< 100$  °C. There is significant uncertainty in olivine water content ( $> 500$  ppm H/Si), owing to observation uncertainties, the resistivity model, and mantle composition. Our results indicate that the cordillera asthenosphere has a low viscosity ( $10^{19}$ - $10^{21}$  Pa s), and there is a subvertical eastward increase in lithosphere thickness from the cordillera to craton below the Rocky Mountain Trench. The cratonic mantle lithosphere viscosity is  $10^{22}$ - $10^{24}$  Pa s and the western edge of the craton may be unstable, suggesting that the present-day geometry is a transient feature.

## **Plain Language Summary**

We are interested in understanding why the rigid part of the Earth (called the lithosphere) below the Southern Canadian Cordillera mountain range is hot and thin over long geological timescales ( $> 200$  Myr), whereas the adjacent craton is thicker and cooler. To do this, we jointly analyze two geophysical observations (seismic velocity and electrical resistivity) at 75-150 km depth. This allows us to determine the properties of the shallow mantle below this region. Our results show that the mountain range has a mantle that is either (1) hot and dry with some melt at 75 km depth or (2) warm and hydrated with no melt. In both cases, the mantle is predicted to be

weak and therefore may be susceptible to rapid convection that maintains the hot, thin lithosphere. The eastern limit of the hot mantle is currently below the Rocky Mountain Trench. The geophysical observations show that the craton mantle east of this has cool temperatures and lower water content. However, this area is not completely dry, and therefore the craton mantle may be weak enough to deform. This suggests that the cordillera-craton boundary may be an area of active deformation, which has implications for the long-term evolution of southwestern Canada.

## 2.1 Introduction

The thermal structure of the continental lithosphere is important for understanding its thickness and strength, as well as the dynamics of the underlying asthenosphere. Direct measurements of temperatures in the continental crust and uppermost mantle come from studies of xenoliths and erupted magmas (e.g., Canil et al., 2021; Harder & Russell, 2006; Saruwatari et al., 2001) which provide detailed local information. In contrast, regional temperature estimates can be obtained indirectly using geophysical data, such as surface heat flow, effective elastic thickness, and mantle seismic velocity, and experimental petrology studies that allow a mapping between the geophysical observations and subsurface temperatures (e.g., Currie & Hyndman, 2006; Goes & van der Lee, 2002; Hyndman et al., 2009; Hyndman & Lewis, 1999; Klöcking et al., 2018; Schutt et al., 2018; Tesauro et al., 2014).

In this study, we examine the thermal structure of the mantle beneath southwestern Canada along with two profiles (ABC\_N and ABC\_S) that extend from the modern Cascadia volcanic arc to the continental interior (Figure 2.1). This region forms the backarc of the Cascadia subduction zone, where the Juan de Fuca oceanic plate subducts below the North America Plate. The continental crust formed through successive accretions of exotic terranes to the western margin of the Laurentian Craton since the Jurassic, resulting in five main tectonomorphic belts that are, from west to east, the Insular, Coast, Intermontane, Omineca, and Foreland Belts (Monger & Price, 2002). The cordillera is geologically defined based on to these five regions. However, there is a clear variation in lithosphere thickness, where the thickness increases below the RMT and Tintina fault (Figure 1.1b); this is based on geophysical observations that are described below. For brevity, this study uses the geophysical classification, such that the craton includes the foreland belt and

cordillera includes the region to the west, such that the RMT and Tintina fault form its eastern boundary. To examine the cordilleran lithosphere and transition zone between cordillera and craton, we focus on the latter three. The Intermontane and Omineca Belts lie within the Canadian Cordillera, a rugged, high elevation region that is 1.5 to 2 km above sea level. This is bounded on the east by the Rocky Mountain Trench (RMT), east of which lies the Foreland Belt. The RMT is currently a linear topographic low. The southern RMT formed through Cenozoic normal faulting. The northern RMT merges with the strike-slip Tintina Fault. The Cordilleran Deformation Front marks the topographic eastern limit of the Foreland Belt.

The cordilleran lithosphere structure has been studied using various geophysical measurements. At a latitude of 50 °N, the cordillera is characterized by a high surface heat flow of  $\sim 75$  mW/m<sup>2</sup> (Figure 2.2a, Currie & Hyndman, 2006; Hyndman & Lewis, 1999). The underlying mantle has anomalously low electrical resistivity (Rippe et al., 2013; Soyer & Unsworth, 2006) and low seismic wave velocities (Bao et al., 2014; Bedle & van der Lee, 2009; Chen et al., 2019; van der Lee & Frederiksen, 2005; Schaeffer & Lebedev, 2014). Collectively, these observations indicate a hot cordilleran lithosphere, with an inferred temperature of  $\sim 800$ - $900$  °C at the base of the crust (Moho) and lithosphere thickness of 60-70 km (Currie & Hyndman, 2006). Seismic studies show that the crust has a relatively uniform thickness of 32-34 km (Hyndman & Lewis, 1999 and references therein). Hyndman & Currie (2011) argue that the high cordilleran elevations are maintained by a hot, low density mantle, rather than a thick crustal root.

The origin of the thin cordilleran lithosphere is debated. It has been proposed that this may mark an area of regional mantle upwelling (Gough, 1986), or that there has been recent thinning through gradual convective erosion (Hardebol et al., 2012) or rapid lithospheric delamination (Bao et al., 2014). Alternately, Hyndman et al. (2005) suggest that the thin lithosphere may be a long-lived feature related to the  $>180$  Ma history of subduction below this region. In the Hyndman et al. (2005) model, the subducting oceanic plate released water into the backarc mantle, lowering its viscosity and enabling vigorous mantle convection that maintains a hot, thin lithosphere. This predicts that the cordilleran mantle is both hot and extensively hydrated over a width of  $\sim 500$  km.

The eastern thermal limit of the cordillera approximately coincides with the southern RMT (Hyndman & Lewis, 1999). Below the RMT, there is an eastward increase in both mantle S-wave velocity ( $V_s$ ; Figures 2.2b and 2.2c) and electrical resistivity (Figures 2.2d and 2.2e). The change

in mantle properties coincides with an eastward decrease in surface heat flow to  $\sim 42$  mW/m<sup>2</sup> (e.g., Hyndman & Lewis, 1999) and an increase in effective elastic thickness from  $23 \pm 14$  km in the cordillera to  $121 \pm 40$  km east of the RMT (Flück et al., 2003). These observations are consistent with cool lithosphere east of the RMT, with a Moho temperature of  $\sim 400$ - $500$  °C and lithosphere thickness of  $>200$  km (Currie & Hyndman, 2006; Hyndman & Lewis, 1999). A joint analysis of  $V_s$  and gravity data shows that the RMT may also mark a compositional change to a chemically depleted mantle east of the RMT (Tesauro et al., 2014). Hyndman & Lewis (1999) argue the RMT marks the thermal edge of the Laurentian Craton, and that the Foreland Belt is a zone of thin-skinned thrust sheets that were emplaced on the cool, strong craton lithosphere.

A recent high resolution  $V_s$  study shows that the eastward velocity increase occurs over a lateral distance of 50-100 km, suggesting a subvertical step change in lithosphere thickness from the thin cordillera to thick craton (Chen et al., 2019). A sharp step in lithosphere thickness is generally eroded by both edge-driven convection and internal gravitational instabilities associated with its cool temperatures (e.g., Currie & van Wijk, 2016 and references therein). Numerical models show that to preserve a subvertical gradient for  $> 50$  Ma, the cratonic mantle lithosphere must be dry ( $<100$  ppm H/Si in olivine), and thus strong, with moderate chemical depletion (Currie & van Wijk, 2016; Hieronymus et al., 2007; Mallyon, 2017).

The above discussion suggests that there may be a contrast in both temperature and mantle hydration state between the cordillera and craton, such that the cordillera mantle is hot and hydrated (Hyndman et al., 2005) and the craton mantle is cool and dry (e.g., Currie & van Wijk, 2016). The goal of this study is to test these hypotheses by quantifying the temperature and water content at 75-150 km depth in Southern Canadian Cordillera. We use two independent geophysical observations to examine the mantle structure along with profiles ABC\_S and ABC\_N (Figure 2.1). Magnetotelluric (MT) data provides constraints on the mantle electrical resistivity, and seismic tomography provides constraints on mantle  $V_s$ . Both resistivity and  $V_s$  depend on the mantle temperature and water content. Ideally, the original seismic and MT observations should be jointly inverted to constrain mantle structure. However, this is a challenging problem. Instead, we take the approach of using published  $V_s$  and resistivity models, as an important first step in reducing uncertainties in upper mantle structure. We develop a joint analysis of the two models, using mineral physics data to link the observations to temperature and water content. In contrast, earlier

Vs analyses only considered the effects of temperature (e.g., Hyndman et al., 2009; Tesauro et al., 2014), and an analysis of resistivity used a fixed temperature structure (Rippe et al., 2013). By solving for temperature and water content simultaneously, we aim to improve the understanding of the mantle structure in southwestern Canada, especially at the cordillera-craton transition, and assess the implications for mantle dynamics.

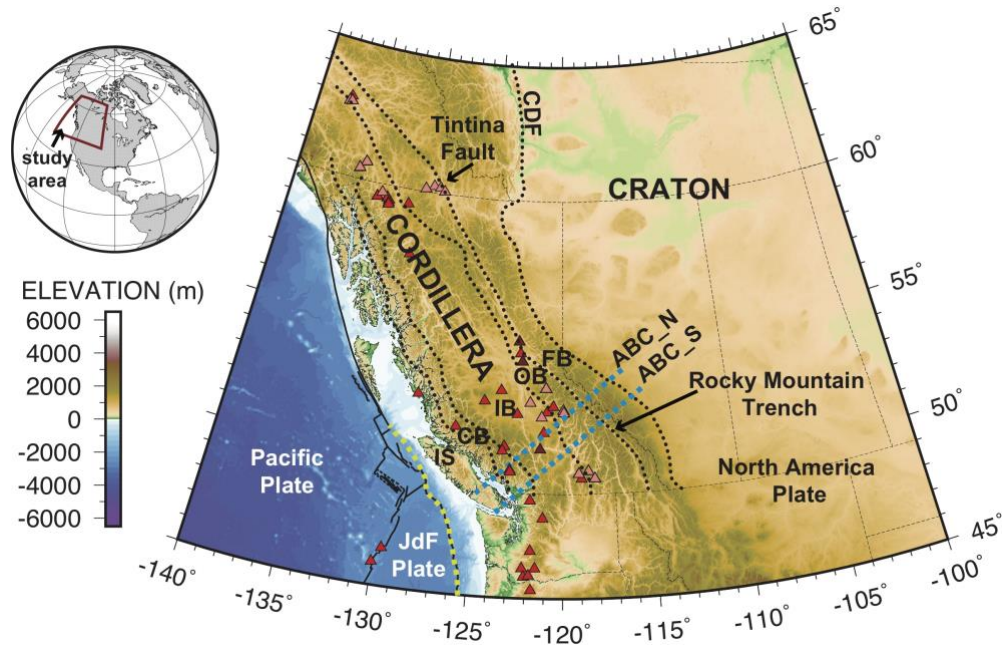


**Figure 2.1** Topography of western Canada, showing the cordillera and craton geological regions. The black dotted lines indicate the Cordilleran Deformation Front (CDF), Tintina Fault, Rocky Mountain Trench, and boundaries between the Foreland Belt (FB), Omineca Belt (OB), Intermontane Belt (IB), Coast Belt (CB), and Insular Belt (IS). Blue dashed lines are profiles ABC\_N and ABC\_S analyzed in this study. The red triangles denote Holocene volcanoes. Locations of lavas with mantle-derived xenoliths are shown as dark purple triangles (eruption age  $\geq 5$  Ma) and pink triangles (eruption age  $< 5$  Ma) (Canil et al., 2021; Francis et al., 2010). JdF is the Juan de Fuca plate, which subducts below North America at the plate margin (yellow dashed line).

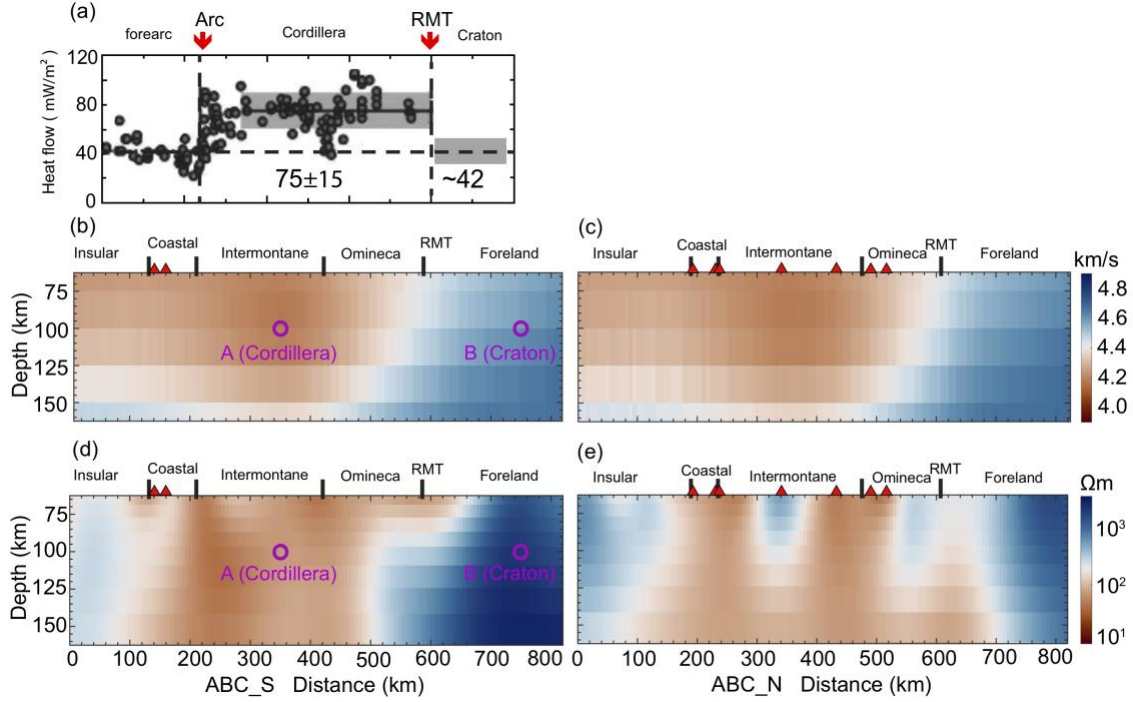


**Figure 2.2** Geophysical observations along the ABC\_S profile (a, b, d) and ABC\_N profile (c, e): (a) surface heat flow after correction for variations in crustal radiogenic heat (Currie & Hyndman, 2006) (b, c) shear wave velocity (Schaeffer & Lebedev, 2014), and (d, e) electrical resistivity (Rippe et al., 2013). Points A and B are used in the analysis in Section 2.3.1. Red triangles are locations of volcanoes erupted since 28 Ma within 50 km of each profile.

## 2.2 Data and analysis methods

### 2.2.1 Seismic shear wave velocity

The seismic analysis in this study uses the upper mantle shear wave velocity model SL2013NA (Schaeffer & Lebedev, 2014). This model provides the absolute isotropic  $V_{SV}$  velocity (i.e., vertically-polarized shear waves) of the upper mantle based on an inversion of surface and body S waves from vertical-component broadband seismograms. The model is discretized in steps of 0.25 degrees horizontally and 25 km vertically. Figure 2.2 shows two cross-sections through SL2013NA, coincident with the magnetotelluric profiles described below.

We follow the workflow of Goes et al. (2012) to map  $V_S$  to variations in temperature ( $T$ , in  $^{\circ}\text{C}$ ) and water content ( $C_{\text{OH}}$ , in ppm H/Si) using the analytic equation for absolute  $V_S$ :

$$V_s(T, C_{OH}) = V_{anh}(T, P, X) \left[ 1 - \frac{Q^{-1}(\omega, T, P, C_{OH}, d)}{2 \tan(\pi\alpha/2)} \right] \quad (2.1)$$

Where  $V_{anh}$  is the anharmonic velocity (i.e.,  $V_s$  at infinite frequency) for a given composition (X), with a correction for anelasticity based on the seismic quality factor (Q);  $\alpha$  is a constant (0.27). Q depends on T,  $C_{OH}$ , frequency ( $\omega$ ), pressure (P), and grain size (d). We use a frequency of 0.03 Hz, compatible with the dominant frequency in SL2013NA at 75 to 150 km depth, and a grain size of 10 mm (Behn et al., 2009; Goes et al., 2012). The pressure (P) is given by the depth, based on the density of the overlying material (3250 kg/m<sup>3</sup>).

Perple\_X (Connolly, 2009) is used to compute  $V_{anh}$  as a function of temperature and pressure from a phase equilibrium model. Based on the composition given by the user, Perple\_X determines the stable mineral phases, and hence their elastic properties and  $V_{anh}$ , at each pressure-temperature condition. We use the pyrolite composition of Xu et al. (2008), corresponding to primitive mantle, and the thermodynamic database NaCFMAS of Stixrude & Lithgow-Bertelloni (2011). Previous studies have shown that composition has a minor effect on  $V_s$  (Cammarano et al., 2003; Schutt & Lesher, 2006), and therefore we assume a homogeneous composition. In Section 2.3.4, the effect of a more depleted composition is examined. The compositions are given in Table 2.1.

$V_{anh}$  is then corrected for anelastic (attenuation) effects using the seismic quality factor (Q) (Karato, 1993). The effect of attenuation increases with increasing temperature, decreasing grain size, and decreasing seismic wave frequency (Jackson & Faul, 2010; Karato, 2003). In addition, hydration may enhance attenuation (e.g., Aizawa et al., 2008; Faul & Jackson, 2005; Karato, 2003). However, Abers et al. (2014) argue that hydration and grain size have competing effects, whereby higher water content leads to grain growth. As a result, hydration may have a minimal effect on attenuation (Abers et al., 2014; Cline et al., 2018). The temperature-dependence of attenuation is also uncertain. Laboratory experiments of Faul & Jackson (2005) suggest a moderate increase in attenuation with temperature. However, more recent studies suggest that there may be a dramatic increase in attenuation as temperatures approach the solidus owing to enhanced grain boundary sliding (McCarthy et al., 2011; Priestley & McKenzie, 2013; Takei, 2017; Yamauchi & Takei, 2016).

Given these uncertainties, we consider two different attenuation corrections,  $Q_F$  and  $Q_K$ .  $Q_F$  is based on the laboratory results of Faul & Jackson (2005) and includes a term for water content in olivine ( $C_{OH}$ ). We use the formulation and parameters from Behn et al. (2009; see Table 2.2). Figure 2.3a shows the calculated  $V_S$  at 100 km depth for olivine water contents ( $C_{OH}$ ) of 50 ppm H/Si (dry), 1000 ppm H/Si (damp) and 5000 ppm H/Si (wet). The anharmonic velocity shows a near-linear decrease with temperature. The effects of attenuation enhance the reduction in  $V_S$ , especially at temperatures greater than  $\sim 900$  °C and as the water content increases (Figure 2.3b).

Attenuation correction  $Q_K$  has no dependence on water content (Klöcking et al., 2018). This correction is based on the experimental results of McCarthy et al. (2011) and uses geophysical and petrological observations to constrain the key parameters (Klöcking et al., 2018; Priestley & McKenzie, 2013). Figure 2.3a shows the variation in  $V_S$  with temperature at 100 km depth for this attenuation correction. Attenuation has only a minor effect on  $V_S$  below  $\sim 1300$  °C. Above this, there is a significant decrease in  $V_S$ . This attenuation correction was applied to the northwestern United States by Klöcking et al. (2018) who showed that the seismically-determined temperatures are in good agreement with petrological and geochemical constraints on shallow mantle temperatures.

For comparison, Figure 2.3a shows the predicted  $V_S$  for two other attenuation corrections that do not depend on water content. The  $Q_S$  correction is based on experimental measurements of dry and nearly melt-free olivine by Jackson & Faul (2010), and the  $Q_Y$  correction is from laboratory measurements of a rock analog by Yamauchi & Takei (2016). These predict a reduction in  $V_S$  at high temperatures, although the temperature-dependence is reduced compared to  $Q_K$ . None of the attenuation corrections shown in Figure 2.3a include the effect of melt. If melt is present, the  $V_S$  may be further reduced. Priestley & McKenzie (2006) argue that the presence of melt leads to small variations in  $V_S$  ( $<1\%$ ), although observations of high seismic attenuation near several subduction zones appear to require the effects of melt (Abers et al., 2014).

### **2.2.2 Electrical resistivity**

To complement the seismic velocity analysis and reduce the non-uniqueness in interpretation, we use the mantle electrical resistivity structure derived from MT observations

(Rippe et al., 2013). Long-period MT observations with periods of 1-10,000s were collected along two parallel profiles (ABC\_S and ABC\_N; Figure 2.1) and inverted to obtain the 2D electrical resistivity to a depth of 150 km. Based on a small interstation spacing (~15 km), the resistivity structure is resolved on a grid with a horizontal spacing of ~6 km and vertical spacing of 9 to 20 km below a depth of 70 km (Figure 2.2).

To first order, the electrical resistivity ( $\rho$ ) of the mantle depends on its temperature and olivine water content (Gardés et al., 2014; Karato, 1990; Wang et al., 2006). There is also a dependence on composition since olivine, pyroxene and amphibole have different resistivities and therefore the overall resistivity will depend on the amount of each mineral. In addition, recent work has shown that hydration of pyroxene and other nominally anhydrous minerals may also affect the conductivity (Özaydın & Selway, 2020 and references therein). Given the uncertainties in the calculations for multiple minerals, in this study, we focus on olivine conductivity. We use the formulation of Gardés et al. (2014), who integrated published experimental measurements to constrain the mantle electrical conductivity (i.e., the inverse of resistivity) at temperatures of 200-1727 °C and olivine water contents of 0-2200 wt ppm H<sub>2</sub>O (0-36080 ppm H/Si). This formulation considers the uncertainties in conductivities, olivine water content, and temperatures, in order to fit experimental data. It is also consistent with most geophysical data with water content constraints by petrological predictions. The electrical conductivity of hydrous olivine as a function of temperature ( $T$ , in degrees K) and water content ( $C_{H_2O}$ , the hydrogen concentration of olivine in weight ppm) is given by:

$$\sigma(T, C_{OH}) = \sigma_0^{\text{Vacancy}} e^{-\frac{\Delta H^{\text{Vacancy}}}{RT}} + \sigma_0^{\text{Polaron}} e^{-\frac{\Delta H^{\text{Polaron}}}{RT}} + \sigma_0^{\text{Hydrous}} C_{H_2O} e^{-\frac{\Delta H^{\text{Hydrous}} - \beta C_{H_2O}^{1/3}}{RT}} \quad (2.2)$$

Where  $R$  is the ideal gas constant, and other parameters are constants from Gardés et al. (2014);  $\sigma_0$  are pre-exponential terms,  $\Delta H$  are activation enthalpy terms, and  $\beta$  is a positive constant. The overall olivine conductivity is the sum of the effects of ionic conduction, polaron hopping, and hydrogen conduction (terms 1, 2 and 3 in Equation 2.2). We use the parameters from the calibration of Withers et al. (2012; Table 2.2). Note that this does not include the effects of melt which enhances the conductivity (e.g., Sifré et al., 2014).

Figures 2.3c and 2.3d show the predicted variations in electrical resistivity with temperature and water content; note that the water content has been converted to ppm H/Si to be consistent with the  $V_s$  analysis (1 ppm H/Si  $\sim$  0.061 wt ppm, Hirth & Kohlstedt, 1996; Jones et al., 2012). Resistivity decreases with both increasing temperature and increasing water content. At a temperature of  $\sim$ 600 °C, the resistivity is  $\sim$ 10<sup>6</sup>  $\Omega$ m for a dry mantle (50 ppm H/Si) and  $\sim$ 10<sup>3</sup>  $\Omega$ m for a wet mantle (5000 ppm H/Si). At  $\sim$ 1400 °C, resistivity is  $\sim$ 10<sup>2</sup>  $\Omega$ m and  $\sim$ 10  $\Omega$ m, for dry and wet mantle, respectively.

For comparison, Figure 2.3c shows the resistivities predicted by Wang et al. (2006). This formulation is based on a Nernst-Einstein relationship from laboratory measurements of olivine (see Section 2.6.1). This also shows that the wet mantle has a lower resistivity than the dry mantle. When the mantle is wet and the temperature is below 700 °C, both Wang et al. (2006) and Gardés et al. (2014) give a similar resistivity. However, at higher temperatures, the resistivity from Wang et al. decreases more rapidly, and the resistivity is a factor of four lower at 1400 °C. For dry mantle, the Wang et al. (2006) resistivity is at least one order of magnitude smaller than Gardés et al. (2014) at temperatures less than 800 °C, but the difference decreases at higher temperatures.

### **2.2.3 Joint analysis of $V_s$ and resistivity**

Figure 2.3 shows that both seismic velocity ( $V_s$ ) and electrical resistivity ( $\rho$ ) depend on the temperature of the mantle. Resistivity is also dependent on the water content. The effect of water content on  $V_s$  is less clear, as hydration may act to decrease the seismic velocity (e.g., Aizawa et al., 2008; Faul & Jackson, 2005; Karato, 2003) or it may have no effect (e.g., Abers et al., 2014; Cline et al., 2018). Using these relationships, we aim to determine mantle temperatures and water content of the mantle in southwestern Canada through a joint analysis of the observed  $V_s$  and resistivity. By using both  $V_s$  and resistivity, the ambiguity in the competing effects of temperature and water content on the two observations is reduced. We use  $V_s$  and resistivity on the MT cross-sections ABC\_N and ABC\_S in the depth range 75 to 150 km. We have resampled these onto a common grid with a spacing of 25 km in the horizontal and vertical directions. This is comparable to the original grid of S2013NA and is coarser than that used in the MT measurements.

The seismic analysis uses two seismic attenuation models ( $Q_F$  and  $Q_K$ ) for a pyrolite (fertile) mantle composition with a grain size of 10 mm and seismic frequency of 0.03 Hz. The model of Gardés et al. (2014) is used to compute the resistivity for a specified temperature and olivine water content. These are used to calculate the predicted  $V_s$  and resistivity for temperatures of  $T=400-1500$  °C and olivine water contents of  $C_{OH}=1-11480$  ppm H/Si (Figure 2.3). At each point along the two profiles, we conduct a grid search to determine the misfit between the observed and predicted  $V_s$  and resistivity for each  $T-C_{OH}$  pair. We then determine the global misfit by summing L1 misfit functions based on the absolute percentage difference between the observed (obs) and predicted (pred) values of  $V_s$  and  $\rho$ :

$$\text{misfit}(V_s, \rho) = \frac{|V_{s_{\text{obs}}} - V_{s_{\text{pred}}}|}{|V_{s_{\text{obs}}}|} * 100 + \frac{|\log \rho_{\text{obs}} - \log \rho_{\text{pred}}|}{|\log \rho_{\text{obs}}|} * 100 \quad (2.3)$$

Because the electrical resistivity varies over orders of magnitude, we use a logarithmic scale to quantify the normalized residual. The misfit between predicted and observed values illustrates the fitting quality. Owing to the lack of a priori conditions on weighting seismic shear wave velocity and resistivity, they are weighted equally (Grose & Afonso, 2013). We also tested different weighting values for the  $V_s$  and resistivity misfits. The location of the global minimum of the total misfit is not significantly affected. The advantage of the L1 misfit is that it reduces the effect of outliers which may arise from other reasons in geophysical data (Zhang et al., 2014 and reference therein).

We conduct the analysis for both  $Q$  functions in order to assess the effects of the attenuation correction. For all data points, this approach produces a single global minimum in the misfit function. This allows us to define the  $T$  and  $C_{OH}$  values at each position that best-fit the observed  $V_s$  and resistivity at each point. We use the size of the misfit function as a measure of the uncertainty in the best-fit values (see Section 2.3.1).

This approach does not consider the presence of partial melt, which strongly decreases both  $V_s$  and resistivity. As shown below, most of the best-fit temperatures lie below the solidus, based on the depth and best-fit  $C_{OH}$  (Hirschmann et al., 2009; Katz et al., 2003; e.g., Figures 2.3c and 2.3d; see Section 2.6.2), and therefore melt is not required to explain the observed  $V_s$  and resistivity for the seismic and resistivity models used here. The exception is the shallow cordillera

mantle (75 km depth), where the  $Q_K$  analysis gives temperatures above the solidus. In addition, melt may be important for attenuation functions that have a lower  $V_S$  temperature-dependence (e.g.,  $Q_S$  on Figure 2.3a). This approach does not consider the presence of partial melt, which strongly decreases both  $V_S$  and resistivity. As shown below, most of the best-fit temperatures lie below the solidus, based on the depth and best-fit  $C_{OH}$  (Hirschmann et al., 2009; Katz et al., 2003; e.g., Figures 2.3c and 2.3d; see Section 2.6.2), and therefore melt is not required to explain the observed  $V_S$  and resistivity for the seismic and resistivity models used here. The exception is the shallow cordillera mantle (75 km depth), where the  $Q_K$  analysis gives temperatures above the solidus. In addition, melt may be important for attenuation functions that have a lower  $V_S$  temperature-dependence (e.g.,  $Q_S$  on Figure 2.3a). In these cases, the best-fit temperature may be an over-estimate. We have also verified that the best-fit  $C_{OH}$  values lie below the olivine saturation value at each depth (Hirschmann et al., 2005; Padron-Navarta et al., 2014).

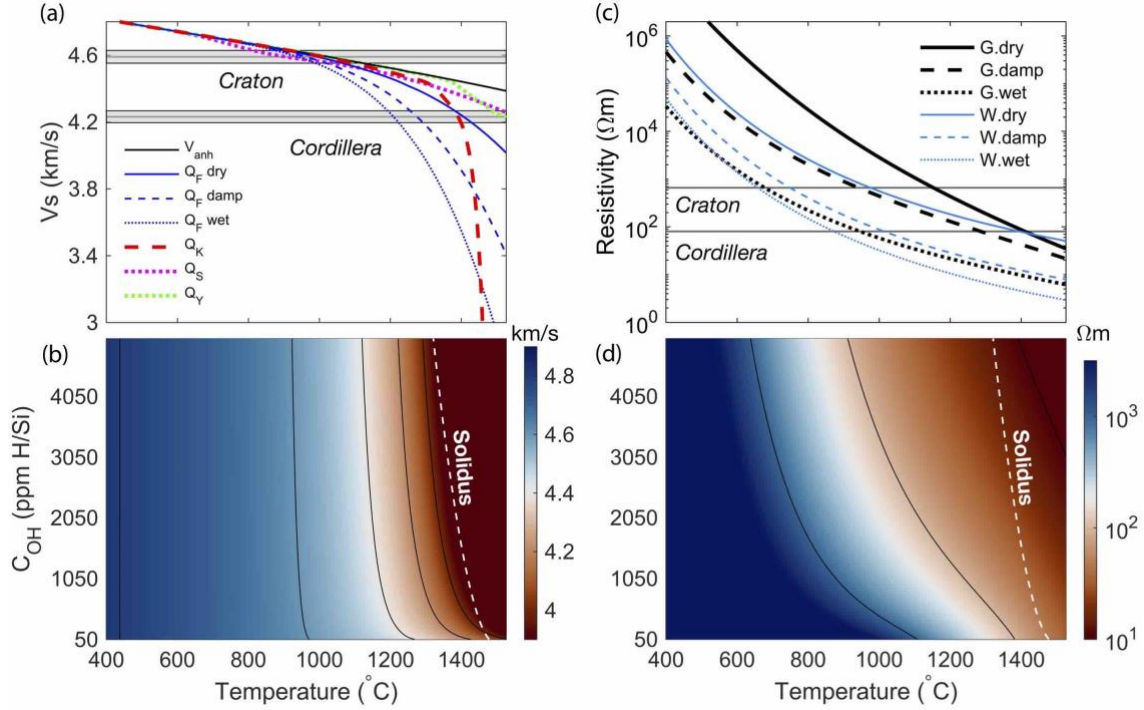


**Figure 2.3** (a) Predicted  $V_S$  at 100 km depth as a function of temperature ( $T$ ) for a pyrolite mantle with 10 mm grain size and 0.03 Hz frequency.  $V_{anh}$  is the anharmonic velocity (black line). The blue lines show the  $Q_F$ -corrected  $V_S$  for different olivine water contents ( $C_{OH}$ ): 50 ppm H/Si (dry; solid line), 1000 ppm H/Si (damp; dashed line), 5000 ppm H/Si (wet; dotted line). The dashed red line is  $Q_K$ -corrected  $V_S$ ; dotted purple line is  $Q_S$ -corrected  $V_S$ ; dotted green line is  $Q_Y$ -corrected  $V_S$ . Gray lines are average  $V_S$  for the cordillera and craton; gray areas are standard deviation. (b) Contour plot of  $V_S$  as a function of  $T$  and  $C_{OH}$  for the  $Q_F$  attenuation correction at 100 km depth with contours every 0.2 km/s. (c) Predicted electrical resistivity as a function of temperature for different olivine water contents, based on Gardés et al. (2014) (G, black) and Wang et al., (2006) (W, blue). (d) Contour plot of resistivity as a function of  $T$  and  $C_{OH}$  for Gardés et al. (2014) on a logarithmic scale. The white dashed line in (b;d) is the mantle solidus temperature for different  $C_{OH}$  (Hirschmann et al., 2009).

## 2.3 Results

### 2.3.1 Example calculations

We first present the analysis for two representative points along with profile ABC\_S. Both are at 100 km depth, with one beneath the cordillera and the other beneath the craton (Figure 2.2).

## Point A : Canadian Cordillera

The cordillera point has an observed  $V_s$  of 4.19 km/s and resistivity of 74  $\Omega\text{m}$ . Figure 2.4a shows the misfit for  $V_s$  and resistivity individually, as well as the joint misfit from Equation 2.3, using the  $Q_F$ -corrected  $V_s$ . As both  $V_s$  and resistivity depend on temperature and water content, the joint calculation allows us to reduce non-uniqueness. The minimum misfit for  $V_s$  occurs in the temperature range 1221 °C and 1367 °C, with lower temperatures corresponding to higher water content. The minimum misfit for resistivity also shows a trade-off between water content and temperature. The minima for  $V_s$  and resistivity are subparallel to one another, and as a result, the summation of the misfits yields an elongated global minimum, with its lowest value at 1294 °C and 1053 ppm H/Si (total misfit of 0.06 %). The narrowness of the minimum is measured using the distance between the global minimum to the point where the misfit is ten times larger along both the temperature and water content axes; the choice of ten times the minimum is arbitrary but provides a consistent way to quantitatively compare the results. The average distance on either side of the minimum is defined as the uncertainty in the best-fit T and  $C_{OH}$  ( $\delta T$  and  $\delta C_{OH}$ , respectively). For point A, the uncertainties are  $\delta T=73$  °C and  $\delta C_{OH}=560$  ppm H/Si.

Figure 2.4b shows the joint analysis of point A using the  $Q_K$ -corrected  $V_s$  function, which does not depend on water content. Hence, the  $V_s$  misfit only depends on temperature and has a minimum value at a temperature of  $\sim 1400$  °C. The joint misfit for seismic velocity and resistivity has an oval-shaped minimum, with a best-fit temperature of 1400 °C and  $C_{OH}$  of 253 ppm H/Si (total misfit of 0.08 %). The uncertainties are  $\delta T=6$  °C and  $\delta C_{OH}=48$  ppm H/Si. These are smaller than in the  $Q_F$  analysis because the individual misfits are not as strongly correlated. The  $Q_K$ -corrected  $V_s$  predicts a higher temperature and lower water content than the  $Q_F$  correction. This is because the  $V_s$ -T relationship is more non-linear (Figure 2.3a). The observed  $V_s$  value requires a higher temperature, and therefore a lower water content is needed to explain the observed resistivity.

## Point B : Craton

The same analysis is applied to point B in the craton ( $V_S=4.62$  km/s,  $\rho=1962$   $\Omega\text{m}$ ). This gives a best-fit temperature of 901 °C and  $C_{\text{OH}}$  of 485 ppm H/Si for the  $Q_F$ -corrected  $V_S$  (Figure 2.4c) with uncertainties of 28 °C and 114 ppm H/Si (global minimum misfit of 0.03 %). The  $Q_K$ -corrected  $V_S$  gives a best-fit temperature of 928 °C ( $\delta T=24$  °C) and  $C_{\text{OH}}$  of 385 ppm H/Si ( $\delta C_{\text{OH}}=84$  ppm H/Si) with a global minimum misfit of 0.02% (Figure 2.4d). For this point, the high  $V_S$  constrains the temperature to be less than  $\sim 1000$  °C for both Q corrections. At these temperatures, the attenuation correction is relatively small (Figure 2.3a), and therefore the best-fit temperature depends mostly on anharmonic  $V_S$ , which is the same for both analyses. This also means that the  $Q_F$  correction is relatively insensitive to the water content at these temperatures, and therefore, the final water content values are primarily determined by the resistivity analysis. In comparison to the cordillera point (A), the higher  $V_S$  and resistivity values for the craton are consistent with a cooler and drier mantle.

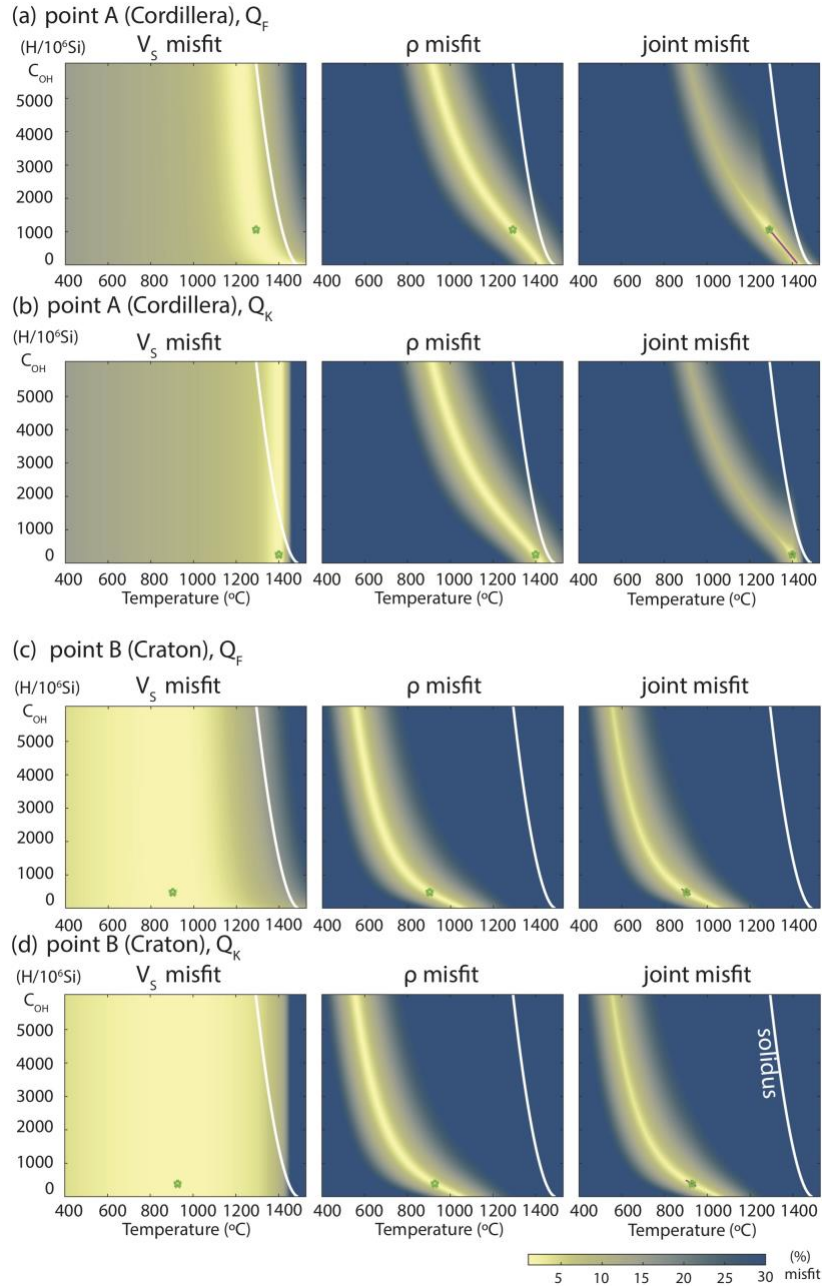


**Figure 2.4** Example analysis for  $V_S$  and resistivity ( $\rho$ ) for two points at 100 km depth along the ABC\_S profile (locations on Figure 2.2). The contour plots show the misfit between the observed and predicted values of  $V_S$  (left column) and  $\rho$  (middle column) and the summed misfit (right column, Equation 2.3) for: (a) cordilleran point and  $Q_F$  attenuation model, (b) cordilleran point and  $Q_K$  attenuation model, (c) craton point and  $Q_F$  attenuation model, and (d) craton point and  $Q_K$  attenuation model. All analyses use the Gardés et al. (2014) resistivity model. Green star shows the global minimum on the joint misfit plot, and magenta contour indicates where the misfit is ten times the global minimum. The white line is the mantle solidus temperature, as plotted in Figure 2.3b.

### 2.3.2 Mantle structure along the ABC\_S profile

The analysis is carried out for all points along with the ABC\_S profile. This profile shows a clear difference in  $V_S$  between the cordillera mantle ( $\sim 4.2$  km/s) and craton mantle ( $\sim 4.6$  km/s), with the transition approximately below the RMT (Figure 2.2b). The electrical resistivity varies from  $\sim 100$   $\Omega\text{m}$  for the cordillera to  $\sim 1000$   $\Omega\text{m}$  for the craton (Figure 2.2d).

The resulting best-fit temperature and  $C_{\text{OH}}$  structure are shown in Figure 2.5a for the  $Q_F$ -corrected  $V_S$  and Figure 2.5b for the  $Q_K$ -corrected  $V_S$ . Below the Intermontane and western Omineca Belts, the observations indicate a warm ( $\sim 1200$   $^{\circ}\text{C}$ ) and hydrated mantle ( $>1500$  ppm H/Si) for the  $Q_F$  correction (Figure 2.5a), whereas the  $Q_K$  correction gives a hotter ( $> 1350$   $^{\circ}\text{C}$ ) and drier ( $<1000$  ppm H/Si) mantle (Figure 2.5b). The uncertainties are generally larger for the  $Q_F$  correction, as the similar shapes of the  $V_S$  and  $\rho$  misfit functions lead to an elongated global misfit (e.g., Figure 2.4a). To the east of the RMT, temperatures are lower than  $1000$   $^{\circ}\text{C}$  and water contents are less than  $1000$  ppm H/Si. For the entire profile, both analyses have a minimum global misfit of  $0.1$  % or less for most points, showing that the observed  $V_S$  and resistivity can be explained by variations in temperature and  $C_{\text{OH}}$ . There is a cluster of points below the Omineca belt at  $100$ - $125$  km depth where the  $Q_K$  analysis gives a large misfit. This corresponds to an area with low  $V_S$  but high resistivity, where the joint analysis gives temperatures of  $1250$   $^{\circ}\text{C}$  and dry conditions. In addition, the best-fit temperatures are below the solidus for the best-fit water content for nearly all points, suggesting that no melt is required for the majority of the profile. The  $Q_K$  analysis gives temperatures that are above the solidus at  $75$  km depth for the Intermontane and western Omineca Belts.

To compare the cordillera and craton mantles, we plot histograms of the best-fit temperature and water content at each depth. For simplicity, the cordillera-craton boundary is taken as a vertical line beneath the RMT (Hyndman & Lewis, 1999). For each region, we calculate the mean and standard deviation for the temperature and water content at each depth. With the  $Q_F$  correction, the cordilleran mantle has an average temperature  $1208$  to  $1254$   $^{\circ}\text{C}$  (Figure 2.5c) and average water content of  $1470$  to  $1907$  ppm H/Si between  $75$  and  $150$  km depth (Figure 2.5e). The analysis with the  $Q_K$  correction gives a higher cordilleran mantle temperature ( $1348$  to  $1388$   $^{\circ}\text{C}$ ; Figure 2.5d) but lower water content ( $C_{\text{OH}}$  of  $512$  to  $686$  ppm H/Si; Figure 2.5f). Both analyses show that the craton mantle is cooler (average temperature of  $947$  to  $1034$   $^{\circ}\text{C}$ ), with a lower water content (average  $C_{\text{OH}}$  of  $238$  to  $887$  ppm H/Si). Although the histograms show scatter in the values

at each depth, there are no obvious depth variations in temperature or water content for either region. The analysis focused on a relatively narrow depth range (75 to 150 km depth). Owing to vertical smearing of the seismic and resistivity observations, as well as data uncertainties and smoothing in the inversion, it may not be possible to resolve small vertical variations in these properties.

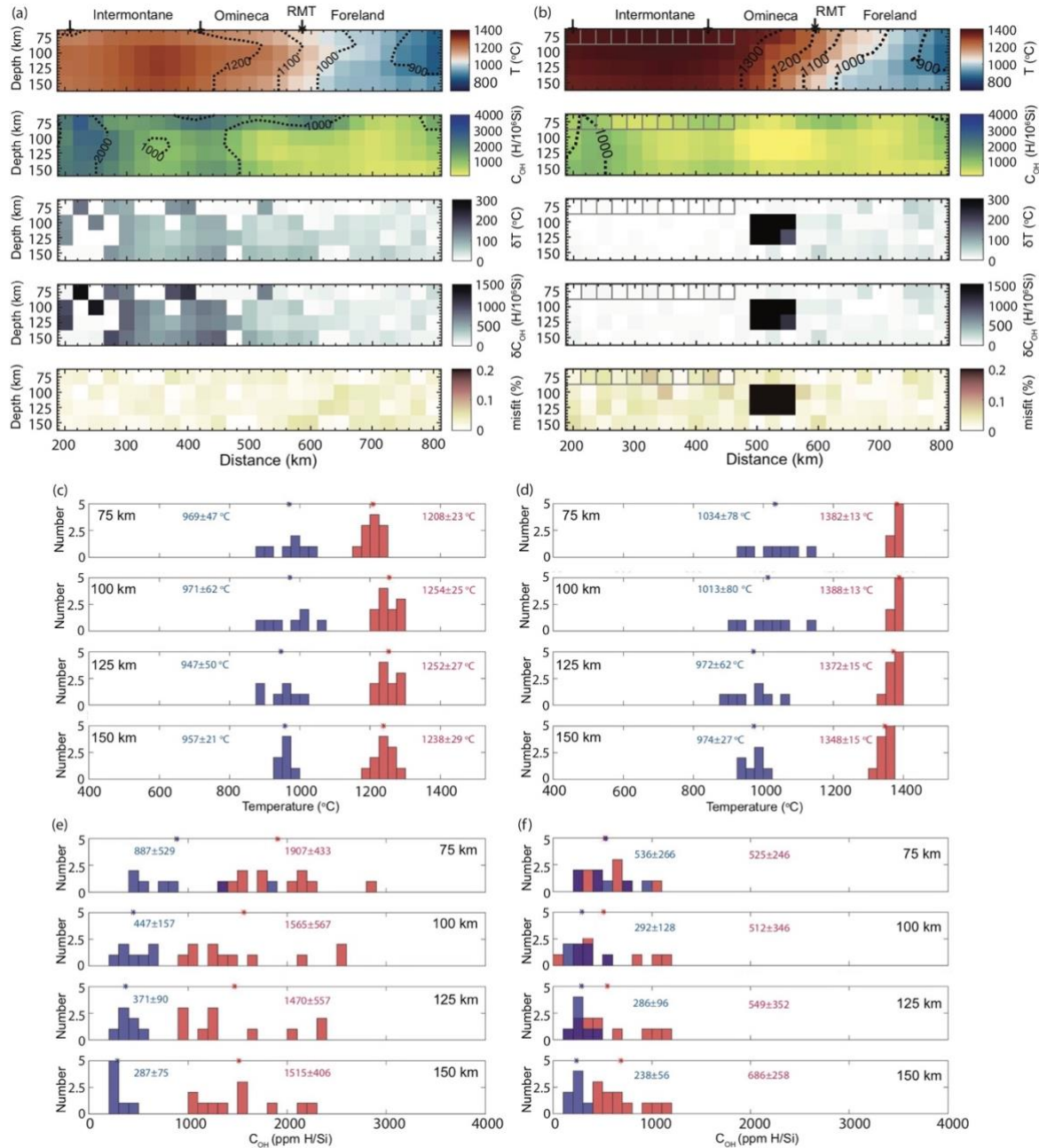


**Figure 2.5** Results of the joint analysis for the ABC\_S profile for the Gardés et al. (2014) resistivity model and Q<sub>F</sub> attenuation model (a, c, e) and Q<sub>K</sub> attenuation model (b, d, f). In (a) and (b), the plots from top to bottom are: best-fit T, best-fit C<sub>OH</sub>, temperature uncertainty (δT), water content uncertainty (δC<sub>OH</sub>) and global minimum misfit. Gray boxes indicate where the temperature is above the solidus based on the best-fit C<sub>OH</sub>. Histograms of best-fit values at each depth for (c) temperature and (e) water content using the Q<sub>F</sub>-corrected V<sub>S</sub>, and (d) temperature and (f) water content for the Q<sub>K</sub>-corrected V<sub>S</sub>. Red indicates cordilleran points (west of RMT) and blue is craton (east of RMT). The average and standard deviation for the cordillera and craton are given at each depth (units °C for temperature and ppm H/Si for water content).

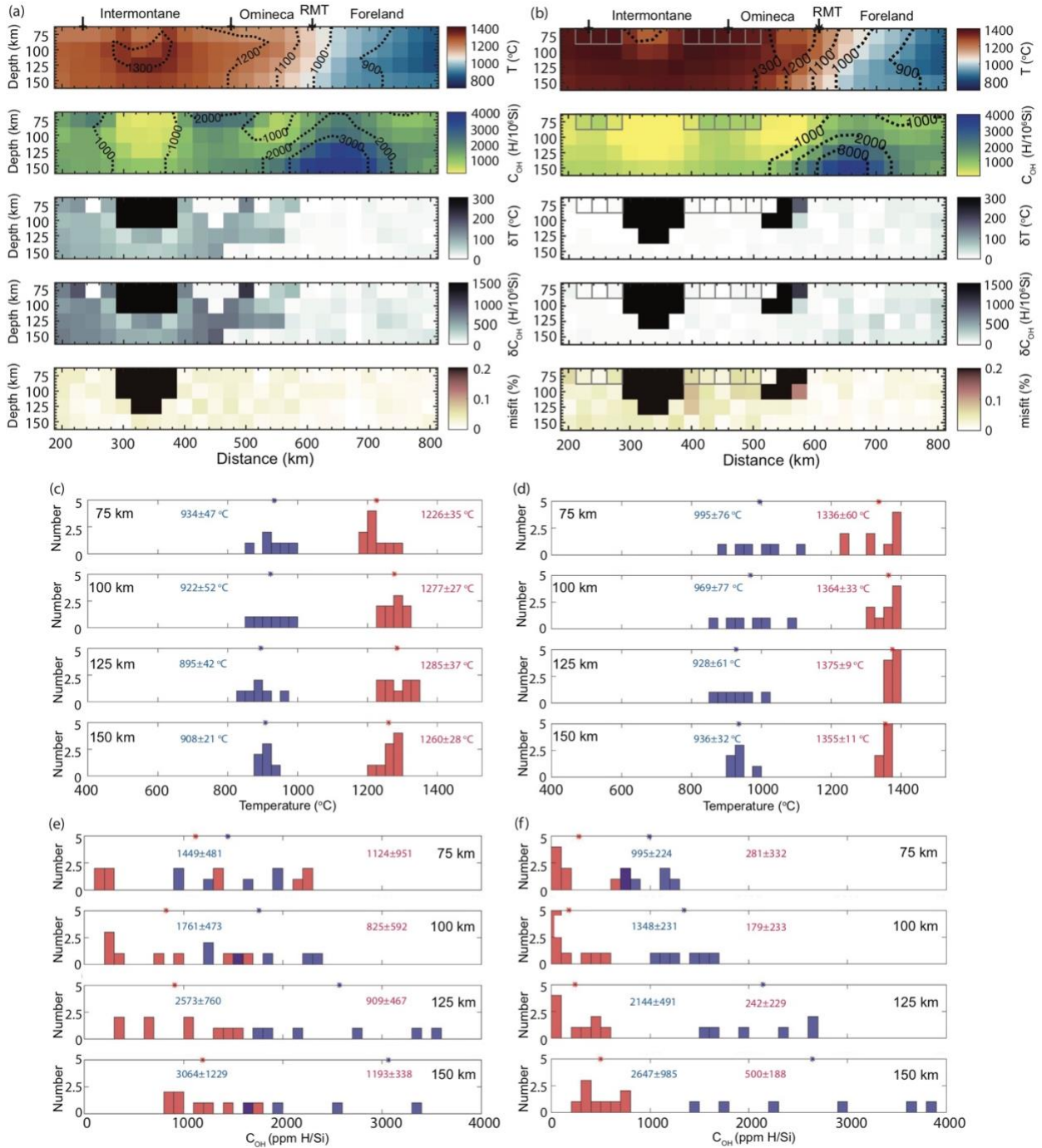
### 2.3.3 Mantle structure along the ABC\_N profile

Figure 2.6 shows the results for the ABC\_N profile. This profile exhibits low  $V_s$  below the cordillera and high  $V_s$  beneath the craton (Figure 2.2c). The MT data show a more heterogeneous resistivity structure than the ABC\_S profile, especially at depths less than 125 km (Figure 2.2e). The results are shown on Figure 2.6a for the  $Q_F$ -corrected  $V_s$  and Figure 2.6b for the  $Q_K$ -corrected  $V_s$ . The best-fit temperatures are similar to those for the ABC\_S profile, where the temperatures decrease from west to east. Below the Intermontane belt, temperatures are  $>1200$  °C for the  $Q_F$  analysis and  $>1300$  °C for the  $Q_K$  analysis, and temperatures below the craton are  $<1000$  °C for both analyses. The best-fit water content is more variable, and there is no clear difference between the cordillera and craton. Most areas have water contents  $>500$  ppm H/Si for both analyses, with some small-scale variations. There are two regions that appear to be anomalous. At 100 km depth below the central Intermontane Belt, both analyses suggest relatively dry ( $<1000$  ppm H/Si) mantle. This coincides with an area of high resistivity (Figure 2.2e) but low  $V_s$  (Figure 2.2c), and therefore, the analysis fits these observations with warm, dry mantle. This area has large uncertainties ( $\delta T > 300$  °C;  $\delta C_{OH} > 1500$  ppm H/Si) and a global misfit  $>10$  % in the  $Q_F$  and  $Q_K$  analysis (Figures 2.6a and 2.6b). The second anomalous region is below the RMT. At shallow depths, the  $Q_K$  analysis gives high temperatures and dry mantle, leading to a large misfit. At depths greater than 100 km, both analyses suggest a region of cool, hydrated mantle, based on the observed high  $V_s$  and low resistivity (Figure 2.2).

Results are summarized in histograms for the  $Q_F$ -corrected  $V_s$  (Figures 2.6c and 2.6e) and  $Q_K$ -corrected  $V_s$  (Figures 2.6d and 2.6f), using the RMT to define the cordillera-craton boundary (values in Table 2.5). The  $Q_F$  correction gives average cordillera mantle temperatures of 1226 to 1285 °C and craton temperatures of 895 to 934 °C, with little variation in depth. The  $Q_K$  correction gives cordillera temperatures of 1336 to 1375 °C and craton temperatures of 928 to 995 °C. For water content, the average cordillera values are  $\sim 1000$  ppm H/Si for the  $Q_F$  analysis and  $\sim 300$  ppm H/Si for the  $Q_K$  analysis. For each analysis, the average craton water content is larger than the cordillera at all depths, although there is significant scatter.

Figure 2.7 compares the observations and results for ABC\_N and ABC\_S at 100 km depth. The best-fit temperatures are similar for both profiles, with cordillera temperatures of  $\sim 1270$  °C for  $Q_F$  (Figure 2.7b) and  $\sim 1380$  °C for  $Q_K$  (Figure 2.7c) and craton temperatures of  $\sim 950$ - $990$  °C

for both Q corrections. For ABC\_S, the cordilleran mantle appears to be more hydrated than the craton. The water content is more variable for ABC\_N, with local variations and no clear difference between the cordillera and craton. The differences between the profiles are due to the resistivity observations, as the seismic shear wave velocity is almost identical for both profiles (Figure 2.7a). In particular, the mantle resistivity is more heterogeneous for ABC\_N, which leads to variations in best-fit  $C_{OH}$ , as resistivity provides the main constraint on water content.



**Figure 2.6** Results of the joint analysis of the ABC\_N profile for the Gardés et al. (2014) resistivity model and the  $Q_F$  attenuation model (a, c, e) and the  $Q_K$  attenuation model (b, d, f), with the format used in Figure 2.5.

### 2.3.4 Effect of parameter variations

In this section, we examine how variations in the seismic attenuation parameters, mantle composition, and resistivity model affect the best-fit mantle temperatures and water contents. We use the  $V_S$  and resistivity observations at 100 km depth along the ABC\_S profile (Figures 2.7a and 2.7b). The effects of parameter variations are reported relative to those obtained using the  $Q_K$  attenuation correction (0.03 Hz frequency), pyrolite composition, and Gardés et al. (2014) resistivity model.

Figure 2.8a shows the best-fit temperature (left column) and water content (right column) for different attenuation corrections. As shown above, the  $Q_F$  and  $Q_K$  corrections give similar craton temperatures and water contents, whereas  $Q_F$  gives cordillera temperatures that are  $\sim 100$  °C lower and water contents that are  $\sim 1000$  ppm H/Si higher than  $Q_K$ . We have also tested the  $Q_S$  attenuation model (Jackson & Faul, 2010), which has a weaker dependence on temperature than  $Q_F$  and  $Q_K$  (Figure 2.3a) and assumes that water content does not affect seismic velocity. For the cordillera, the  $Q_S$  correction gives temperatures that are up to  $\sim 100$  °C higher than  $Q_K$  and a dry mantle (Figure 2.8a). Near the western end of the profile, temperatures are close to the dry solidus and thus melt may occur. Owing to the low temperature-dependence of  $Q_S$ , the low cordillera  $V_S$  requires high temperatures. These high temperatures result in low resistivity, and therefore hydration is not needed to fit the observed resistivity. For the craton region,  $Q_S$  yields temperatures that are  $\sim 50$  °C lower and water contents that are  $\sim 500$  ppm H/Si higher than the reference  $Q_K$  results.

Figures 2.8b and 2.8c examine variations in seismic wave frequency and mantle composition, respectively, using the  $Q_K$  correction. Variations in wave frequency by an order of magnitude (Figure 2.8b) result in changes to cordillera temperatures of 20 °C and water content of  $\sim 200$  ppm H/Si, relative to the reference values, with higher temperatures and lower water content for higher frequencies. Variations in frequency have a smaller effect for the craton. Figure 2.8c shows variations in mantle composition, which is used in *Perple\_X* to obtain the anharmonic velocity. The reference pyrolite composition corresponds to a fertile composition. We also examine the more depleted compositions of modified harzburgite (Xu et al., 2008) and dunite (Griffin et al., 2009), which may be more representative of lithospheric mantle in cratonic regions. Changes in composition do not significantly change the cordillera structure. For the craton, the

pyrolite and modified harzburgite compositions give similar water contents. However, the modified harzburgite composition gives temperatures that are  $\sim 20$  °C cooler. Moreover, the dunite composition yields temperatures up to  $\sim 60$  °C higher and water contents up to  $\sim 300$  ppm H/Si lower.

The final test uses the resistivity model of Wang et al. (2006), with the reference  $Q_K$  attenuation correction (Figure 2.8a). Temperatures using this model are similar to those from the Gardés et al. (2014) model, but the water content is up to  $\sim 1000$  ppm H/Si lower than Gardés et al. for the cordillera and is  $< 100$  ppm H/Si for the craton. This is consistent with the variations in resistivity shown in Figure 2.3c at high temperatures.

An additional source of uncertainty comes from seismic tomography and magnetotelluric observations. Reasonable uncertainties in  $V_S$  for the SL2013NA model are  $\pm 0.1$  km/s in the shallow mantle (A. Schaeffer, personal communication, 2021). Uncertainties in observed resistivity are about a factor of two (i.e., variations in absolute resistivity by a factor of 0.5 or 2), corresponding to an even uncertainty on a log scale (Karato & Wang, 2013; Rippe, 2012). To assess the effects of data uncertainties, we redo the analysis for the example data points (Section 2.3.1), using the  $Q_K$  correction (with reference parameters) and Gardés et al. (2014) resistivity model. For Point A in the cordillera, adding the uncertainties to both  $V_S$  and  $\rho$  yields a best-fit temperature of 1338 °C and  $C_{OH}$  of 1 ppm H/Si (i.e., dry); subtracting the uncertainties gives  $T=1415$  °C and  $C_{OH}=1109$  ppm H/Si (Figure 2.13). For Point B in the craton, the data uncertainties give best-fit values of  $T=651$  to 1121 °C and  $C_{OH}=5$  to 1833 ppm H/Si, with the lowest  $T$  and highest  $C_{OH}$  for the upper limits of  $V_S$  and resistivity (Figure 2.14). This shows that data uncertainties lead to variations in temperature ( $\sim 40$  °C) for the cordillera point but significant variations for the craton point ( $\sim 250$  °C). For both regions, uncertainties in water content are as much as  $\sim 2000$  ppm H/Si.

Figure 2.8 shows that the choice of attenuation correction ( $Q_K$ ,  $Q_F$ , or  $Q_S$ ) has the greatest effect on cordillera temperatures and water contents. Cordillera water contents also depend strongly on the choice of resistivity models, with the Wang et al. (2006) model requiring lower water contents to fit the observed low resistivity. For the craton, the choice of the  $Q$  models has a lesser effect on the calculated structure, but a depleted composition results in temperature increase of up to  $\sim 60$  °C and water content decrease of 200-300 ppm H/Si. The resistivity model of Wang

et al. (2006) gives a nearly dry craton mantle. We conclude that if the seismic Q model is well-constrained, the temperature structure at 100 km depth in the cordillera, a region with low  $V_s$  and low resistivity, can be obtained with uncertainties ( $<100$  °C). In contrast, temperatures in the craton, a region with higher  $V_s$  and resistivity, depend more strongly on both individual parameter choices and uncertainties in the observed  $V_s$  and resistivity. If observations have low uncertainties, we estimate that the craton temperature uncertainty is  $\sim 100$  °C. These uncertainties are similar to those from previous studies that have used seismic velocities to obtain upper mantle temperatures. Goes & van der Lee (2002) estimated uncertainties of 150 °C between 50 and 250 km depth beneath western North America, and Cammarano et al. (2003) give an uncertainty of 100 °C if the mantle composition is well known.

Uncertainties in the olivine water content are fairly high, especially when data uncertainties are considered. Even with well-constrained observations, the choice of the attenuation correction and resistivity model strongly affects the best-fit water content (Figure 2.8a). For the different Q models, there is a trade-off between temperature and water content, where higher temperatures correspond to lower water contents.

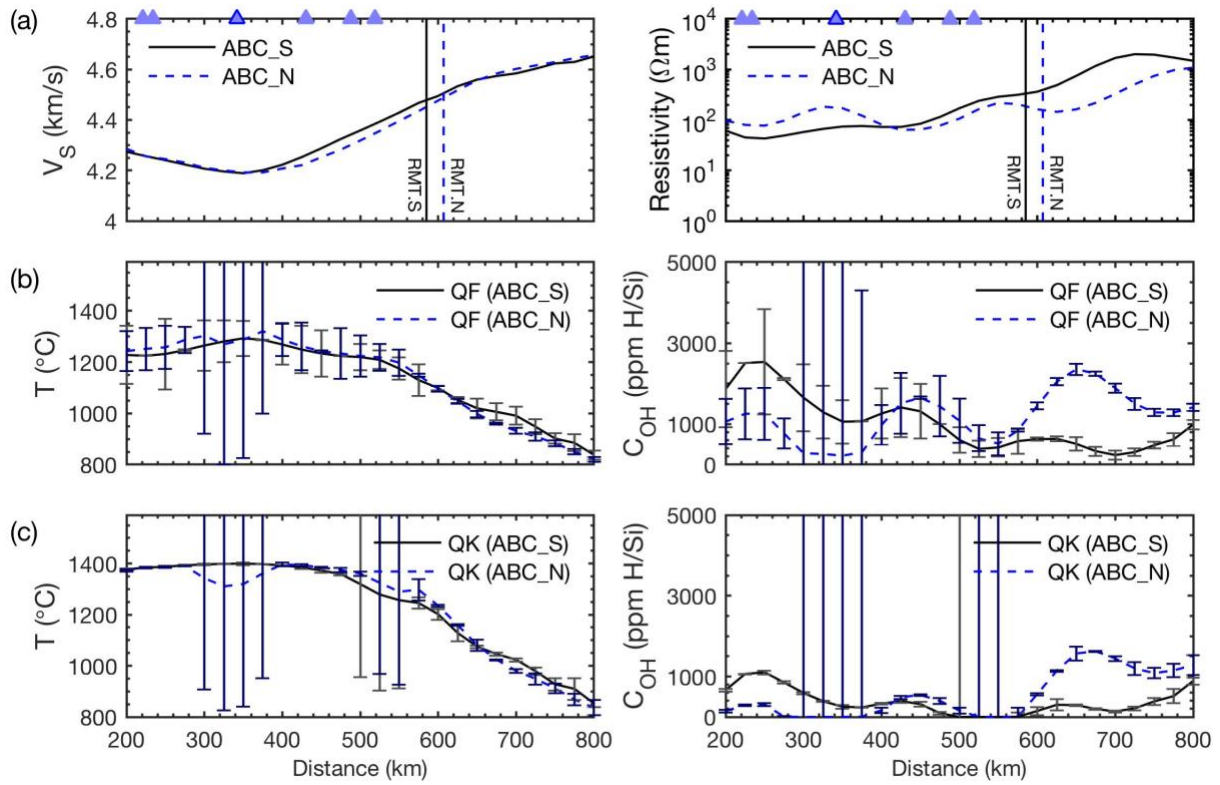


**Figure 2.7** (a) Observed  $V_S$  (left) and resistivity (right) at 100 km depth for profiles ABC\_S (black line) and ABC\_N (dashed blue line), with the RMT.S and RMT.N labels indicating where the RMT crosses the ABC\_S and ABC\_N profiles, respectively and shown as a vertical line with the same line style. (b) The results of the joint analysis showing the best-fit temperatures (left) and water contents (right) and their uncertainties using the  $Q_F$  correction for each profile. (c) Best-fit temperatures (left) and water contents (right) their uncertainties using the  $Q_K$  correction. Volcanoes on the ABC\_N profile note as blue triangles. The triangle with black outline is the oldest volcano (6 Ma) that sites between the two profiles (location in Figure 2.1).

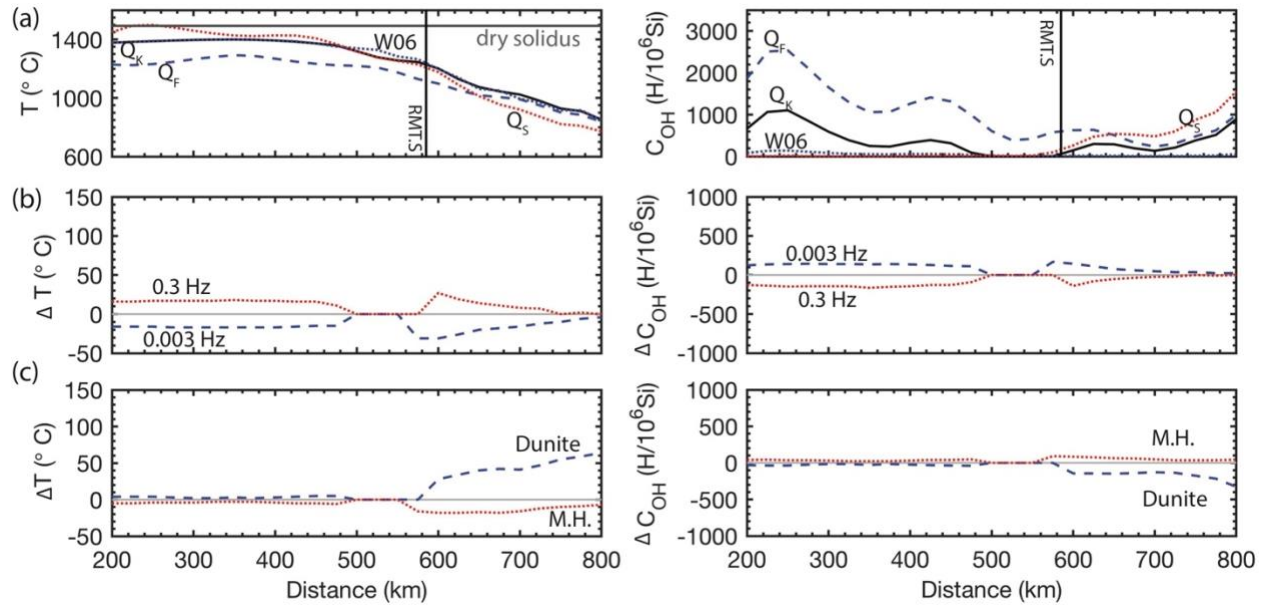


**Figure 2.8** Effect of parameter variations for the joint analysis for the ABC\_S profile at 100 km depth. (a) Best fit temperatures (left) and water content (right) for different Q corrections ( $Q_K$  solid black line,  $Q_F$  dashed black line;  $Q_S$  dotted red line), using a grain size of 10 mm, seismic frequency of 0.03 Hz, pyrolite composition, and the Gardés et al. (2014) resistivity model. The dotted black line (W06) shows the results using the reference  $Q_K$  attenuation correction and Wang et al. (2006) resistivity model. The lower plots show the difference in temperature (left) and water content (right) relative to the reference  $Q_K$  values for variations in: (b) seismic wave frequency, (c) mantle composition. M.H. is Modified Harzburgite.

## 2.4 Discussion

### 2.4.1 Cordilleran mantle structure

Geophysical observations show a significant contrast between the cordillera and craton regions of southwest Canada. Relative to the craton, the cordillera has higher surface heat flow, lower mantle  $V_S$  and lower mantle resistivity, where the transition between the two regions occurs in the vicinity of the RMT (Figure 2.2). In this study, we have conducted a joint analysis of  $V_S$  and resistivity to determine the mantle temperature and water content at 75 to 150 km depth. Figure 2.9 shows the average geotherm and olivine water content profile for the cordillera region along the ABC\_S profile. Our analysis gives mantle temperatures of  $\sim 1240$  °C for the  $Q_F$  correction and  $\sim 1370$  °C for the  $Q_K$  correction. The average olivine water content is  $\sim 1600$  and  $\sim 600$  ppm H/Si

for the  $Q_F$  and  $Q_K$  corrections, respectively. As noted above, there is a trade-off between temperature and water content in fitting the observed  $V_S$  and resistivity. Variations in temperature as a function of depth are small. Along the ABC\_N profile, the mantle temperatures from the two Q corrections are similar to those of ABC\_S, but water content is more variable owing to changes in resistivity along this profile (Figure 2.7).

Our cordillera temperatures can be compared to those from previous geophysical and geological studies near the ABC\_S profile (Figure 2.9a). Surface heat flow for the cordillera is  $75 \pm 15$  mW/m<sup>2</sup> after correction for lateral variations in crustal radiogenic heat, indicating temperatures  $>800^\circ\text{C}$  at the Moho ( $\sim 33$  km depth) (Currie & Hyndman, 2006). At greater depths, seismic velocities have been used to determine mantle temperatures. Hyndman et al. (2009) determined a regional mantle geotherm for the Canadian Cordillera based on the NA04  $V_S$  model (van der Lee & Frederiksen, 2005). Their geotherm is in good agreement with results from the  $Q_F$  correction. Tesauro et al. (2014) combined gravity observations and seismic tomography data and found temperatures in excess of  $1300^\circ\text{C}$  at 100 km depth for the cordillera, which is similar to temperature estimates from the  $Q_K$  correction. Both  $Q_F$  and  $Q_K$  corrections demonstrate two end-member geotherms, highlighting the importance of this correction.

Direct constraints on mantle temperatures come from thermobarometry measurements of xenoliths and analysis of olivine compositions from lavas (Figure 2.9a). Greenfield et al. (2013) obtained a Moho temperature between  $800$  and  $850^\circ\text{C}$  from xenoliths in the southern Canadian Cordillera. Below the Moho, xenolith analyses give temperatures of  $900$ - $1040^\circ\text{C}$  at  $35$ - $50$  km depth (Saruwatari et al., 2001) and up to  $\sim 1300^\circ\text{C}$  at  $60$ - $70$  km depth, which was inferred to be the base of the lithosphere (Ross, 1983). The cordilleran region is characterized by basaltic magmatism that originates in the shallow mantle. A study of recent alkaline lavas inferred temperatures of  $1300$ - $1475^\circ\text{C}$  at  $45$ - $100$  km depth (Canil et al., 2021). These temperatures are similar to those obtained farther south where analyses of magmas from the Basin and Range and Rio Grande Rift (western United States) indicate temperatures of  $1336 \pm 67^\circ\text{C}$  (Klöcking et al., 2018; Plank & Forsyth, 2006).

Water content for the cordilleran mantle has been determined in two ways. First, Rippe et al. (2013) used electrical resistivities along ABC\_S to infer water content, assuming a 1-D geotherm corresponding to a  $1300^\circ\text{C}$  mantle adiabat with a gradient of  $0.4^\circ\text{C}/\text{km}$  below  $50$  km

depth. Using the Wang et al. (2006) resistivity model, they suggested average olivine water contents of ~1640-3280 ppm H/Si in the 75 km and 150 km depth range to the west of the RMT. At 100 km depth, Jones et al. (2014) estimated water contents in olivine of <10 wt. ppm (<170 ppm H/Si). Water content has also been inferred from the chemical analysis of igneous rocks (Figure 2.9b). Hyndman and Canil (2021) and Canil et al. (2021) argue that the source region of alkaline lavas contains 150-300 ppm H<sub>2</sub>O (~1000-2000 ppm H/Si in olivine), based on similarities to basaltic magmas from the western United States. In contrast, mantle xenoliths suggest a much drier mantle lithosphere (<660 ppm H/Si in olivine; depths <65 km), which may reflect the lower storage capacity of olivine in the spinel stability field (Canil et al., 2021; Hyndman & Canil, 2021). Additionally, laboratory studies estimate that globally, the upper mantle has a minimum of ~400 ppm H/Si in olivine and that water content may increase with depth (Kovács et al., 2012).

Our results with the Q<sub>F</sub> correction suggest a relatively hydrated cordilleran mantle at depths greater than 75 km, in agreement with Hyndman & Canil (2021) and Canil et al. (2021). However, the temperatures for the Q<sub>F</sub> correction are ~200 °C lower at 100 km depth (Figure 2.9a). In contrast, the Q<sub>K</sub> correction predicts higher mantle temperatures (1388 °C) but a relatively dry upper mantle (512 ppm H/Si) owing to the trade-off between temperature and water content needed to explain the observed V<sub>s</sub> and resistivity. Therefore, our analysis of the geophysics data suggests either a warm, wet mantle or a hot, dry mantle, whereas the alkaline lavas are interpreted to reflect hot and wet conditions. Further work is needed to assess the discrepancy between the geophysical and petrological analyses. Possible factors affecting our study include limitations of the geophysical observations (e.g., lateral smoothing, anisotropy), as described in the next section. The geophysical data sample the present-day mantle structure, but give a smoothed view of the structure over distances of 10 to 100 km (Rippe et al., 2013; Schaeffer & Lebedev, 2014), whereas the analyses of xenoliths and lavas represent local samples at the time of eruption. For southwestern Canada, these samples range in age from 28 Ma to <5 Ma (Figure 2.1).

For most of the cordillera, we find the mantle temperatures are below the hydrated mantle solidus, especially if the Q<sub>F</sub> correction is used (Hirschmann et al., 2009; Katz et al., 2003), and thus no widespread melt is required to explain the observed V<sub>s</sub> and resistivity. This appears to be at odds with the basaltic magmatism found throughout the southern Canadian Cordillera (e.g., Canil et al., 2021). However, such melts are proposed to occur at depths shallower than 70 km

(e.g., Canil et al., 2021; Klöcking et al., 2018). Further, Priestley & McKenzie (2013) argue that there is unlikely to be more than 0.1% melt present in the convecting mantle. This amount of retained melt may not have a significant effect on  $V_s$  and resistivity. We note that the  $Q_K$  correction gives conditions above the hydrated solidus at 75 km depth for the cordillera mantle, which may be consistent with ponding of melt at shallow depths inferred by Klöcking et al. (2018) and Hyndman & Canil (2021).

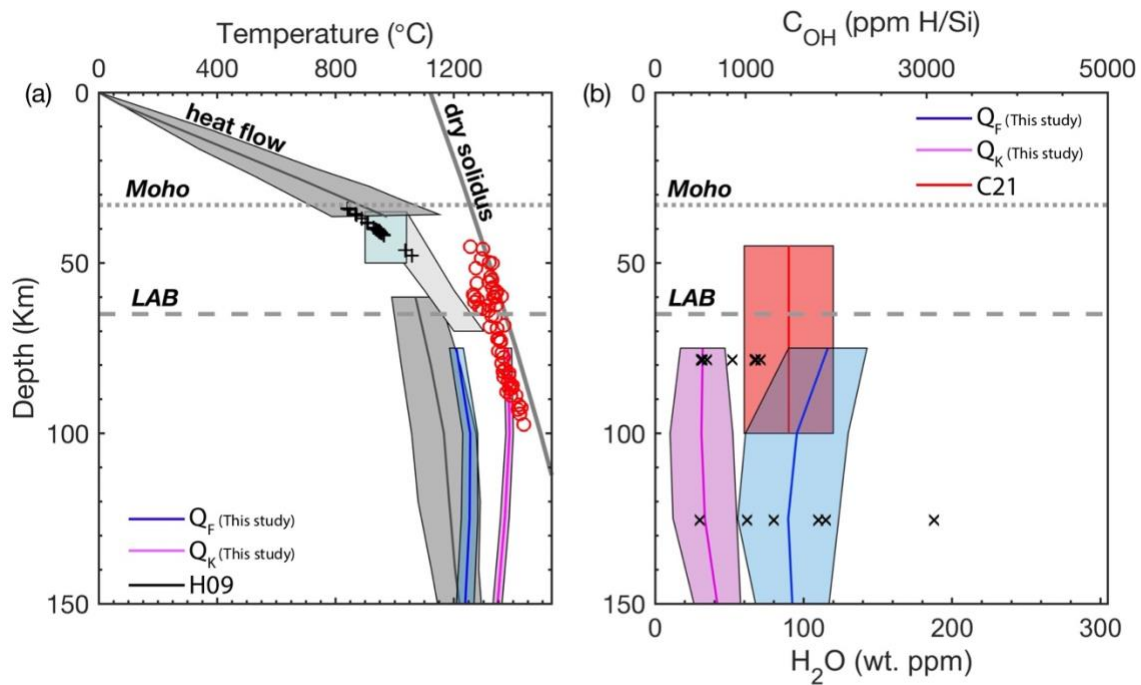


**Figure 2.9** (a) Vertical temperature profile for the cordillera from the joint analysis using the  $Q_F$  correction (blue) and  $Q_K$  correction (magenta) based on the average and standard deviation for ABC\_S. Gray shaded regions show temperatures from Hyndman et al. (2009; H09) based on surface heat flow (crust) and  $V_s$  (mantle). Symbols show temperatures from mantle xenoliths from Greenfield et al. (2013; black pluses), Saruwatari et al. (2001; light turquoise), and Ross (1983; light gray) and mantle-derived magmas from Canil et al. (2021; red circles). Dark gray line is the dry solidus (Hirschmann et al., 2009). (b) Vertical profile of olivine water content from this study ( $Q_F$  in blue;  $Q_K$  in magenta), with experimental measurements (Kovács et al., 2012, black crosses) and the value inferred by Canil et al. (2021; C21) at 45-100 km depth.

### 2.4.2 Craton mantle structure

Figure 2.10 shows the average geotherm and olivine water content for the craton region along the ABC\_S profile. Our analysis gives mantle temperatures of  $\sim 960$  °C for the  $Q_F$  correction and  $\sim 1000$  °C for the  $Q_K$  correction, with little depth variation. The average olivine water content is  $\sim 700$  ppm H/Si at 75 km depth and decreases to  $< 400$  ppm H/Si below 100 km depth. The higher water content at 75 km depth is due to low resistivity. This area underlies a region of low crustal resistivity, which may affect resolution of the shallow mantle resistivity structure (Rippe et al., 2013). Along the ABC\_S profile, there is a decrease in both temperature and water content from the cordillera to the craton. The craton temperatures along the ABC\_N profile are similar to the ABC\_S profile, but water content is more variable, owing to local variations in the resistivity values along this profile. Rippe et al. (2013) suggested that the enhanced resistivity beneath the ABC\_N profile is associated with variations in the plate boundary from a subduction zone to a strike-slip motion.

The craton thermal structure in southwest Canada has been determined using geophysical observations (Figure 2.10a). The surface heat flow is  $42 \pm 10$  mW/m<sup>2</sup>, indicating Moho temperatures of 400-500 °C at 40-50 km depth (Currie & Hyndman, 2006; Hyndman & Lewis, 1999). Previous analyses of mantle  $V_s$  give temperatures that increase from  $\sim 770$  to  $\sim 980$  °C at depths of 75 km to 150 km (Hyndman et al., 2009),  $\sim 800$ -1000 °C at 100 km depth (Tesauro et al., 2014), and  $\sim 950$ -1100 °C at 150 km depth (Chen et al., 2019). There have been no xenolith studies of the craton in our study area. However, xenoliths from kimberlite pipes in other parts of North America, including the Slave Craton (Russell & Kopylova, 1999), Sask Craton (Czas et al., 2020), and Buffalo Head Terrane (Aulbach et al., 2004) give temperatures that increase from  $\sim 650$  °C at  $\sim 80$  km depth to  $\sim 1280$  °C at  $\sim 155$  km.

There are also no direct measurements of olivine water content in our study area. Xenolith studies of the Slave (Baptiste et al., 2012), Kaapvaal (Doucet et al., 2014), and Siberian Cratons (Kilgore et al., 2020) suggest that cratonic mantle lithosphere is generally quite dry, with olivine water contents of  $< 800$  ppm H/Si (Figure 2.10b). These are similar to what we obtain for the deep craton in southwestern Canada from the geophysical data (Figure 2.10b).

Our craton temperatures agree with those from previous studies at  $> 125$  km depth (Figure 2.10a). However, at shallower depths our temperatures are 200-300°C higher than those from

xenolith studies (Figure 2.10a), and these differences can not be reduced with reasonable variations in the parameters used in our analysis (Figure 2.8). The high temperatures in our study are related to the relatively low  $V_s$  ( $\sim 4.5$ - $4.6$  km/s) at these depths in the SL2013NA tomography model. Using the NA04 model, Hyndman et al. (2009) also found that the temperature of the shallow craton in western Canada is somewhat higher than the xenolith trend. They suggest that the  $V_s$  values are anomalously low due to vertical smoothing of seismic velocities (i.e., contamination by the crust) or that the uppermost mantle is within the spinel stability field (Hyndman et al., 2009; Lebedev et al., 2009). Several other factors may also influence the geophysical observations, and thus temperatures, in this area. First, the measurements are within 200 km of the RMT, which marks an abrupt change in mantle properties. The  $V_s$  and MT measurements are not well-suited to mapping the edges of sharp anomalies, owing to the long wavelengths of Rayleigh waves and electromagnetic signals (Hyndman et al., 2009; Unsworth & Rondenay, 2013). Therefore, some of the high temperatures obtained for the shallow craton may reflect lateral averaging with the adjacent cordilleran properties. Further, the craton edge may have been heated over time. Eaton et al. (2018) show that this can result in a reduction in seismic velocity, especially at shallow depths. Another possibility is that the craton may have experienced metasomatism, which may result in lower regional seismic velocities (Eeken et al., 2018). Our analysis does not include the effects of hydrous minerals (e.g., amphibole, antigorite) or carbonate on seismic velocity. Finally, the SL2013NA tomography model uses vertically-polarized Rayleigh waves ( $V_{sv}$ ). If there is significant radial anisotropy, the isotropic shear wave velocity will be underestimated (Garber et al., 2018). To date, there have been no detailed studies of the anisotropic  $V_s$  values in our study area, although anisotropy in the shallow craton has been observed (e.g. Bao et al., 2016; Currie et al., 2004; Wang et al., 2020). The global anisotropy model SUMUCB\_WM1 (French & Romanowicz, 2014) shows radial anisotropy in our study area, with horizontal shear wave velocities ( $V_{sh}$ ) higher than  $V_{sv}$  (Figure 2.9c).

If the  $V_s$  values are anomalously low due to one or more of the factors listed above, this will affect the water content obtained in our analysis, which is primarily determined by the electrical resistivity values. To assess this, we assume that the temperature at 100 km depth is 700 °C, similar to that from xenolith studies (Figure 2.10a). At this temperature, the observed craton resistivities ( $\sim 700 \Omega\text{m}$ ) would require a relatively hydrated mantle with  $\sim 5000$  ppm H/Si in olivine (Figure 2.3c). This is below the storage capacity of olivine (Padrón-Navarta & Hermann, 2017),

but it is much higher than water contents inferred for other cratons (e.g., Peslier et al., 2010). One possibility is that the observed resistivity may reflect metasomatism and/or the presence of hydrous minerals (e.g., phlogopite) within a cool mantle lithosphere, as both factors will result in a decreased resistivity (Li et al., 2016; Özaydın et al., 2021); as noted above, these will also affect  $V_s$  (Eeken et al., 2018). Further work is needed to test this.

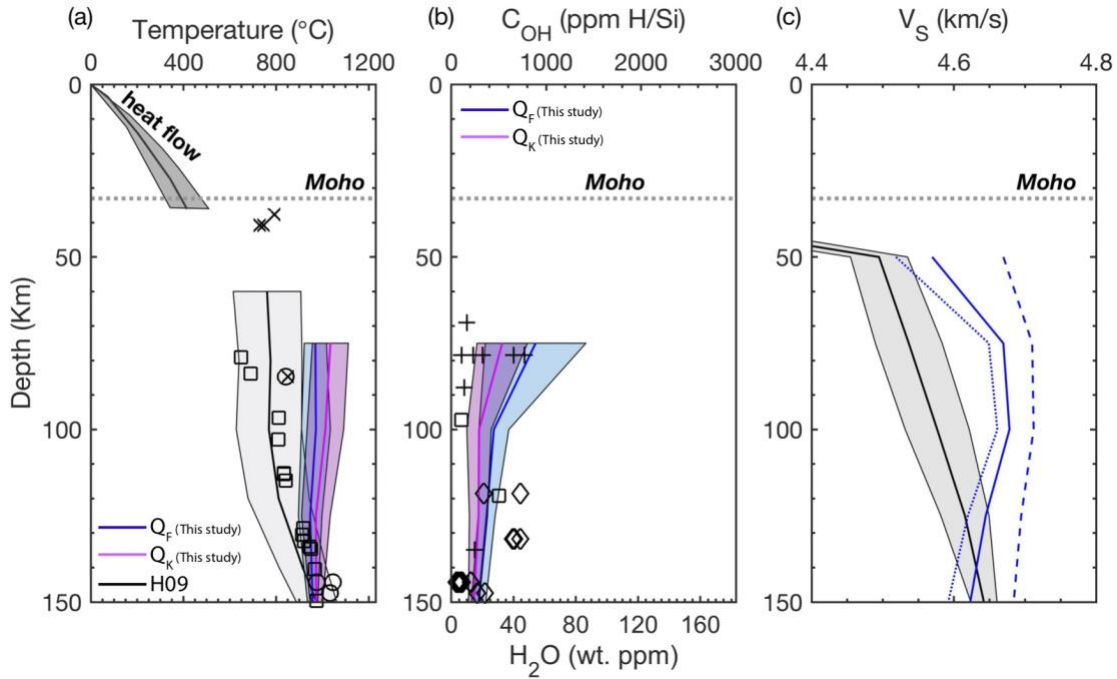


**Figure 2.10** (a) Vertical profile of the craton mantle temperature ( $Q_F$  in blue;  $Q_K$  in magenta) based on ABC\_S, with temperatures from Hyndman et al. (2009; H09 in gray) based on surface heat flow (crust) and  $V_s$  (mantle), and mantle xenoliths from Slave Craton, Buffalo Hills kimberlites, and Sask Craton, respectively (Kopylova & Russell, 2000, squares; Aulbach et al. 2004, crosses; Czas et al., 2020, circles). (b) Vertical profile of olivine water content ( $Q_F$  in blue;  $Q_K$  in magenta), with olivine water content of mantle xenoliths from kimberlite pipes in Kaapvaal, Siberian, and Slave Cratons, respectively (Baptiste et al., 2012, diamonds; Doucet et al., 2014, pluses; Kilgore et al., 2020, squares). (c)  $V_s$  from SL2013NA (black line and grey shaded area; Schaeffer & Lebedev, 2014) and SEMUCB\_WM1 (blue line :  $V_{SISO}$ ; blue dashed line :  $V_{SH}$ ; blue dotted line :  $V_{SV}$ ; French & Romanowicz, 2014).

### 2.4.3 Regional Q values

One of the key uncertainties in our determination of cordillera temperatures is the seismic attenuation (Q) correction (Equation 2.1). We have used Q corrections that are based on laboratory measurements of attenuation, although we note that the  $Q_K$  correction was calibrated using experimental studies from McCarthy et al. (2011) and geophysical and petrological observations (Priestley & McKenzie, 2013). The laboratory results must be extrapolated to mantle conditions, which leads to large uncertainty, especially in the grain size and strain rate (Abers et al., 2014). Therefore, having independent measurements of Q for the mantle would allow for a more robust temperature determination (Cammarano et al., 2003).

As part of finding the temperature and water content that are consistent with the observed  $V_s$  and resistivity, we obtain the corresponding Q value. Figure 2.11 shows the predicted Q values based on the  $V_s$  and resistivity with the depth. Q is generally 20-70 for the cordillera and ~200-2000 for the craton for both ABC\_N and ABC\_S. There are no regional Q observations for this area to confirm our predictions. However, at 100-200 km depth, global studies suggest that Q values are <70 for western North and South America, and Q values for stable regions such as eastern North America are higher (>100) (e.g., Mitchell, 1995). The global attenuation model QRFSI12 (Dalton et al., 2008) shows Q values of 60 to 100 for western Canada, with some indication that Q is higher in the craton.

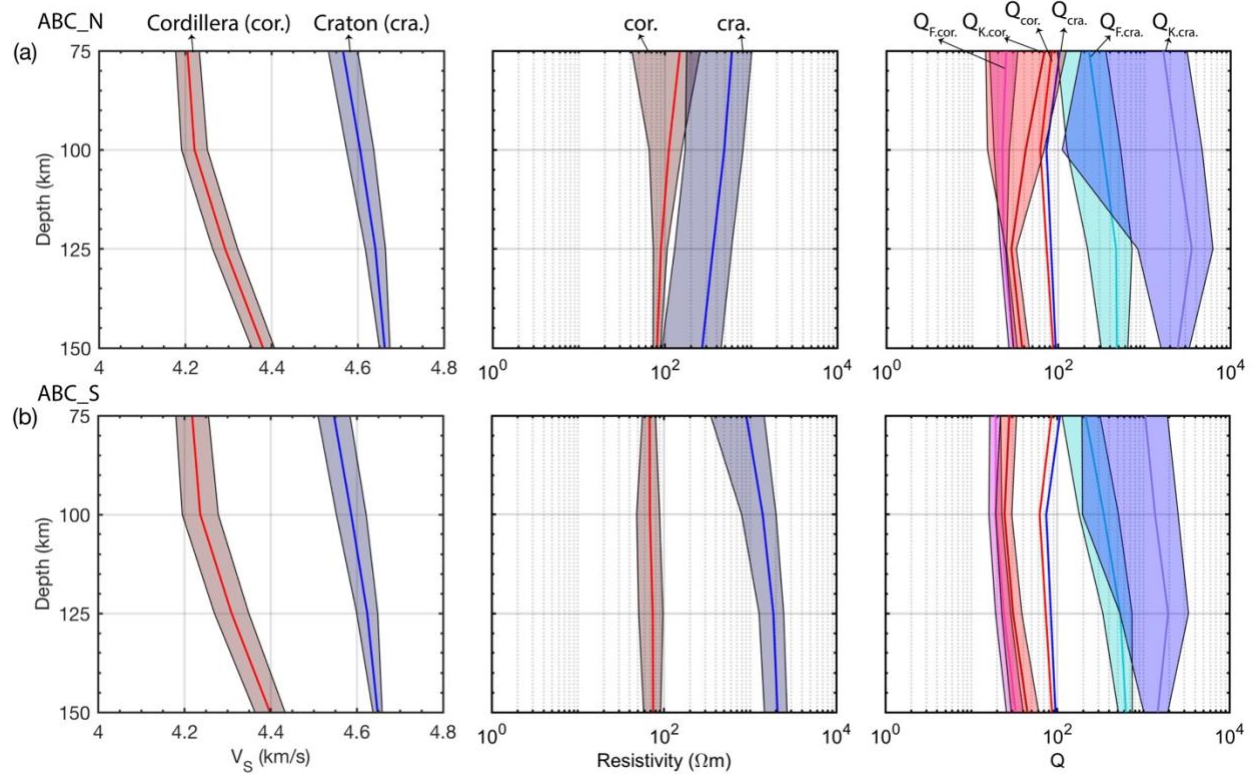


**Figure 2.11** Observed average and standard deviations of  $V_s$  (left), resistivity (center), and seismic Q (right) along (a) ABC\_N and (b) ABC\_S from Schaeffer & Lebedev (2014), Rippe et al. (2013), and Dalton et al. (2008), respectively, for the cordillera (red line) and craton (blue line). The predicted Q from the joint analysis is also shown.

#### 2.4.4 Mantle viscosities below western Canada

We can use the mantle structure obtained in our analysis to make inferences about the mantle viscosity and dynamics in western Canada, as mantle rheology primarily depends on its temperature and the water content of olivine (e.g., Hirth & Kohlstedt, 1996, 2003). Here, we consider dislocation creep and diffusion creep, where the effective viscosity is:

$$\eta_i(T_K, P, \sigma, C_{OH}, d, \phi) = \frac{1}{2} (A_i d^{-p_i} C_{OH}^{r_i})^{-1} \sigma^{1-n_i} \exp\left[\frac{(E_i + PV_i)}{RT_K}\right] \exp(-\alpha\phi) \quad (2.4)$$

where  $i$  is the creep mechanism,  $R$  is the gas content, and the rheological parameters are the pre-exponential factor ( $A$ ), the water content exponent ( $r$ ), the stress exponent ( $n$ ), the activation energy ( $Q$ ), and the activation volume ( $V^*$ ). The effective viscosity decreases with increasing temperature, water content, and stress, and it increases with increasing pressure (depth). The effective viscosity ( $\eta_{eff}$ ) of the composite rheology is:

$$\eta_{eff} = \left(\frac{1}{\eta_{dif}} + \frac{1}{\eta_{dis}}\right)^{-1} \quad (2.5)$$

where  $\eta_{dis}$  is the dislocation creep viscosity and  $\eta_{dif}$  is the diffusion creep viscosity. More information is given in the Section 2.6.3.

We use the best-fit temperature and water contents to calculate the effective viscosity of the mantle for ABC\_S and ABC\_N profiles based on Equations 2.4 and 2.5. Our calculations use the rheological parameters for wet olivine aggregates from Hirth & Kohlstedt (2003) and Behn et al. (2009) (in Table 2.4) and a constant stress of 0.3 MPa. This stress is compatible with that inferred from geophysical observations (Hirth & Kohlstedt, 2003) and from geodynamic models (e.g., Behn et al., 2009; Currie & van Wijk, 2016). At depths <150 km and low stresses, deformation grain boundary sliding can generally be ignored (Hirth & Kohlstedt, 2003). An increase in stress by a factor of 2 results in a decrease in effective viscosity by a factor of ~0.18. We do consider the effect of melt on mantle viscosity. However, the  $Q_K$  analysis suggests that there may be melt at 75 km depth for the cordillera mantle, which may lead to lower viscosities that given here.

Figure 2.12 shows the predicted effective viscosity for each profile. Both  $Q$  analyses suggest that the cordillera mantle has low viscosity, owing to its high temperatures and/or hydrated

conditions. We obtain viscosities of  $<10^{21}$  Pa s for the  $Q_F$  analysis and  $<10^{20}$  Pa s for the  $Q_K$  analysis. The differences are primarily due to the higher temperatures for the  $Q_K$  analysis. These viscosities are similar to the values of  $10^{20}$ - $10^{21}$  Pa s derived from post-glacial rebound for the Intermontane belt (James et al., 2000). In the craton, we predict viscosities of  $>10^{23}$  Pa s more than 100 km east of the RMT, owing to the cooler temperatures and somewhat drier conditions. The viscosity contrast between cordillera and craton is similar to that found in the western United States between tectonically active regions, which are inferred to be hot and hydrated in the backarc regions, and cool, dry craton regions (Dixon et al., 2004).

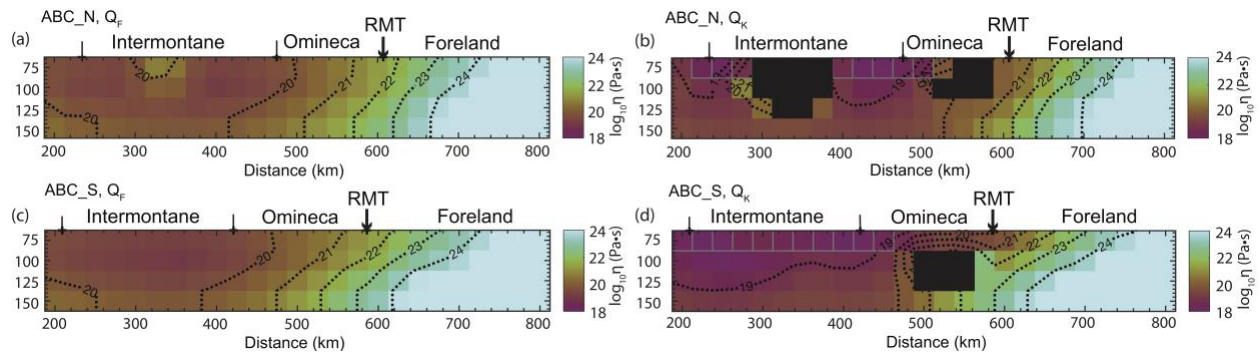


**Figure 2.12** Effective viscosity for the mantle based on the best-fit temperature and olivine  $C_{OH}$  along (a, b) ABC\_N and (c, d) ABC\_S. Left column is from the  $Q_F$  attenuation function and right column is from the  $Q_K$  attenuation function; both use the Gardés et al. (2014) resistivity model. Areas shown in black have large misfit values (shown in Figure 2.5b and Figure 2.6b).

### 2.4.5 The cordillera-craton boundary and implication for mantle dynamics

Our results show that the contrast in geophysical properties between cordillera and craton primarily reflects temperature variations, where the cordilleran mantle is 300-400 °C hotter than the craton at 100-150 km depth. This is generally compatible with earlier geophysical and petrological studies and is consistent with the juxtaposition of hot, thin (50-70 km) cordilleran lithosphere with cool, thick ( $>200$  km) craton lithosphere (e.g. Hyndman & Lewis, 1999). Although there are uncertainties in the quantification of mantle water content, the  $V_s$  and resistivity observations suggest that the cordilleran mantle appears to have a water content of  $\sim 600$  to

~1600 ppm H/Si along ABC\_S, compared ~300 ppm H/Si for the craton. For ABC\_N, water content is more variable and there is no clear difference between the cordillera and craton. Our results shown here do not unambiguously support the hypothesis of Hyndman et al. (2005) that the cordillera mantle is both hot and hydrated. There are trade-offs between the temperatures and water contents needed to explain the geophysical observations. If the petrological constraints on mantle temperature are correct (~1400 °C; Canil et al., 2021), the mantle may only have an olivine water content of ~600 ppm H/Si; in contrast, a more hydrated mantle would have lower temperature. In either case, the results give viscosities  $<10^{21}$  Pa s for the cordillera mantle (Figure 2.12). Therefore, our results support the idea of a low viscosity cordillera mantle, where small-scale convection maintains the hot, thin lithosphere (Hyndman et al., 2005).

The transition in geophysical properties from the cordillera to the craton is centred approximately below the RMT. The transition occurs over a width of 100-150 km, and the boundary between the two regions appears to dip toward the west (e.g., Figure 2.12). Our study uses long wavelength surface waves and electromagnetic waves, and thus has relatively low lateral resolution. A recent high-resolution seismic study using P- and S- body waves also shows a subvertical to westward dipping craton boundary, with the transition over a width of 50-100 km (Chen et al., 2019). Dense MT stations ( $<15$  km) would enhance the lateral resolution.

The contrast in properties allows us to assess the stability of the western edge of the craton. Numerical models show that a step in lithosphere thickness remains stable only if the thick lithosphere is both cool and nearly dry ( $<50$  ppm H/Si in olivine, e.g., Currie & van Wijk, 2016; Mallyon, 2017). From our analysis, we find that the craton along ABC\_S is less hydrated than the cordillera; the difference in hydration below ABC\_N is less clear. However, for both profiles, the geophysical data appear to require some water ( $>200$  ppm H/Si in olivine) in the cratonic mantle, and thus the craton edge may be susceptible to deformation. With this water content, geodynamic models show that the cratonic mantle may undergo deformation due to both internal gravitational instabilities and stresses from edge-driven convection (Currie & van Wijk, 2016b; Hardebol et al., 2012; Mallyon, 2017). Therefore, the present-day geometry (e.g., Figure 2.2) may be a transient feature. Lithosphere instability in this region has been suggested to occur through both the progressive erosion of the craton margin (Hardebol et al., 2012) and through episodic delamination (Bao et al., 2014). Ongoing erosion and thinning of the lithosphere has been proposed to be occurring today immediately south of our study area (DiCaprio et al., 2020). Geodynamic models

that link mantle dynamics with geophysical and magma observations are needed to assess the implications for the cordillera-craton boundary evolution in western Canada.

## 2.5 Conclusions

Our study uses two independent geophysical data sets ( $V_s$  and resistivity) to assess the mantle structure of southwestern Canada at 75 to 150 km depth. By carrying out a joint analysis of the two datasets, we aim to determine both the mantle temperature and water content, in order to gain insights into the mantle properties of the cordillera and craton, and the transition between the two regions. The main conclusions are:

1. The average cordillera mantle temperature is  $\sim 1240$  to  $\sim 1370$  °C and the average olivine water content is  $\sim 600$  to  $\sim 1600$  ppm H/Si, with no clear variations with depth. The main uncertainty comes from the seismic attenuation correction, and our analysis shows that there is a trade-off between the temperature and water content needed to fit the observed  $V_s$  and resistivity. For most of the cordilleran mantle, no widespread melt is predicted. However, if the  $Q_K$  attenuation correction is used, the conditions at 75 km depth are above the solidus and some melt may occur.

2. Craton mantle temperatures are  $\sim 960$ - $1000$  °C. The craton water content, although poorly constrained, appears to be  $< 500$  ppm H/Si at 75 km depth and decreases with depth. The average temperatures at  $< 125$  km depth are higher ( $\sim 200$  °C) than those expected from xenoliths in other cratons, which may reflect the presence of seismic anisotropy or hydrous minerals.

3. Using our preferred attenuation correction, our analysis shows that the cordilleran mantle has a viscosity of  $10^{19}$  to  $10^{21}$  Pa s, compared to  $10^{22}$ - $10^{24}$  Pa s for the craton. Thus, the mantle may be weak enough undergo small-scale and edge-driven convection that can maintain the high temperatures and thin (50-70 km) lithosphere.

4. The transition between the cordillera and craton western boundary occurs below the RMT, and the boundary between the two regions is subvertical to west-dipping. Although the craton appears to be less hydrated than the cordillera, the geophysical observations require some hydration, and therefore the craton mantle may be weak enough to undergo deformation. Future

geodynamic models are needed to assess the dynamics of the cordillera-craton boundary based on the structure obtained in this study.

## 2.6 Appendix

### 2.6.1 Calculation of shear wave velocity and resistivity

The calculation of shear wave velocity ( $V_s$ ) follows the method used by Goes et al. (2012). First, the anharmonic  $V_s$  is calculated using `Perple_X` (Connolly, 2005) and Stixrude & Lithgow-Bertelloni (2011) NaCFMAS thermodynamic database (STX11). We have tested the three compositions given in the Table 2.1: pyrolite (fertile), modified harzburgite (melt-depleted), and dunite (depleted). The modified harzburgite given by Xu et al. (2008) represents as a basalt-harzburgite mixture.

**Table 2.1** Bulk oxide composition for the three mantle compositions considered in this study.

Component (mol%)	Na <sub>2</sub> O	MgO	Al <sub>2</sub> O <sub>3</sub>	SiO <sub>2</sub>	CaO	FeO
Pyrolite <sup>a</sup>	0.11	49.85	2.22	38.71	2.94	6.17
Dunite <sup>b</sup>	0	59.95	0.144	35.06	0.073	4.77
Modified harzburgite <sup>a</sup>	0	56.54	0.65	36.04	0.79	5.97

<sup>a</sup> Xu et al., 2008

<sup>b</sup> Griffin et al., 2009

Second, the parameters in Table 2.2 are used to calculate seismic quality factor ( $Q$ ), values. We have examined four  $Q$  formulations: Faul & Jackson (2005;  $Q_F$ ), Klöcking et al. (2018;  $Q_K$ ), Yamauchi & Takei (2018;  $Q_Y$ ), and Jackson & Faul (2010;  $Q_S$ ). The parameters used in the  $Q_F$  correction are based on those given by Behn et al. (2009). Seismic  $Q$  is applied to the anharmonic velocity to get  $V_s$ , following Equation (2.1).

**Table 2.2** Parameters used in calculations of  $V_s$  and  $Q_F$ 

Parameter	Value	Units	Description
$V_s$		m/s	S wave velocity
$V_{anh}$		m/s	S wave velocity at infinite frequency
T		Kelvin	temperature
P		Pa	pressure
X			composition
$\alpha$	0.27		non-dimensional frequency dependence
$\omega$	0.03	Hz	frequency
d	10	mm	grain size
$Q_F(\omega, T, P, C_{OH}, d)$			Faul & Jackson (2005); Behn et al. (2009)
pQ	1		grain size exponent
$p_{Qref}$	1.09		reference grain size exponent
$d_{Qref}$	1.24E-5	m	reference grain size
$B_0$	1.28E8	$m^{pQ} s^{-1}$	prefactor for Q
$C_{OH(Qref)}$	50	ppm H/Si	reference water content in olivine
rQ	1.2		water content exponent
$P_{Qref}$	300	MPa	reference pressure
$E_Q$	420	$kJ mol^{-1}$	activation energy
$V_Q$	1.2E-5	$m^3 mol^{-1}$	activation volume
$E_{Qref}$	505	$kJ mol^{-1}$	reference activation energy
$V_{Qref}$	1.2E-5	$m^3 mol^{-1}$	reference activation volume
$T_{Qref}$	1265	$^{\circ}C$	reference temperature

The calculation of electrical resistivity is based on studies hydrous olivine. We have examined two conductivity models from Gardés et al. (2014) and Wang et al. (2006). Equation (2.2) gives the formulation of Gardés et al. (2014), where the conductivity is the inverse of the resistivity. From Wang et al. (2006), the electrical resistivity is given by

$$\rho_{ol}(T, C_{H_2O}) = \sigma_0^{Hydrous} C_{H_2O}^r e^{-\frac{\Delta H^{Hydrous}}{RT}} \quad (2.6)$$

The parameters for the two models are given in Table 2.3.

**Table 2.3** Hydrous olivine conductivity parameters

Parameter	Value	Units	Description
<b>Gardés et al. (2014) formulation (Equation 2.2)</b>			
$C_{\text{H}_2\text{O}}$		wt ppm	
$\log \sigma_0^{\text{Vacancy}}$	5.07	$\text{S m}^{-1}$	ionic conduction
$\Delta H^{\text{Vacancy}}$	239	$\text{kJ mol}^{-1}$	ionic activation enthalpies
$\log \sigma_0^{\text{Polaron}}$	2.34	$\text{S m}^{-1}$	conductivity due to polaron hopping
$\Delta H^{\text{Polaron}}$	144	$\text{kJ mol}^{-1}$	activation enthalpy due to polaron hopping
$\log \sigma_0^{\text{Hydrous}}$	-1.37	$\text{S m}^{-1}$	conductivity due to hydrogen
$\Delta H^{\text{Hydrous}}$	89	$\text{kJ mol}^{-1}$	activation enthalpy due to hydrogen
$\beta$	2080	$\text{kJ mol}^{-1} \text{wt ppm}^{-1/3}$	positive parameter
<b>Wang et al. (2006) formulation (Equation 2.6)</b>			
$C_{\text{H}_2\text{O}}$		wt %	
$\log \sigma_0^{\text{Hydrous}}$	3	$\text{S m}^{-1}$	conductivity due to hydrogen
$\Delta H^{\text{Hydrous}}$	87	$\text{kJ mol}^{-1}$	activation enthalpy due to hydrogen
$r$	0.62		water content exponent

### 2.6.2 Calculation of the mantle solidus

The effect of water on the solidus temperature is calculated following Katz et al. (2003) and Langmuir et al. (2006). The equilibrium between solid phase and melt phases can be measured by the batch melting equation:

$$C_L^{H_2O} = \frac{C_0}{(D_{H_2O} * (1-F) + F)} \quad (2.7)$$

Where  $D_{H_2O}$  is the partitioning coefficient of bulk water.  $D_{H_2O}$  given by Katz et al. (2003) is 0.01, which is compatible with the laboratories studies (Aubaud, 2004).  $C_0$  is the bulk water in the units of wt %. At the solidus, the amount of melt (F) is 0.

The amount of water in liquid ( $C_L^{H_2O}$ ) will reduce the mantle solidus temperature by an amount:

$$\Delta T(C_L^{H_2O}) = K(C_L^{H_2O})^y \quad (2.8)$$

Where  $C_L^{H_2O}$  is the amount of water in the melt. The other parameters are constants, where K is 60 and y is 0.54 based on studies of back-arc basins (Langmuir et al., 2006). The solidus for hydrated mantle is then:

$$T(P) = T_{dry\ solidus}(P) - \Delta T(C_L^{H_2O}) \quad (2.9)$$

Where P is the pressure, and  $T_{dry\ solidus}$  is the solidus of dry peridotite from Hirschmann, (2000).

### 2.6.3 Calculation of effective viscosity

The calculations of effective viscosity are based on the rheology of olivine. Viscous deformation can occur through either diffusion or dislocation creep. In both cases, the strain rate ( $\dot{\epsilon}_1$ ) is related to the stress ( $\sigma$ ) according to:

$$\dot{\epsilon}_1(T_K, P, \sigma, C_{OH}, d, \phi) = d^{-p_i} A_i C_{OH}^{r_i} (\sigma)^{n_i} \exp \left[ \frac{-(E_i + PV_i)}{RT_K} \right] \exp(\alpha \phi) \quad (2.10)$$

Where d is grain size,  $p_i$  is grain size exponent,  $A_i$  is the pre-exponential constant,  $C_{OH}$  is olivine water content,  $r_i$  is the water content exponent,  $n_i$  is a stress exponent,  $E_i$  is the activation energy,

$V_i$  is an activation volume,  $P$  is the pressure,  $R$  is the ideal gas constant,  $T_K$  is the temperature,  $\alpha$  is a constant, and  $\phi$  is melt fraction. The subscript  $i$  represents the diffusion or dislocation creep. The parameters are given in Table 2.4.

Based on the applied stress and strain rate, the effective viscosity is:

$$\eta_i = \frac{\sigma}{2\dot{\epsilon}_i} \quad (2.11)$$

Combining Equations 2.10 and 2.11, the effective viscosity can be written as:

$$\eta_i(T_K, P, \sigma, C_{OH}, d, \phi) = \frac{1}{2} (A_i d^{-p_i} C_{OH}^{r_i})^{-1} \sigma^{1-n_i} \exp \left[ \frac{(E_i + PV_i)}{RT_K} \right] \exp(-\alpha\phi) \quad (2.12)$$

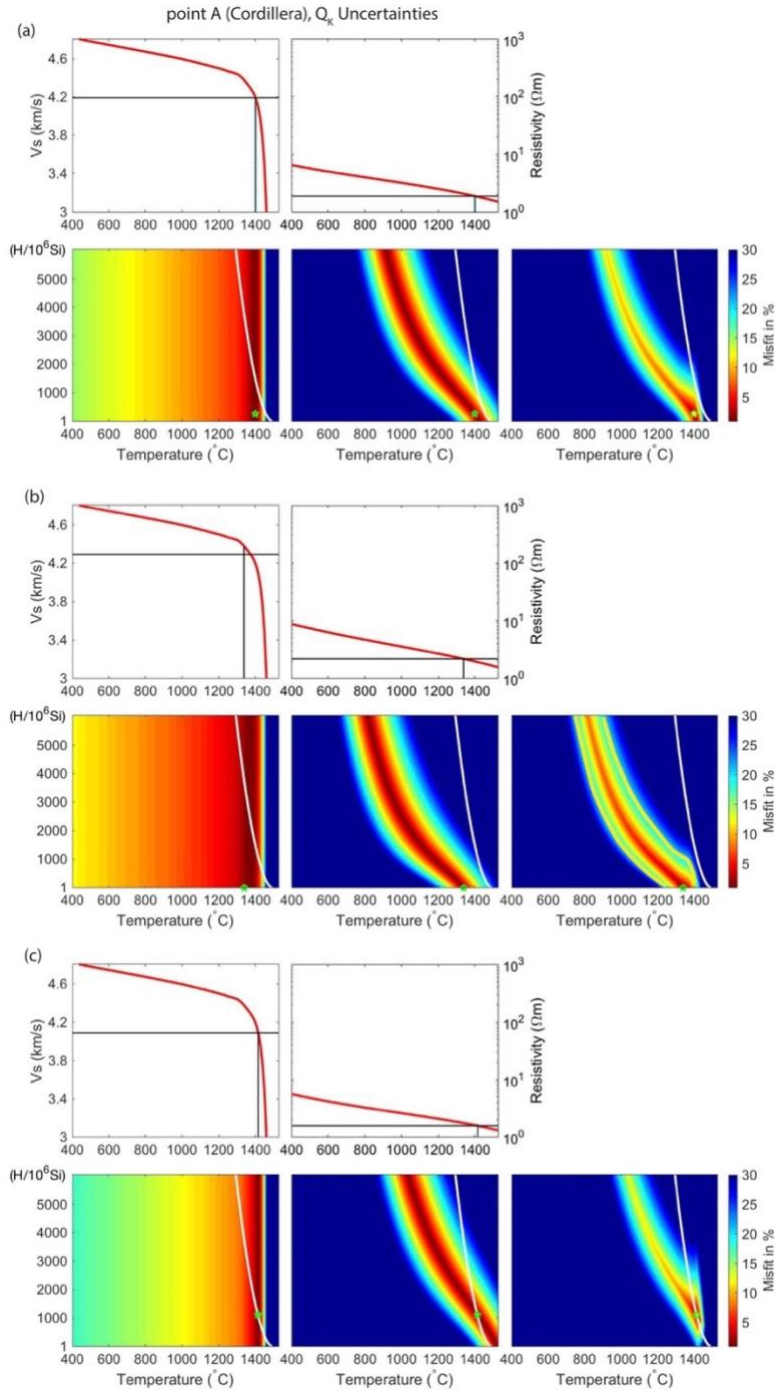
The individual viscosity for diffusion creep ( $\eta_{dif}$ ) and dislocation creep ( $\eta_{dis}$ ) is calculated, and the overall effective viscosity ( $\eta_{eff}$ ) is given by:

$$\eta_{eff} = \left( \frac{1}{\eta_{dif}} + \frac{1}{\eta_{dis}} \right)^{-1} \quad (2.13)$$

We use  $T_K$  and  $C_{OH}$  from the joint analysis of  $V_s$  and resistivity, and  $P$  is given by the depth. The calculations use a constant stress of 0.3 MPa, grain size of 1cm, and no melt ( $\phi=0\%$ ).

**Table 2.4** Rheology parameters for diffusion creep (dif) and dislocation creep (dis) of olivine (Behn et al., 2009; Hirth & Kohlstedt, 2003).

Parameter	Values	Units	Description
$n_{\text{dif}}$	1		diffusion creep exponent
$A_{\text{dif}}$	3.33E5	$\text{MPa}^{-n_{\text{dif}}\text{s}^{-1}}$	diffusion creep prefactor
$E_{\text{dif}}$	335	$\text{kJ mol}^{-1}$	diffusion creep activation energy
$V_{\text{dif}}$	4E-6	$\text{m}^3\text{mol}^{-1}$	diffusion creep activation volume
$p_{\text{dif}}$	3		diffusion creep grain size exponent
$r_{\text{dif}}$	1		diffusion creep water content exponent
$n_{\text{dis}}$	3.5		Dislocation creep exponent
$A_{\text{dis}}$	30	$\text{MPa}^{-n_{\text{dis}}\text{s}^{-1}}$	dislocation creep prefactor
$E_{\text{dis}}$	480	$\text{kJ mol}^{-1}$	dislocation creep activation energy
$V_{\text{dis}}$	1.1E-5	$\text{m}^3\text{mol}^{-1}$	dislocation creep activation volume
$p_{\text{dis}}$	0		dislocation creep grain size exponent
$r_{\text{dis}}$	1.2		dislocation creep water content exponent
$\alpha$	30		constant
$\phi$		%	melt fraction
T		K	temperature
P		Pa	pressure
d		m	grain size
$C_{\text{OH}}$		ppm H/Si	water content
$\sigma$		Pa	stress
R	8.3145	$\text{J mol}^{-1}\text{K}^{-1}$	gas constant



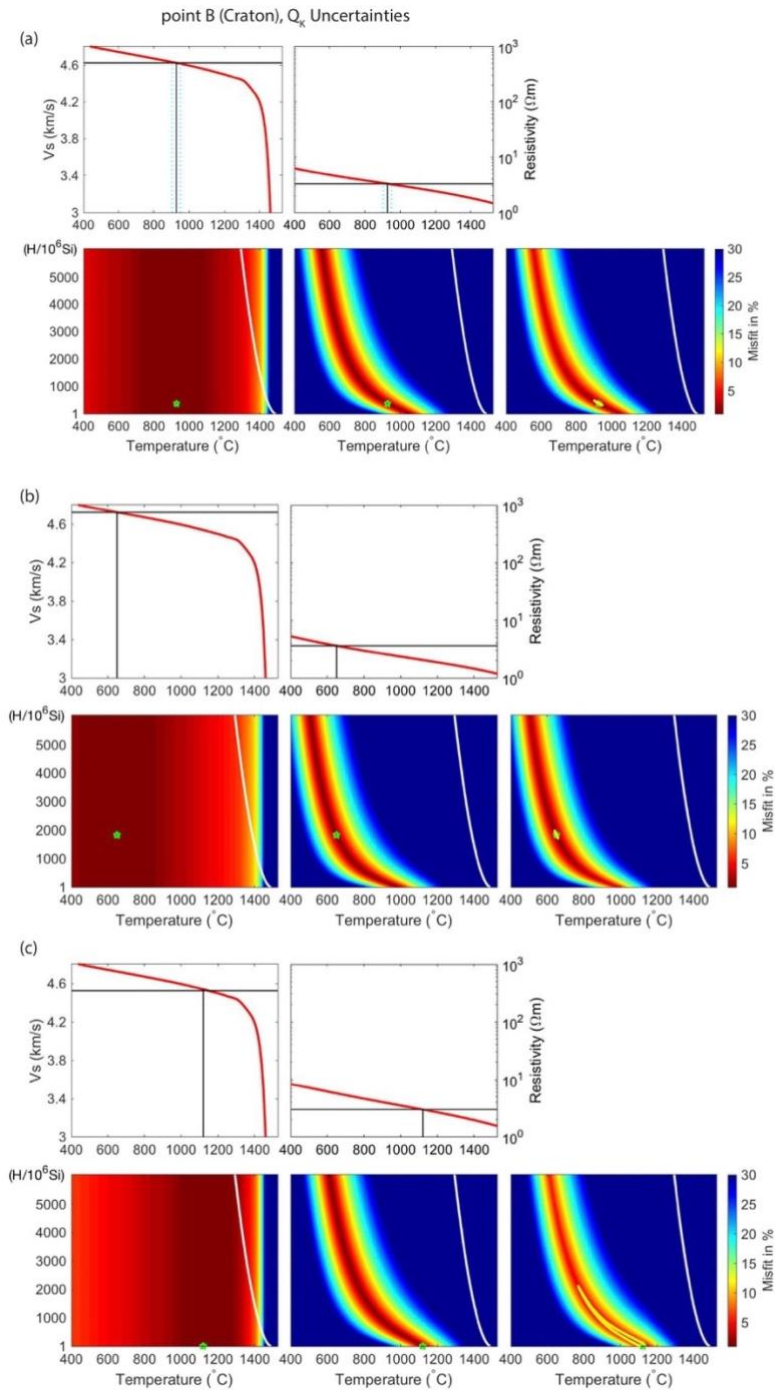


**Figure 2.14** Effect of uncertainties in  $V_S$  and resistivity for the  $Q_K$  analysis on point B (craton). (a) Fitting of the observed  $V_S$  and resistivity shows a global minimum at 928  $^{\circ}C$  and 385 ppm H/Si with a misfit of 0.02 %. (b) Increase in  $V_S$  by 0.1 km/s and increase in resistivity by a factor of 2 relative to the observed values. The global minimum lies at 651  $^{\circ}C$  and 1833 ppm H/Si with a misfit of 0.01 %. (c) Decrease in  $V_S$  by 0.1 km/s and decrease in resistivity by a factor of 2 relative to the observed values. The global minimum is at 1121  $^{\circ}C$  and 5 ppm H/Si with a misfit of 0.35 %.

**Table 2.5** Average and one standard deviation of temperature and olivine water content for the cordillera and craton regions.

Analysis	75 km depth		100 km depth		125 km depth		150 km depth	
<b>ABC_S profile</b>								
Cordillera temperature (°C)								
Q <sub>F</sub>	1208	±23	1255	±25	1253	±28	1238	±30
Q <sub>K</sub>	1382	±13	1388	±13	1372	±15	1347	±15
Cordillera water content (ppm H/Si olivine)								
Q <sub>F</sub>	1908	±433	1565	±567	1470	±558	1515	±406
Q <sub>K</sub>	525	±246	512	±346	549	±352	686	±258
Cordillera water content (ppm H <sub>2</sub> O)								
Q <sub>F</sub>	116	±26	95	±35	90	±34	92	±25
Q <sub>K</sub>	32	±15	31	±21	33	±21	42	±16
Craton temperature (°C)								
Q <sub>F</sub>	970	±48	972	±62	947	±51	958	±22
Q <sub>K</sub>	1034	±78	1013	±79	972	±62	974	±27
Craton water content (ppm H/Si olivine)								
Q <sub>F</sub>	888	±529	448	±158	371	±90	288	±75
Q <sub>K</sub>	536	±266	292	±128	286	±96	238	±56
Craton water content (ppm H <sub>2</sub> O)								
Q <sub>F</sub>	54	±32	27	±10	23	±5	18	±5
Q <sub>K</sub>	33	±16	18	±8	17	±6	15	±3
<b>ABC_N profile</b>								
Cordillera temperature (°C)								
Q <sub>F</sub>	1227	±36	1277	±28	1285	±37	1260	±28
Q <sub>K</sub>	1336	±60	1364	±33	1375	±9	1355	±11
Cordillera water content (ppm H/Si olivine)								
Q <sub>F</sub>	1124	±952	825	±592	910	±467	1193	±339
Q <sub>K</sub>	281	±332	179	±233	242	±229	500	±188
Cordillera water content (ppm H <sub>2</sub> O)								
Q <sub>F</sub>	69	±58	50	±36	55	±28	73	±21
Q <sub>K</sub>	17	±20	11	±14	15	±14	30	±11
Craton temperature (°C)								
Q <sub>F</sub>	934	±47	922	±53	895	±43	908	±22
Q <sub>K</sub>	995	±76	969	±77	928	±61	936	±32
Craton water content (ppm H/Si olivine)								
Q <sub>F</sub>	1449	±481	1762	±473	2573	±760	3064	±1229
Q <sub>K</sub>	995	±224	1348	±231	2144	±491	2647	±985
Craton water content (ppm H <sub>2</sub> O)								
Q <sub>F</sub>	88	±29	107	±29	157	±46	187	±75
Q <sub>K</sub>	61	±14	82	±14	131	±30	161	±60

## **Chapter 3**

### **Numerical model methodology**

The two-dimensional (2D) geodynamic numerical models that will be presented in Chapters 4 and 5 use the SOPALE code that was developed at Dalhousie University (Fallsack, 1995). This finite element code has been used in numerous studies that investigate orogen evolution (e.g., Beaumont et al., 2006; Jamieson & Beaumont, 2013), subduction (e.g., Currie et al., 2015), and continental lithosphere dynamics, including lithospheric removal (Göğüş & Pysklywec, 2008a; Gray & Pysklywec, 2012; Krystopowicz & Currie, 2013; Wang & Currie, 2015). Two advantages of this code are (1) its ability to model large magnitudes of crustal and mantle deformation using realistic nonlinear material properties, and (2) the use of a stress-free top model boundary, so that topography can be monitored during the model run. The computational accuracy of the code has been established through benchmarking tests and analytical comparisons to Rayleigh-Taylor instabilities (Currie et al., 2015; Houseman & Molnar, 1997; Pysklywec et al., 2002; Wang & Currie, 2017).

In this thesis, 2D thermal-mechanical models are used to investigate dynamics of lithospheric removal through delamination, including an assessment of the viability of delamination to explain the present-day observations in the Northern Canadian Cordillera (Chapter 4) and generic models that investigate the conditions that promote delamination and the resulting surface expressions (Chapter 5). This chapter presents the numerical modelling methods, including the governing equations and key material properties.

### **3.1 Governing equations**

The SOPALE code uses the Arbitrary Lagrangian-Eulerian (ALE) finite element formulation to solve for the thermal-mechanical evolution of the lithosphere-upper mantle system in two dimensions (Fallsack, 1995). The code solves the governing equations including conservation of mass, momentum, and energy, under the assumptions of material incompressibility, plain strain, and a zero Reynolds number. The incompressibility condition means that the volume does not change with pressure and temperature and is a commonly used approximation where the volume changes are small (e.g., Gerya, 2009). The plain strain assumption allows for strain to occur within the 2D model plane, with no deformation along the normal direction of the model plan. The Reynolds number gives the ratio of internal forces to viscous forces. A zero Reynolds number occurs for materials with high viscosities and low

velocities. This is similar to the Stokes flow (creeping flow), which describes the flow of highly viscous fluids where inertial forces can be neglected.

The conservation of mass means that the net influx and net outflux of the mass into and out of the system are equilibrium. Under the assumption of incompressible materials, it is written as:

$$\frac{\partial v_i}{\partial x_i} = 0 \quad (3.1)$$

where  $v_i$  are components of the velocity vector;  $x_i$  are the spatial coordinate directions, with  $i = 1, 2$ .

The conservation of momentum is also called the force balance equation or the Stokes equation for a creeping flow. It is based on a balance between body forces (i.e., gravity) and surface forces (i.e., the spatial derivatives of the stress). This is written as:

$$\frac{\partial \sigma_{ij}}{\partial x_i} + \rho g = 0 \quad (3.2)$$

where  $\sigma_{ij}$  are components of the Cauchy stress tensor,  $\rho$  is the density,  $g$  is the gravitational acceleration (9.81 m/s<sup>2</sup> for the Earth).

The stress tensor components are:

$$\sigma_{ij} = -P\delta_{ij} + \sigma'_{ij} \quad (3.3)$$

$$\sigma'_{ij} = 2\eta_{eff} \dot{\epsilon}_{ij} \quad (3.4)$$

Where  $P$  is pressure (mean stress),  $\delta_{ij}$  is the Kronecker delta ( $\delta_{ij} = 1$  for  $i = j$ ; otherwise,  $\delta_{ij} = 0$ ),  $\sigma'_{ij}$  is the deviatoric stress tensor,  $\eta_{eff}$  is effective viscosity, and the strain rate tensor is:

$$\dot{\epsilon}_{ij} = \frac{1}{2} \left( \frac{\partial v_i}{\partial x_j} + \frac{\partial v_j}{\partial x_i} \right) \quad (3.5)$$

The conservation of energy, or heat balance equation, includes the evolution and transport of thermal energy by advection, conduction, and another heating processes such as internal heating ( $H_r$ ), frictional heating, and adiabatic heating. It is written as:

$$\rho c_p \left( \frac{\partial T}{\partial t} + v_i \cdot \frac{\partial T}{\partial x_i} \right) = k \frac{\partial}{\partial x_i} \frac{\partial T}{\partial x_i} + H_r + \sigma'_{ij} \dot{\epsilon}_{ij} + v_2 \alpha g T \rho \quad (3.6)$$

where  $c_p$  is heat capacity,  $T$  is absolute temperature (degrees Kelvin), and  $k$  is thermal conductivity. The last three terms on the right-hand side account for processes may produce

thermal energy. The third term ( $H_r$ ) is heat production by the decay of radioactive elements (primarily U, Th, and K). The fourth term accounts for shear heating, which is the product of the deviatoric stress and strain rate; this gives the heat produced during material deformation. The final term is the adiabatic heating, which accounts for thermal changes due to material compression or expansion due to changes in pressure (depth). This is proportional to a thermal expansion ( $\alpha$ ), temperature ( $T$ ), the density of material ( $\rho$ ), and vertical velocity of moving material ( $v_2$ ).

The governing equations solve for the coupled thermal and mechanical evolution of the lithosphere-upper mantle system. The thermal and mechanical fields are coupled in a number of ways, including the temperature-dependence of material density and rheology, the shear heating and adiabatic heating terms in Equation 3.6, and redistribution of thermal properties by the movement of materials.

In the ALE approach, the governing equations are solved to determine the temperature, velocity and pressure fields on an Eulerian mesh that is fixed in space but can deform vertically to conform to the top boundary of the model (i.e., the ground surface). The material properties (e.g., rheology, density, and thermal conductivity) are tracked on the Lagrangian mesh, with additional Lagrangian particles that are injected during the model run to maintain a minimum number of particles within each Eulerian cell. In each time step, the particles are advected according to the calculated velocity field, and the new distribution of materials is used to update the properties of each cell in the Eulerian mesh.

### 3.2 Material properties

In numerical models, all materials have temperature-dependent densities and viscous-plastic rheologies, including frictional-plastic (brittle) and viscous (ductile) properties (Fallsack, 1995; Willett, 1999). The material density is:

$$\rho(T) = \rho_0[1 - \alpha(T - T_0)] \quad (3.7)$$

where  $\rho_0$  is reference density at reference temperatures ( $T_0$ ) and  $\alpha$  is the volumetric thermal expansion coefficient.

The deformation mechanism is determined by the ambient conditions. When the stress is above the frictional-plastic yield stress, materials deform through frictional-plastic failure based on a Drucker-Prager yield criterion:

$$J'_2 = P \sin \phi_{eff} + C_0 \cos \phi_{eff} \quad (3.8)$$

where  $J'_2$  is the square root of the second invariant of the deviatoric stress tensor ( $J'^2_2 = 0.5\sigma'_{ij}\sigma'_{ij}$ ),  $C_0$  is the cohesion.  $\phi_{eff}$  is the effective internal angle of friction, which includes the effects of the dry angle of friction ( $\phi$ ) and the Hubbert-Rubey pore pressure ratio ( $\lambda$ ) such that:

$$\sin(\phi_{eff}) = (1 - \lambda)\sin\phi \quad (3.9)$$

(Beaumont et al., 2006). The pore pressure ratio is the ratio of the pore fluid pressure to the mean stress ( $P$ ).

Frictional-plastic deformation is modeled by placing the state of stress on yield, in order to define a plastic effective viscosity ( $\eta^p_{eff}$ ):

$$\eta^p_{eff} = \frac{(J'_2)^{1/2}}{2(i'_2)^{1/2}} \quad (3.10)$$

where  $i'_2$  is a square root of the second invariant of the strain rate tensor ( $i'^2_2 = 0.5\dot{\epsilon}_{ij}\dot{\epsilon}_{ij}$ ) (Fullsack, 1995; Willett, 1999). This allows frictional-plastic deformation to be modeled as a creeping flow that occurs at the yield stress.

Materials can undergo frictional-plastic strain-softening or strain-hardening, which results in mechanical weakening or strengthening with cumulative strain. Owing to an increase in pore-fluid pressure, mineral reactions, and infiltration of fluids, materials softening can be modeled by a decrease in  $\phi_{eff}$  and/or  $C_0$ . For example, strain-softening can be included through a decrease in  $\phi_{eff}$  from  $15^\circ$  to  $2^\circ$  as the accumulated strain rate increases from 0.5 to 1.5 (Huisman & Beaumont, 2003; Warren et al., 2008).

When the stress is below the yield stress, materials deform through ductile flow. This deformation follows a viscous temperature-dependent power-law rheology:

$$\eta^v_{eff} = fB^*i'^{(1-n)/n}_2 \exp\left(\frac{Q+PV^*}{nRT}\right) \quad (3.11)$$

where  $\eta_{eff}^v$  is the viscous effective viscosity,  $f$  is a scaling factor,  $B^*$  is a pre-exponential factor,  $n$  is a stress exponent,  $Q$  is activation energy,  $V^*$  is an activation volume,  $R$  is an ideal gas constant ( $8.3145 \text{ mol}^{-1} \text{ K}^{-1}$ ), and  $T$  is the absolute temperature. The parameter ( $B^*$ ) is given by:

$$B^* = 2^{\frac{1-n}{n}} 3^{\frac{-(n+1)}{2n}} A^{\frac{-1}{n}} \quad (3.12)$$

where  $A$  is the pre-exponential factor determined from uniaxial laboratory experiments. This equation converts the laboratory measurements to the tensor-invariant state of stress of the numerical models.

The four rheological parameters ( $A$ ,  $n$ ,  $Q$ , and  $V^*$ ) are obtained from laboratory deformation experiments of crust and mantle rocks, and therefore they depend on the composition of the material. The scaling factor ( $f$ ) is used to linearly vary the viscosity relative to the laboratory samples. This allows a way to approximate the strength changes associated with changes in composition (including hydration and the presence of melt) relative to the laboratory samples, as well as a method to investigate the effects of uncertainties in the laboratory-based parameters (Beaumont et al., 2006). For example, the viscous strength of dry olivine is 5-10 times stronger than wet olivine in a depth range between 50 and 100 km for the same temperature and strain rate conditions (Hirth & Kohlstedt, 2003; Karato & Wu, 1993). The scaling factor can also be used to model viscous strain-weakening by decreasing  $f$  linearly with increasing cumulative strain.

Details of the material properties are discussed in more detail in Chapters 4 and 5. These chapters also include a discussion of the initial conditions (material geometry and temperature structure) and the thermal and mechanical boundary conditions used during the model run.

## **Chapter 4**

### **Recent delamination below the Northern Canadian Cordillera?**

A version of the manuscript submitted to *Geology*

## Abstract

The Northern Canadian Cordillera is a high-elevation mountain belt characterized by a hot, and thin lithosphere, widespread magmatism (up to 400 km from the nearest plate margin), and thrust seismicity within the southern Mackenzie Mountains (50-150 km west of the Cordilleran Deformation Front). Using thermal-mechanical numerical models, we show that these observations can be explained by gravitational removal of previously thick cordilleran lithosphere via delamination. Removal is driven by foundering of the cool, dense mantle lithosphere and high-density eclogitized lower crust. This results in a thin crust and lithosphere, high elevation, and high surface heat flow, in good agreement with present-day observations. A delamination event initiating at ~15 Ma can also explain the occurrence of Neogene magmatism in the Northern Cordilleran Volcanic Province. Modeled crustal horizontal strain shows that delamination creates contraction at the margins of the thinned region, potentially explaining the concentration of the present-day thrust type focal mechanisms in the southern Mackenzie Mountains.

## 4.1 Introduction

Deformation within mountain belts is usually attributed to loading from regional tectonic processes and large-scale mantle flow (e.g., Humphreys & Coblenz, 2007). In recent years, local lithosphere dynamics have also been shown to have a first-order effect on mountain belt evolution. In numerous regions, rapid gravitational removal of the dense lower lithosphere has created observable changes in lithospheric structure, surface topography, and magmatism (e.g., Göğüş & Pysklywec, 2008a; Wang et al., 2021).

Here we explore the possibility of lithospheric removal for the Northern Canadian Cordillera (NCC) in northwestern Canada (Figure 4.1). This ~1.1 km high, active orogen exhibits magmatism and seismicity well inboard of the nearest plate margin. Seismic studies show that the crustal thickness throughout the NCC is  $35 \pm 2$  km (Audet et al., 2020; Clowes et al., 2005), and thus the NCC is not supported by a thick crustal root. Instead, the NCC appears to be buoyantly supported by high mantle temperatures (Hyndman & Currie, 2011). Seismic receiver functions (Audet et al., 2019) and xenolith thermobarometry data (e.g., Harder & Russell, 2006) indicate a lithospheric thickness of 50-60 km for the NCC west of the Tintina Fault. Thin lithosphere is

consistent with observations of high surface heat flow (Lewis et al., 2003), low mantle seismic velocity (e.g., Schaeffer & Lebedev, 2014; Estève et al., 2021), and low mantle electrical resistivity (Ledo & Jones, 2005). Further, the NCC is characterized by ongoing basaltic magmatism of the Northern Cordilleran Volcanic Province (NCVP) that initiated in the last 20 Ma (Edwards & Russell, 2000).

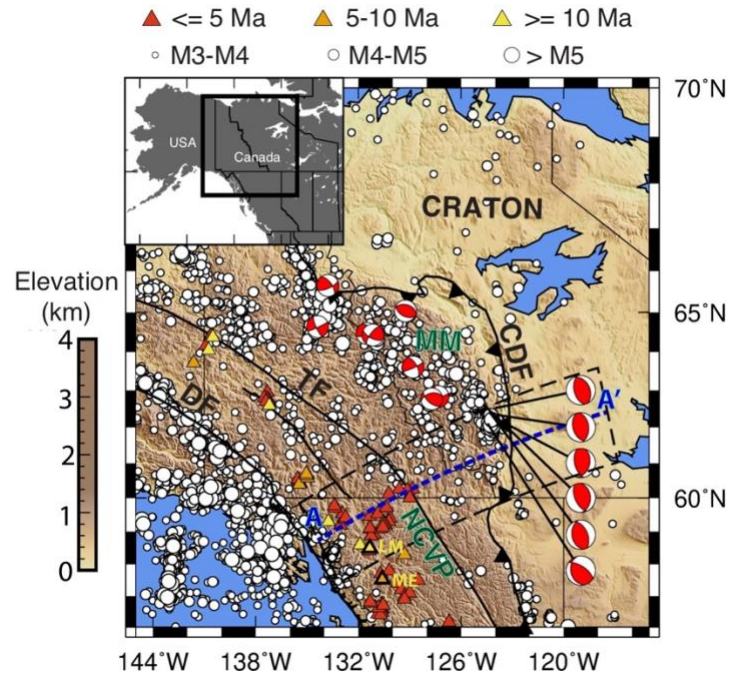


**Figure 4.1** Geological setting of northwest Canada, with model profile A-A'. Triangles are Northern Cordilleran Volcanic Province (NCVP) volcanoes (ages from Edwards & Russell, 2000; Abraham et al., 2005, and references therein), including Level Mountain (LM) and Mount Edziza (ME). Earthquakes (depth  $\leq 30$  km,  $M \geq 3$ ) are from the Geological Survey of Canada National Earthquakes Database. Focal mechanisms ( $M \geq 4.5$ ) are from the Global Harvard CMT catalog for the Mackenzie Mountains (MM). Barbed line is the Cordilleran Deformation Front (CDF); black lines are Denali fault (DF) and Tintina fault (TF).

The lithosphere structure beneath the NCC shows the Tintina Fault (TF), a lithosphere-scale fault that separates allochthonous cordilleran terranes from the Foreland Belt (i.e., ancestral North American Craton) and accommodated  $\sim 430$  km of right-lateral motion of the cordilleran lithosphere during the Eocene (Gabrielse et al., 2006). East of the TF, the North American Craton

lithosphere is cooler and thicker, based on high mantle seismic velocity (Schaeffer & Lebedev, 2014), absence of NCVP magmatism (Edwards & Russell, 2000) and surface heat flow analysis (Lewis et al., 2003). Geological field studies show that this area includes some parts of the Intermontane and Foreland domains, such as the Cassiar platform, Medial basin, and Rocky Mountain platform (Johnston 2008). This area consists of sediments and hosts the Mackenzie Mountains (MM), a thrust and fold belt that developed on the craton margin in the Mesozoic (Cook, 1991). In contrast to the sparse seismicity across the central NCC, a region of concentrated seismicity is found within the MM, 50-150 km west of the Cordilleran Deformation Front (CDF). Although this is a high-elevation region, most earthquakes exhibit thrust mechanisms. These have been explained by either localization of far-field compressive stress from Yakutat block collision ~800 km to the west (Mazzotti & Hyndman, 2002) or mantle drag on the base of the lithosphere (Finzel et al., 2014), although it remains unclear how stress can be transmitted through the hot and weak cordilleran lithosphere.

Two end-member models have been proposed to explain the thin NCC lithosphere. One hypothesis is that the thin lithosphere is a long-lived structure, possibly maintained by vigorous convection of hydrated mantle associated with past subduction below this region (Hyndman et al., 2005). Initiation of NCVP magmatism is attributed to mantle upwelling following termination of Pacific-Kula subduction by slab break-off at ~40 Ma (Fuston & Wu, 2021) or the formation of a slab window at ~20 Ma (Thorkelson et al. 2011). However, geodynamic models show that slab break-off and slab window formation may not result in significant vertical mantle flow (Király et al., 2020) or mantle melting (Freeburn et al., 2017).

The alternate idea is that the thin lithosphere is a more recent feature. Audet et al. (2019) proposed that the NCC may have experienced gravitational removal of the lower lithosphere in the last 5-25 m.y. In this study, we use a numerical model of delamination, a form of rigid gravitational removal, to explore the dynamics and surface expressions of lithospheric removal. We show that a delamination event at ~15 Ma can explain the present-day NCC lithospheric structure and that local lithosphere dynamics provide a self-consistent mechanism for NCVP magmatism and compressional deformation in the MM.

## 4.2 Numerical model of delamination

We use the two-dimensional finite element code SOPALE (Fullsack, 1995) to model delamination along profile A-A' (Figure 4.1). The code solves for the thermal-mechanical evolution of the lithosphere-upper mantle system, assuming plane strain and materials with viscous-plastic rheologies and temperature-dependent densities (Section 4.7). The model domain is 2000 km wide and 660 km deep and consists of continental lithosphere overlying sublithospheric mantle. The continent is divided laterally into craton and cordillera, with the boundary corresponding to the TF. West of the TF, the cordilleran lithosphere is initially 100 km thick, with a 60 km crust, assuming prior crustal thickening during Cretaceous-Eocene compression (e.g., Nelson & Colpron, 2007). Note that variations in the initial crustal thickness cause only minor changes in the dynamics and consequence of delamination. The thickened lower crust extends to >40 km depth, and it is therefore in the eclogite stability field, where dense lower crust may occur through either metamorphic eclogitization or magmatic differentiation (DeCelles et al., 2009; Jull & Kelemen, 2001; Leech, 2001). The initial Moho is at 36 km depth, which is based on the seismic receiver function image (Audet et al., 2019). The initial cratonic lithospheric thickness increases from 100 km below the MM to 200 km inboard, consistent with the geometry from seismic studies (Hammer & Clowes, 2004; Schaeffer & Lebedev, 2014). The simplified model includes the dominant geological features in the study area and allows us to examine the surface expressions triggered by delamination dynamics.

Based on seismic tomography and receiver function studies, it has been proposed that recent gravitational removal has occurred beneath the NCC (Audet et al., 2019). Hence, our study focuses on the surface effects of delamination; plate motions, plate boundary forces, and surface erosion are not included. Following earlier work (e.g., Göğüş & Pysklywec, 2008a; Krystopowicz & Currie, 2013; Wang & Currie, 2015), two features enable delamination in our model. First, a 100 km-wide weak zone is placed at the western side of the cordilleran mantle lithosphere (viscosity of  $5 \times 10^{19}$  Pa s). This may represent a localized shear zone or former volcanic arc (e.g. Bird, 1979). For example, the western side of the NCC includes the Denali fault system, which includes deformation, magmatism, and sedimentation since the Eocene (Trop et al., 2019), and therefore this may be a pre-existing area of weak lithosphere. The weak zone allows for the creation of a low viscosity conduit. Second, the lowermost cordilleran crust is assumed to have

transformed to the dense lower crust (e.g., eclogite) and its density is  $200 \text{ kg/m}^3$  greater than the underlying mantle (at the same temperature) (e.g., Jull & Kelemen, 2001). The dense lower crust is gravitationally unstable and therefore assists in the detachment of the lowermost lithosphere from the buoyant overlying crust.

Figure 4.2D shows the evolution of the model. Initially, the weak zone undergoes gravitational instability, as it is cooler and therefore denser than the underlying mantle. Removal of the weak zone allows high-temperature mantle to upwell to the base of the cordilleran crust at 13-14 m.y. after the start of the model. This triggers foundering of the lower cordilleran lithosphere, driven by both the high-density eclogitized crust and the cool mantle lithosphere. The lower lithosphere detaches toward the east as a quasi-rigid block within  $\sim 4$  m.y., with delamination terminating at the TF. Delamination results in removal of the lower cordilleran lithosphere over a width of  $\sim 450$  km, leaving a crustal thickness of 34-39 km, with greater thickness at the edges of the thinned region. The cordilleran mantle then begins to conductively cool, as shown by the slow deepening of the  $1200^\circ\text{C}$  isotherm from 20 to 29 m.y. in the model. As discussed below, we take 29 m.y. to be the present-day structure based on NCVP magmatism; therefore, the onset of delamination at  $\sim 14$  m.y. in the model corresponds to a geological time of 15 Ma.

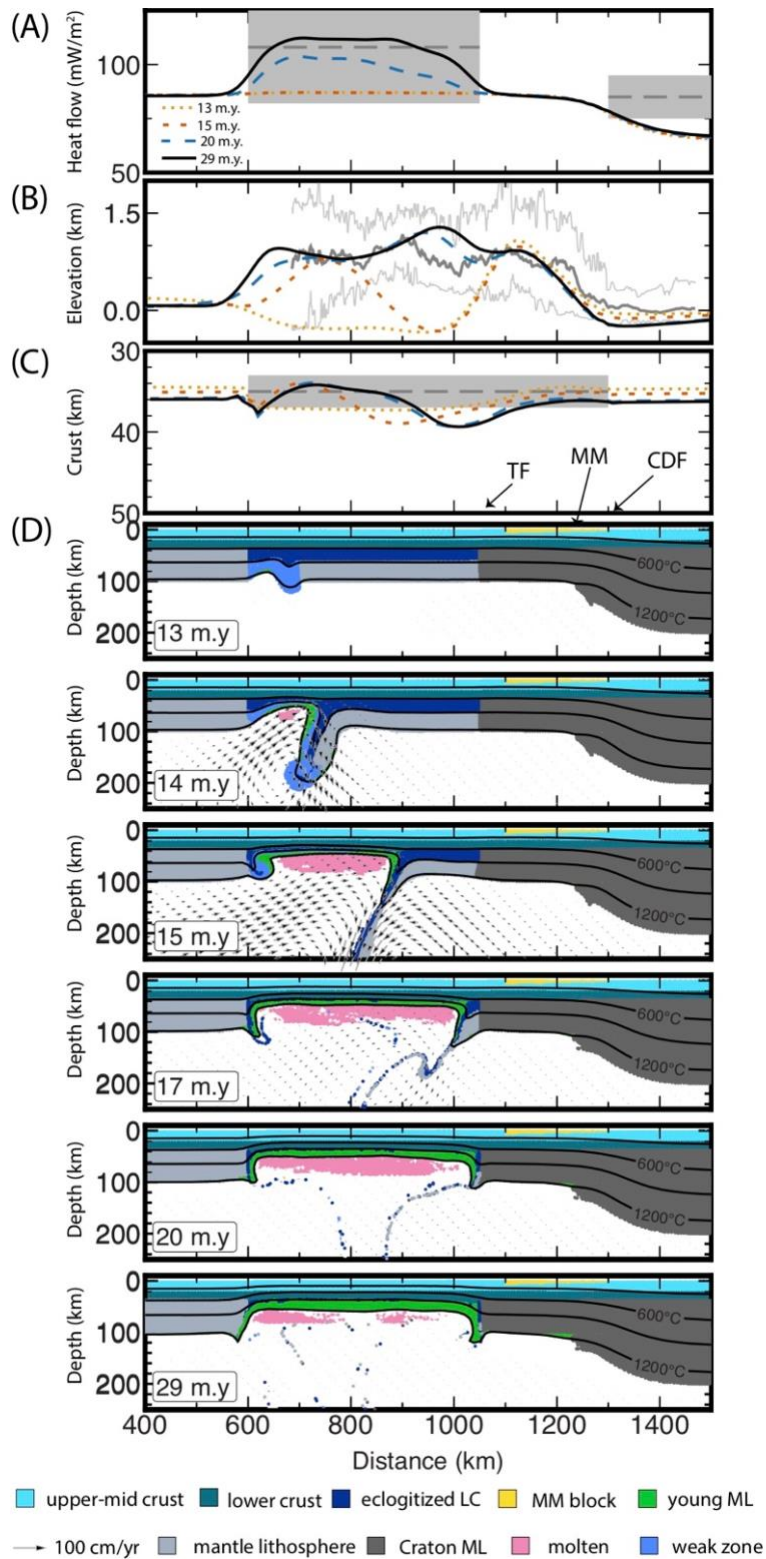


**Figure 4.2** Numerical model of delamination. Surface observations are (A) heat flow, (B) elevation relative to the craton, and (C) crustal thickness. Grey-shaded area shows present-day observations (see text). (D) Evolution of model. LC=lower crust, ML=mantle lithosphere.

### 4.3 Surface expressions of delamination

Delamination has a profound effect on the cordillera. Prior to delamination, the cordilleran elevation is  $\sim 0.2$  km below the craton, owing to the high-density eclogite and thick mantle lithosphere. The relatively low elevation results from the high-density anomaly of the crust, which is imposed at the start of the model. Paleoelevation estimates indicate the extremely high elevations ( $>3$ - $4$  km) in the Canadian Cordillera (Mulch et al., 2007). This may reflect a previously thick low-density crust. If the eclogite or dense lower crust was formed at 15 Ma, there may have been insufficient time for subsidence such that the crustal density anomaly has no significant influence on elevations. Future models that include dynamic eclogitization are needed to examine this. Removal of the lower lithosphere causes rapid uplift of  $\sim 1$  km over the entire region (Figures 4.2B and 4.3A). After delamination, the NCC crust is heated by the upwelling hot mantle. The Moho temperature increases to  $850$ - $900^{\circ}\text{C}$  within 1-2 m.y. (Figure 4.3C). Conductive heating of the crust results in a gradual increase in surface heat flow by  $\sim 20$  mW/m<sup>2</sup> over  $\sim 10$  m.y. (Figure 4.3B).

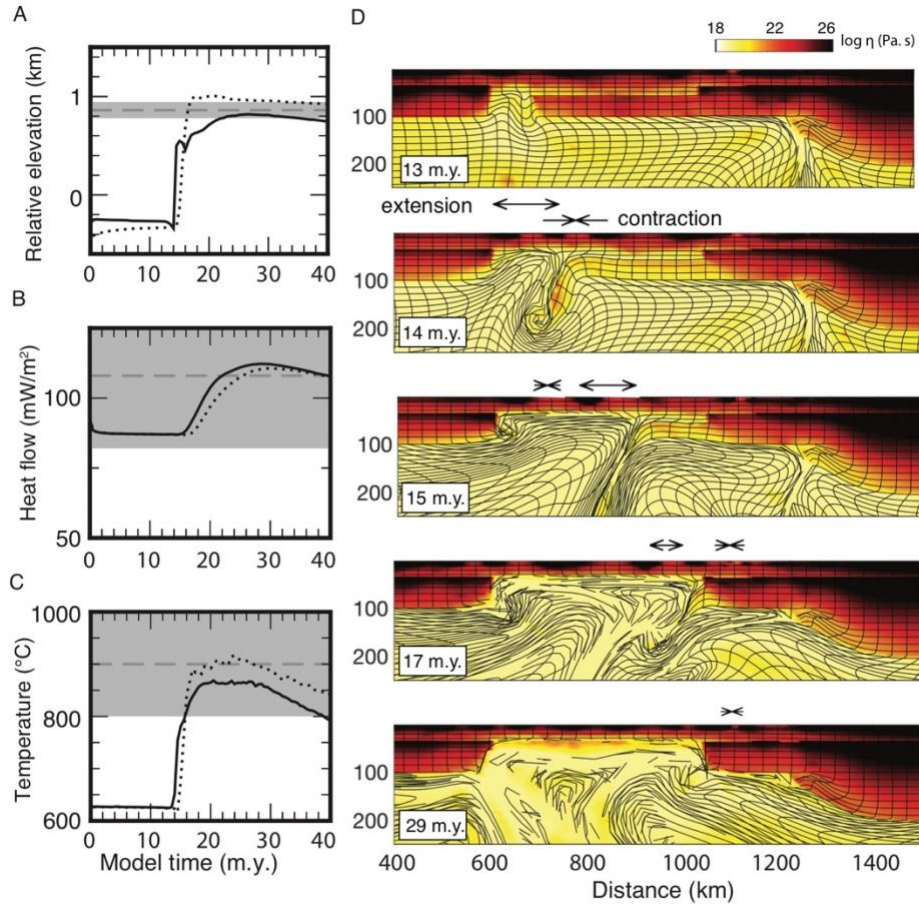


**Figure 4.3** Temporal variations in (A) relative elevation, (B) surface heat flow, and (C) Moho temperature at  $x=700$  km (solid line) and  $900$  km (dotted line). Grey shows observed values (see text). (D) Effective viscosity and Lagrangian mesh at given model times. Arrows indicate upper crust deformation.

The modeled values of elevation and surface heat flow at 29 m.y. are in good agreement with present-day observations for the NCC. The modeled craton heat flow is lower than observed because we have not fully accounted for anomalously high crustal heat production here (Lewis et al., 2003). The modeled cordilleran crustal thickness is similar to the thickness of  $35 \pm 2$  km from seismic receiver functions (Audet et al., 2020). Delamination also provides a mechanism to create the present-day Moho temperatures of  $800\text{-}1000^\circ\text{C}$  determined from heat flow (Lewis et al., 2003) and xenolith thermobarometry (Harder & Russell, 2006). Our model predicts that Neogene delamination is accompanied by  $\sim 1$  km of surface uplift, which may not be resolvable in thermochronological data in the central NCC (D. Kellett, personal communication, 2022).

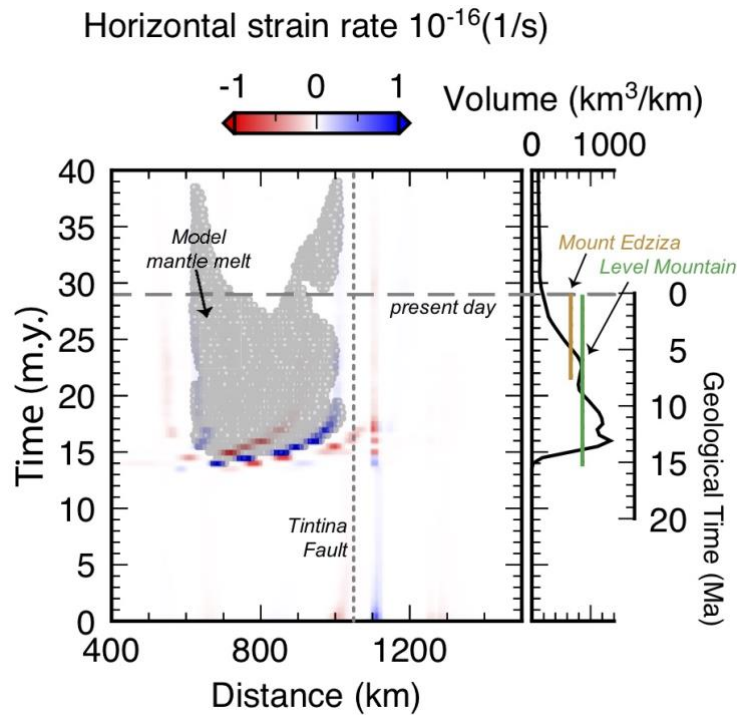
However, thermochronological data from the northern MM and thermal history models indicate a rapid Late Cenozoic exhumational cooling pulse (Enkelmann et al., 2019; Powell et al., 2019). This cooling history may also include the effects of contemporaneous Cordilleran deformation.

Figure 4.3D shows the evolution of effective viscosity in the model. Delamination is promoted by low viscosity in the cordilleran lower crust. Following removal, the cordilleran lithospheric thickness is 40-50 km at ~20 m.y. It gradually thickens to ~60 km at 29 m.y., with a corresponding increase in viscosity. East of the TF, the lithospheric thickness is >100 km and thickens toward the east. The modeled lithospheric thicknesses for the cordillera and craton are compatible with those inferred from heat flow (Lewis et al., 2003), seismic studies (Audet et al., 2019; Schaeffer & Lebedev, 2014) and xenoliths (Abraham et al., 2005; Harder & Russell, 2006). Our model implies that the present-day NCC mantle lithosphere formed through cooling after delamination and is therefore young (Figure 4.2D). Using xenolith geothermometry, Canil et al. (2021) argue that there has been no recent cooling of the mantle lithosphere in the Southern Canadian Cordillera (SCC). However, it is unclear whether this can be applied to the NCC, which has a different tectonic history (e.g., Nelson & Colpron, 2007). The NCC has similar features to the SCC, including a thin and hot cordilleran lithosphere, flat Moho, thin cordilleran crust, and high elevation (1-1.5 km). However, there are also several important differences between the two areas, mainly from past tectonic events, e.g., the Eocene extension regions and post-Eocene normal faulting for the southern RMT in the SCC and the Eocene dextral displacement >400 km for the northern RMT and Tintina fault in the NCC. Hence, a study similar to that of Canil et al. (2021) is needed in the NCC to test the delamination model.

#### **4.4 Implications for magmatism**

We also assess mantle melting triggered by delamination (Section 4.7). Delamination allows hot mantle to ascend into the space vacated by the foundering lithosphere, where it undergoes decompression melting at <100 km depth. Melting initiates at the western side of the NCC, but spreads across the ~450 km wide thinned region within 4 m.y. A time-distance plot (Figure 4.4) shows that melting persists for ~25 m.y. following delamination, with a gradual waning as the shallow mantle cools. We calculate the total melt volume as a function of time, assuming 0.3 wt % melt per °C above the mantle solidus (Wang & Currie, 2015). The model melt

volume increases at the start of delamination (~14 m.y.), reaching a maximum when the entire lithosphere is removed at 17 m.y. and then decreases with time (Figure 4.4). Crustal temperatures increase due to heating from below, however, they remain below the dry granite solidus. Thus, the model predicts no significant crustal melting.



**Figure 4.4** Time-distance plot showing the distribution of horizontal strain rate in the upper 3 km of the crust (positive values are extension) and mantle melting (gray circles). The plot on the right shows the calculated melt volume across the width of the model (per km perpendicular to the model plane). Also shown are total magma volumes at Level Mountain (green, ~ 860  $km^3$ ) and Mount Edziza (yellow, ~ 665  $km^3$ ); line length indicates duration of magmatism (Edwards & Russell, 2000).

Delamination provides a mechanism to generate a widespread mantle melting and may explain the origin of the NCVP. The NCVP is a wide region of Neogene alkali volcanic rocks that have compositions similar to oceanic island basalts. The NCVP is bounded on the west and east by the Denali Fault and Tintina Fault, respectively (Figure 4.1). Although sporadic magmatism occurred as early as 20 Ma in the northern NCVP, significant activity in its southern extent did not begin until 15 Ma (Edwards & Russell, 2000). Two long-lasting, high-volume volcanic centers are

Level Mountain and Mount Edziza, that initiated at ~15 Ma and ~7 Ma respectively. We propose that the onset of significant magmatism at 15 Ma marks the initiation of NCC delamination. Previous studies have linked NCVP magmatism to the termination of subduction and formation of a slab window at ~20 Ma (Thorkelson et al., 2011). However, a recent plate reconstruction suggests that the slab window may have formed earlier, culminating with a slab breakoff at ~40 Ma (Fuston & Wu, 2021). Our model does not preclude slab window tectonism, which may have perturbed the NCC lithosphere and contributed to initiating delamination. Subsequent removal of the lithosphere west of the TF explains the onset of NCVP magmatism and its correlation with the area of present-day thin lithosphere.

#### **4.5 Crustal deformation induced by delamination**

Another consequence of delamination is a change in the lithosphere stress field due to changes in the density distribution and surface topography. Figure 4.3D shows the deformation of the initially rectangular Lagrangian mesh in our model. Removal of the weak zone is marked by extension of the overlying crust as sublithospheric mantle upwells. Once delamination initiates, the crust above the detachment point undergoes compression due to the stresses from the foundering lithosphere. Adjacent to this, crustal extension occurs above the newly thinned lithosphere. The compression-extension front migrates laterally as delamination proceeds (Figure 4.4D). Importantly, our model predicts a change in horizontal deformation from compression to extension along the TF and the initiation of compression within the MM following delamination, especially if the MM contains weak sediments (Section 4.7).

Our model shows that delamination creates temporal changes in the lithosphere stress field. This may allow for periods of extension and compression within the NCC. As well, our model provides a local mechanism for creating compression within the southern MM. This may explain the present-day seismicity in this area, where the largest earthquakes ( $M \geq 4.5$ ) are concentrated. These earthquakes exhibit thrust mechanisms with an ENE-WSW compression (Leonard et al., 2008 and references therein). The adjacent crustal seismicity also includes strike-slip events (Figure 4.1). We note that our model is two-dimensional, and future 3D models are needed to assess the effects of out-of-plane stresses and regional tectonics.

## **4.6 Conclusions**

Local lithosphere dynamics in the NCC may have played a previously unrecognized role in its tectonic evolution. Our model shows that delamination of the lower lithosphere at ~15 Ma can explain the present-day hot, thin NCC lithosphere, which has an elevation >1 km despite a thin crust. As the lower lithosphere foundered, widespread mantle melting was initiated, leading to abundant mantle-derived NCVP magmas west of the TF. Delamination also changed the crustal stress field, creating a region of crustal compression that may explain recent thrust seismicity in the MM. Our model provides quantitative predictions that can be tested in future studies of the NCC and other mountain belts.

## **4.7 Appendix**

### **4.7.1 Numerical model set-up and material properties**

The initial geometry of the numerical model is shown in Figure 4.5. The model is oriented along a profile parallel to A-A' in Figure 4.1. The arbitrary Eulerian-Lagrangian finite element method is used to solve the equations of conservation of mass, momentum and energy, using the two-dimensional code SOPALE (Fallsack, 1995). The model domain is 2000 km wide and 660 km deep. The equations are solved on an Eulerian mesh with 200 horizontal elements (10 km width), and 102 vertical elements. There are 20 elements in the upper 60 km (3 km height), 44 elements from 60 to 280 km depth (5 km height), and 38 elements in the lower 380 km (10 km height). Material properties are tracked on a Lagrangian mesh and additional tracer particles (Fallsack, 1995).

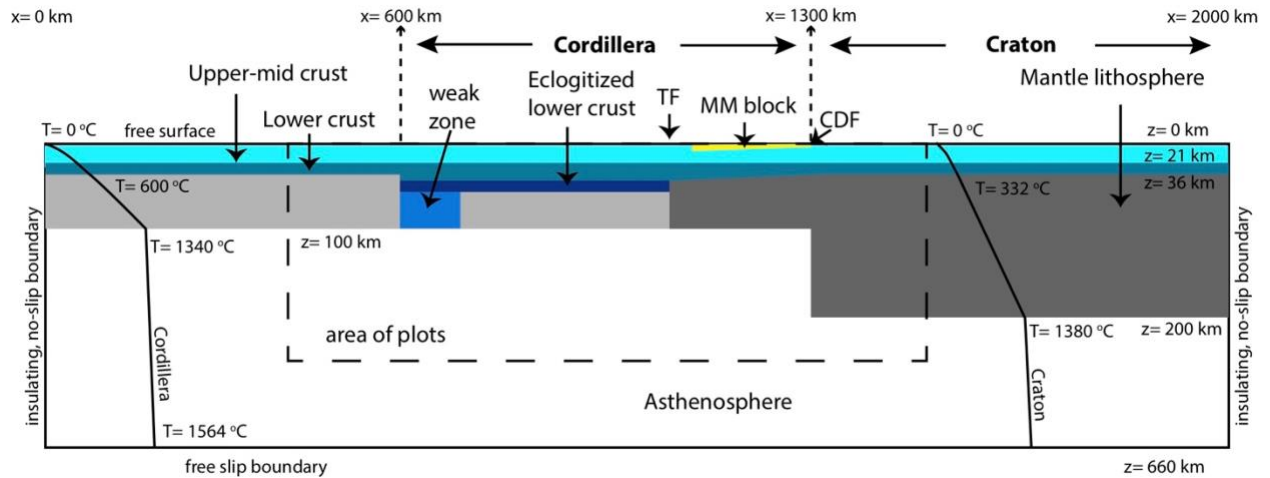


**Figure 4.5** Initial model geometry and boundary conditions. Colours denote materials in the model domain (as in Figure 4.2). The weak zone has a viscosity of  $5 \times 10^{19}$  Pa s and its reference density is equal to that of the adjacent mantle lithosphere ( $3250 \text{ kg/m}^3$ ). The MM block is a region with weak sediments with  $\phi = 1^\circ$  and reference density of  $2700 \text{ kg/m}^3$ . The reference density of the eclogitized lower crust is  $3450 \text{ kg/m}^3$ . The initial thermal structures of the cordillera and craton are also shown. To clearly show each material in the model, vertical and horizontal scales are not equal.

The model consists of cordilleran lithosphere (initially 100 km thick) and craton lithosphere (thickness of 100 to 200 km). We construct the model so that delamination occurs in the central cordilleran region (i.e., from  $x=600$  to  $1050$  km in the model domain) as our goal is to examine the surface effects of delamination. The region of delamination and adjacent craton is placed in the middle of the domain, in order to avoid model boundary effects. The distance of  $x=1050$  km corresponds to the location of the Tintina Fault (TF), which marks an eastward increase in mantle seismic velocity (Schaeffer & Lebedev, 2014), as well as the eastern limit of volcanism in the Northern Cordilleran Volcanic Province (Edwards & Russell, 2000; Harder & Russell, 2006). These observations indicate a thicker and cooler lithosphere east of the TF, and therefore we assume that delamination does not extend east of this point. Our model does not include the plate boundaries that are currently located west of the Northern Canadian Cordillera (Figure 4.1).

From  $x=600$  to  $1050$  km, the crust has a thickness of 60 km to the west of TF assuming an earlier episode of crustal thickening. From  $x=1050$  to  $1300$  km (corresponding to the Cordilleran Deformation Front, CDF), the crustal thickness linearly decreases from 39 to 36 km, in accordance

with seismic studies (Audet et al., 2020). In all other areas, the crustal thickness is 36 km. The crust is divided into an upper-mid and lower crust, with the thicknesses shown on Figure 4.5. The Mackenzie Mountains (MM) is a former thrust and fold belt that contains weak sediments (Mazzotti & Hyndman, 2002). This is included in our model as a prism (3-9 km thickness) between  $x=1100$  and  $1300$  km with an internal angle of friction of  $1^\circ$  (Figure 4.5).

To initiate delamination, a 100 km wide weak zone is placed in the mantle lithosphere at  $x=600$  km, and we assume that the lower part of the thickened crust (below 39 km depth) has transformed to high-density eclogite, owing to its temperature and pressure conditions (e.g., Hacker et al., 2003). For simplicity, we impose the eclogite density at the start of the model, as our focus is on the consequences of delamination. Changes in the depth of eclogitization affect the final crustal thickness in the model, but do not affect the dynamics of delamination. Delamination can also be induced by the presence of a weak layer in the shallow mantle lithosphere below an area of thin crust (e.g., Göğüş & Pysklywec, 2008a), and the resulting surface expressions are similar to those shown in our models.

The thermal and mechanical properties for all model materials are given in Table 4.1. Materials have a temperature-dependent density and viscous plastic rheology. Frictional-plastic deformation is defined by a Drucker-Prager yield criterion:

$$J'_2 = P \sin \phi_{eff} + C_0 \cos \phi_{eff} \quad (4.1)$$

where  $J'_2$  is the square root of the second invariant of the deviatoric stress tensor ( $J'^2_2 = 0.5\sigma'_{ij}\sigma'_{ij}$ ),  $P$  is pressure (mean stress),  $C_0$  is the cohesion, and  $\phi_{eff}$  is the effective internal angle of friction. The internal angle of friction decreases from  $15^\circ$  to  $2^\circ$  for accumulated strain of 0.5 to 1.5 to approximate material softening during deformation (Beaumont et al., 2006).

At stresses below the frictional-plastic yield strength, deformation is viscous and follows a power-law creep rheology:

$$\eta_{eff}^v = f B^* \dot{I}'_2^{(1-n)/n} \exp\left(\frac{Q+PV^*}{nRT}\right) \quad (4.2)$$

where  $\eta_{eff}^v$  is the effective viscosity,  $f$  is a scaling factor,  $B^*$  is the pre-exponential factor,  $\dot{I}'_2$  is the square root of the second invariant of the strain rate tensor ( $\dot{I}'^2_2 = 0.5\dot{\epsilon}_{ij}\dot{\epsilon}_{ij}$ ),  $n$  is the stress exponent,  $Q$  is the activation energy,  $V^*$  is the activation volume,  $R$  is the ideal gas constant

( $8.3145 \text{ mol}^{-1} \text{ K}^{-1}$ ), and  $T$  is the absolute temperature. The rheological parameters ( $B^*$ ,  $n$ ,  $Q$ ,  $V^*$ ) are obtained from reliable laboratory studies of crust and mantle rocks (e.g., Beaumont et al., 2006). The upper-mid crust use the parameters of wet quartzite (Gleason & Tullis, 1995), and the lower crust, including the eclogitized layer, uses the parameters of mafic granulite (Wang et al., 2012). The mantle lithosphere and asthenosphere use the parameters of wet olivine with a water content of 1000 ppm H/Si (Hirth & Kohlstedt, 2003; Behn et al., 2009). The scaling factor ( $f$ ) is used to linearly vary the model viscosity relative to the laboratory materials (Beaumont et al., 2006). We assume that the mantle lithosphere is relatively dry and therefore a scaling factor of  $f=10$  is used to approximate its higher strength relative to the more hydrated sublithospheric mantle. All other materials use the lab-based rheologies directly ( $f=1$ ).

The initial thermal structure is determined based on the distribution of model materials, such that the lithosphere has a conductive geotherm that intersects a 1300 °C mantle adiabat at the base of the lithosphere, and the sublithospheric mantle has an adiabatic gradient of 0.4 °C/km (Figure 4.5). The model is then run for a short time to allow the continental lithosphere to come into isostatic equilibrium. Model is started at this point (model time of 0 m.y.). The top boundary is a stress-free surface with  $T=0$  °C. This allows topography to dynamically develop in response to the subsurface structure and dynamics. The model elevation is relative to the craton on the right-hand side of the model, which is 300 m above sea level (see below). The base of the model is a closed, free slip boundary with  $T=1564$  °C. Both side boundaries are insulated, no-slip boundaries. We do not include plate shortening (e.g., Mazzotti & Hyndman, 2002), plate boundary processes, or regional mantle flow (e.g., Finzel et al., 2014), as our goal is to examine the effects of delamination alone. Our model also does not include any surface processes (e.g., erosion and sedimentation).

#### **4.7.2 Additional results from the preferred model**

Figure 4.6 shows vertical temperature profiles at  $x=700$  and  $900$  km, to show how the thermal structure varies at different times and the implications for lithospheric thinning/thickening and mantle melting. For the mantle, the model temperatures are compared to the damp solidus, which is based on an olivine water content of 1000 ppm H/Si and partition coefficients for a

peridotite composition (Ardia et al., 2012; Hirschmann, 2000; Kelley et al., 2010). Where temperatures are above the solidus, the mantle undergoes melting. At 14 m.y., temperatures at  $x=700$  km increase as delamination initiates in this region, rapidly thinning the lithosphere (thickness of  $\sim 50$  km, based on a temperature of  $1200$  °C). By 17 m.y., heating has affected the region at  $x=900$  km, and from 17 to 20 m.y., the shallow mantle in both areas has temperatures higher than the solidus. This represents hot mantle that has upwelled to fill the space vacated by the delaminating lithosphere. Both areas then start to cool, which reduces the amount of melting. Delamination also results in a Moho temperature of  $800$  to  $900$  °C. However, the crustal temperatures are below the solidus of dry granite (Elkins-Tanton, 2005) and no extensive crustal melting is predicted.

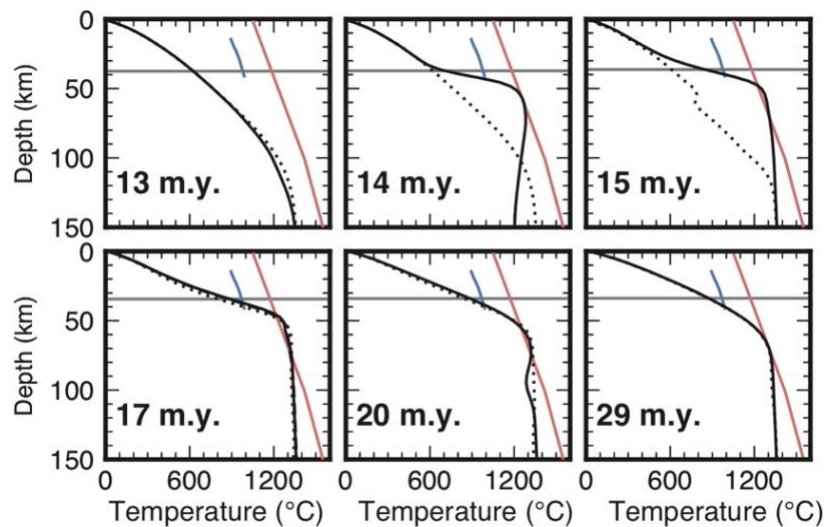


**Figure 4.6** Temperature-depth profiles over time at  $x=700$  km (solid black line) and  $x=900$  km (dotted line) for the preferred model. The red line is the damp peridotite solidus (see text). The blue line is the dry granite solidus (Elkins-Tanton, 2005). The gray solid line is the average Moho depth in the models between 700 and 900 km at each time.

Figure 4.7 shows a distance-time plot for the surface elevation and rate of vertical displacement for the preferred model. Before delamination, surface topography is relatively low to the west of the Tintina Fault because of the dense eclogitized lower crust, and there is little

vertical motion. Delamination initiates at 13-14 m.y., which creates  $>0.5$  km of surface uplift in the cordilleran region, with an uplift of  $\sim 1$  mm/yr that progresses toward the Tintina Fault over 3-4 m.y. Delamination also induces a small amount of transient subsidence of the adjacent regions due to both the high density of the delaminating slab and by mantle flow induced by lithospheric removal. After 20 m.y., there is little vertical change in the surface elevation.

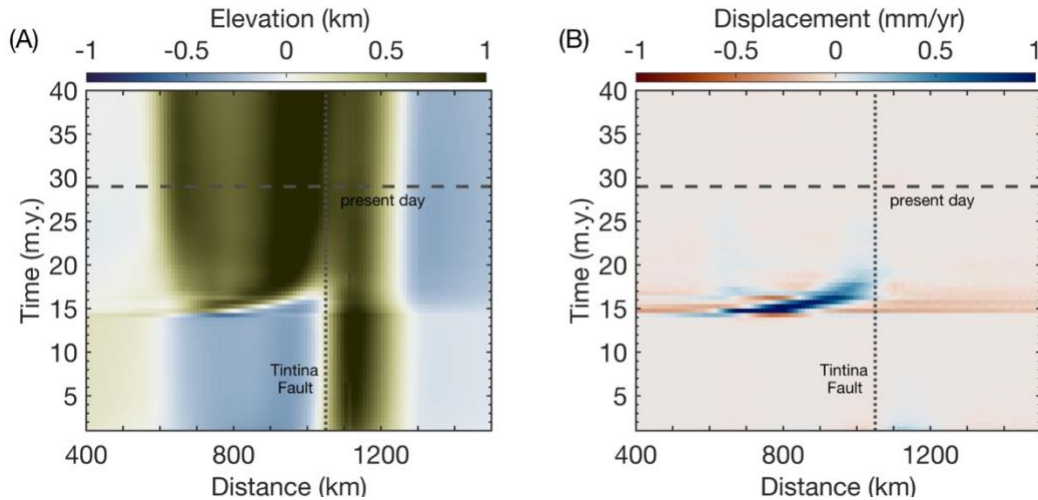


**Figure 4.7** Spatiotemporal evolution of (A) surface topography and (B) rate of vertical displacement for the reference model, where positive values indicate uplift.

The maximum shear strain rate for the preferred model is shown in Figure 4.8 to illustrate the dynamics of delamination. Before delamination, the removal of the mantle weak zone creates an asthenospheric conduit and a region of high shear strain rate in the deep crust. Deformation concentrates in this layer owing to its weaker rheology compared to mantle lithosphere. By 14 m.y. delamination has initiated and this causes the shear strain rate to transfer to the upper crust. Delamination is accompanied by a lateral migration of crustal deformation. After delamination, the shear strain rate in the upper crust decreases. In addition, delamination induces enhanced strain rates in the thicker lithosphere adjacent to the Tintina Fault, including the weak MM block. This persists after delamination has ended, although the magnitude decreases. As the cordilleran mantle starts to cool after 20 m.y., the shallow mantle becomes stronger, and the weak lower crust is visible as a region of higher strain rate.

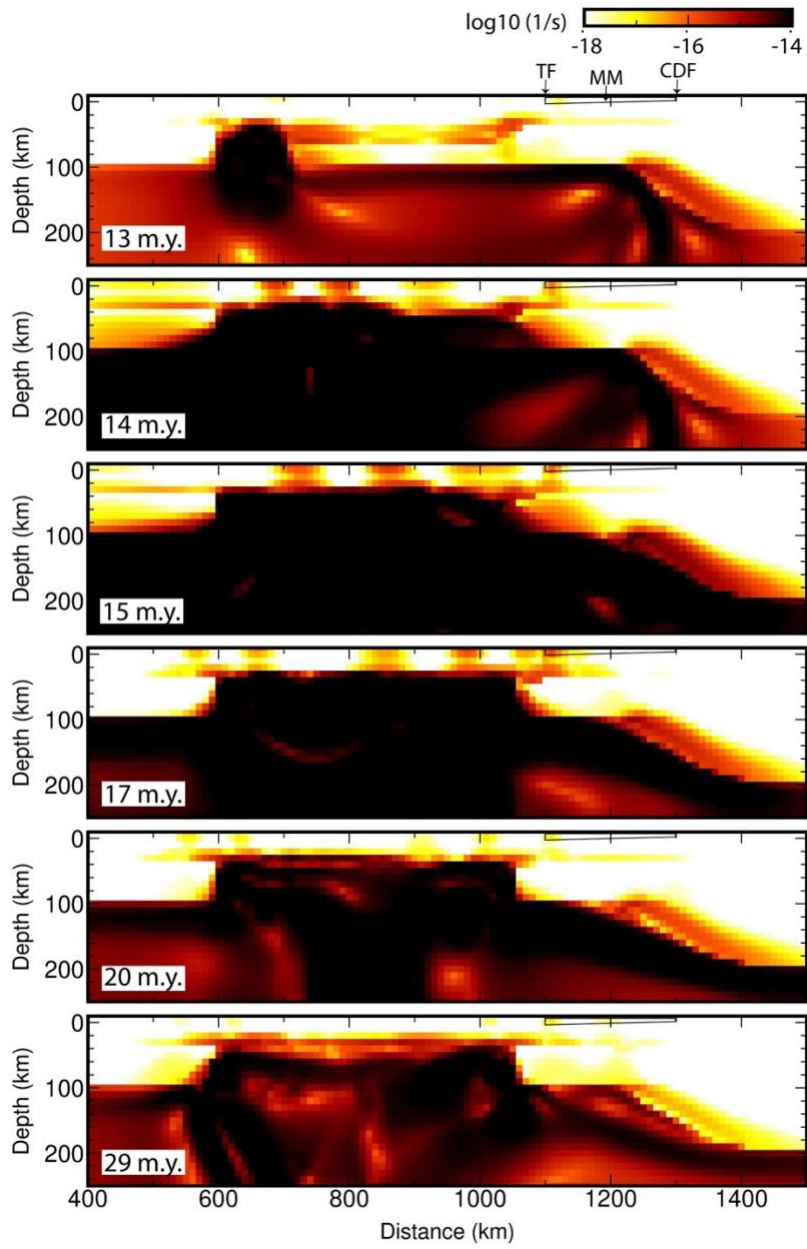


**Figure 4.8** Effect of delamination on the maximum shear strain rate field at the given model times for the preferred model.

**Table 4.1** Material parameters used in the model shown in Figure 4.2 (the preferred model). MM=Mackenzie Mountains block, uc. = upper crust (0-9 km depth), mc. = mid-crust (9-21 km depth), ec. = eclogitized lower crust, cr. = craton mantle lithosphere.

	Upper-middle crust	Lower Crust	Mantle lithosphere	Sublithospheric mantle
<b>Plastic rheology</b>				
$C_0$ (MPa)	20, 0 (MM)	0	0	0
$\phi_{eff}$	15° to 2°, 1° (MM)	15° to 2°	15° to 2°	15° to 2°
<b>Viscous rheology</b>				
$f$	1	1	10	1
$A_{uni}$ (Pa <sup>-n</sup> s <sup>-1</sup> )	1.1x10 <sup>-28</sup>	6.3x10 <sup>-22</sup>	3x10 <sup>-20</sup>	3x10 <sup>-20</sup>
$C_{OH}$ (ppm H/Si)	n/a	n/a	1000	1000
$r$	0	0	1.2	1.2
$B^*$ (Pa <sup>-n</sup> s <sup>-1</sup> ppm H/Si <sup>r</sup> ) <sup>a</sup>	2.9x10 <sup>6</sup>	1.3x10 <sup>6</sup>	1.1x10 <sup>4</sup>	1.1x10 <sup>4</sup>
$n$	4	3.2	3.5	3.5
$Q$ (kJ mol <sup>-1</sup> )	223	244	480	480
$V^*$ (cm <sup>3</sup> mol <sup>-1</sup> )	0	0	11	11
<b>Density<sup>b</sup></b>				
$\rho_0$ (kg m <sup>-3</sup> )	2800, 2700 (MM)	3000, 3450 (ec.)	3250, 3230 (cr.)	3250
$T_0$ (°C)	627	627	1327	1327
$\alpha$ (K <sup>-1</sup> )	3 x 10 <sup>-5</sup>	3 x 10 <sup>-5</sup>	3 x 10 <sup>-5</sup>	3 x 10 <sup>-5</sup>
<b>Thermal parameters</b>				
$k$ (W m <sup>-1</sup> K <sup>-1</sup> )	3	3	3	3
$A$ (μW m <sup>-3</sup> ) <sup>c</sup>	4.4 (uc.), 0.9 (mc.)	0.5	0 1250	0
$C_P$ (J kg <sup>-1</sup> )	750	750		1250
Eclogite $\rho_0$ (kg m <sup>-3</sup> )		3400		

<sup>a</sup>  $B^* = \left[ \frac{1}{2} \left( \frac{3}{2} \right)^{\frac{n+1}{2}} \right]^{-\frac{1}{n}} A_{uni}^{-\frac{1}{n}} (C_{OH}^r)^{-\frac{1}{n}}$ , where the term in the square bracket converts rheological parameters from uniaxial laboratory experiments ( $A_{uni}$ ) to the plain strain,  $C_{OH}$  is water content,  $r$  is the water content exponent (Hirth & Kohlstedt, 2003; Behn et al., 2009).

<sup>b</sup> Temperature dependent density:  $\rho(T) = \rho_0 [1 - \alpha(T - T_0)]$ , where  $\rho_0$  is a reference density,  $T_0$  is a reference temperature, and  $\alpha$  is a volumetric thermal expansion coefficient.

<sup>c</sup> Radiogenic heat production follows values from Lewis et al. (2003).

### 4.7.3 Additional models

We have conducted an extensive set of delamination models to examine the factors that affect the surface expressions and the geometry of the lithosphere. Here we show two models to demonstrate two important factors: a dense lower crust that extends east of the Tintina Fault (Model 2) and a model with no weak MM block (Model 3). For each model, all other parameters are the same as in our preferred model (Figure 4.2, Table 4.1).

In Model 2 (Figure 4.9), the eclogitized lower crust has a reference density of  $3400 \text{ kg/m}^3$  ( $50 \text{ kg/m}^3$  less than that of the preferred model), and it extends to the east of the TF; this layer has a thickness of 3 km at the TF and linearly decreases eastward to 0 km at the CDF. Delamination below the cordillera is very similar to the preferred model. However, the presence of the eclogitized layer east of the TF causes the lithosphere below the MM to bend downwards and detach from the low-density crust. The detachment point is located at  $x=1100 \text{ km}$  at 29 m.y., 50 km east of the TF. This creates more horizontal compression in the MM block than in the preferred model, and the crustal thickness (defined as the base of the low-density crust) is 39-40 km below the MM. This model demonstrates how the deep lithosphere can affect the structure and stress within the overlying crust. However, the modelled mantle melt occurs up to 50 km east of the Tintina Fault after 25 m.y., and the presence of the dense eclogite and inclined lithosphere layer produce a relatively low elevation in the MM compared to the cordillera, which are inconsistent with present-day observations.

Figure 4.10 shows Model 3 in which there is no weak MM block. This does not affect the dynamics of delamination. However, with the absence of weak near-surface rocks, there is less deformation in the MM region. In addition, this creates small differences in sublithospheric mantle flow, such that there is a reduction in the amount of model mantle melt to the west of Tintina Fault after 23 Myr.

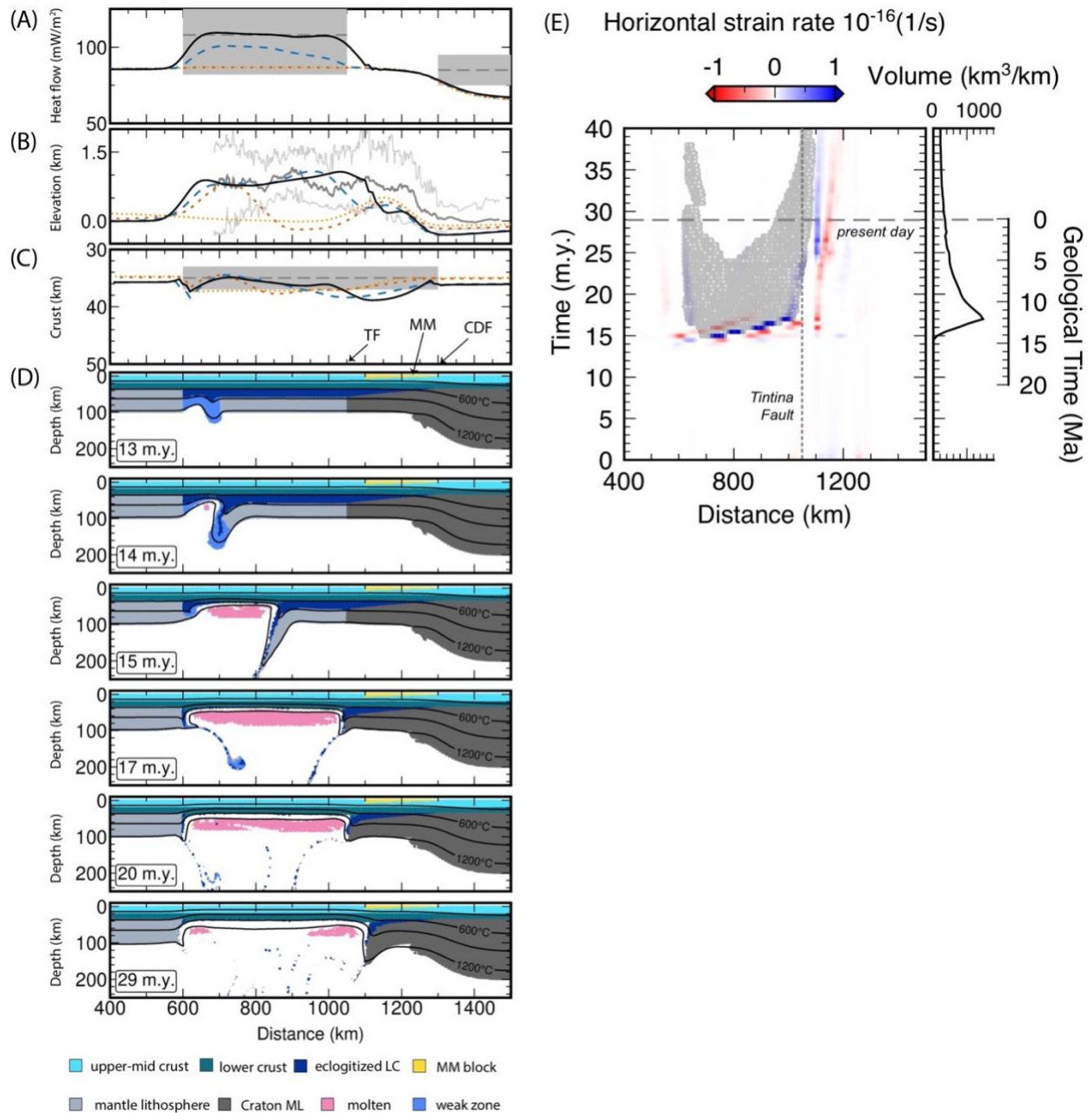


**Figure 4.9** Evolution of Model 2 in which reference density of the eclogitized lower crust is 3400 kg/m<sup>3</sup> and extends beneath the Mackenzie Mountains (MM) where its thickness decreased from 3 km at the Tintina Fault (TF) to 0 km at the Cordilleran Deformation Front (CDF). (A) Surface heat flow, (B) elevation relative to the craton, and (C) crustal thickness at 13 m.y. (dotted yellow line), 15 m.y. (short-dashed orange line), 20 m.y. (long-dashed blue line), and 29 m.y. (solid black line). The observations are in grey. (D) The model geometry and temperature field at the given times. (E) The spatial and temporal distribution of the modeled mantle melt (grey) and surface horizontal strain rate, as well as the total melt volume over time (right side).

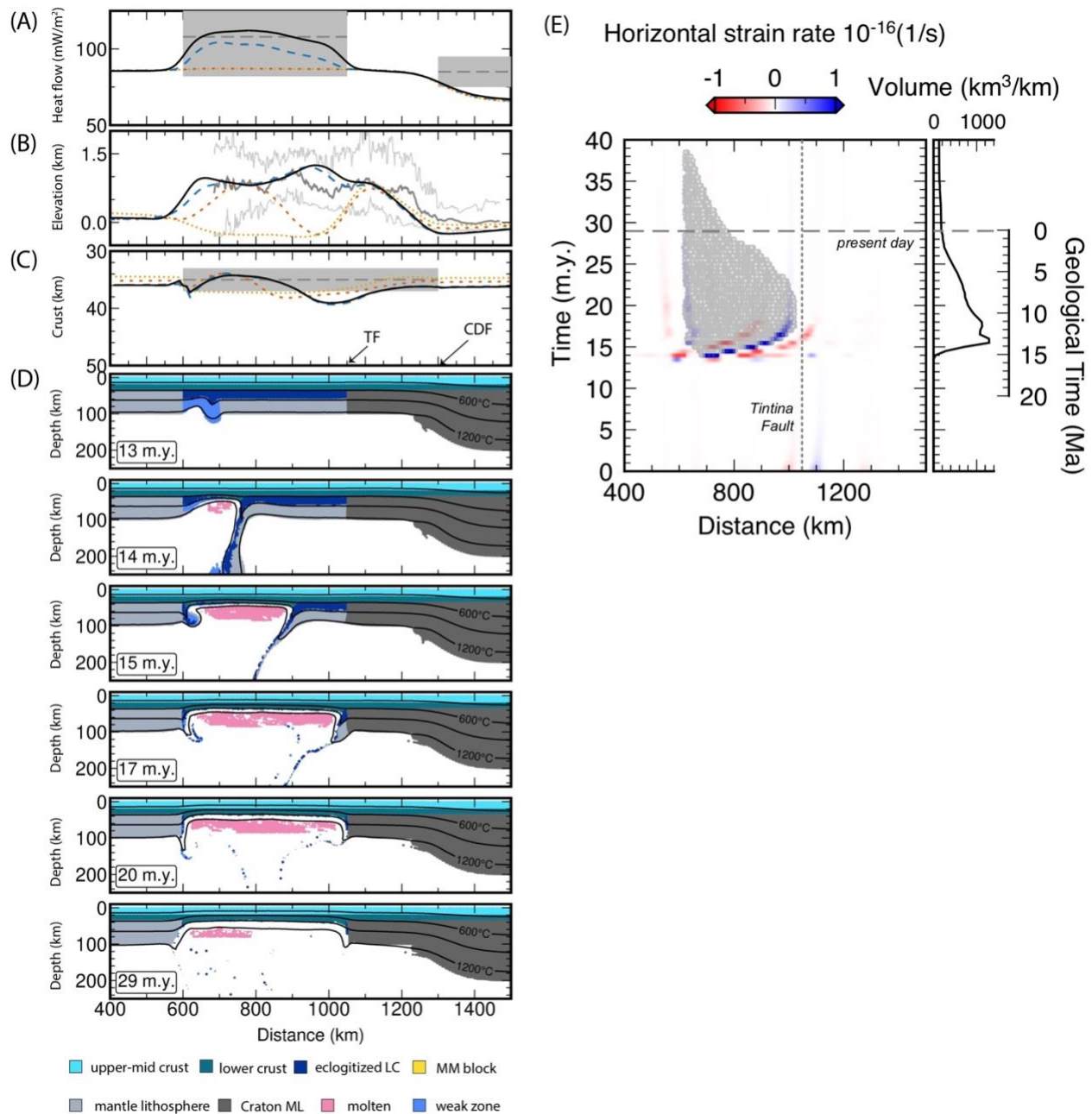


**Figure 4.10** Evolution of Model 3 in which there is no weak Mackenzie Mountains block. (A) Surface heat flow, (B) elevations relative to craton, (C) crustal thickness, and (D) model geometry and thermal structure at the given model times, using the same format as in Figure 4.9. (E) The spatial and temporal distribution of the modeled mantle melt (grey) and surface horizontal strain rate, as well as the total melt volume over time (right side).

#### 4.7.4 Observed surface topography and heat flow

Figure 4.11A shows the surface topography from the ETOPO1 model (Amante & Eakins, 2009) and the location of surface heat flow measurements (Lewis et al., 2003). The model profile approximately corresponds to line A-A' (with data extracted from within the dashed box on Figure 4.11A). The surface heat flow is shown in Figure 4.11B. At present day, surface heat flow has high values ( $\sim 108 \text{ mW/m}^2$ ) in the cordillera and lower values ( $\sim 85 \text{ mW/m}^2$ ) in the craton. The high heat flow in the craton is primarily a consequence of high crustal radiogenic heat within the Paleoproterozoic Wopmay Orogen (Lewis et al., 2003). The deeper temperatures are relatively cool, consistent with the thick lithosphere inferred from seismic tomography studies (e.g., Schaeffer & Lebedev, 2014). We have not included detailed variations in crustal heat production in our models, and therefore there is a mismatch between our craton heat flow and the observed heat flow. Figure 4.11C shows the surface topography in the region centred on A-A'. Elevations in the cordillera west of the TF are  $\sim 800 \text{ m}$  greater than those in the craton.

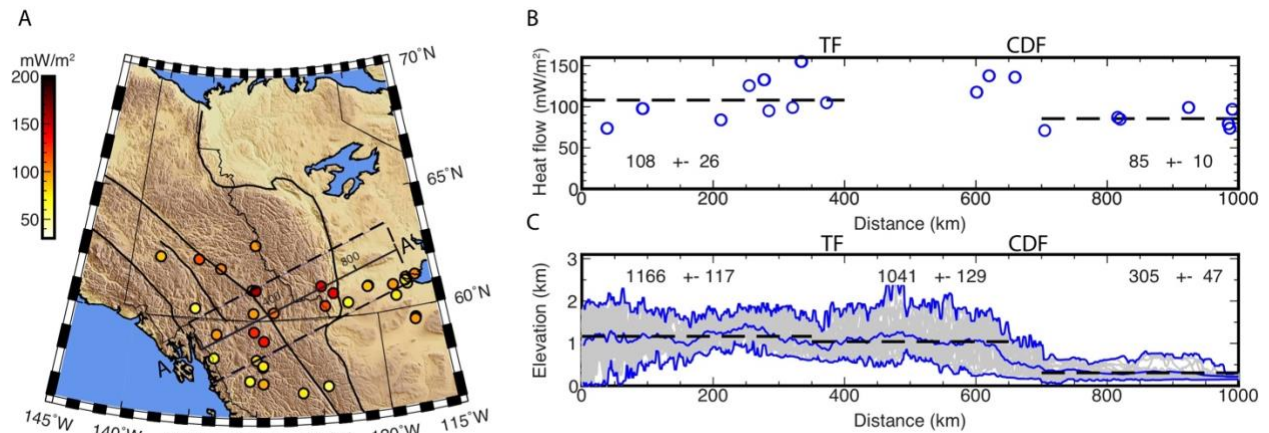


**Figure 4.11** (A) Map of ETOPO1 surface topography (Amante & Eakins, 2009) and heat flow measurements (Lewis et al., 2003). A-A' is the model profile and the black dashed line shows region over which heat flow and topography are extracted. (B) Surface heat flow along A-A'. The dashed lines show the mean values for the cordilleran and craton regions. (C) Surface elevation (relative to sea level) along A-A'. Blue lines are minimum, maximum, and mean values of observed topography; labels give the mean and standard deviation (in m above sea level).

## **Chapter 5**

### **Styles and surface expressions of lithosphere delamination**

## **Abstract**

After continental shortening, many orogenic regions exhibit anomalous surface uplift, magmatism, and crustal deformation. These observations are often attributed to gravitational removal of the lower lithosphere. Here, we investigate the dynamics of delamination, where the lower lithosphere is removed by peeling from the overlying crust. Our 2D thermal-mechanical models assume a pre-thickened crust from earlier shortening, where delamination is induced by eclogitization of the lower crust. If the density of the eclogite layer is close to that of the adiabatic mantle, delamination occurs for an eclogite viscosity of  $\leq 10^{20}$  Pa s; at higher eclogite densities, delamination can occur at higher viscosities. In models with delamination, the eclogite layer detaches from the overlying crust at a point that migrates laterally, resulting in wholesale removal of the mantle lithosphere, mantle decompression melting, and surface uplift. Three styles of delamination are observed. For high eclogite layer viscosities or a cool, thick lithosphere, slab-like delamination occurs, where the detaching slab grows in length and its negative buoyancy increases. This results in rapid removal of the lithosphere ( $< 5$  Myr) and a migrating wave of subsidence followed by uplift. For low eclogite viscosities or a warmer, thinner lithosphere, the detaching lithosphere undergoes internal deformation. Stringy delamination involves necking of the detached lithosphere, which reduces its negative buoyancy and causes a longer delamination timescale (5-20 Myr) and little subsidence. If the eclogite layer is both dense and weak (e.g., temperature  $> 800$  °C), removal occurs through a combination of stringy delamination and drips, leading to a more complex pattern of uplift and magmatism. The topographic expression is also affected by the viscous strength of the shallower crust. If the crust is weak (hot), stresses from the delaminating slab result in crustal thickening and uplift above the detachment point. For a strong (cool) crust, there is little crustal deformation. The models demonstrate the range of surface expressions associated with lithosphere delamination, which may explain the different observations in the western United States.

## **5.1 Introduction**

Mountain belts form through continental plate shortening due to compressive stresses from plate boundary processes. This should lead to a gradual thickening of the continental lithosphere

and increase in surface elevation. However, in many mountain belts, there are a number of observations that indicate episodes of local lithosphere thinning through gravitationally-driven foundering during or after mountain building (e.g., Göğüş & Ueda, 2018; Ueda et al., 2012). One key observation is surface topography, where local areas of short-lived surface uplift or subsidence have been attributed to removal of the deep lithosphere (e.g., DeCelles et al., 2009; Stern et al., 2013). In addition, lithospheric removal has been invoked to explain areas of anomalous magmatism that can not be tied to plate boundary processes (e.g., Bird, 1979). Lithospheric removal during plate shortening may also explain the migration of basins and surface uplift, increased surface heat flow, and volcanic activity (e.g., Göğüş et al., 2016).

Lithospheric removal is driven by the high density of the lower lithosphere relative to the underlying mantle. The mantle lithosphere is cooler than the sublithospheric mantle and therefore its density will be higher, assuming that it is not chemically depleted (e.g., Conrad & Molnar, 1999; Poudjom Djomani et al., 2001). Removal can also be induced if there are compositionally dense materials within the lower lithosphere. One possibility is the presence of eclogite, either due to metamorphic phase changes within thickened lower crust (Krystopowicz & Currie, 2013; Leech, 2001) or through magmatic differentiation that creates a mafic pyroxenite cumulate or residue (Jull & Kelemen, 2001; Lee et al., 2006).

Lithospheric removal can be divided into two end-member mechanisms: viscous Rayleigh-Taylor-type instability (RTI) (e.g., Houseman & Molnar, 1997) and delamination (Bird, 1979). In an RTI, lithospheric removal occurs through local foundering, forming a drip that descends vertically into the deeper mantle, with little horizontal motion. This style of removal is generally limited to the lowermost mantle lithosphere, owing to the high viscosities of the shallower lithosphere (e.g., Conrad & Molnar, 1999). However, a greater thickness of lithosphere can be involved in the drip if the lithosphere viscosity does not depend on temperature (e.g., Göğüş & Pysklywec, 2008a) or the shallower lithosphere contains dense eclogite (e.g., Wang et al., 2015). In contrast, delamination occurs through lateral peeling of the lower lithosphere as a coherent block. Geodynamic modeling studies have shown that delamination occurs if there is a sub-horizontal plane of weakness within the lithosphere that may enable decoupling of the lower lithosphere. In many studies, the weak layer resides in the lowermost continental crust. Early work shows that continental lower crust tends to be aseismic, suggesting ductile deformation and low strength (Chen & Molnar, 1983). This leads to the “jelly-sandwich model” of continental

lithosphere strength, where the lower crust is a zone of weakness that is overlain by strong upper crust (due to cooler temperatures) and underlain by strong mantle lithosphere (due to an ultramafic composition) (e.g., Burov & Watts, 2006). Delamination also requires that the weak layer is connected to the sublithospheric mantle through a low-viscosity conduit with a width of 50-100 km (Göğüş & Ueda, 2018; Morency & Doin, 2004). The conduit may form by local thinning due to mantle convection (Morency & Doin, 2004), locally increased temperatures (Arcay et al., 2007), hydration (Schott & Schmeling, 1998), or deformation (Krystopowicz & Currie, 2013; Stein et al., 2022). It should be noted that hybrid removal mechanisms that involve combinations of RTI and delamination have been identified, including triggered dripping induced by a large lithosphere perturbation (Beall et al., 2017) and lateral shearing of a drip by regional mantle flow (Wang et al., 2021).

In this study, we focus on lithospheric removal through delamination. This has been argued to be an important process in a number of orogens, such as the North America Cordillera, the Carpathians, and the East Anatolian Plateau (e.g., Göğüş & Ueda, 2018 and references therein). We use simplified thermal-mechanical models in order to assess the conditions needed to promote delamination due to the presence of eclogitized lower crust and through systematic variations in density and strength of the eclogite layer, we assess the timescales of delamination and the associated surface expressions (e.g., surface topography, crustal deformation, and magmatism). The models highlight different styles of delamination and demonstrate how the surface expressions depend on the style of removal, as well as the properties of the overlying crust. The models are designed to study a generic continental lithosphere without external forces (e.g., plate motions), and therefore, the results provide new insights into how delamination may be recognized in continental interior regions.

## **5.2 Method**

### **5.2.1 Numerical model setup**

The numerical models use the SOPALE code to compute the coupled thermal-mechanical evolution of the lithosphere-upper mantle system. In this code, the arbitrary Eulerian-Lagrangian finite element technique is used to solve the governing equations of conservation of mass, momentum, and energy, under the assumptions of plane strain and incompressibility (Fullsack, 1995). The thermal and mechanical fields are coupled through the use of temperature-dependent

material properties (viscous rheology and density). The SOPALE code has been used in a number of previous studies to examine the dynamics of lithospheric removal (Currie et al., 2015; Göğüş & Pysklywec, 2008a; Gray & Pysklywec, 2012; Krystopowicz & Currie, 2013; Memiş et al., 2020; Wang & Currie, 2015).

Figure 5.1a shows the initial geometry and boundary conditions of the models. The model domain has a width of 2000 km and a height of 660 km. The Eulerian computation mesh has 200 elements horizontally (10 km width), and 102 elements vertically. The element height varies with depth, with a height of 3 km from the surface to 60 km depth, 5 km height between 60 and 280 km depth, and 10 km height below 280 km depth. The smaller elements in the upper part of the model allow local lithosphere dynamics to be resolved. Material properties are tracked on a Lagrangian mesh and additional Lagrangian tracer particles. The Lagrangian particles are moved at each time step based on the model velocity field and are used to update the distribution of materials in the Eulerian mesh; they are also used to track properties such as cumulative strain.

The model consists of continental lithosphere that overlies sublithospheric mantle. The continental lithosphere has an initial lithospheric thickness of 100 km everywhere. The model is constructed so that lithospheric removal occurs over a width of 800 km in the middle of the model plane (Figure 5.1a). We assume that the central region underwent an earlier period of crustal shortening, and therefore the crustal thickness is 60 km, including an 18 km upper-mid crust, 27 km lower crust, and a 15 km layer of eclogitized lower crust (Gordon et al., 2013; Kay & Kay, 1993; Krystopowicz & Currie, 2013; Valera et al., 2014); this is underlain by the mantle lithosphere layer. Our models examine how variations in the density and rheology of the eclogite layer affect gravitational removal. At the left side of this region, there is a 50 km wide weak zone in the mantle lithosphere that has a constant viscosity of  $10^{19}$  Pa s and the same density as the mantle lithosphere. This zone is needed in order to create an asthenospheric conduit that triggers gravitational removal (Göğüş & Pysklywec, 2008a; Wang & Currie, 2015), and it is assumed that this represents an area of weakness due to earlier hydration or strain-induced weakening. Tests show that the width of the weak zone has a negligible effect on surface expressions. Outside of the central region, the continental lithosphere has an 18 km upper crust, 27 km lower crust, and 55 km mantle lithosphere.

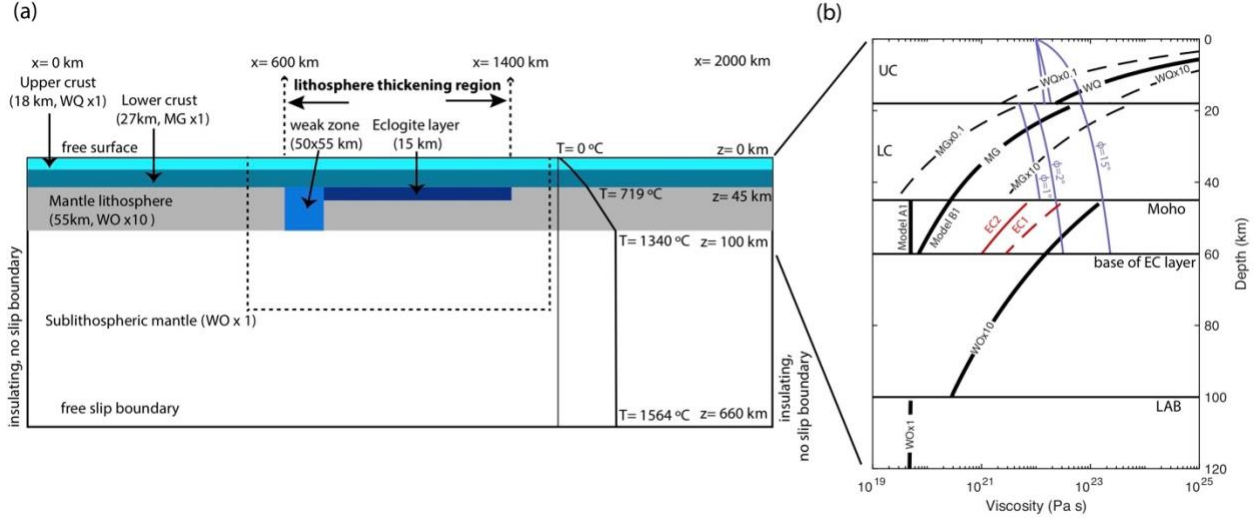


**Figure 5.1** (a) Initial model geometry and thermal-mechanical boundary conditions; the initial geotherm is also shown. The upper crust rheology is wet quartzite (WQ). Lower crust is mafic granulite (MG). Mantle lithosphere and sublithospheric mantle are wet olivine (WO). The dashed rectangle is the area of the plots shown in later figures. (b) Lithosphere viscosity profile based on the initial thermal structure and strain rate of  $10^{-15} \text{ s}^{-1}$ . Thick lines show the effective viscosity for the reference crust and mantle lithosphere (Models A1 and B1). Dashed lines indicate the range of crustal rheologies tested in the Type B models (see text for details). Red lines show the effective viscosity of eclogite (EC) based on two experimental studies: EC1 (Jin et al., 2001) and EC2 (Zhang & Green, 2007). Blue lines are frictional-plastic yield stress for unsoftened ( $\phi = 15^\circ$ ) and softened ( $\phi = 1^\circ$ ;  $\phi = 2^\circ$ ) materials.

## 5.2.2 Material properties

The material properties are given in Table 5.1. All materials have a viscous-plastic rheology. Frictional-plastic deformation is based on the Drucker-Prager yield stress criterion:

$$(J'_2)^{1/2} = P \sin \phi_{eff} + C_0 \cos \phi_{eff} \quad (5.1)$$

where  $J'_2$  is the second invariant of the deviatoric stress tensor  $\sigma'_{ij}$  ( $2J'_2 = \sigma'_{ij}\sigma'_{ij}$ ),  $P$  is dynamic pressure (mean stress),  $C_0$  is cohesion, and  $\phi_{eff}$  is the effective angle of internal friction. Strain softening is included by reducing  $\phi$  from  $15^\circ$  to  $2^\circ$  over an accumulated strain between 0.5 and 1.5 (Huismans & Beaumont, 2003). Frictional-plastic deformation is modelled by using an effective viscosity that places the material on the yield stress:

$$\eta_{eff}^p = \frac{\sqrt{I_2'}}{2\sqrt{I_2}} \quad (5.2)$$

where  $\eta_{eff}^p$  is effective viscosity for a plastic material and  $I_2$  is the square root of the second invariant of the strain rate tensor  $\dot{\epsilon}_{ij}$  ( $I_2^2 = 0.5\dot{\epsilon}_{ij} \dot{\epsilon}_{ij}$ ) (Willett, 1999). At stresses below the frictional-plastic yield stress, materials deform viscously, using a temperature-dependent power-law rheology with an effective viscosity ( $\eta_{eff}^v$ ):

$$\eta_{eff}^v = fB^*I_2^{\left(\frac{1-n}{n}\right)} e^{\left[\frac{Q+PV^*}{nRT}\right]} \quad (5.3)$$

where  $f$  is a scaling factor,  $R$  is the ideal gas constant, and  $T$  is the temperature in Kelvin. The rheological parameters, including the preexponential factor ( $B^*$ ), stress exponent ( $n$ ), activation energy ( $Q$ ), and activation volume ( $V^*$ ), are obtained from laboratory studies of deformation of crust and mantle rocks. The scaling factor ( $f$ ) is used to linearly vary the viscosity relative to the reference laboratory materials, in order to account for variations in composition and hydration (Beaumont et al., 2006).

**Table 5.1** Materials parameters used in numerical models.

	Upper crust	Lower Crust	Mantle lithosphere	Sublithospheric mantle
<b>Plastic rheology</b>				
$C_0$ (MPa)	20	0	0	0
$\phi_{eff}$	15° to 2°	15° to 2°	15° to 2°	15° to 2°
<b>Viscous rheology parameters<sup>a</sup></b>				
$f$	1	1	10	1
$A_{uni}$ (Pa <sup>-n</sup> s <sup>-1</sup> )	1.1x10 <sup>-28</sup>	6.3x10 <sup>-22</sup>	3x10 <sup>-20</sup>	3x10 <sup>-20</sup>
$C_{OH}$ (ppm H/Si)	n/a	n/a	1000	1000
$r$	0	0	1.2	1.2
$B^*$ (Pa <sup>-n</sup> s <sup>-1</sup> (ppm H/Si) <sup>r</sup> )	2.9x10 <sup>6</sup>	1.3x10 <sup>6</sup>	1.1x10 <sup>4</sup>	1.1x10 <sup>4</sup>
$n$	4	3.2	3.5	3.5
$Q$ (kJ mol <sup>-1</sup> )	223	244	480	480
$V^*$ (cm <sup>3</sup> mol <sup>-1</sup> )	0	0	11	11
<b>Density parameters</b>				
$\rho_0$ (kg m <sup>-3</sup> )	2800	3000	3250	3250
$T_0$ (°C)	627	627	1327	1327
$\alpha$ (K <sup>-1</sup> )	3d-5	3d-5	3d-5	3d-5
<b>Thermal parameters</b>				
$k$ (W m <sup>-1</sup> K <sup>-1</sup> )	2.5	2.5	2.5	2.5
$A$ ( $\mu$ W m <sup>-3</sup> )	1.1	0.4	0	0
$C_P$ (J kg <sup>-1</sup> )	750	750	1250	1250

<sup>a</sup> the pre-exponential factor of the viscous rheology is:  $B^* = [\frac{1}{2}(\frac{3^{\frac{n+1}{2}}}{2})^{-\frac{1}{n}}]A_{uni}^{-\frac{1}{n}}(C_{OH}^r)^{-\frac{1}{n}}$ , where the first term in the square bracket converts rheological parameters from uniaxial laboratory experiments ( $A_{uni}$ ) to the plain strain,  $C_{OH}$  is a water content,  $r$  is a water content exponent (Hirth & Kohlstedt, 2003; Behn et al., 2009).

The upper-mid crust, lower crust, and mantle use the viscous rheologies of wet quartzite (WQ, Gleason & Tullis, 1995), mafic granulite (MG, Wang et al., 2012), and wet olivine with a water content of 1000 ppm H/Si (WO, Hirth & Kohlstedt, 2003), respectively (Table 5.1). The layered crust reflects the compositional layering inferred from the analysis of seismic velocities of continental crust in general (e.g., Christensen & Mooney, 1995). We assume that the mantle lithosphere is relatively dry owing to dehydration during lithosphere formation, whereas the sublithospheric mantle is more hydrated (e.g., Hirth & Kohlstedt, 1996; Hyndman & Canil, 2021).

Therefore, the mantle lithosphere uses the rheology of WO with  $f=10$ , such that it is 10 times stronger than the sublithospheric mantle at the same temperature and strain rate. All other materials use  $f=1$ . The model experiments examine variations in the rheology of the eclogite layer, as discussed in Section 5.2.4. The lithospheric strength profile at the start of the models is shown in Figure 5.1b.

The density of each material ( $\rho$ ) varies with temperature ( $T$ ):

$$\rho(T) = \rho_0[1 - \alpha(T - T_0)] \quad (5.4)$$

where  $T_0$  is the reference temperature,  $\rho_0$  is reference density, and  $\alpha$  is thermal expansion coefficient, with the values in Table 5.1. The models use material densities based on earlier studies (e.g., Currie & van Wijk, 2016; Krystopowicz & Currie, 2013). Figure 5.2a shows the initial density profile based on the starting geotherm, and Figure 5.2b shows the density difference relative to the sublithospheric (adiabatic) mantle. These plots show that the mantle lithosphere is more dense than the sublithospheric mantle because of its cooler temperature, and therefore it is gravitationally unstable. In the models below, variations in the density of the eclogite layer are investigated.

The thermal properties for each material are the thermal conductivity ( $k$ ), radiogenic heat production ( $A$ ), and heat capacity ( $C_p$ ). The upper-mid crust and lower crust have a heat production of  $1.1 \mu\text{W}/\text{m}^3$  and  $0.4 \mu\text{W}/\text{m}^3$ , respectively; there is no heat production in other materials. All model materials have a thermal conductivity of  $2.5 \text{ W m}^{-1} \text{ K}^{-1}$ .

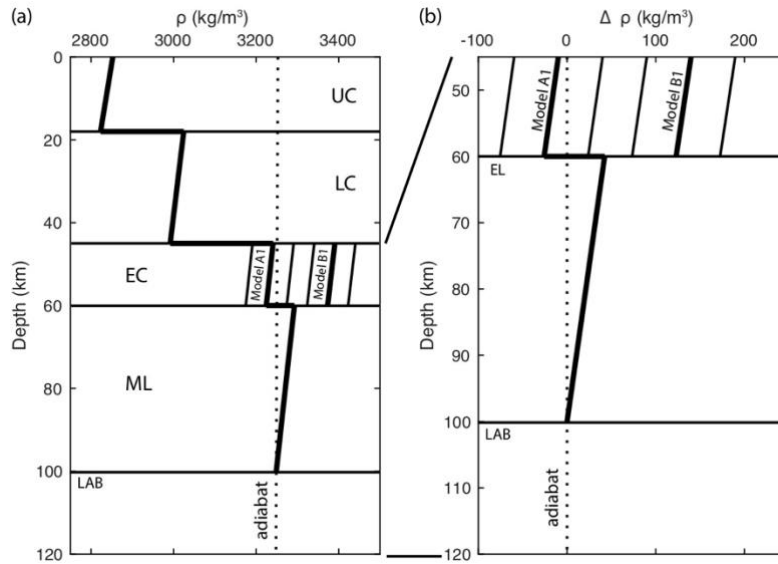


**Figure 5.2** (a) Density profile and (b) profile of the density difference relative to the adiabatic mantle, based on the initial model geotherm. The densities include the effects of composition and temperature. Within the eclogite layer, the lines correspond to compositional density contrasts of -118, -68, -18, +32, +82 and +132 kg/m<sup>3</sup> (from left to right), where the density contrast is relative to mantle at the same temperature. UC=upper crust, LC=lower crust, EC=eclogite layer, ML=mantle lithosphere, EL=bottom of the eclogite layer, LAB=lithosphere-asthenosphere boundary.

### 5.2.3 Model initiation and boundary conditions

The models are initiated in two steps. First, the initial model temperature is assigned based on the geotherm shown in Figure 5.1; there are no lateral variations in temperature. The geotherm has a surface heat flow of 59 mW/m<sup>2</sup>, a temperature of 719 °C at 45 km depth, and a temperature of 1340 °C at the base of the lithosphere; below this, the sublithospheric mantle follows a 1300 °C adiabat, with an adiabatic temperature gradient of 0.4 °C/km. The models are then run for a short time to allow for isostatic equilibrium between the central region with thick crust and the regions on the sides. The model experiments start at this point. The models have a uniform lithospheric thickness, so there is no significant effect on the model results if the isostatic equilibrium phase is not included.

Figure 5.1a shows thermal and mechanical boundary conditions during the model run. The top boundary has a temperature of 0 °C, and it is a stress-free surface, so that topography can develop due to subsurface dynamics and lateral density variations. The models do not include

surface processes such as sedimentation and erosion. The base of the model (660 km depth) is a free-slip boundary with a temperature of 1564 °C. The sides of the model domain are no-slip boundaries with no lateral heat flow (i.e., insulating boundaries). The region that undergoes lithosphere thinning region is 600 km away from the side boundaries, and tests show that both no-slip and free-slip conditions on the side boundaries give similar results.

#### 5.2.4 Numerical model experiments

The goal of this study is to examine the factors that control the dynamics of delamination and the resulting surface expressions. In the models, delamination is induced by the presence of the eclogite layer in pre-existing thick crust. Lower crust eclogitization is likely to occur at depths larger than 45 km (e.g., Hacker et al., 2003; Krystopowicz & Currie, 2013). Therefore, we assume that lower 15 km of thickened crust (i.e., between depths of 45 and 60 km) has been eclogitized, and our models examine how variations in the rheology and density of this layer affect delamination.

The models are divided into two groups. In Type A models (Section 5.3), the eclogite layer has a constant viscosity in order to simplify the models. The reference model (Model A1) has a viscosity of  $5 \times 10^{19}$  Pa s. Other models test viscosities from  $10^{19}$  to  $10^{25}$  Pa s. We also examine different densities of the eclogite layer. Eclogite is 50 to 300 kg/m<sup>3</sup> greater than mantle at the same temperature (Austrheim, 1991; Bousquet et al., 1997), but lower values may occur if the crust does not fully eclogitize. We report the eclogite layer density using its density contrast ( $\Delta\rho$ ) relative to mantle materials at the same temperature (i.e., the compositional density difference). In Model A1, the eclogite layer has a density contrast of  $\Delta\rho = -68$  kg/m<sup>3</sup>, where the negative sign indicates that the eclogite is less dense than mantle. We have tested  $\Delta\rho$  values of -118 to +132 kg/m<sup>3</sup> for the eclogite layer (Figure 5.2a). Owing to the lower temperatures in the eclogite layer, these correspond to variations in the actual density of this layer that range from ~75 kg/m<sup>3</sup> less than the adiabatic mantle to ~190 kg/m<sup>3</sup> more dense (Figure 5.2b).

In Type B models (Section 5.4), the eclogitized layer uses the rheology of mafic granulite (MG, Wang et al., 2012), which is the same rheology as the uneclogitized lower crust (Figure 5.1b). The rheology of eclogite is uncertain, with some studies suggesting that eclogite may be

weak because of the presence of water and omphacite (Austrheim, 1991; Leech, 2001), whereas other studies suggest a relatively high strength (e.g., Jin et al., 2001; Zhang & Green, 2007; Figure 5.1b). The effect of a stronger rheology is discussed in Section 5.4.3. Model B1 use an eclogite  $\Delta\rho$  of +82 kg/m<sup>3</sup>. The Type B models are also used to examine the effects of variations in the viscous and frictional-plastic strength of the crust above the eclogite layer and changes in the initial lithosphere thermal structure. Table 5.2 lists the models that are discussed below.

**Table 5.2** List of models discussed in text. EC=eclogite layer.

Model	Rheology variation	EC density contrast (kg/m <sup>3</sup> )	$\phi_{\text{eff}}$ (°)	Temperature at top of EC (°C)	Model type	Figure number
<b>Type A</b> EC has a constant viscosity						
A1	5x10 <sup>19</sup> Pa s	-68	15-2	~700	Reference	5.3; 5.4
A2	10 <sup>22</sup> Pa s	-68	15-2	~700	High viscosity EC	5.6
A3	10 <sup>23</sup> Pa s	132	15-2	~700	High viscosity & high density EC	5.7
A4	10 <sup>19</sup> Pa s	82	15-2	~700	Low viscosity & high density EC	5.8
<b>Type B</b> Upper crust scaling factor (EC has mafic granulite rheology with f=1 for all models)						
B1	f = 1	82	15-2	~700	Reference	5.9; 5.10
B2	f = 0.1	82	15-2	~700	Weak crust	5.11a; 5.12a/b
B3	f = 10	82	15-2	~700	Strong crust	5.11b; 5.12c/d
B4	f = 1	82	1	~700	Softened crust	5.13a
B5	f = 0.1	82	1	~700	Softened & weak crust	5.13b
B6	f = 1	82	15-2	~600	Cool lithosphere	5.14a; 5.15
B7	f = 1	82	15-2	~800	Hot lithosphere	5.14b; 5.16

### 5.2.5 Surface observables

One of the goals of the models is to assess the surface expressions of delamination, including topography, crustal thickness, surface heat flow, Moho temperature, and horizontal

strain rate at the surface. The surface topography is obtained directly from the model, where an elevation of 0 km corresponds to the elevation of the region on either side of the delamination area (i.e., the region without an eclogite layer). The crustal thickness is the sum of the surface elevation and Moho depth, where the elevation and depth are relative to an elevation of 0 km and the Moho is taken as the base of the uneclogitized crust, as this interface is expected to correspond to a downward increase in seismic velocity. In most models, the eclogite layer is fully removed, and therefore the base of the uneclogitized crust corresponds to the crust-mantle boundary. The surface heat flow is calculated by multiplying the vertical thermal gradient at the model surface and the thermal conductivity ( $2.5 \text{ W m}^{-1} \text{ K}^{-1}$ ). The Moho temperature is the temperature at the base of the uneclogitized crust. The horizontal strain rate is determined from the lateral gradient in horizontal velocity field for each Eulerian element at the model surface; a positive value indicates surface horizontal extension, whereas a negative value indicates contraction.

Previous studies have shown that lithospheric removal can induce decompression melting of the mantle and that melting may also occur in the foundering and/or overlying lithosphere as they undergo heating (e.g., Elkins-Tanton, 2005; Wang & Currie, 2015). To assess melting in our current models, the pressure-temperature conditions for mantle materials are compared to the solidus temperature of hydrated peridotite (Hirschmann, 2000). The solidus is determined based on a water content of 1000 ppm H/Si in olivine, compatible with the water content used for the sublithospheric mantle rheology. Continental crustal melting is assessed by comparing the crustal conditions to the dry granite solidus (e.g., Elkins-Tanton, 2005; Wang & Currie, 2015).

### **5.3 Results: Dynamics of delamination**

The Type A models investigate the dynamics of delamination. Through systematic variations in the viscosity and density of the eclogite layer, these models demonstrate the parameters needed for delamination to occur, and the characteristics of delamination, including the timescale and style of removal.

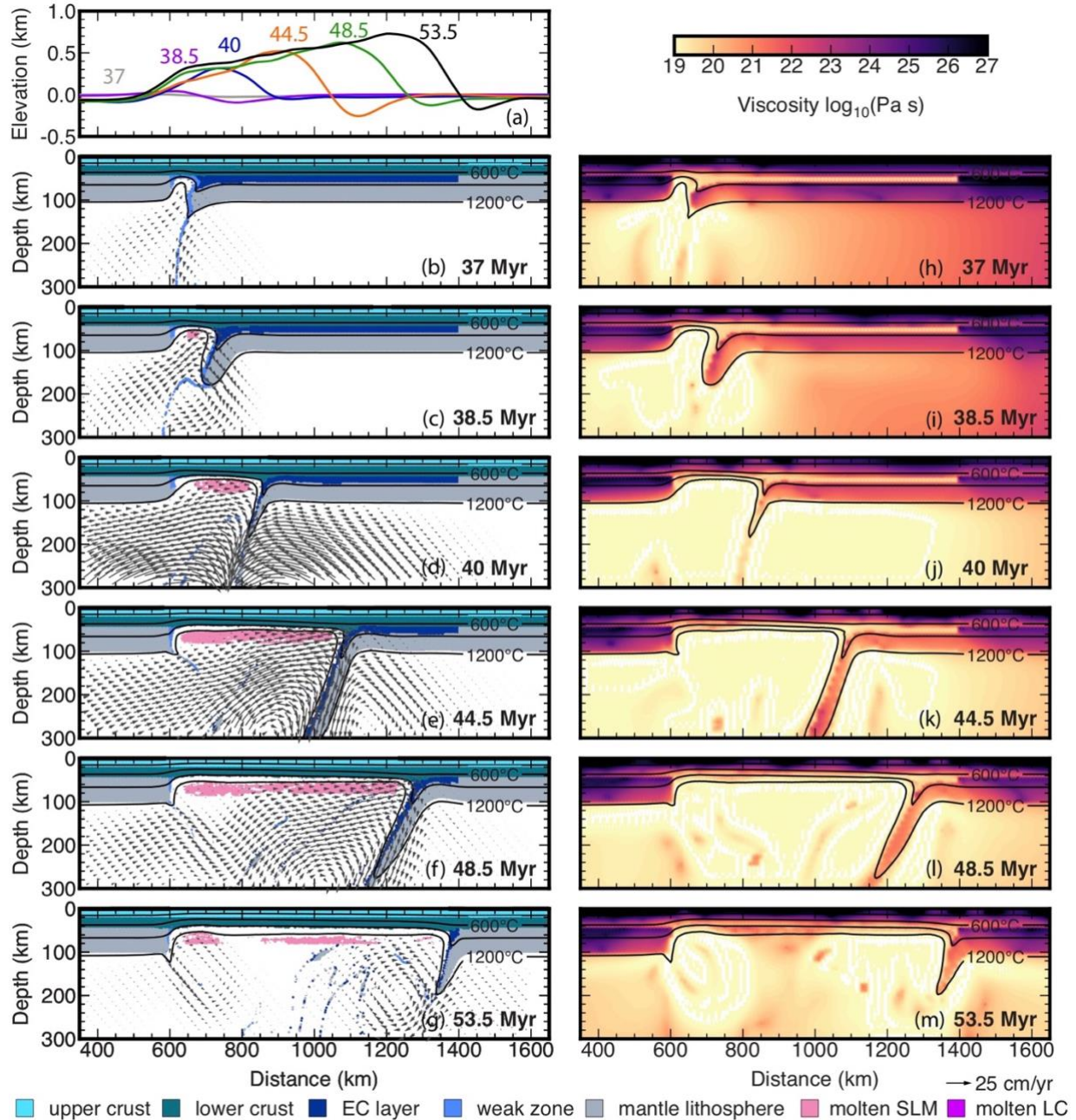
#### **5.3.1 Reference model (Model A1)**

Figure 5.3 shows the evolution of Model A1, in which the eclogite layer is weak (viscosity of  $5 \times 10^{19} \text{ Pa s}$ ) and has a density contrast of  $-68 \text{ kg/m}^3$  compared to the sublithospheric mantle.

It should be noted that the average temperature within the eclogite layer is  $\sim 800$  °C, which makes it  $\sim 550$  °C cooler than the uppermost sublithospheric mantle, and therefore its density is similar to that of the sublithospheric mantle (Figure 5.2).

At the start of the model, the weak zone in the mantle lithosphere creates a low-viscosity conduit at the left end of the eclogite layer and initiates delamination (Figure 5.3h). This allows the edge of the eclogite layer and the underlying mantle lithosphere to begin to destabilize, owing to their high density. At the same time, the weak zone is gravitationally unstable because it is cooler and thus more dense than the underlying mantle. Initially the instabilities grow slowly, but by 30-35 Myr, the weak zone drips into the mantle, allowing sublithospheric mantle to upwell to the base of the eclogite layer in this region (Figure 5.3b). This initiates delamination, as the eclogite layer and mantle lithosphere begin to separate from the overlying crust. The lower lithosphere peels along the top part of the low viscosity eclogite layer, causing the detachment point to migrate laterally toward the right. The delaminating lithosphere forms a slab that steepens to a  $\sim 60^\circ$  dip angle. As delamination proceeds, several slab break-off events occur at  $\sim 40$  Myr,  $\sim 45$  Myr, and  $\sim 49$  Myr. Delamination results in removal of the lower lithosphere across a width of 800 km within  $\sim 15$  Myr of initiation of delamination, with 90% of it being removed in  $\sim 10$  Myr. Delamination is accompanied by a migrating topographic wave, with subsidence to the right of the detachment point and rapid uplift above the area where the lithosphere was thinned to the left of the detachment point (Figure 5.3a).

Lithospheric removal is primarily driven by the high density of the cool mantle lithosphere and it is aided by the low viscosity within the eclogite layer that enables the lower lithosphere to peel away as a semi-coherent slab (Figures 5.3h-m). Removal results in rapid heating of the overlying crust, with the 1200 °C isotherm at a depth of  $\sim 50$  km immediately following removal. Over time, the thinned region undergoes conductive cooling, leading to a gradual deepening of the 1200 °C isotherm and an increase in the viscosity in the shallow mantle (e.g., Figure 5.3m).



**Figure 5.3** Evolution of Model A1 in which the eclogite layer has a viscosity is  $5 \times 10^{19}$  Pa s and a density contrast of  $-68 \text{ kg/m}^3$ . This model exhibits stringy delamination (see text for information). Plots show: (a) surface topography (numbers denote the model time in Myr), (b-g) model structure, and (h-m) viscosity structure at the given times after the start of the model. The black lines are isotherms every  $300 \text{ }^\circ\text{C}$ . LC=lower crust; EC = eclogite; SLM = sublithospheric mantle.

Figure 5.4 shows time-distance plots of several observations associated with delamination, as well as the location of the detachment point. As delamination migrates across the model, there is a narrow zone of crustal thickening above the detachment point (Figure 5.4a). This is created by the downward stresses induced by the dense slab that cause a deepening of the Moho by 3-5 km (Figure 5.4c). Delamination is also marked by a region of high elevation to the left of the detachment point, resulting primarily from sublithospheric mantle upwelling that is triggered by removal of the dense lower lithosphere (Figure 5.4b). The migration of delamination is punctuated by slab break-offs that cause rapid increases in elevation. After 53.5 Myr, delamination stalls at the right edge of the eclogite layer. The removal of the lithosphere leads an area of thin crust and high elevation in the lithosphere thinning region (centre of the model). Between  $x=600$  and  $800$  km the crustal thickness is  $\sim 40$  km and surface elevation is  $\sim 0.4$  km. Crustal thickness and elevation increase toward the right, with the maximum values at approximately  $x=1400$  km. These are the result of crustal thickening induced by the high-density slab that remains in this area (Figure 5.3g). It should be noted that the lower part of the thickened crust is likely at the pressure and temperature conditions where eclogitization may occur (e.g., Hacker et al., 2003). Our models assume that this material remains metastable. Future work should examine the effects of eclogitization of this material, and possible feedback between the delamination process and crustal structure.

Delamination also affects the thermal structure of the continent. The removal of the lower lithosphere results in heating of the overlying crust, where the Moho temperature rapidly increases from  $719$  to  $>900$  °C following the emplacement of the hot sublithospheric mantle (Figure 5.4e). The shallower crust then experiences conductive heating, and the surface heat flow in the thinned region gradually increases from  $60$  to  $\sim 75$  mW/m<sup>2</sup> over  $\sim 10$  Myr (Figure 5.4d).

Figure 5.4f shows the horizontal strain rate at the surface of the model. Delamination is marked by a migrating wave of upper crustal extension in between the high topography and the thick crust. On either side, there is an area of contraction, which may be partially related to lateral compression induced by the adjacent high topography, and on the right side of the detachment point, the contraction may also be the result of the downward stresses associated with the foundering lithosphere. The migration of extension occurs in an unsteady manner, depending on the length of the detached lithosphere slab. The most rapid migration occurs prior to slab break-

offs at ~40, ~45 and ~49 Myr, and there is slower migration at the start of delamination and immediately following the break-offs. The slab break-offs also correspond to times of rapid surface uplift (Figure 5.4b).

Delamination causes the removal of the lower ~55 km of the lithosphere in the central region of the model, allowing hot sublithospheric mantle to upwell. A comparison between the model structure and the mantle and crust solidi shows that the crustal materials do not melt, but decompression melting of the sublithospheric mantle occurs at depths of ~50 to ~90 km (Figures 5.3c-5.3g). The time-distance plot in Figure 5.4f shows that the region of mantle melting expands across the entire width of the thinned lithosphere during delamination. After ~50 Myr, the mantle melt decreases as shallow mantle cools. The longer duration of melt at  $x < 700$  and  $x > 1100$  km coincides with areas of upwelling induced by edge-driven convection at the transition between thick and thin lithosphere.

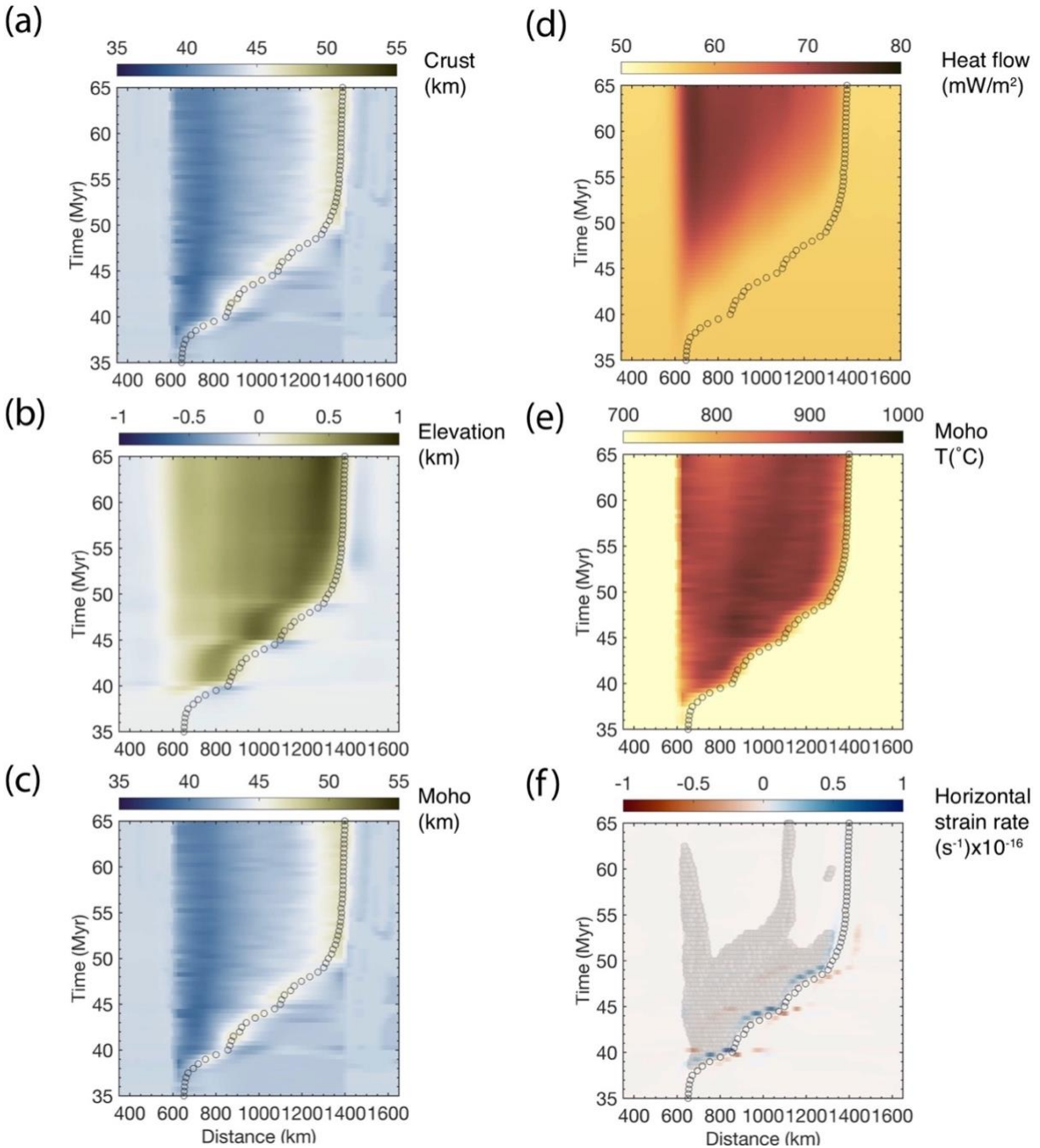


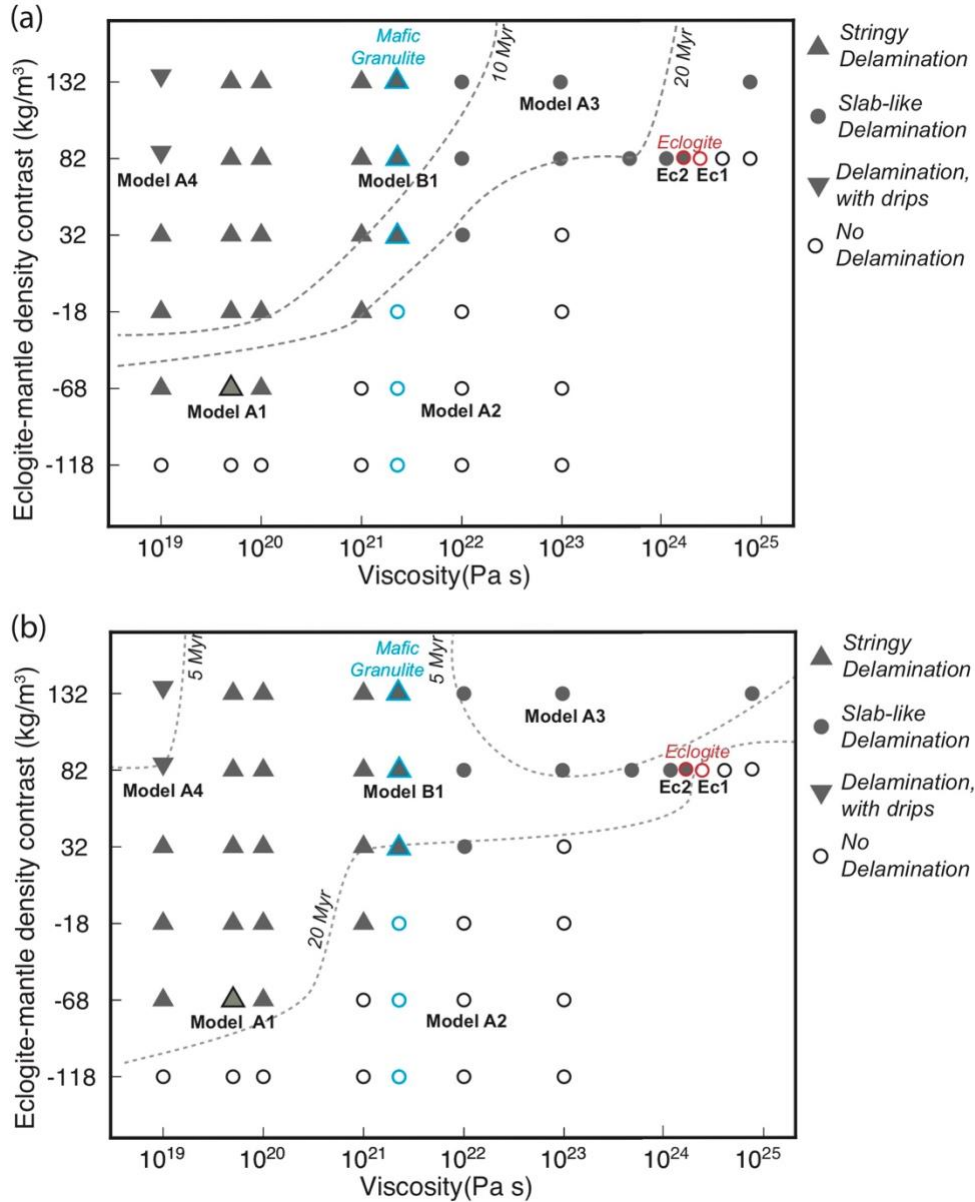
**Figure 5.4** Time-distance plots for Model A1 with the upward direction on the y-axis corresponding to an increase in model time. These show the evolution of: (a) crustal thickness, (b) surface elevation, (c) Moho depth, (d) surface heat flow, (e) Moho temperature, and (f) distribution of mantle melting (dark grey circles) and horizontal strain rate at the surface (positive indicates extension). Delamination begins at  $\sim 38.5$  Myr and proceeds in an unsteady manner. The temporal changes in surface elevation and horizontal strain rate are associated with slab break-offs at  $\sim 40$  Myr,  $\sim 45$  Myr, and  $\sim 49$  Myr. Open circles show the location of the lithosphere detachment point.

### 5.3.2 Style, initiation, and duration of delamination

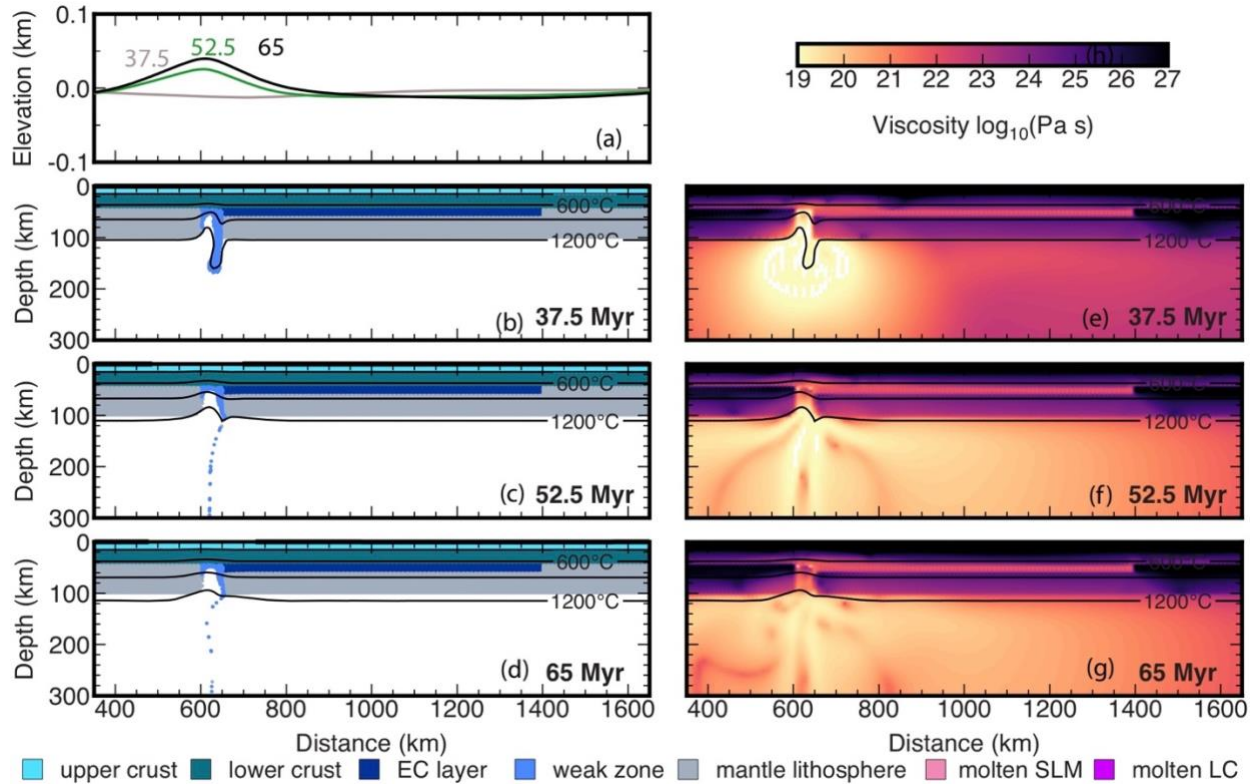
In this section, variations in the viscosity and reference density of the eclogite layer are explored, using the Type A model set-up. The models examine variations in layer viscosity from  $10^{19}$  to  $10^{25}$  Pa s and density contrasts of -118 to +132  $\text{kg/m}^3$ , in order to determine the parameters needed for delamination to occur and the resulting dynamics of delamination. All models are run to 65 Myr.

Figure 5.5 summarizes the models results in terms of the observed behaviour and the timescales of delamination. These plots illustrate the boundary between models that undergo delamination and those that do not. Model A2 is an example of a model that does not delaminate (Figure 5.6). This model has the same density contrast as Model A1 ( $-68 \text{ kg/m}^3$ ) but the eclogite layer viscosity is  $10^{22}$  Pa s. Gravitational removal of the weak zone occurs in this model (Figure 5.6e), causing a localized area of surface uplift (Figure 5.6a). However, the high-viscosity eclogite layer prevents gravitational foundering of the lower lithosphere, and over time, thermal diffusion causes the conduit to cool and become stronger, further inhibiting removal.

Figure 5.5a shows that the occurrence of delamination is controlled by both the density and viscosity of the eclogite layer. The critical density contrast needed to induce delamination increases as the layer viscosity increases, from  $-68 \text{ kg/m}^3$  for a viscosity of  $10^{19}$  Pa s to  $+132 \text{ kg/m}^3$  for a viscosity of  $10^{25}$  Pa s. For the models that do undergo delamination, three styles of delamination are observed, depending on the eclogite layer viscosity and density.



**Figure 5.5** Effects of variations in the eclogite layer viscosity and density contrast on the (a) initiation time for delamination and (b) duration of the delamination; the symbols indicate the style of delamination. The initiation time is given by the time of first mantle melting and the duration is the time between initiation and removal of 90% of the mantle lithosphere below the eclogite layer. Blue outlines are Type B models that used mafic granulite rheology, and red outlines are eclogite rheology (Ec1, Jin et al., 2001; Ec2, Zhang & Green, 2007); see text for discussion. The position of the Type B models is based on the dynamics of delamination; the effective viscosity of the eclogite layer in these models varies with time, depending on the temperature and strain rate.



**Figure 5.6** Evolution of Model A2, in which the eclogite layer has a viscosity is  $10^{22}$  Pa s and a density contrast of  $-68 \text{ kg/m}^3$ . Delamination does not occur in this model. Plots show: (a) surface topography, (b-d) model structure, and (e-g) viscosity structure at the given times after the start of the model. The black lines are isotherms every  $300^\circ\text{C}$ . LC=lower crust; EC = eclogite; SLM = sublithospheric mantle.

**Style 1 - Slab-like delamination.** This behaviour occurs for models in which the eclogite layer has both a high density and high viscosity. Model A3 is an example (density contrast of  $+132 \text{ kg/m}^3$ ; viscosity of  $10^{23}$  Pa s). The evolution of this model is shown in Figure 5.7. During gravitational removal of the weak zone, delamination is initiated. The lower lithosphere detaches along the top of the eclogite layer and sinks into the mantle as a coherent slab that grows in length. As the detachment point migrates to the right, it is accompanied by a wave of surface subsidence, where the magnitude increases as the slab length grows. At 12.5 Myr, there is a surface subsidence of  $\sim 3$  km. Delamination proceeds rapidly across the width of the eclogitized region, with 90% of the removal occurring within 5 Myr. Importantly, the detached lithosphere exhibits little internal deformation, although there are two abrupt slab break-offs at 13 Myr and 16 Myr that are accompanied by pulses of surface uplift. The 13 Myr event occurs when the foundering slab has a

length of ~400 km, and its negative buoyancy exceeds the strength of the slab. The 16 Myr break-off occurs as detachment reaches the right side of the eclogite layer at  $x=1400$  km. Delamination creates an area of thin lithosphere and decompression melting of the mantle. In addition, the lowermost crust exceeds its solidus temperature and a small amount of crustal melt is predicted (e.g., Figures 5.7e-5.7g).

**Style 2 - Stringy delamination.** This style of delamination is observed for the majority of models, including Model A1 (Figure 5.3). It is characterized by internal deformation of the detaching slab, such that the slab stretches and undergoes necking as it detaches, leading to multiple breakoffs that leave narrow “strings” of lithosphere material (e.g., Figure 5.3d). This style of removal occurs in models in which the eclogite layer has a viscosity less than  $10^{22}$  Pa s; it appears that the low viscosity makes this layer susceptible to deformation. In contrast, in slab-like delamination, the higher viscosity eclogite layer reduces internal deformation of the detaching slab.

**Style 3 - Delamination with drips.** In models in which the eclogite layer has high density contrast ( $+82$  kg/m<sup>3</sup> or  $+132$  kg/m<sup>3</sup>) and a low viscosity ( $10^{19}$  Pa s), the lithospheric removal process is more complex, as seen in Figure 5.8 (Model A4). Delamination initiates within 1.5 Myr of the start of the model. Owing to the high density and low strength of the eclogite layer, the detaching slab undergoes significant internal deformation as it sinks. In addition, the high-density eclogite layer is gravitationally unstable, and owing to its low viscosity, local Rayleigh-Taylor (RT) drips form on the right side of the eclogite region (at  $x > 1100$  km). The growth rate of drips is greater than the lateral detachment rate of the delaminating lithosphere, and therefore removal on the right side occurs through RT drips. This causes removal of most of the lower lithosphere, but some mantle lithosphere and a thin layer of eclogite remain at  $x=1250-1400$ km. Lithospheric removal is accompanied by surface uplift (Figure 5.8a), although there is less uplift on the right side because of the residual mantle lithosphere. Delamination also creates a wide region of mantle melting from  $x = 600-1100$  km. In the area of the RT-drips ( $x=1100$  to  $1400$  km), melting is less extensive.

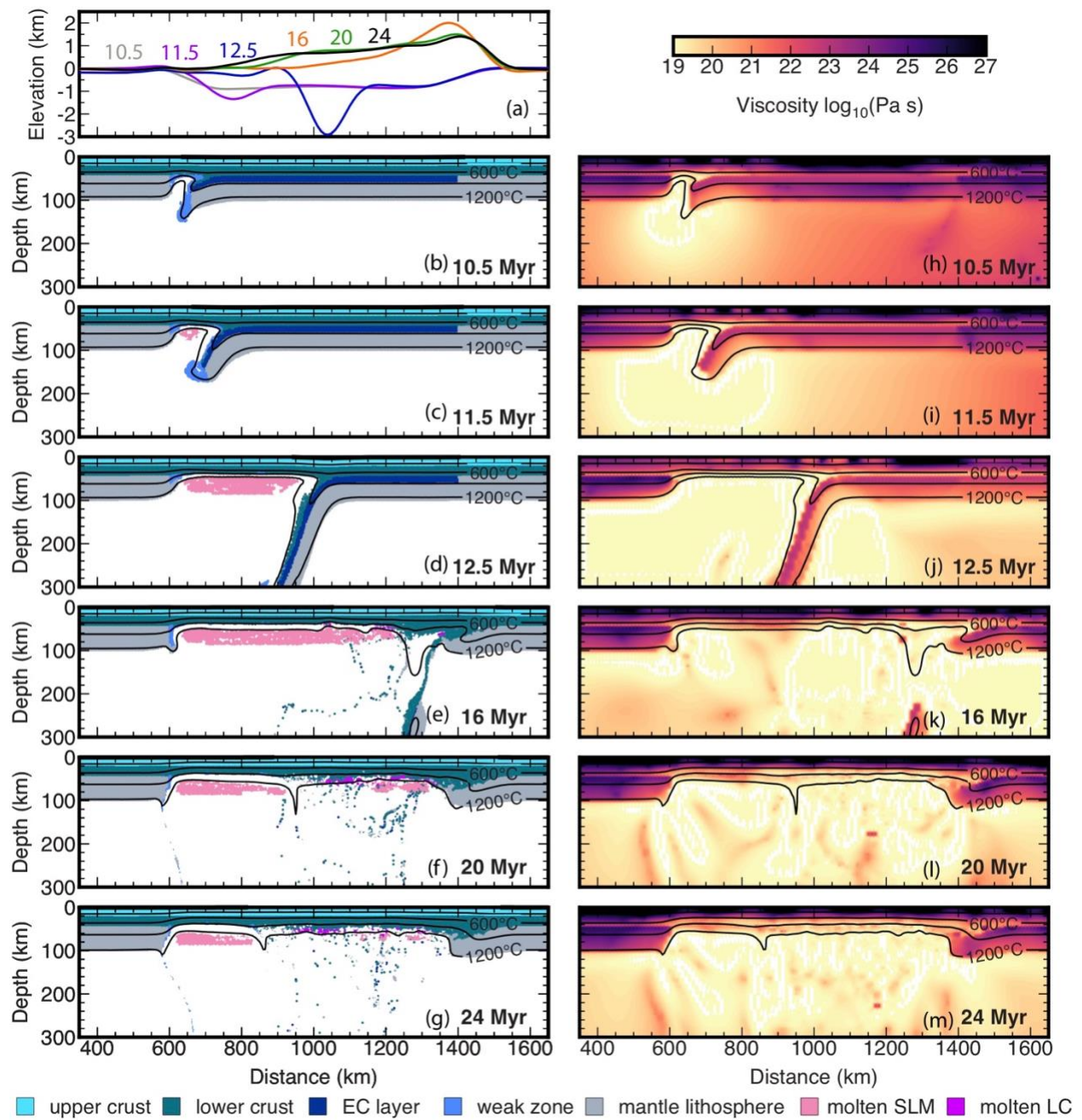


**Figure 5.7** Evolution of Model A3, in which the eclogite layer has a viscosity is  $10^{23}$  Pa s and a density contrast of  $+132 \text{ kg/m}^3$ . This model exhibits slab-like delamination. Plots show: (a) surface topography, (b-g) model structure, and (h-m) viscosity structure at the given times after the start of the model. The black lines are isotherms every  $300^\circ\text{C}$ . LC = lower crust; EC = eclogite; SLM = sublithospheric mantle.

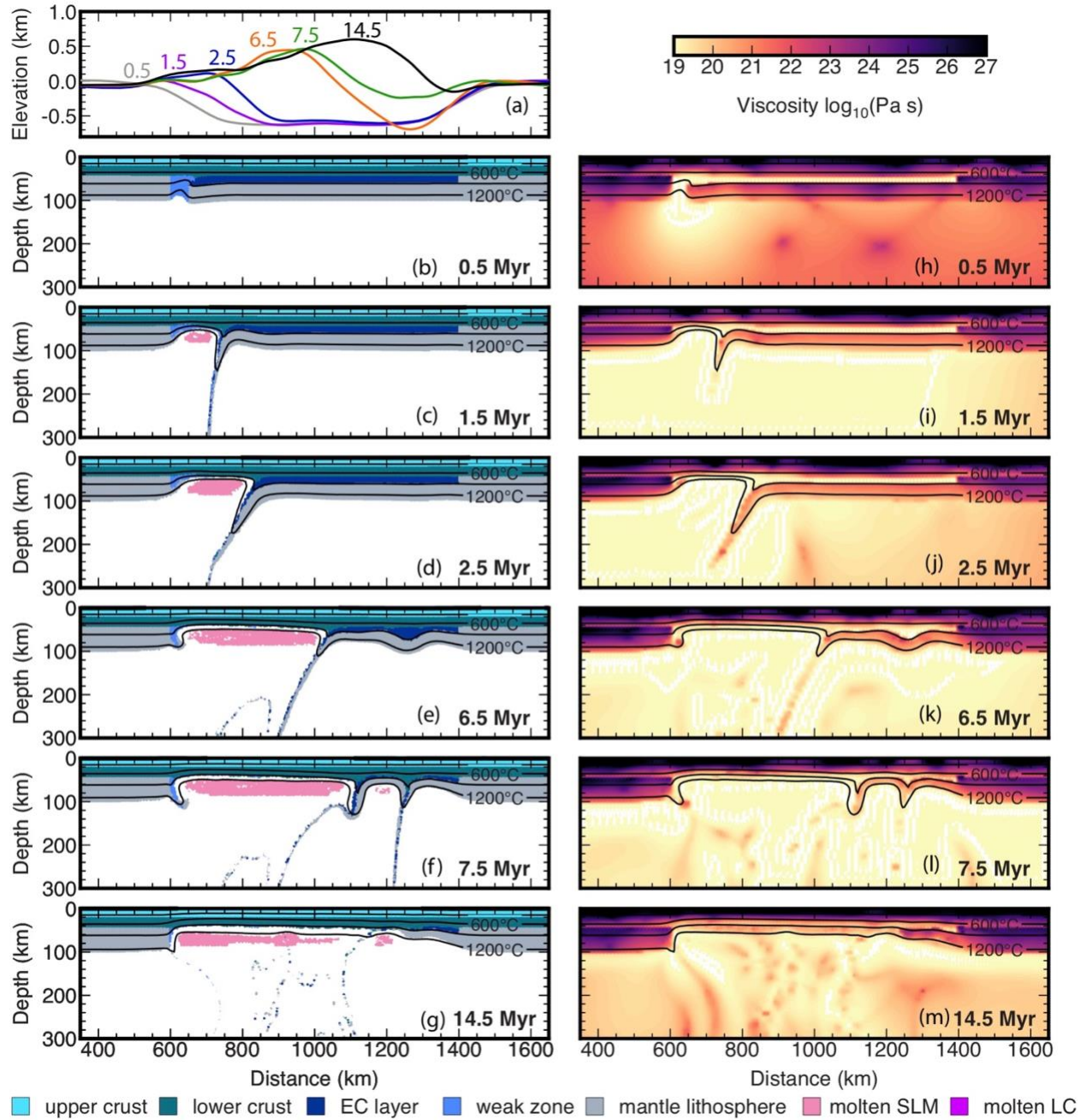


**Figure 5.8** Evolution of Model A4, in which the eclogite layer has a viscosity is  $10^{19}$  Pa s and a density contrast of  $+82 \text{ kg/m}^3$ . This model exhibits delamination with drips. Plots show: (a) surface topography, (b-g) model structure, and (h-m) viscosity structure at the given times after the start of the model. The black lines are isotherms every  $300^\circ\text{C}$ . LC = lower crust; EC = eclogite; SLM = sublithospheric mantle.

Figure 5.5a shows the conditions under which each style of delamination occurs, as well as the initiation time for delamination following the start of the model. For consistency, the initiation time is taken as the time at which the mantle first melts. The initiation time is lowest ( $<5$  Myr) if the eclogite layer has both a large density contrast and low viscosity. The initiation time increases as the eclogite density decreases and/or its viscosity increases. For most models, delamination initiates within 20 Myr, except in models in which the eclogite viscosity is high ( $10^{24}$ - $10^{25}$  Pa s) or the density contrast is low ( $-68$  kg/m<sup>3</sup>). For example, in Model A1 (Figure 5.3), delamination does not initiate until 38.5 Myr.

Figure 5.5b shows the duration of lithospheric removal, based on the time between initiation and when 90% of the mantle lithosphere within the eclogite layer region ( $x=600$ - $1400$  km) has been removed. Removal takes less than  $\sim 20$  Myr in all models. The models with delamination and drips (Style 3) have the shortest duration ( $<5$  Myr), as removal is promoted by both the high density and low viscosity of the eclogite. Slab-like delamination (Style 1) also has a short duration, especially for models with a large density contrast. This is because the delaminating slab remains intact, and therefore the increasing negative buoyancy of the growing slab allows for rapid removal. Stringy delamination (Style 2) exhibits longer durations of removal ( $>5$  Myr to  $\sim 20$  Myr). In these models, the detaching slab undergoes deformation and breakoffs, and therefore there is a smaller area of dense material driving the removal.

The Type A models highlight the important role that lower crust eclogitization may play in driving delamination. To create a wide area of thinned lithosphere, the density of this layer must be close to, or greater than, the density of the underlying mantle, where the density is determined by both the composition and density of the eclogite. Once delamination is initiated, the style and timescales of removal depend on both the density and viscosity of the eclogite layer.

#### **5.4 Results: Surface effects of delamination**

The models in the previous section provide insight into the conditions needed for delamination and the resulting styles of delamination. Here, we present models that consider a more realistic rheology of eclogitized lower crust. The Type B models are used to explore how variations in the rheology of the crust above the eclogite layer and changes in the lithosphere

thermal structure affect the dynamics and surface expressions of delamination, including topography, crustal deformation and heating, and magmatism.

#### **5.4.1 Reference model with a lower crust eclogitization (Model B1)**

Model B1 is the reference Type B model (shown in Table 5.2). The eclogite layer has the rheology of mafic granulite (Wang et al., 2012) and its density contrast relative to the mantle is  $+82 \text{ kg/m}^3$ . With this rheology, the viscous strength of the eclogite layer depends on both temperature and strain rate. Figure 5.9 shows the model evolution. Delamination starts by 2.5 Myr, and at this time, the effective viscosity of the eclogite layer varies from  $\sim 10^{19} \text{ Pa s}$  near the weak zone to  $\sim 10^{23} \text{ Pa s}$  farther to the right, reflecting the decrease in strain rate toward the right (Figure 5.9h). The low viscosity enables the lower lithosphere to detach, and delamination occurs through stringy delamination (Figures 5.9d-5.9g). Delamination results in removal across the full width of the eclogite region by  $\sim 15 \text{ Myr}$ , with 90% removed within 10 Myr of the initiation of delamination.

Figure 5.10 shows time-distance plots of the different surface expressions. Prior to delamination, the crust overlying the eclogite layer has a thickness of 45 km, and this region has an initial elevation of -0.3 km relative to the surroundings because of the high-density eclogite layer. The lateral migration of delamination is marked by a 3-5 km thickening of the crust above the detachment point (Figure 5.10a) and surface uplift to the left of the detachment point (Figure 5.10b). The crustal thickening results from the stresses associated with the underlying high-density slab that cause the deep Moho (Figure 5.10c). This region also exhibits extension at the surface, with areas of lower magnitude contraction on either side (Figures 5.10f).

Delamination results in the removal of both the eclogite layer and underlying mantle lithosphere. After delamination, the region of thinned lithosphere becomes an area of high topography, with elevations that range from +0.1 km to +0.6 km from left to right (Figure 5.10b). This asymmetry reflects the crustal thickness, which varies from  $\sim 35 \text{ km}$  on the left side of the thinned region to  $\sim 50 \text{ km}$  on the right side (Figure 5.10a). Delamination also causes rapid heating of the crust (Moho temperatures  $>900 \text{ }^\circ\text{C}$ ) and mantle decompression melting (Figures 5.10e and 5.10f). Melting occurs for  $\sim 15 \text{ Myr}$  following delamination in the central part of the thinned lithosphere, with a longer duration at the sides due to edge-driven convection that allows upwelling

of hot mantle. Surface heat flow increases within the thinned region over the 5-10 Myr following delamination, as the crust is conductively heated (Figure 5.10d).

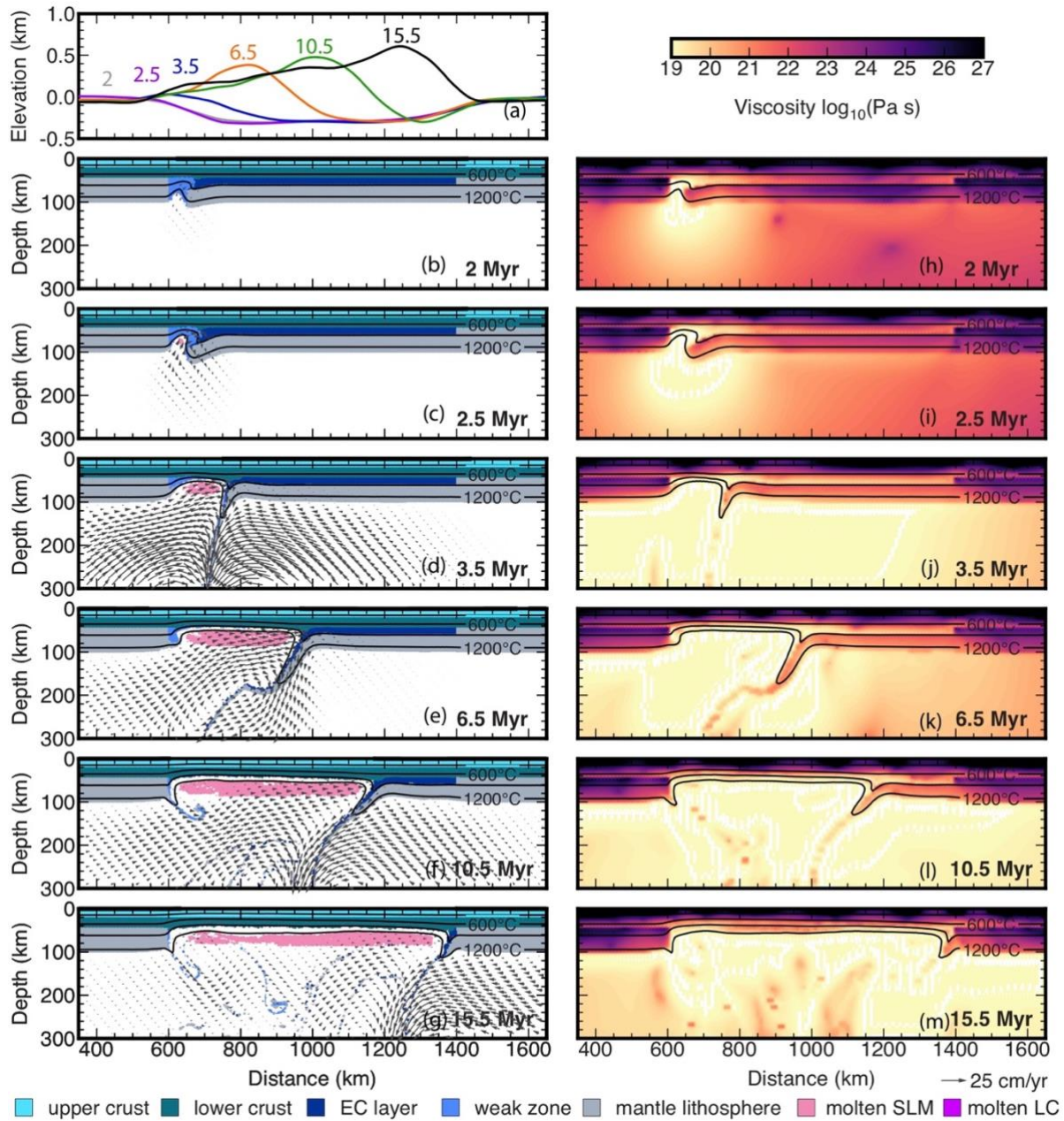


**Figure 5.9** Evolution of Model B1. The eclogite layer uses the rheology of mafic granulite and has a density contrast of  $+ 82 \text{ kg/m}^3$ . Plots show: (a) surface topography, (b-g) model structure, and (h-m) viscosity structure at the given times after the start of the model. The black lines are isotherms every  $300 \text{ }^\circ\text{C}$ . LC = lower crust; EC = eclogite; SLM = sublithospheric mantle.

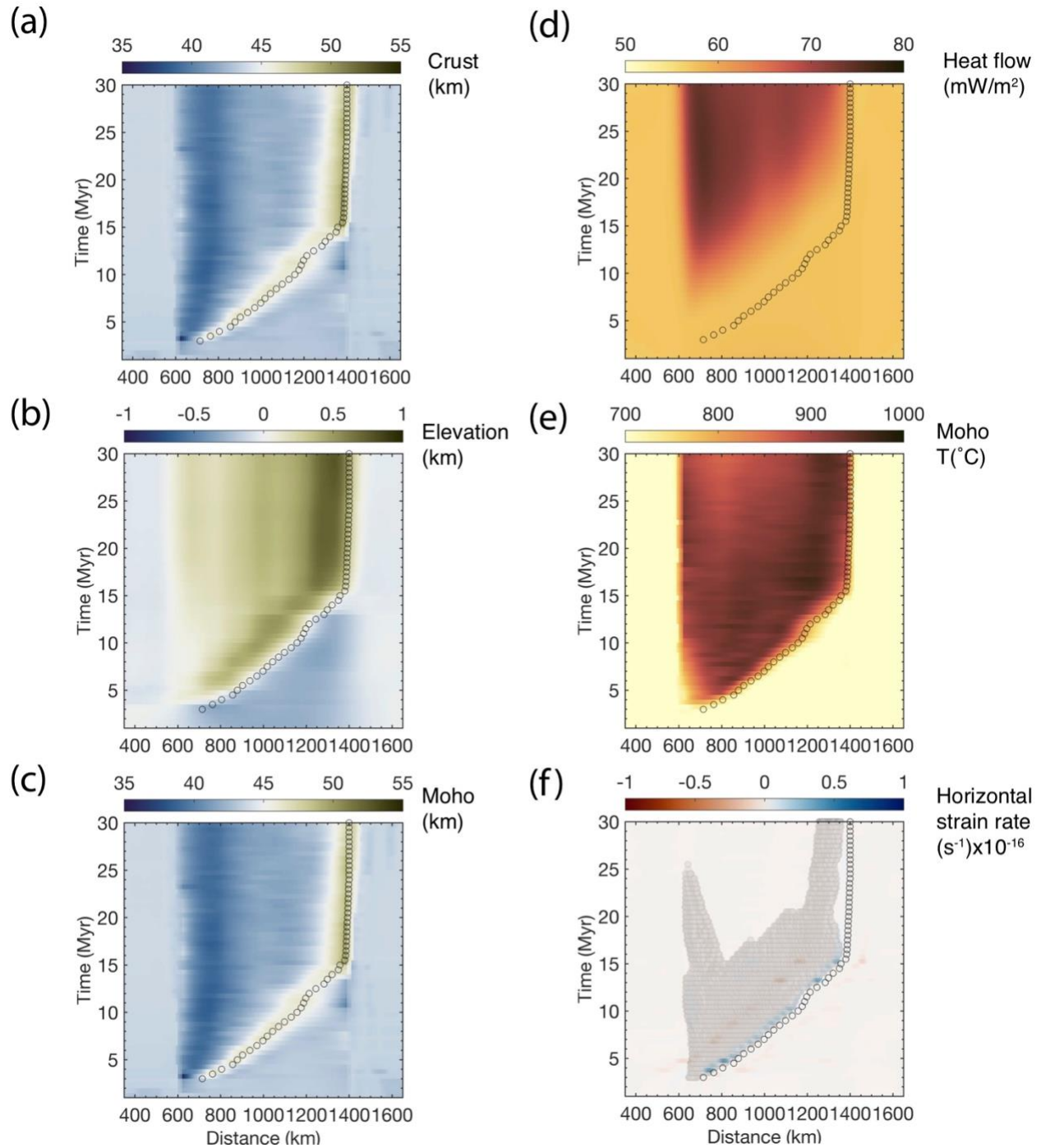


**Figure 5.10** Time-distance plots for Model B1 showing the evolution of: (a) crustal thickness, (b) surface elevation, (c) Moho depth, (d) surface heat flow, (e) Moho temperature, and (f) distribution of mantle melting (dark grey circles) and horizontal strain rate at the surface (positive indicates extension). Delamination begins at  $\sim 2.5$  Myr and lithospheric removal occurs through stringy delamination with frequent slab necking and breakoffs. Open circles show the location of the lithosphere detachment point.

### 5.4.2 Comparison between Model A1 and B1

The overall behaviour of Model B1 is similar to that in Model A1. In both models, the eclogite layer and underlying mantle lithosphere are removed through stringy delamination. Delamination in Model B1 initiates earlier in the model run owing to the higher density eclogite layer, but the duration of delamination in both models is similar. In addition, delamination causes decompression melting of the mantle and heating of the overlying crust, as shown by the increased Moho temperatures and surface heat flow in the region of thinned lithosphere.

Both models also exhibit a narrow region of crustal thickening above the detachment point and a migrating wave of surface uplift above the area of thinned lithosphere. In Model A1, there is an area of larger subsidence to the right of the detachment point (Figure 5.3a), and delamination occurs at a variable rate. In contrast, there is little surface subsidence in Model B1 (Figure 5.9a) and delamination is more continuous. Following delamination, the area of high topography is asymmetric in both models, but Model B1 shows a greater asymmetry (Figure 5.10b vs. Figure 5.4b). These differences are attributed to differences in the eclogite layer density in the two models. In Model A1, the eclogite layer has a density contrast of  $-68 \text{ kg/m}^3$ , which suggests that delamination is triggered not only by the density of the eclogite layer but also the underlying cool and dense mantle lithosphere. During delamination, the length of the detached slab varies, including times when the slab length is relatively long. The negative buoyancy increases with slab length, inducing rapid migration of delamination and surface subsidence. Delamination is punctuated by slab break-offs that result in pulses of uplift and a slowing of delamination. In contrast, in Model B1, delamination is driven by both the higher eclogite density ( $+82 \text{ kg/m}^3$ ) and the mantle lithosphere (Figure 5.2). The higher density causes greater internal deformation and necking of the detaching lithosphere, and thus the detaching slab remains relatively short throughout the delamination process. As a result, the negative buoyancy driving delamination is nearly constant, leading to steady removal and minimal subsidence. In addition, the high-density eclogite causes greater thickening of the overlying crust, resulting in the more asymmetric crustal thickness and topography profiles.

### 5.4.3 Effect of eclogite layer rheology

In the Type A models, the viscosity of the eclogite layer was shown to affect the dynamics of delamination. Model B1 uses the rheology of mafic granulite (Wang et al., 2012) for the eclogite layer, which is the same rheology used for the lower crust; this assumes eclogitization only affects the density. There is considerable uncertainty in the rheology of eclogitized crust, where laboratory measurements of eclogite suggest a relatively high strength, but additional factors such as the presence of fluids or changes in grain size during eclogitization may result in weakening (Krystopowicz & Currie, 2013 and references therein). To date, there have been two laboratory studies on eclogite rocks, which we denote as Ec1 (Jin et al., 2001) and Ec2 (Zhang & Green, 2007). We have tested models with each of these rheologies in the eclogite layer, using a density contrast of  $82 \text{ kg/m}^3$ , as in Model B1. The Ec1 rheology results in the highest strength for the eclogite layer (Figure 5.1b) and no delamination occurs within 40 Myr. With the weaker Ec2 rheology, delamination initiates by 20 Myr, and removal occurs in  $\sim 5$  Myr through slab-like delamination, similar to the behaviour of Model A3 (Figure 5.7). The Ec2 rheology is stronger than mafic granulite (but weaker than Ec1), and therefore the higher strength of this layer inhibits internal deformation of the detaching slab.

### 5.4.4 Variations in crustal rheology

In this section, we examine how changes in the crustal strength above an area of delamination affect the resulting lithosphere structure and surface observations. The models use the eclogite layer properties of Model B1 (density contrast of  $+82 \text{ kg/m}^3$  and mafic granulite rheology), and only the viscous and frictional-plastic properties of the upper crust and uneclogitized lower crust are varied.

#### *Viscous strength variations (Models B2 and B3)*

Models B2 and B3 examine variations in the viscous rheology of the crust. The viscous parameters are determined through laboratory studies of deformation of crustal compositions; the models use the parameters of wet quartzite (Gleason & Tullis, 1995) and mafic granulite (Wang et al., 2012) for the upper and lower crust, respectively. However, variations in composition and

hydration of the crust relative to the laboratory samples can affect the crustal strength. For example, a more mafic or drier composition is expected to be stronger (e.g., Beaumont et al., 2006). In addition, the laboratory results have uncertainty and must be extrapolated over several orders of magnitude in strain rate in order to apply to geological deformation. To account for these factors, we follow Beaumont et al. (2006) in using the scaling factor  $f$  (Equation 5.3) to test the effects of viscous rheologies that are stronger or weaker than the reference laboratory values. Here, we present two end-member models. In Model B2, the upper and lower crust are 10 times weaker ( $f=0.1$ ) than in Model B1 and in Model B3, the upper and lower crust are 10 times stronger ( $f=10$ ).

The evolution of models B2 (weak crust) and B3 (strong crust) are shown in Figures 5.11a and 5.11b, respectively. Both models exhibit stringy delamination that results in removal of the eclogite layer and underlying mantle lithosphere. Variations in crustal strength have small influences on the timescales of delamination. With a weak crust, delamination initiates within  $\sim 1.5$  Myr, compared to  $\sim 4$  Myr for the strong crust. In addition, the duration of delamination is  $\sim 5$  Myr shorter for the weak crust. These differences occur because the weak crust allows for the dense lower lithosphere to detach more readily.

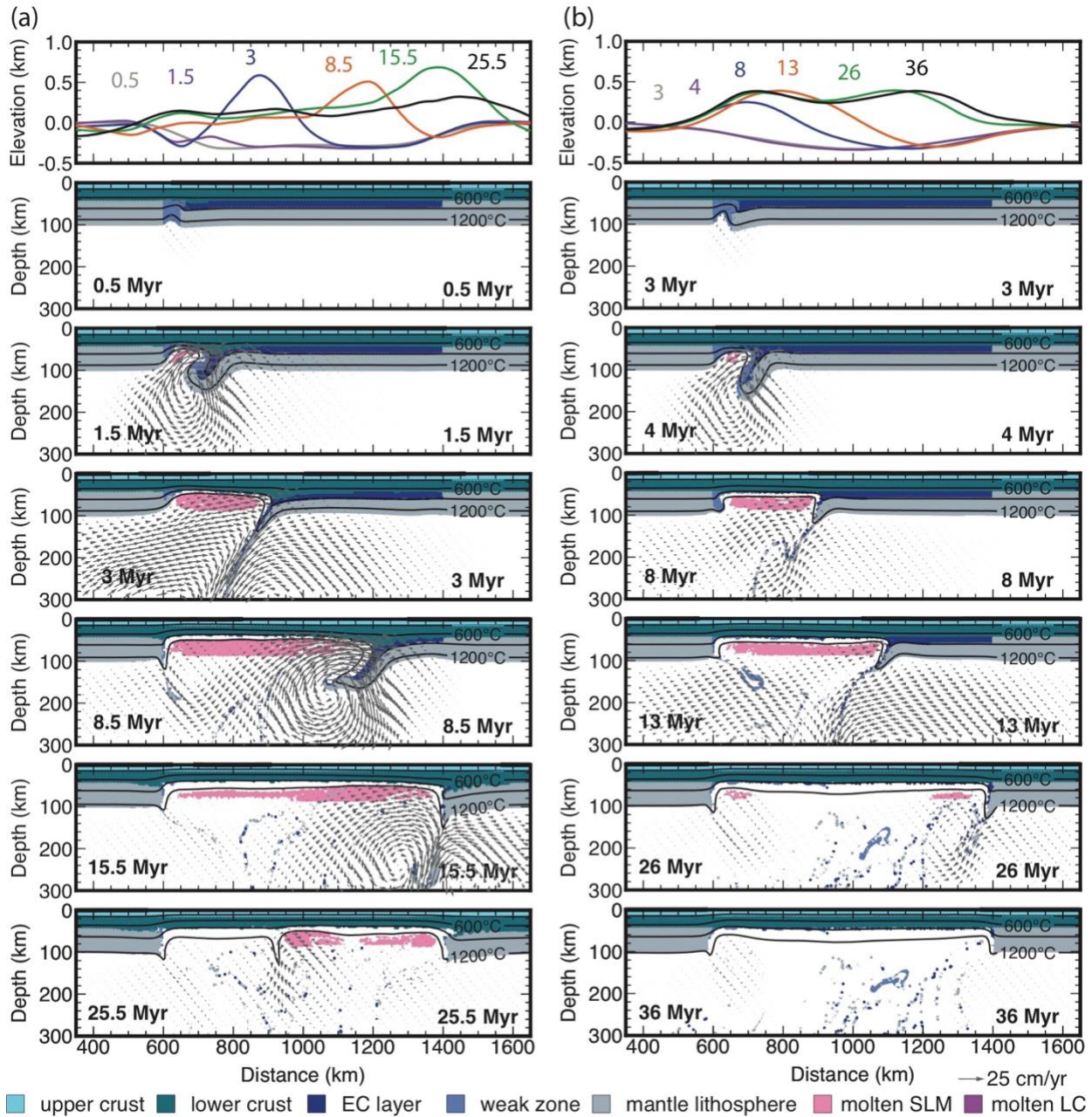


**Figure 5.11** Evolution of the surface topography (top plot) and model geometry at the given model times for: (a) Model B2 and (b) Model B3, in which the upper and lower crust are 10 times weaker and 10 times stronger than in Model B1, respectively. The black lines are isotherms every 300 °C. LC = lower crust; EC = eclogite; SLM = sublithospheric mantle.

In both models, delamination is accompanied by surface uplift and mantle melting within the thinned area. In Model B2, delamination is accompanied by significant variations in topography and crustal thickness that migrate laterally as delamination proceeds (Figures 5.12a and 5.12b). The thickened crust causes surface uplift that is centred approximately above the detachment point, rather than to the left, and no subsidence occurs ahead of the detachment point. After the detachment point has migrated past a given point in the model, the crust then thins to ~32 km, and the elevation decreases. After migration is complete, the area of thinned lithosphere has an elevation of 0.2 km to 0.7 km, relative to the undisturbed lithosphere. In addition, the area of high elevation extends outside of the delamination area, especially on the right side at  $x=1400$  km, as the weak crust allows thickening to be more broadly distributed. This model demonstrates that the stresses associated with delamination can cause significant crustal deformation, if the overlying crust is weak.

In Model B3, the crust is too strong to be significantly deformed during delamination and there are no significant changes in crustal thickness (Figure 5.12c). Delamination is marked by surface uplift to elevations of ~0.4 km above the area of thinned lithosphere (Figure 5.12d). The area of uplift is relatively symmetric above the area of thinned lithosphere, with gentle slopes on the sides due to the strong crust. This amount of uplift is consistent with the isostatic calculations, where the dense eclogite layer and cool mantle lithosphere are replaced by hotter, low-density sublithospheric mantle.

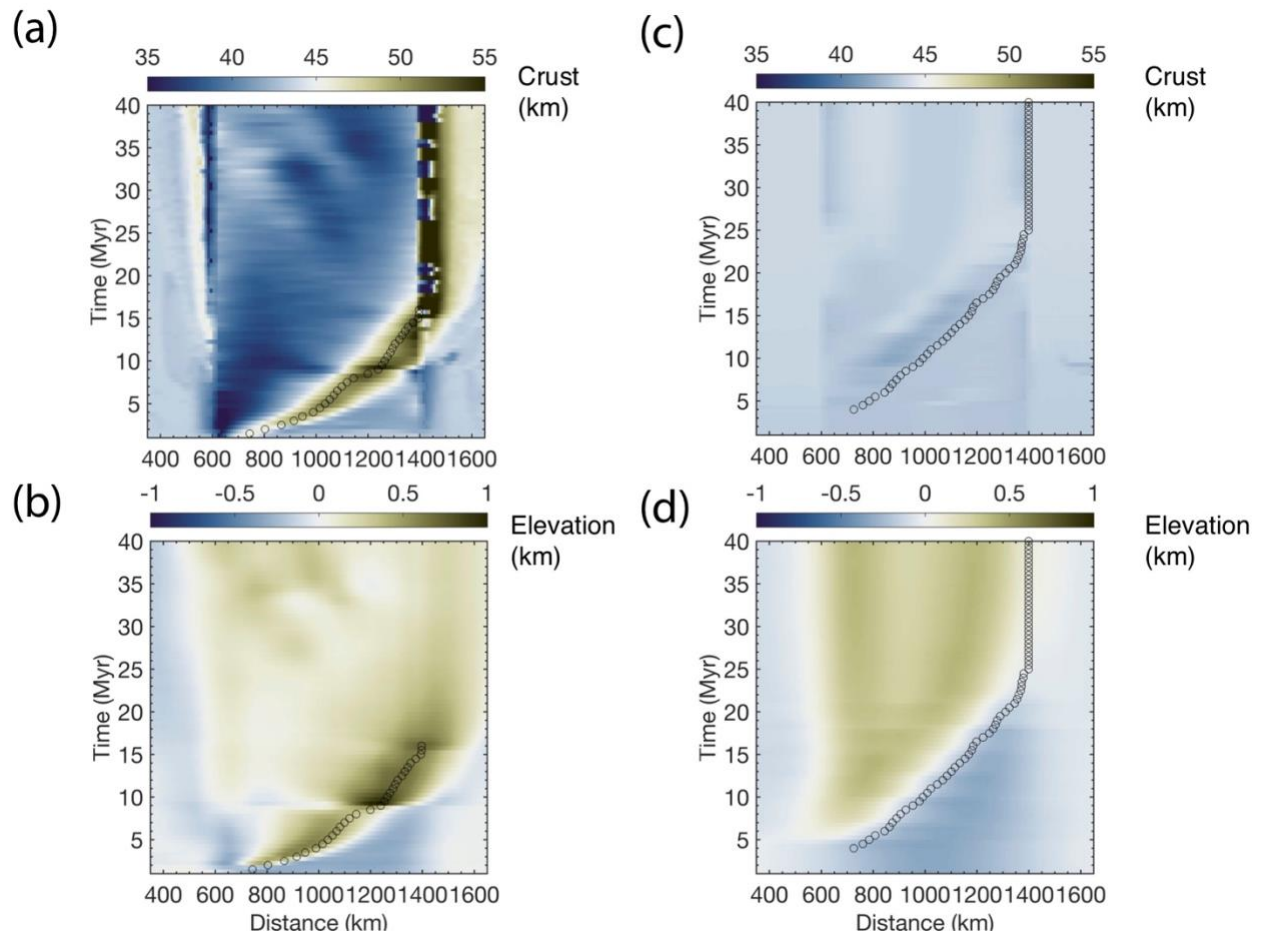


**Figure 5.12** Temporal distributions of crustal thickness and surface elevation in: Model B2 (a and b) and Model B3 (c and d), respectively. Open circles show the location of the lithosphere detachment point.

### ***Frictional-plastic strength (Models B4 and B5)***

Deformation of crustal rocks also depend on their frictional-plastic properties. In particular, the frictional-plastic parameters are the dominant control on the strength in the uppermost crust, where temperatures are low (Figure 5.1b). In Model B1, the internal angle of friction ( $\phi$ ) varies from  $15^\circ$  to  $2^\circ$  with increasing strain. However, if the crust has experienced earlier deformation or has a high pore fluid pressure, the  $\phi$  value will decrease (e.g., Huismans & Beaumont, 2003).

Model B4 tests the effect of  $\phi = 1^\circ$ . The viscous rheologies use the reference values ( $f=1$ ) and therefore the only difference between this model and Model B1 is the low  $\phi$  value. Figure 5.13a shows the evolution of this model. The overall dynamics of delamination and the surface effects are similar to those in Model B1. Delamination is accompanied by a small amount of crustal thickening above the detachment point and an area of uplift to the left of the detachment point. Lithospheric removal results in an area of thinned lithosphere with high, asymmetric elevations. The main difference between the two models is that the slopes on the sides of the high elevation region are steeper in Model B4 because the lower frictional-plastic angle allows for more localized deformation near the surface.

Model B5 shows of effect of  $\phi = 1^\circ$  for a crust that is also viscously weak ( $f=0.1$ ) This model is equivalent to Model B3, except for the  $\phi$  value. The evolution of this model also shows that the general delamination behaviour is not strongly affected by the softening of crustal materials (Figure 5.13b). The main difference is that the topographic uplift has a shorter wavelength, leading to steeper slopes on the edges of the uplifted region.

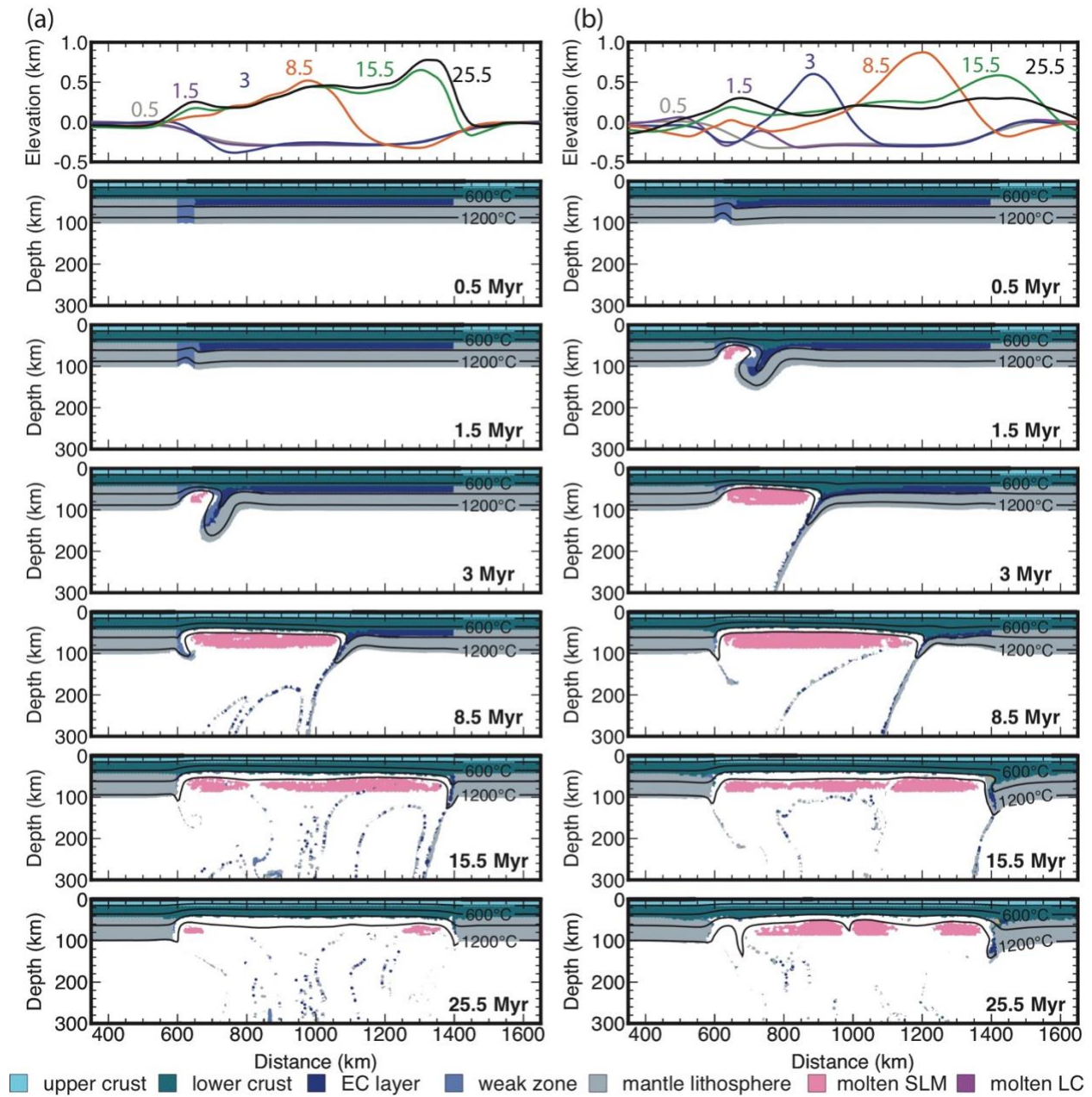


**Figure 5.13** Evolution of the surface topography (top plot) and model geometry at the given model times for: (a) Model B4 which uses the reference crustal viscous rheology. (b) Model B5 uses a crustal viscous rheology that is 10 times weaker. Both models use a weak frictional-plastic rheology (internal friction angle of  $1^\circ$ ) for the upper and lower crust. The black lines are isotherms every 300 °C. LC = lower crust; EC = eclogite; SLM = sublithospheric mantle.

#### 5.4.5 Lithosphere thermal structure (Models B6 and B7)

The last two models examine variations in the thermal structure of the lithosphere. The thermal structure governs a number of important characteristics of the lithosphere, including its thickness, viscous strength, and density. The previous models use a 100 km lithosphere, with an initial temperature of  $\sim 719$  °C at 45 km depth (i.e., the top of the eclogite layer) (Figure 5.1a). Model B6 has an initially cooler lithosphere ( $\sim 600$  °C at 45 km depth,  $\sim 130$  km thick), and Model 7 that has an initially hotter lithosphere ( $\sim 800$  °C at 45 km depth,  $\sim 80$  km thickness). In both cases, all other properties are the same as those in Model B1.

##### *Cool lithosphere (Model B6)*

Figure 5.14a shows the evolution of Model B6. Delamination initiates at 17 Myr and rapidly migrates to the right, with 90% removal by  $\sim 20$  Myr (i.e., within 3 Myr of initiation). Delamination occurs through slab-like delamination, with little internal deformation of the detaching lithosphere. However, this model exhibits two slab break-off events at 19 Myr and 20.5 Myr, when the slab length is  $\sim 400$  km. The behaviour of this model is the result of the cool, thick mantle lithosphere, which creates a higher density (that drives rapid delamination) and a higher strength (that minimizes deformation of the detached slab). The high strength is also the reason that the delamination was slower to initiate than in Model B1.

The surface expressions for Model B6 are shown in Figure 5.15. Delamination does not cause significant crustal deformation, likely because the cool crust has a high strength (Figures 5.15a and 5.15c). However, delamination is marked by significant topographic changes that rapidly migrate across the model (Figures 5.14a and 5.15b). During delamination, subsidence of up to 1.3 km occurs to the right of the detachment point, owing to the negative buoyancy of the detaching lithosphere. To the left of the detachment point, the thinned lithosphere uplifts to an elevation  $\sim 1$  km, and the elevation profile is more symmetric than in earlier models because of the lack of crustal deformation. In the geological record, it may be difficult to resolve these spatio-temporal variations in topography, as removal occurs in  $< 4$  Myr. Instead, removal may appear as regional plateau-like uplift. Delamination also causes significant horizontal strain at the surface, with areas of contraction and extension that migrate across the model (Figure 5.15f). Some residual

strain remains at the right side of the thinned region after delamination. The strain appears to be associated with the high topographic slopes at the surface.

Delamination results in an area of thinned lithosphere for Model B6, with a rapid temperature increase at the Moho (Figure 5.15e) and a more gradual increase in surface heat flow (Figure 5.15d). The Moho temperature reaches a maximum of  $\sim 930$  °C, which is  $\sim 40$  °C cooler than in Model B1 because of the cooler starting temperature in this model. Delamination also triggers decompression melting of the mantle (Figure 5.15f). In the central part of the thinned region, melting occurs for  $\sim 5$  Myr following lithospheric removal, whereas melts at the sides persist for at least  $\sim 15$  Myr. The shorter duration of melting in this model compared to Model B1 (5 Myr vs. 10 Myr) is related to the temperature structure. In both models, the mantle cools from above after delamination, but because Model B6 has a cooler lithosphere, the mantle temperature falls below its solidus temperature more quickly.

### ***Hot lithosphere (Model B7)***

Figure 5.14b shows the evolution of Model B7, where the Moho temperature is initially  $\sim 800$  °C. Delamination initiates at  $\sim 1.5$  Myr, and because of the hot, thin mantle lithosphere, the detaching lithosphere exhibits significant internal deformation. Removal occurs through stringy delamination that migrates toward the right, reaching a position of  $x = \sim 800$  km at  $\sim 7$  Myr. Another short period of stringy delamination occurs between 11 Myr and 12.5 Myr (Figures 5.16c). On the right side of the eclogite layer, RT drips form and removal occurs through a combination of local drips and stringy delamination after 13 Myr (Figures 5.16). This results in the piecemeal removal of the remaining lower lithosphere.

In Model B7, the high temperatures lead to a weak crust, and lithospheric removal is accompanied by crustal thickening of 2-3 km (Figures 5.16a and 5.16c), as the foundering lithosphere induces vertical stresses on the crust. Delamination is marked by rightward migration of crustal thickening above the detachment point, and the transition to drips at times after 13 Myr is marked by local areas of crustal thickening overlying the drips. The final variations in crustal thickness lead to variations in the topography across the thinned region. At 40 Myr, on the left side (from  $x = 600$  to 900 km), the surface is 0.1 to 0.2 km higher than the unthinned region, whereas on the right side, the elevation is 0.3 to 0.5 km. Note that elevation change in this model is less than

that in Models B1 and B6, because the mantle lithosphere is both thinner and hotter in this model. Lithospheric removal is accompanied by heating of the overlying crust (Figures 5.16d and 5.15e). The longer duration of removal in this model, as well as the hotter initial conditions, result in a longer period of mantle melting (Figure 6.16c), and the occurrence of both delamination and RT drips leads to a more complex pattern of melting than in earlier models.

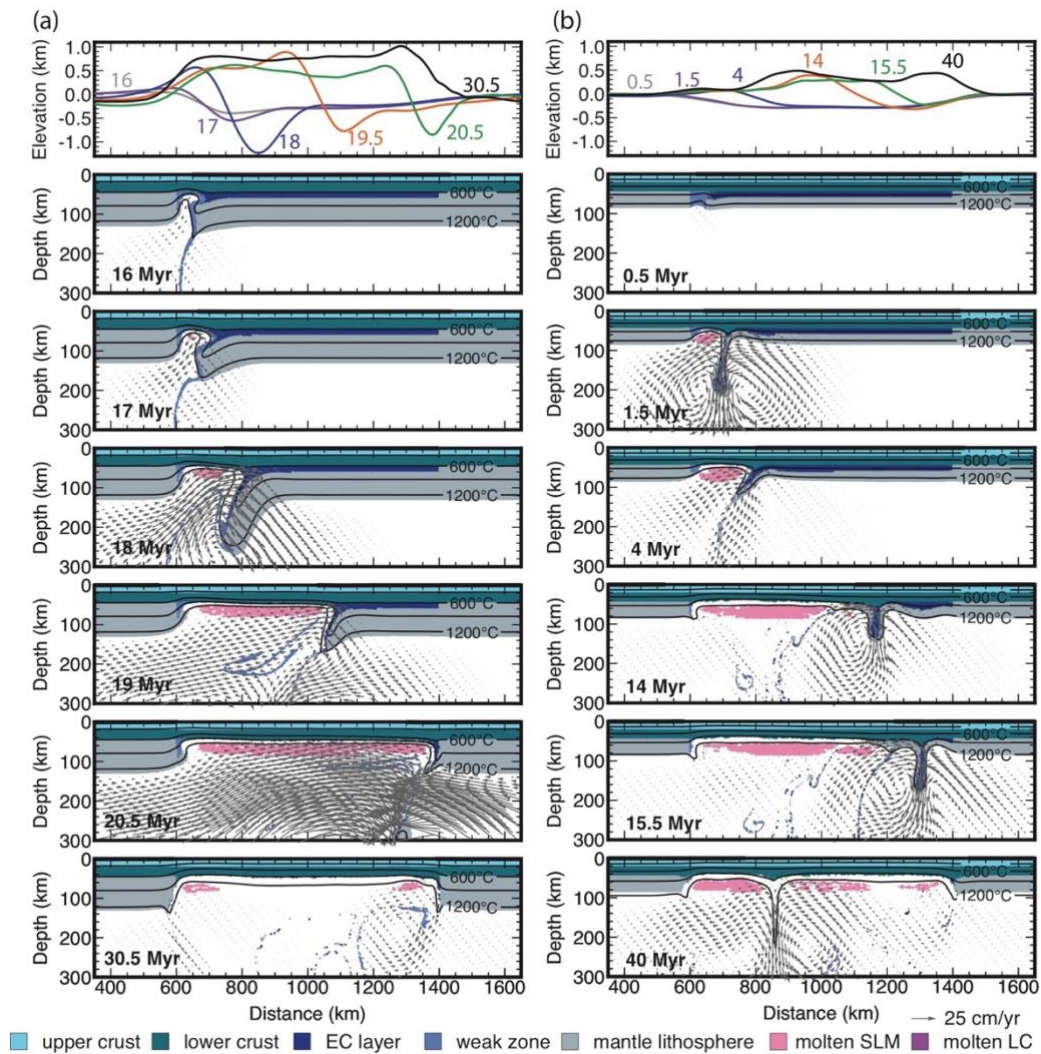


**Figure 5.14** Evolution of the surface topography (top plot) and model geometry at the given model times for: (a) Model B6 with a cooler lithosphere (~600 °C Moho), and (b) Model B7 with a hotter lithosphere (~800 °C Moho). The black lines are isotherms every 300 °C. LC = lower crust; EC = eclogite; SLM = sublithospheric mantle. The Moho is taken as the top of the eclogite layer (i.e., base of uneclogitized lower crust).

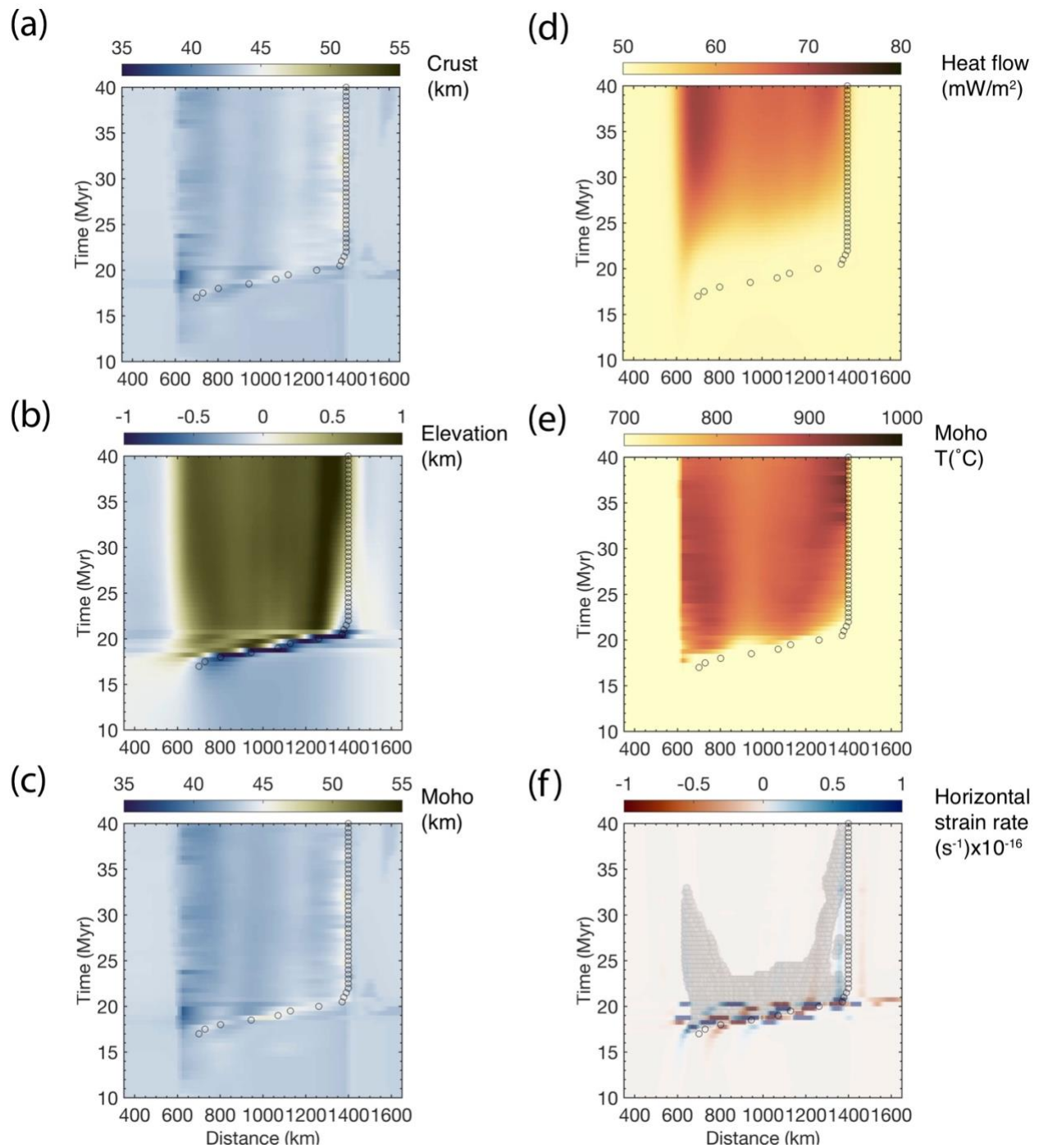


**Figure 5.15** Time-distance plots for Model B6 ( $\sim 600^{\circ}\text{C}$  Moho) showing the evolution of: (a) crustal thickness, (b) surface elevation, (c) Moho depth, (d) surface heat flow, (e) Moho temperature, and (f) distribution of mantle melting (dark grey circles) and horizontal strain rate at the surface (positive indicates extension). Open circles show the location of the lithosphere detachment point.

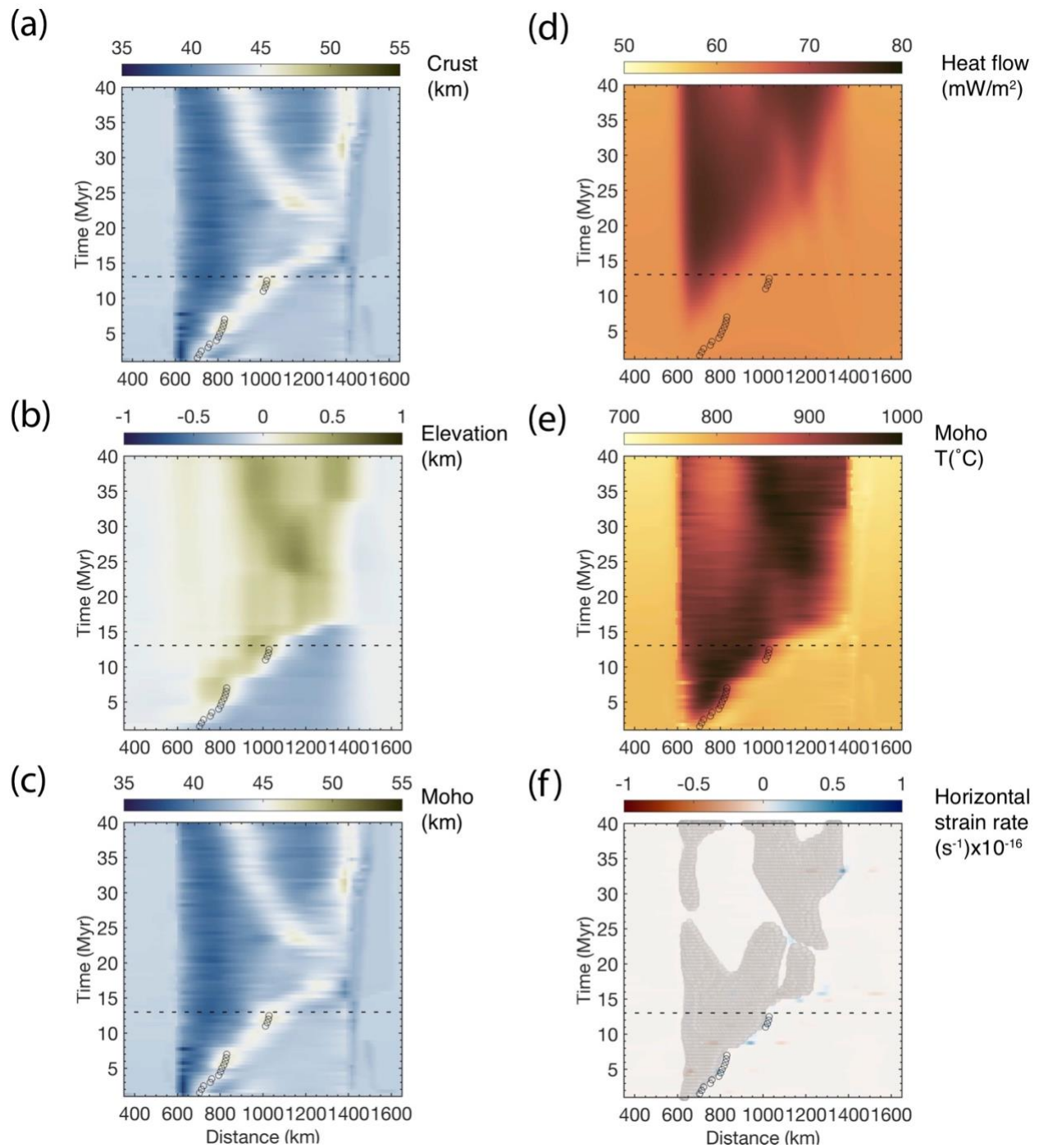


**Figure 5.16** Time-distance plots for Model B7 ( $\sim 800$   $^{\circ}\text{C}$  Moho) showing the evolution of: (a) crustal thickness, (b) surface elevation, (c) Moho depth, (d) surface heat flow, (e) Moho temperature, and (f) distribution of mantle melting (dark grey circles) and horizontal strain rate at the surface (positive indicates extension). Open circles show the location of the lithosphere detachment point. Black dashed line indicates the style of removal changes from stringy delamination to local drips.

## 5.5 Discussion

### 5.5.1 Dynamics of lithosphere delamination

Our study addresses gravitational removal of the deep lithosphere through delamination, whereby the lower lithosphere undergoes wholesale removal. As in previous work, the models show that delamination requires both a decoupling layer within the lithosphere and a low-viscosity conduit that connects the layer to the sublithospheric mantle (e.g., Bird, 1979; Morency & Doin, 2004). Delamination is driven by the negative buoyancy of the lower lithosphere. In our models, the mantle lithosphere is assumed to have the same reference density as the underlying mantle (i.e., it is not chemically depleted). Although this material is cooler than the sublithospheric mantle (Figure 5.2), its density is insufficient to drive removal. The mantle lithosphere in our models is 40-55 km thick. Schott and Schmeling (1998) show that a mantle lithosphere thickness of at least 100 km is needed in order to provide sufficient negative buoyancy to drive removal; delamination also requires that the lower crust viscosity is less than  $10^{21.5}$  Pa s.

To induce delamination in our models, we find that a weak and compositionally dense phase within the lithosphere is needed. We attribute this to eclogitization of thickened lower crust, consistent with previous geodynamic models of continental collision and shortening that suggest that the presence of eclogitized lower crust can trigger delamination (Gray & Pysklywec, 2012; Krystopowicz & Currie, 2013; Lei et al., 2019; Li et al., 2016). Geological studies also show that eclogite is found in the continental collision areas (Austrheim, 1991; Bousquet et al., 1997). One example is the Western Gneiss Region of the Caledonian orogen, where crustal thickening and eclogitization are interpreted to have induced delamination, surface uplift and exhumation of the deep crust at ~410-400 Ma (Andersen et al., 1991; Austrheim et al., 1997; Gordon et al., 2013). Gögüş & Ueda (2018) also argue that the mantle lithosphere density may increase through refertilization by mafic melts. Moreover, petrological data show magma residues include dense material (i.e., eclogite) with increasing depth (DeCelles et al., 2009). Hence, volcanic activities in a cordilleran orogen are susceptible to lithosphere removal, as has been proposed for western North and South America (e.g., southern Sierra Nevada and Puna plateau) (Saleeby et al., 2013; Schurr et al., 2006).

Eclogitization of the lower crust during crustal deformation and thickening is a complex process that requires the presence of hydrous fluids (Jackson et al., 2004; Leech, 2001). The fluids may also cause weakening of the deep crust, further promoting delamination. Our models use a simplified approach where the lower crust is assumed to have already undergone eclogitization, so that we can study the dynamics of delamination. Our Type A models show how variations in the density and viscosity of the eclogite layer affect the occurrence of delamination (Figure 5.6). If the lower crust has a viscosity of  $10^{19}$ - $10^{20}$  Pa s, delamination occurs if the eclogite layer has a density contrast of  $-68 \text{ kg/m}^3$  relative to the mantle. This corresponds to  $\sim 40\%$  eclogitization of the lowermost crust, assuming densities of  $3000$  and  $3600 \text{ kg/m}^3$  for uneclogitized and fully eclogitized crust, respectively. Greater amounts of eclogitization are needed for a more viscous lower crust.

For models that undergo delamination, the dynamics of removal are controlled by the relative magnitudes of driving and resisting forces. The driving force is the high density of the lower lithosphere, whereas the resisting forces include the viscosity of the lower crust, bending resistance of the lithosphere, and viscous resistance of the asthenosphere (Bajolet et al., 2012). In the Type A models, we do not vary the properties of the mantle lithosphere or sublithospheric mantle and therefore the resisting forces are determined by the eclogite layer viscosity. The driving forces depend on the density of the eclogite layer and the length of the delaminating slab (which in turn depends on the viscosity of the eclogite layer). Our models show that delamination initiates earlier if the lower crust is both dense and low viscosity (Figure 5.5a). The style and timescale of delamination also depend on the eclogite layer properties (Figure 5.5b). Rapid delamination ( $< 5$  Myr) occurs if the eclogite layer has a high density (density contrast  $\geq 82 \text{ kg/m}^3$ ) and the viscosity is either low ( $\leq 10^{19}$  Pa s) or high ( $\geq 10^{22}$  Pa s). For a low viscosity, removal occurs through both delamination and RT drips (Style 3), as the low viscosity promotes the growth of local gravitational instabilities. For a high viscosity, removal occurs through slab-like delamination (Style 1), where the detached slab length increases over time, creating a greater negative buoyancy that drives detachment. For intermediate viscosities and/or lower eclogite densities, delamination occurs through stringy delamination (Style 2), where the detaching slab is internally deformed and undergoes break-offs. This limits the negative buoyancy driving removal and delamination takes longer (5-20 Myr in most models).

The occurrence of different styles of delamination appears to be a consequence of the lithospheric thickness in our model. The eclogite layer and underlying mantle lithosphere form a 55 km thick slab that is susceptible to internal deformation as it detaches. In contrast, many previous modelling studies have used a thicker mantle lithosphere, where the cooler and stronger lithosphere detaches through slab-like delamination (Gögüş & Ueda, 2018 and references therein). This range of behaviours is consistent with Models B1, B6 and B7 that show that the style of delamination varies with lithospheric thickness, which in turn depends on the Moho temperature.

### **5.5.2 Surface expressions of delamination**

Our models demonstrate that delamination results in an area of thinned lithosphere and leads to increased surface elevation, Moho temperature, and surface heat flow in this area. An important result is that the topographic expression depends on the style of removal. For most models, delamination is marked by a migrating wave of surface uplift, where the region of uplift overlies the area of thinned lithosphere. In addition, surface extension may occur in this area, with regions of contraction on either side. In models with slab-like delamination, the negative buoyancy of the detaching lithosphere creates surface subsidence ahead of the detachment point, and therefore delamination may be marked by subsidence, followed by uplift. If the detaching slab undergoes break-off during detachment, the rate of delamination can vary and slab break-off is accompanied by rapid surface uplift (Figure 5.15b). Subsidence is reduced in models with stringy delamination, but delamination is marked by a migration of uplift (e.g., Figure 5.10b). If removal occurs through a combination of delamination and RT drips, there is an initial migration of uplift during the early stages of delamination, but then a more complicated pattern of uplift as drips occur (Figure 5.16b).

Our models predict that delamination is accompanied by a lateral migration of mantle melting, triggered by decompression of the mantle upwells into the space created by lithospheric removal. Mantle melting generally occurs for 5-10 Myr following delamination, but can last for longer if removal also involves RT drips. In addition, melting persists near the edges of the thinned region due to edge-driving convection. Melting terminates as the shallow mantle undergoes cooling from above. In the majority of models, no melting of the detached lithosphere was

observed and there was little melting of overlying crust based on the dry granite solidus. A more detailed assessment of the solidus for other crustal compositions is needed.

Another important result is that delamination can cause deformation of the overlying crust, affecting the surface topography. In most models, the negative buoyancy of the detaching slab causes crustal thickening above the detachment point. This leads to asymmetric crustal thickness and asymmetric elevation across the thinned region following delamination. The amount of deformation is largest in models with either a weak viscous rheology (e.g., Model B2) or high temperatures (e.g., Model B7). In Model B2, the weak crust enabled crustal thickening above the detachment point (Figure 5.12a), causing surface uplift (Figure 5.12b). In contrast, if the crust is strong and/or cool (e.g., Models B3 and B6), there is little crustal deformation, and the surface elevation changes are mostly an isostatic response to lithospheric removal and the resulting topographic profile is more symmetric (e.g., Figures 5.12c, 5.12d, and 5.15). These variations in surface expressions are affected by the viscous strength of the deep crust. If the crust has a weak frictional-plastic rheology (e.g., Model B4), the surface topography changes are more localized and have steeper slopes. This is similar to what Wang et al. (2015) found in models of lithosphere drips.

The models in this study are simplified in order to allow for a systematic study of delamination dynamics and surface effects. The models do not include surface processes (erosion and sedimentation), dynamic eclogitization, regional crustal shortening, or three-dimensional effects, and these are all factors that should be examined in future work. Surface erosion will influence elevation and exhumation, and sedimentation may occur in basins that are created during delamination, and therefore these may affect the geological record of delamination. Erosion also changes the rheological structure by removing the cool upper crust (e.g., Beaumont et al., 2001), which may affect the dynamics of delamination. We have assumed a pre-thickened and eclogitized lower crust, whereas eclogitization should be incorporated dynamically as the crust thickens (e.g., Krystopowicz & Currie, 2013), as this may affect the evolution of shortening and the surface expressions (e.g., Stein et al., 2022). Finally, the models in this study are two-dimensional and assume an infinitely wide delaminating slab. In three-dimensions the slab width may affect the rate of delamination, as mantle may flow around the edges of the slab. Three-dimensional models will be important for understanding natural orogenic systems, such as Carpathians and

Mediterranean region where delamination appears to have affected small areas (e.g., Faccenda et al., 2009; Göğüş et al., 2016).

### **5.5.3 Implication for surface expressions of delamination in the western United States**

Lithospheric removal through delamination is inferred to have occurred in a number of mountain belts (e.g., Göğüş & Ueda, 2018 and references therein). Here, we compare our model results to two regions in the western United States where delamination has been previously proposed: the southern Sierra Nevada of California (Le Pourhiet et al., 2006; Saleeby et al., 2013) and the southwestern Colorado Plateau (Bird, 1979).

In the southern Sierra Nevada, surface uplift of ~1 km at ~3.5 Ma in the Kern Arch has been documented (Le Pourhiet et al., 2006 and references therein). This area overlies a low seismic velocity in the shallow mantle and a high Bouguer gravity anomaly, and this region has had widespread alkaline magmatism since 4 Ma. In contrast, the Tulare Basin to the west has undergone surface subsidence of ~0.7 km across ~100 km width since ~6 Ma; this area corresponds to an east dipping of Isabella anomaly suggesting lithosphere foundering due to the batholithic crust, as well as negative gravity anomaly (Saleeby et al., 2013). The V-shaped Moho hole is imaged beneath Great Valley (adjacent to Tulare Basin), causing crustal thickening by 7 km relative to ~35 km thick crust (Gilbert et al., 2012; Zandt et al., 2004). These observations have been attributed to a lithospheric removal episode (e.g., Cecil et al., 2014; Le Pourheit et al., 2006; Saleeby et al., 2013), where the replacement of the cold and dense mantle lithosphere by hotter asthenosphere has created regional uplift in the Sierra Nevada and promoted mantle melting, and the observed lithosphere drip sinking into the sublithospheric mantle has created subsidence beneath the Tulare basin shown in Figure 5.17a. We suggest that this is an area where slab-like delamination has occurred, based on the significant topographic variations.

Lithospheric removal has also been proposed for the southwestern Colorado Plateau (Bird, 1979). Since 6 Ma, uplift of ~0.7 km has occurred between Colorado Plateau and the adjacent Basin and Range, and the plateau edge has undergone ~0.5 km uplift relative to the Grand Canyon (Karlstrom et al., 2008). Below the edge of the Colorado Plate, a planar structure of high seismic velocity is observed at 60 to 200 km depth (Karlstrom et al., 2008). A thicker crust is found in the southwestern part of the plateau, whereas a thinner crust is observed in the middle part of the

plateau (Levander et al., 2011). Further, this area has abundant magmatism, with alkali basalts that have migrated inboard from the western plateau edge since ~5 Ma (Crow et al., 2011). Previous studies conclude that these observations are consistent with lithospheric removal through delamination, where the asthenospheric flow may cause dynamic uplift of the plateau edge and inboard migration of alkali volcanism (Crow et al., 2011; Karlstrom et al., 2008; Levander et al., 2011). As the observations indicate uplift with no clear subsidence, as well as a relatively shallow seismic velocity anomaly in the mantle shown in Figure 5.17b, we suggest that lithospheric removal may have occurred through either stringy delamination or a combination of delamination and RT drips.

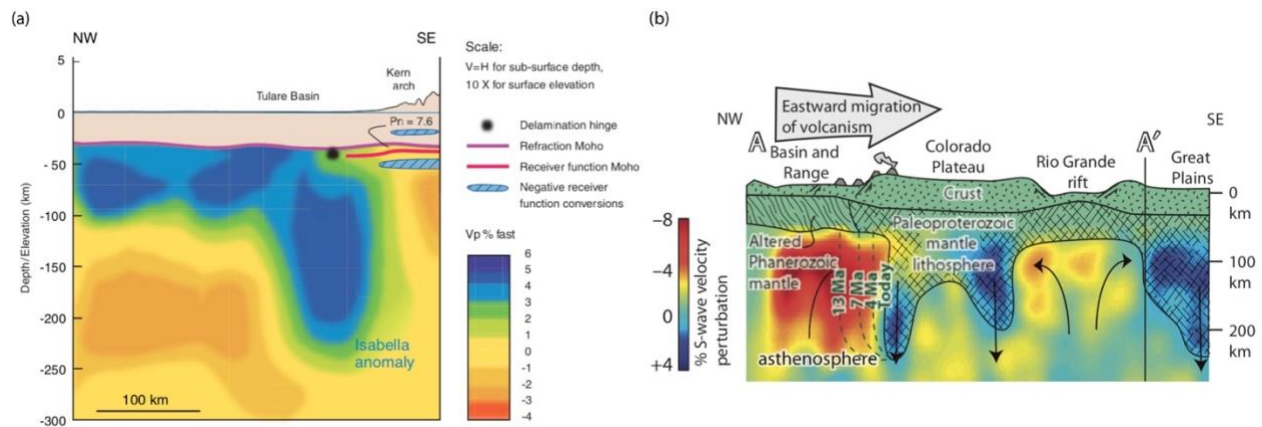


**Figure 5.17** Seismic tomography in (a) the southern Sierra Nevada from Saleeby et al. (2012) and (b) southwestern edge of Colorado Plateau from Karlstrom et al. (2008).

## 5.6 Conclusions

The models in this study explore the dynamics of delamination using a simplified model set up. For the conditions in our models (80-130 km thick lithosphere), we find that the occurrence of delamination requires (1) a weak eclogite layer in the lower crust, and (2) a weak conduit through the mantle lithosphere that enable the lower lithosphere to detach along the eclogite layer. The simplified models allow for an exploration of the effects of variations in density and viscosity of the eclogite layer on the dynamics of delamination and the associated surface observations. The key results from the models are:

1. Delamination generally occurs within 20 Myr for a generic lithosphere (45 km Moho depth and 100 km lithospheric thickness) and the occurrence of delamination depends on both the viscosity and density of the eclogite layer (assuming a thickened crust of 60 km). If the density of the eclogite layer is similar to that of the adiabatic mantle, delamination occurs for an eclogite viscosity  $\leq 10^{20}$  Pa s. As the eclogite layer density increases, delamination can occur for higher layer viscosities.
2. Three styles of delamination are observed in the models (Figure 5.18). At high eclogite layer viscosities ( $\geq 10^{22}$  Pa s), delamination occurs through slab-like delamination (Style 1), where the detaching slab grows in length, which enhances the negative buoyancy and leads to rapid removal over a width of 800 km (generally  $< 5$  Myr). At lower viscosities, the detaching lithosphere undergoes internal deformation. For most density-viscosity combinations, this leads to stringy delamination (Style 2), where necking and break-off of the detached lithosphere reduce the negative buoyancy and result in a longer timescale for delamination (generally 5-20 Myr). However, if the eclogite layer is both weak ( $10^{19}$  Pa) and dense, local gravitational instabilities form in the eclogite layer, leading to removal through a combination of stringy delamination and drips on timescales  $< 5$  Myr (Style 3).
3. Each style of delamination has a distinct topographic expression. Slab-like delamination is associated with a migrating wave of subsidence followed by uplift. Subsidence is suppressed in stringy delamination. If drips also occur, the topographic migration is less clear, and there is regional uplift. All styles result in thinned lithosphere, crustal heating, and decompression melting of the mantle.
4. Delamination creates stresses on the overlying crust that can lead to thickening of the crust above the detachment point. If the crust has a weak viscous rheology, thickening may lead to uplift, rather than subsidence. For a strong crust, there is little crustal deformation, and the topographic changes are primarily an isostatic response to the removal of the dense lower lithosphere.
5. The style of delamination and resulting surface topography also depend on the thermal structure of the lithosphere (summarized in Figure 5.18). A cool, thick lithosphere is both strong and dense. Removal occurs through rapid slab-like delamination, resulting in regional uplift and little crustal deformation (Figure 5.15). As the lithosphere becomes thinner, the higher temperatures result in a weaker and less dense lower lithosphere, resulting in removal through stringy delamination,

possibly with local drips. Delamination occurs over a longer timeframe and the hotter crust is weak enough to experience thickening and a complex pattern of surface uplift and magmatism (Figure 5.16).

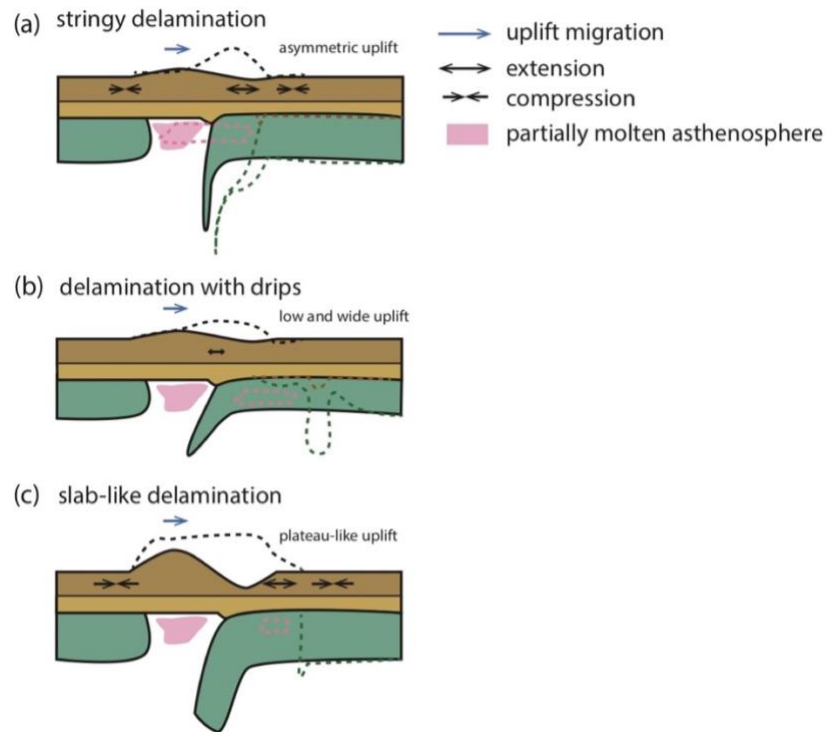


**Figure 5.18** Surface expressions are associated with styles of delamination, including (a) stringy delamination (b) delamination with drips (c) slab-like delamination. Dashed lines show the profiles of the surface topography, distribution of the mantle melt, and base of lithosphere after delamination.

## **Chapter 6**

### **Conclusions and future work**

## 6.1 Main conclusions

Western Canada consists of two main topographic regions: the high-elevation Canadian Cordillera (mountain belt) on the west and the low-elevation Laurentian Craton to the east. My Ph.D. thesis examines the structure and dynamics of the mantle below these two areas. Geophysical observations show that the cordillera is characterized by a thin and hot lithosphere (50-70 km thick), whereas the Laurentian Craton lithosphere is thicker and cooler. There are two main hypotheses for the thin cordilleran lithosphere: (1) this is a long-lived feature that is maintained by small-scale convection of a hydrated sublithospheric mantle (e.g., Hyndman et al., 2005), and (2) this is a more recent feature that developed through gravitational removal of the lower lithosphere (e.g., Audet et al., 2019). In the first two parts of my thesis, I use a combination of geophysical and geological observations and numerical models to test these hypotheses. The last part of my thesis extends this work to examine the dynamics and surface expressions of lithospheric removal through delamination for a generic continental lithosphere. The primary conclusions for each project are listed below.

### **a) The structure and dynamics of the uppermost mantle of southwestern Canada from a joint analysis of geophysical observations (Chapter 2):**

The first part of my thesis uses geophysical observations of southwestern Canada to study the mantle structure and the implications for mantle dynamics. In the mantle, seismic shear wave velocity ( $V_s$ ) and electrical resistivity vary with temperature and olivine water content. Previous studies proposed that this area has a hot, hydrated cordilleran mantle (Hyndman et al., 2005) and dry, cool cratonic mantle (Currie & van Wijk, 2016). To test both hypotheses, I develop a joint analysis of  $V_s$  and resistivity to quantify the temperature and water content at depths of 75-150 km along two profiles. For the ABC\_S profile, I find that the geophysical observations for the mantle below the Southern Canadian Cordillera can be explained by a tradeoff between temperature and water content. One end-member possibility is that the mantle is hot ( $\sim 1370$  °C) and relatively dry mantle ( $\sim 600$  ppm H/Si in olivine), with partial melt at depth of 75 km. The other end-member is that the mantle is warm ( $\sim 1240$  °C) and hydrated ( $\sim 1600$  ppm H/Si), with no extensive partial melt. The first possibility agrees with petrological estimates on mantle temperature from recent

magmatism in this area (Canil et al., 2021), but the geophysical data suggests a drier mantle than the petrology. To the east of the Rocky Mountain Trench, the mantle beneath the craton is cooler (~960-1000 °C) and drier (<500 ppm H/Si). The ABC\_N profile also has a mantle temperature contrast of ~300-400 °C between the two regions, but the olivine water content is heterogeneous, with no clear difference between the cordillera and craton. The largest sources of uncertainty in the analysis come from the resistivity model and seismic attenuation correction (Q), as well as uncertainties in the seismic and magnetotelluric models. If the Q attenuation is well-constrained, the uncertainty of mantle temperature is <100 °C below the cordillera and ~100 °C below the craton at 100 km depth. However, even if the geophysical observations are well-constrained, there remains significant uncertainty in the olivine water content (uncertainties of <1500 ppm H/Si below the cordillera and <1000 ppm H/Si craton at 100 km depth), owing to uncertainties in the resistivity model. Despite these uncertainties, the analysis yields important new predictions that can be tested in future studies. First, the cordilleran mantle seismic attenuation is predicted to be greater than that of craton by one order of magnitude (Q of 20-70 vs. Q of ~200-2000). Secondly, the cordilleran mantle viscosity is  $10^{19}$ -  $10^{21}$  Pa s, compared to  $10^{22}$ - $10^{24}$  Pa s for the craton. These results have implications for mantle dynamics in this area. For the cordillera, the low viscosities mean that the sublithospheric mantle in this region may be weak enough to undergo small-scale convection, as shown in Figure 6.1a. However, the results do not unambiguously confirm the hypothesis of Hyndman et al. (2005) that the cordillera mantle is extensively hydrated in this region. The boundary between the cordillera and craton mantle is subvertical and occurs approximately below the Rocky Mountain Trench. The results suggest that the craton mantle lithosphere is partially hydrated, and thus it is susceptible to deformation and the cordillera-craton boundary may be unstable.

**b) Recent delamination below the Northern Canadian Cordillera? (Chapter 4):**

The second part of my thesis investigates whether lithospheric delamination has occurred below the Northern Canadian Cordillera. This work is motivated by seismic studies that show a thin lithosphere (~50 km thick) (e.g., Audet et al., 2019) and the occurrence of magmatism in the Northern Cordilleran Volcanic Province (NCVP) that initiated at 15-20 Ma (Edwards & Russell, 2000). I use 2D thermal-mechanical models to quantitatively test this hypothesis. The model starts

with a thick lithosphere below the cordillera, assuming prior lithospheric thickening and eclogitization of the lowermost crust. To initiate delamination, a weak zone is placed in the mantle lithosphere, which may represent a region of hydrated mantle or shear zone. After the weak zone drips, the eclogitized lower crust starts detaching from the mantle lithosphere from the crust. This leads to full removal of the lower lithosphere across a width of ~450 km within ~4 Myr and causes surface uplift of ~1 km and heating of the overlying crust. The model results are compatible with present-day observations for the NCC, including surface elevation, surface heat flow, crustal thickness, and lithospheric thickness. The model predicts that delamination is accompanied by widespread decompression melting of the mantle. This may explain the Neogene alkaline olivine volcanism in the NCVP. On the basis of the timing of NCVP magmatism, I propose that delamination occurred at 15 Ma. The model also predicts that delamination causes extensional crustal stress within the cordillera, with compression at the edges of the thin lithosphere. The surface extension at the edges of the thinned region is affected by the corner flow created by the upwelling of the sublithosphere mantle. The surface contraction in the margins of the thinned region is triggered by delamination dynamics. When the detached lithosphere sinks into the sublithosphere mantle, the magnitude of the surface contraction depends on the crustal strength, e.g., slab-like delamination leading to surface subsidence. These stresses may explain the present-day compressional seismicity within the Mackenzie Mountains (~50-150 km away from the Cordilleran Deformation Front), as shown in Figure 6.1b.

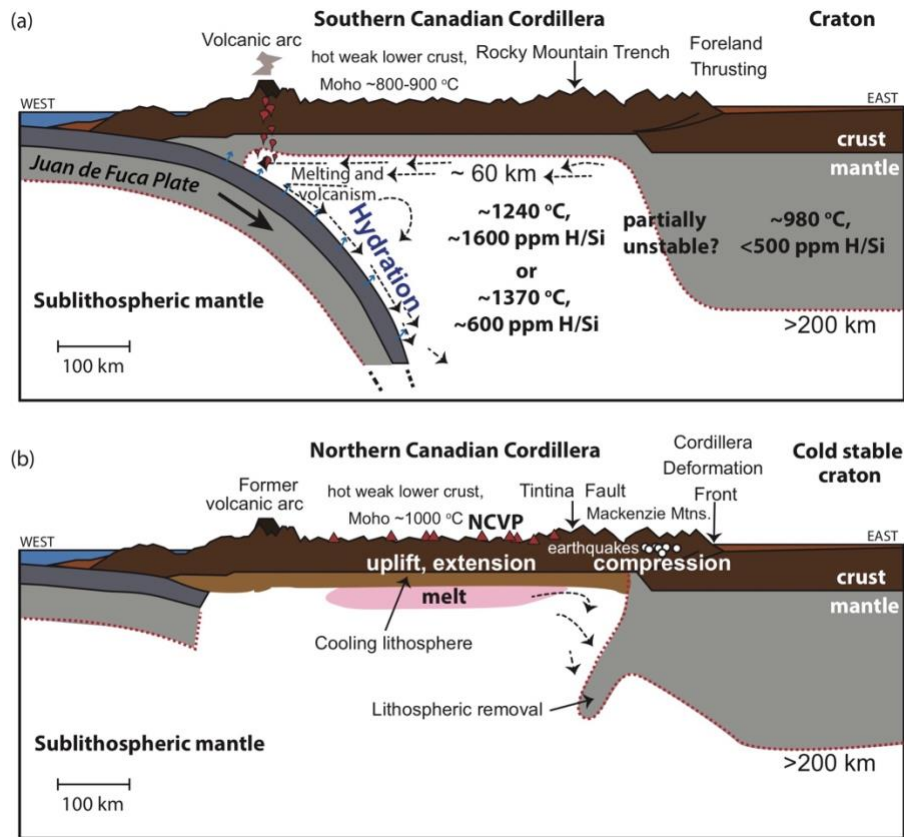


**Figure 6.1** Summary of the key results from this thesis for present-day western Canada. (a) For the Southern Canadian Cordillera, the cordilleran mantle is hydrated and hot, and the craton mantle is cool and partially dry; there is an increase in lithospheric thickness to the east of the Rocky Mountain Trench. These results support the hypothesis of small-scale convection for the cordilleran mantle and suggest that the cordillera-craton lithosphere step may be partially unstable. (b) Lithosphere delamination at 15 Ma for the Northern Canadian Cordillera can explain the present-day structure of this region, magmatism in the Northern Cordilleran Volcanic Province (NCVP), and earthquakes in the Mackenzie Mountains.

### c) **Styles and surface expressions of lithosphere delamination** (Chapter 5):

The last part of my thesis investigates the factors that control the dynamics of delamination for a generic continental lithosphere, in order to provide quantitative insights into how delamination may be recognized in surface observations. The numerical models use an eclogitized lower crust and a weak zone in the mantle lithosphere to trigger delamination. The models explore a range of densities and rheologies for the eclogite layer and different rheologies and temperatures for the continental lithosphere. I find that delamination occurs in three distinct styles depending on the density and strength of the deep lithosphere: (1) slab-like delamination where the detaching slab remains intact and delamination proceeds rapidly (<5 Myr), (2) stringy delamination where the detaching slab undergoes internal deformation and necking, resulting in slower removal (5-20 Myr), and (3) delamination with drips, where removal occur both stringy delamination and local Rayleigh-Taylor type drips. Slab-like delamination occurs for a strong lithosphere, due to either rheology or temperature, and is accompanied by a migrating wave of subsidence followed by uplift. As the lower lithosphere becomes weaker (hotter), the style changes to stringy delamination and then to delamination and drips. Because these styles do not develop a long detaching slab, there is little surface subsidence and delamination is marked by uplift. For all styles, delamination results in lithospheric thinning, mantle decompression melting, and crustal heating, where the Moho temperature increases rapidly and surface heat flow increases more gradually, as the heat must diffuse through the crust. The models also show that delamination can cause deformation of the overlying crust, leading to extension/compression at the surface and crustal thickening. If the crust is weak (e.g., due to high temperatures), significant crustal thickening results in surface uplift, partially masking the topographic changes associated with the delaminating slab. These results provide new insights into how delamination affects the evolution of different mountain belts, including the Sierra Nevada and Colorado Plateau regions of the North American Cordillera. A summary of places where gravitational removal has been proposed is shown in Figure 6.2. These include areas where removal has occurred through lithosphere drips and/or delamination, as compiled from published papers based on seismic tomography, surface elevations, magmatism, xenolith data, surface deformation, and gravity data.

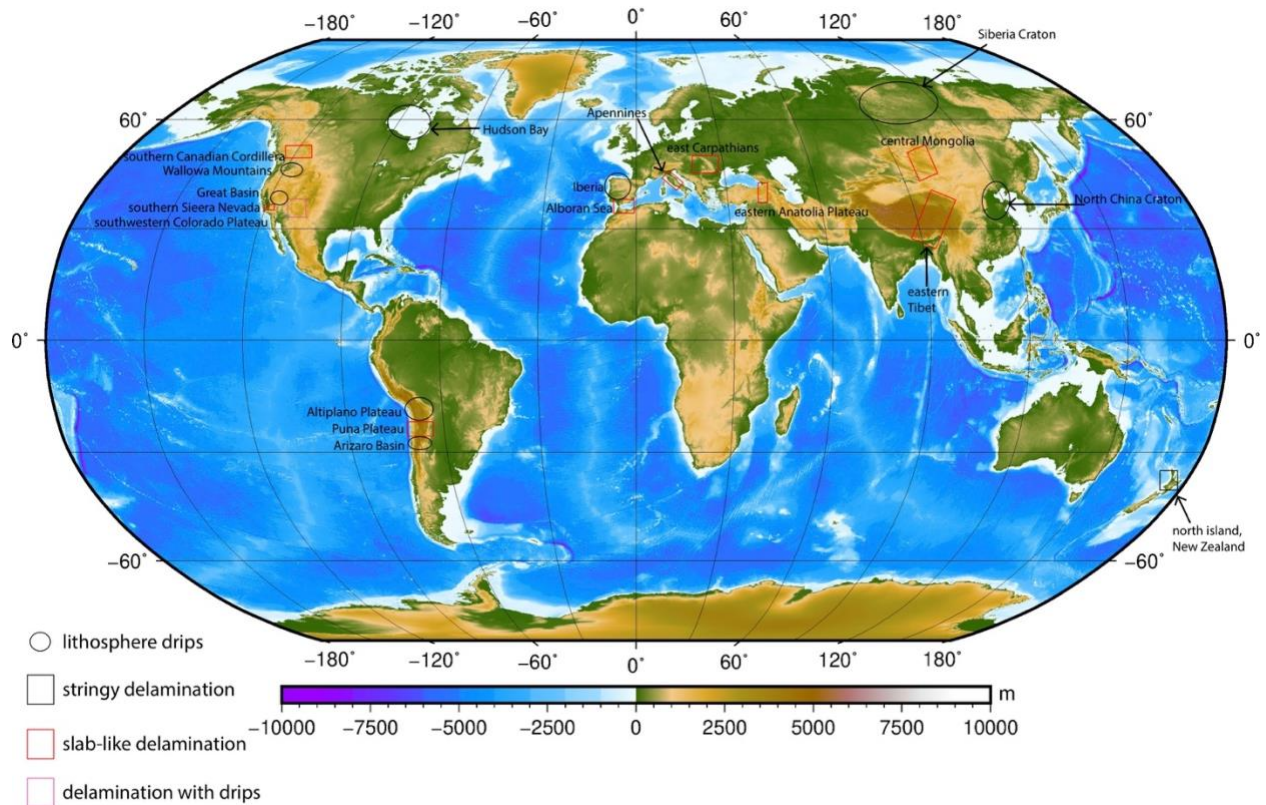


**Figure 6.2** Global locations of proposed lithosphere drips (Darold & Humphreys, 2013; Elkins-Tanton & Hager, 2000; Gorczyk et al., 2012; Gutiérrez-Alonso et al., 2011; Handy et al., 2015; Pinet et al., 2013, 2013; Pysklywec & Beaumont, 2004; Wang et al., 2021; West et al., 2009; Zhu et al., 2012) and delamination (Bao et al., 2014; Chung et al., 2005; Comeau et al., 2021; Göğüş et al., 2016; Göğüş & Pysklywec, 2008b; Karlstrom et al., 2008; Krystopowicz & Currie, 2013; Saleeby et al., 2012; Schurr et al., 2006; Stern et al., 2013; Valera et al., 2008; van Wijk et al., 2010).

## 6.2 Future work

There are a number of different aspects of this research that should be explored in future work. In the first part of my thesis, I determine the mantle temperatures and olivine water contents from geophysical observations for southwestern Canada. However, recent work has shown that hydration of pyroxene and other nominally anhydrous minerals may affect the conductivity (Özaydın & Selway, 2020 and references therein). To estimate the olivine water content from the observed resistivity, it is important to assess the effects of water content in different compositions. Additionally, as discussed in Chapter 2, the geophysical-based temperatures below craton are

higher than those obtained from xenoliths. Factors that may influence the geophysical temperatures include the low resolution of the observations, radial/azimuthal anisotropy, and the presence of hydrous minerals. The geophysical observations show clear lateral changes in subsurface structure (e.g., the cordillera-craton-boundary), which may affect the geophysical observations through lateral smearing. The vertical variations are harder to evaluate and may require additional geophysical observations, such as a combination of seismic body waves and shear waves. Second, radial anisotropy will result in differences in wavespeed between Rayleigh and Love waves, which are vertically ( $V_{SV}$ ) and horizontally ( $V_{SH}$ ) polarized, respectively. The SL2013NA tomography model used in my study (Schaeffer & Lebedev, 2014) is based on Rayleigh waves and results in relatively high temperatures in the craton. The observed low  $V_{SV}$  in the shallowest craton mantle may be related to radial anisotropy, as  $V_{SH} > V_{SV}$  has been observed in other cratons (e.g., Kaapvaal Craton; Jones et al., 2017); therefore the craton temperatures may be overestimated in my study. Third, the presence of hydrous minerals or metasomatism in craton mantle lithosphere affects the observed  $V_s$  and resistivity. For example, seismic studies suggest that metasomatism may form hydrous minerals (i.e., phlogopite) below the crust (to  $\sim 100$  km depth), creating anomalously low seismic velocities (Eeken et al., 2018). This will affect the  $V_s$ -based temperature calculations if the hydrous minerals are not considered. Magnetotelluric studies also suggest that the presence of hydrous minerals affects the amount of water content determined from resistivity values (Özaydın et al., 2021). A future study of the Laurentian Craton structure should build on my work by considering these additional factors.

The second and third parts of my thesis use numerical model to examine the dynamics of delamination. The models use a simplified structure, in order to focus on the delamination process without other factors (e.g., plate motions, continental shortening). There are a number of things that should be explored for Northern Canadian Cordillera (NCC) model. One important point is that the evolution of the Canadian Cordillera may have an impact on the current mantle structure and dynamics, including continental shortening, movement of continental terranes and plate boundary process (e.g., formation of a slab-window). The models should also test other mechanisms that have been proposed to affect the lithospheric thickness and crustal stresses. This includes collision of the Yakutat block collision at the western side of the NCC since 5-10 Ma (Mazzotti & Hyndman, 2002) and basal traction caused by regional mantle convection (Finzel et al., 2014). Future models should also include the formation of the St. Elias Mountain Range on the

west side of the NCC and surface erosion. Studies show that the St. Elias region has experienced surface erosion, with the highest precipitation on the seaward side of the mountains (Pavlis et al., 2014). Models with both regional uplift and surface erosion are important for comparing the models to thermochronology studies. Such models could examine whether the regional exhumation and surface uplift (up to ~ 5 km, Enkelmann et al., 2009) in the NCC are associated with delamination or other processes, such as the termination of subduction and Yakutat block collision. For both the NCC model and the generic models of lithosphere delamination, the model started with a pre-thickened crust which has already undergone eclogitization. Future models should include a dynamic eclogite phase transformation that occurs as the crust is thickened. This may affect the timescale of delamination. In addition, my models show that the delaminating slab can cause crustal thickening above the detachment point and eclogitization of this crustal root may accelerate lithosphere detachment. Lastly, the models in this study focus on delamination in a 2D plane. Future 3D delamination models are needed to investigate whether the temporal-spatial variations in surface responses and mantle dynamics associated with delamination are different from 2D models (Bajolet et al., 2012; Göğüş et al., 2011). For the mantle flow, the similar direction of the mantle flow between 2D and 3D models includes the corner flow, upward flow, and counter flow (Figure 6.3a). In the 3D model, the additional mantle flows such as poloidal and toroidal flows may affect the velocity of delamination (Figure 6.3b).

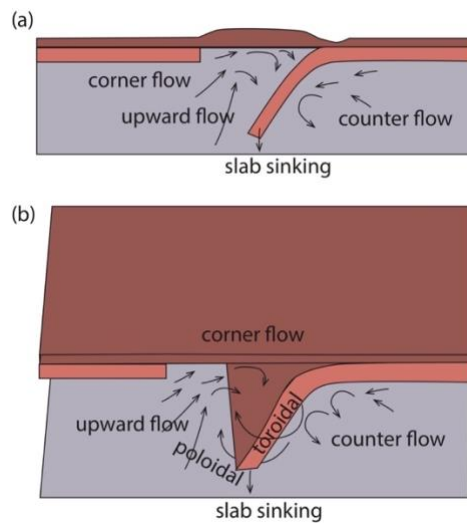


**Figure 6.3** Schematic diagrams showing mantle flow directions in (a) 2D and (b) 3D models of lithosphere delamination.

### 6.3 Concluding remarks

My thesis research uses a number of approaches to study the structure and dynamics of the mantle below western Canada and mountain belts in general. The first part uses a joint analysis of two independent geophysical observations (S-wave velocity and electrical resistivity), and it is demonstrated that this can allow for determination of both mantle temperature and olivine water content at 75-150 km depth. This is an improvement on earlier studies where assumptions had to be made about the composition (e.g., Hyndman et al., 2009) or temperature (e.g., Rippe et al., 2013). My work also provides new assessments of mantle dynamics in western Canada, based on the structure from geophysical observations (Chapter 2) and numerical models of lithospheric removal (Chapter 4). By using a range of approaches, my work provides new insights into the origin of the thin cordilleran lithosphere in western Canada.

Numerical models are used in the last two parts of my thesis (Chapters 4 and 5). The physics-based models use realistic properties for the crust and mantle materials, making them a powerful tool for exploring the range of possible subsurface dynamics. However, it is important to recognize that “all models are wrong, but some are useful” (Box, 1976). The models contain a number of simplifications, and they do not contain all the heterogeneities and processes that occur in the real Earth. However, the models calculate the thermal and mechanical evolution of the subsurface on timescales of millions of years, and they make quantitative predictions (e.g., the timing of delamination and magnitude/rate of topographic changes) that can be tested against observations. They also highlight unexpected linkages and feedbacks. For example, my models show how delamination may lead to magmatism and crustal stress changes, leading to a new interpretation of earthquakes in the Mackenzie Mountains. Collectively, the studies in this thesis demonstrate the advantages of integrating multiple types of observations and physics-based numerical models. A similar approach should be used in other areas.

## References

- Abers, G. A., Fischer, K. M., Hirth, G., Wiens, D. A., Plank, T., Holtzman, B. K., et al. (2014). Reconciling mantle attenuation-temperature relationships from seismology, petrology, and laboratory measurements. *Geochemistry, Geophysics, Geosystems*, *15*(9), 3521–3542. <https://doi.org/10.1002/2014GC005444>
- Abraham, A. C., Francis, D., & Polvé, M. (2005). Origin of recent alkaline lavas by lithospheric thinning beneath the northern Canadian Cordillera. *Canadian Journal of Earth Sciences*, *42*(6), 1073–1095. <https://doi.org/10.1139/e04-092>
- Aizawa, Y., Barnhoorn, A., Faul, U. H., Fitz Gerald, J. D., Jackson, I., & Kovacs, I. (2008). Seismic properties of Anita Bay dunite: an exploratory study of the influence of water. *Journal of Petrology*, *49*(4), 841–855. <https://doi.org/10.1093/petrology/egn007>
- Amante, C., & Eakins, B. E. (2009). ETOPO1 1 arc-minute global relief model: Procedures, data sources and analysis. *NOAA Technical Memorandum NESDIS NGDC-24*, 1–19. <https://doi.org/10.1594/PANGAEA.769615>
- Andersen, T. B., Jamtveit, B., Dewey, J. F., & Swensson, E. (1991). Subduction and exhumation of continental crust: major mechanisms during continent-continent collision and orogenic extensional collapse, a model based on the south Norwegian Caledonides. *Terra Nova*, *3*(3), 303–310. <https://doi.org/10.1111/j.1365-3121.1991.tb00148.x>
- Arcay, D., Tric, E., & Doin, M.-P. (2007). Slab surface temperature in subduction zones: Influence of the interplate decoupling depth and upper plate thinning processes. *Earth and Planetary Science Letters*, *255*(3–4), 324–338. <https://doi.org/10.1016/j.epsl.2006.12.027>
- Ardia, P., Hirschmann, M. M., Withers, A. C., & Tenner, T. J. (2012). H<sub>2</sub>O storage capacity of olivine at 5–8 GPa and consequences for dehydration partial melting of the upper mantle. *Earth and Planetary Science Letters*, *345–348*, 104–116. <https://doi.org/10.1016/j.epsl.2012.05.038>
- Aubaud, C., Hauri, E. H., & Hirschmann, M. M. (2004). Hydrogen partition coefficients between nominally anhydrous minerals and basaltic melts. *Geophysical Research Letters*, *31*(20), L20611. <https://doi.org/10.1029/2004GL021341>

- Audet, P., Currie, C. A., Schaeffer, A. J., & Hill, A. M. (2019). Seismic evidence for lithospheric thinning and heat in the northern Canadian Cordillera. *Geophysical Research Letters*, *46*(8), 4249–4257. <https://doi.org/10.1029/2019GL082406>
- Audet, P., Schutt, D. L., Schaeffer, A. J., Estève, C., Aster, R. C., & Cubley, J. F. (2020). Moho variations across the Northern Canadian Cordillera. *Seismological Research Letters*, *91*(6), 3076–3085. <https://doi.org/10.1785/0220200166>
- Aulbach, S., Griffin, W. L., O'Reilly, S. Y., & McCandless, T. E. (2004). Genesis and evolution of the lithospheric mantle beneath the Buffalo Head Terrane, Alberta (Canada). *Lithos*, *77*(1–4), 413–451. <https://doi.org/10.1016/j.lithos.2004.04.020>
- Austrheim, H. (1991). Eclogite formation and dynamics of crustal roots under continental collision zones. *Terra Nova*, *3*(5), 492–499. <https://doi.org/10.1111/j.1365-3121.1991.tb00184.x>
- Austrheim, H., Erambert, M., & Engvik, A. K. (1997). Processing of crust in the root of the Caledonian continental collision zone: the role of eclogitization. *Tectonophysics*, *273*(1–2), 129–153. [https://doi.org/10.1016/S0040-1951\(96\)00291-0](https://doi.org/10.1016/S0040-1951(96)00291-0)
- Bajolet, F., Galeano, J., Funiciello, F., Moroni, M., Negrodo, A.-M., & Faccenna, C. (2012). Continental delamination: Insights from laboratory models. *Geochemistry, Geophysics, Geosystems*, *13*(2), n/a-n/a. <https://doi.org/10.1029/2011GC003896>
- Bao, X., Eaton, D. W., & Guest, B. (2014). Plateau uplift in western Canada caused by lithospheric delamination along a craton edge. *Nature Geoscience*, *7*(11), 830–833. <https://doi.org/10.1038/ngeo2270>
- Bao, X., Eaton, D. W., & Gu, Y. J. (2016). Rayleigh wave azimuthally anisotropic phase velocity maps beneath western Canada: Azimuthal Anisotropy in Western Canada. *Journal of Geophysical Research: Solid Earth*, *121*(3), 1821–1834. <https://doi.org/10.1002/2015JB012453>
- Baptiste, V., Tommasi, A., & Demouchy, S. (2012). Deformation and hydration of the lithospheric mantle beneath the Kaapvaal craton, South Africa. *Lithos*, *149*, 31–50. <https://doi.org/10.1016/j.lithos.2012.05.001>

- Beall, A. P., Moresi, L., & Stern, T. (2017). Dripping or delamination? A range of mechanisms for removing the lower crust or lithosphere. *Geophysical Journal International*, 210(2), 671–692. <https://doi.org/10.1093/gji/ggx202>
- Beaumont, C., Jamieson, R. A., Nguyen, M. H., & Lee, B. (2001). Himalayan tectonics explained by extrusion of a low-viscosity crustal channel coupled to focused surface denudation. *Nature*, 414(6865), 738–742. <https://doi.org/10.1038/414738a>
- Beaumont, C., Nguyen, M. H., Jamieson, R. A., & Ellis, S. (2006). Crustal flow modes in large hot orogens. *Geological Society, London, Special Publications*, 268(1), 91–145. <https://doi.org/10.1144/GSL.SP.2006.268.01.05>
- Bedle, H., & van der Lee, S. (2009). S velocity variations beneath North America. *Journal of Geophysical Research*, 114(B7), B07308. <https://doi.org/10.1029/2008JB005949>
- Behn, M. D., Hirth, G., & Elsenbeck II, J. R. (2009). Implications of grain size evolution on the seismic structure of the oceanic upper mantle. *Earth Planet. Sci. Lett.*, 282, 178–189. <https://doi.org/10.1016/j.epsl.2009.03.014>
- Bird, P. (1979). Continental delamination and the Colorado Plateau. *Journal of Geophysical Research: Solid Earth*, 84(B13), 7561–7571. <https://doi.org/10.1029/JB084iB13p07561>
- Bousquet, R., Goffé, B., Henry, P., Le Pichon, X., & Chopin, C. (1997). Kinematic, thermal and petrological model of the Central Alps: Lepontine metamorphism in the upper crust and eclogitisation of the lower crust. *Tectonophysics*, 273(1–2), 105–127. [https://doi.org/10.1016/S0040-1951\(96\)00290-9](https://doi.org/10.1016/S0040-1951(96)00290-9)
- Box, G. E. P. (1976). Science and Statistics. *Journal of the American Statistical Association*, 71(356), 791–799. <https://doi.org/doi:10.1080/01621459.1976.10480949>
- Burchfiel, B. C., & Davis, G. A. (1975). Nature and controls of Cordilleran orogenesis, western US: Extensions of an earlier synthesis. *American Journal of Science*, 275A, 363–396.
- Burov, E. B., & Watts, A. B. (2006). The long-term strength of continental lithosphere: “jelly sandwich” or “crème brûlée”? *GSA TODAY*, 16(1), 4–10. [https://doi.org/10.1130/1052-5173\(2006\)016<4:tltSOc>2.0.cO;2](https://doi.org/10.1130/1052-5173(2006)016<4:tltSOc>2.0.cO;2)

- Cammarano, F., Goes, S., Vacher, P., & Giardini, D. (2003). Inferring upper-mantle temperatures from seismic velocities. *Physics of the Earth and Planetary Interiors*, 138(3–4), 197–222. [https://doi.org/10.1016/S0031-9201\(03\)00156-0](https://doi.org/10.1016/S0031-9201(03)00156-0)
- Canil, D., Russell, J. K., & Fode, D. (2021). A test of models for recent lithosphere foundering or replacement in the Canadian Cordillera using peridotite xenolith geothermometry. *Lithos*, 398–399, 106329. <https://doi.org/10.1016/j.lithos.2021.106329>
- Canil, D., Hyndman, R. D., & Fode, D. (2021). Hygrometric control on the lithosphere–asthenosphere boundary: A 28 million year record from the Canadian Cordillera. *Geophysical Research Letters*, 48(9). <https://doi.org/10.1029/2020GL091957>
- Cecil, M. R., Saleeby, Z., Saleeby, J., & Farley, K. A. (2014). Pliocene–Quaternary subsidence and exhumation of the southeastern San Joaquin Basin, California, in response to mantle lithosphere removal. *Geosphere*, 10(1), 129–147. <https://doi.org/10.1130/GES00882.1>
- Chen, W.-P., & Molnar, P. (1983). Focal depths of intracontinental and intraplate earthquakes and their implications for the thermal and mechanical properties of the lithosphere. *Journal of Geophysical Research: Solid Earth*, 88(B5), 4183–4214. <https://doi.org/10.1029/JB088iB05p04183>
- Chen, Y., Gu, Y. J., Currie, C. A., Johnston, S. T., Hung, S.-H., Schaeffer, A. J., & Audet, P. (2019). Seismic evidence for a mantle suture and implications for the origin of the Canadian Cordillera. *Nature Communications*, 10(1), 2249. <https://doi.org/10.1038/s41467-019-09804-8>
- Chung, S.-L., Chu, M.-F., Zhang, Y., Xie, Y., Lo, C.-H., Lee, T.-Y., et al. (2005). Tibetan tectonic evolution inferred from spatial and temporal variations in post-collisional magmatism. *Earth-Science Reviews*, 68(3–4), 173–196. <https://doi.org/10.1016/j.earscirev.2004.05.001>
- Christensen, N. I., & Mooney, W. D. (1995). Seismic velocity structure and composition of the continental crust: A global view. *Journal of Geophysical Research: Solid Earth*, 100(B6), 9761–9788. <https://doi.org/10.1029/95JB00259>
- Cline II, C. J., Faul, U. H., David, E. C., Berry, A. J., & Jackson, I. (2018). Redox-influenced seismic properties of upper-mantle olivine. *Nature*, 555(7696), 355–358. <https://doi.org/10.1038/nature25764>

- Clowes, R. M., Hammer, P. T. C., Fernández-Viejo, G., & Welford, J. K. (2005). Lithospheric structure in northwestern Canada from Lithoprobe seismic refraction and related studies: a synthesis. *Canadian Journal of Earth Sciences*, 1277–1293. <https://doi.org/10.1139/E04-069>
- Comeau, M. J., Stein, C., Becken, M., & Hansen, U. (2021). Geodynamic Modeling of Lithospheric Removal and Surface Deformation: Application to Intraplate Uplift in Central Mongolia. *Journal of Geophysical Research: Solid Earth*, 126(5). <https://doi.org/10.1029/2020JB021304>
- Connolly, J. A. D. (2005). Computation of phase equilibria by linear programming: A tool for geodynamic modeling and its application to subduction zone decarbonation. *Earth Planet. Sci. Lett.*, 236, 524–541. <https://doi.org/10.1016/j.epsl.2005.04.033>
- Connolly, J. A. D. (2009). The geodynamic equation of state: What and how. *Geochemistry, Geophysics, Geosystems*, 10(10), Q10014. <https://doi.org/10.1029/2009GC002540>
- Conrad, C. P., & Molnar, P. (1999). Convective instability of a boundary layer with temperature- and strain-rate-dependent viscosity in terms of “available buoyancy.” *Geophysical Journal International*, 139(1), 51–68. <https://doi.org/10.1046/j.1365-246X.1999.00896.x>
- Cook, D. G. (1991). Mackenzie Mountains, Franklin Mountains and Colville Hills. In *Geology of the Cordilleran Orogen in Canada, Vol. G2, Edited by H. Gabrielse and C. J. Yorath and Compiled by H. Gabrielse, p. 571-675, Geology Society of America, Boulder, Colorado.*
- Cook, F. A., Clowes, R. M., Snyder, D. B., van der Velden, A. J., Hall, K. W., Erdmer, P., & Evenchick, C. A. (2004). Precambrian crust beneath the Mesozoic northern Canadian Cordillera discovered by Lithoprobe seismic reflection profiling. *Tectonics*, 23, TC2010. <https://doi.org/10.1029/2002TC001412>
- Cook, F. A., & Erdmer, P. (2005). An 1800 km cross section of the lithosphere through the northwestern North American plate: lessons from 4.0 billion years of Earth’s history. *Canadian Journal of Earth Sciences*, 42(6), 1295–1311. <https://doi.org/10.1139/e04-106>
- Crow, R., Karlstrom, K., Asmerom, Y., Schmandt, B., Polyak, V., & DuFrane, S. A. (2011). Shrinking of the Colorado Plateau via lithospheric mantle erosion: Evidence from Nd and

- Sr isotopes and geochronology of Neogene basalts. *Geology*, 39(1), 27–30. <https://doi.org/10.1130/G31611.1>
- Currie, C. A., & Hyndman, R. D. (2006). The thermal structure of subduction zone back arcs. *Journal of Geophysical Research*, 111(B8), B08404. <https://doi.org/10.1029/2005JB004024>
- Currie, C. A., & van Wijk, J. (2016). How craton margins are preserved: Insights from geodynamic models. *Journal of Geodynamics*, 100, 144–158. <https://doi.org/10.1016/j.jog.2016.03.015>
- Currie, C. A., Cassidy, J. F., Hyndman, R. D., & Bostock, M. G. (2004). Shear wave anisotropy beneath the Cascadia subduction zone and western North American craton. *Geophysical Journal International*, 157(1), 341–353. <https://doi.org/10.1111/j.1365-246X.2004.02175.x>
- Currie, C. A., Huisman, R. S., & Beaumont, C. (2008). Thinning of continental backarc lithosphere by flow-induced gravitational instability. *Earth and Planetary Science Letters*, 269(3–4), 436–447. <https://doi.org/10.1016/j.epsl.2008.02.037>
- Currie, C. A., Ducea, M. N., DeCelles, P. G., & Beaumont, C. (2015). Geodynamic models of Cordilleran orogens: Gravitational instability of magmatic arc roots. In P. G. DeCelles, M. N. Ducea, B. Carrapa, & P. A. Kapp, *Geodynamics of a Cordilleran Orogenic System: The Central Andes of Argentina and Northern Chile*. Geological Society of America. [https://doi.org/10.1130/2015.1212\(01\)](https://doi.org/10.1130/2015.1212(01))
- Czas, J., Pearson, D. G., Stachel, T., Kjarsgaard, B. A., & Read, G. H. (2020). A Palaeoproterozoic diamond-bearing lithospheric mantle root beneath the Archean Sask Craton, Canada. *Lithos*, 356–357, 105301. <https://doi.org/10.1016/j.lithos.2019.105301>
- Dalton, C. A., Ekström, G., & Dziewoński, A. M. (2008). The global attenuation structure of the upper mantle. *Journal of Geophysical Research*, 113(B9), B09303. <https://doi.org/10.1029/2007JB005429>
- Darold, A., & Humphreys, E. (2013). Upper mantle seismic structure beneath the Pacific Northwest: A plume-triggered delamination origin for the Columbia River flood basalt eruptions. *Earth and Planetary Science Letters*, 365, 232–242. <https://doi.org/10.1016/j.epsl.2013.01.024>

- DeCelles, P. G., Ducea, M. N., Kapp, P., & Zandt, G. (2009). Cyclicity in Cordilleran orogenic systems. *Nature Geoscience*, 2(4), 251–257. <https://doi.org/10.1038/ngeo469>
- DiCaprio, L., Maiti, T., Dettmer, J., & Eaton, D. W. (2020). Moho Structure Across the Backarc-Craton Transition in the Northern U.S. Cordillera. *Tectonics*, 39(2). <https://doi.org/10.1029/2019TC005489>
- Dixon, J. E., Dixon, T. H., Bell, D. R., & Malservisi, R. (2004). Lateral variation in upper mantle viscosity: role of water. *Earth and Planetary Science Letters*, 222(2), 451–467. <https://doi.org/10.1016/j.epsl.2004.03.022>
- Doucet, L. S., Peslier, A. H., Ionov, D. A., Brandon, A. D., Golovin, A. V., Goncharov, A. G., & Ashchepkov, I. V. (2014). High water contents in the Siberian cratonic mantle linked to metasomatism: An FTIR study of Udachnaya peridotite xenoliths. *Geochimica et Cosmochimica Acta*, 137, 159–187. <https://doi.org/10.1016/j.gca.2014.04.011>
- Eaton, D. W., Bao, X., & Perry, C. (2018). Frayed edges of cratonic mantle keels: Thermal diffusion timescales and their predicted imprint on mantle-velocity structure. In H. Yuan & B. Romanowicz (Eds.), *Geophysical Monograph Series* (1st ed., pp. 125–138). Wiley. <https://doi.org/10.1002/9781119249740.ch7>
- Edwards, B. R., & Russell, J. K. (2000). Distribution, nature, and origin of Neogene–Quaternary magmatism in the northern Cordilleran volcanic province, Canada. *Geological Society of America Bulletin*, 112, 1280–1295. [https://doi.org/10.1130/0016-7606\(2000\)112<1280:DNAOON>2.0.CO;2](https://doi.org/10.1130/0016-7606(2000)112<1280:DNAOON>2.0.CO;2)
- Eeken, T., Goes, S., Pedersen, H. A., Arndt, N. T., & Bouilhol, P. (2018). Seismic evidence for depth-dependent metasomatism in cratons. *Earth and Planetary Science Letters*, 491, 148–159. <https://doi.org/10.1016/j.epsl.2018.03.018>
- Elkins-Tanton, L. T. (2005). Continental magmatism caused by lithospheric delamination. In G. R. Foulger, J. H. Natland, D. C. Presnall, & D. L. Anderson, in *Foulger, G.R., Natland, J.H., Presnall, D.C., and Anderson, D.L., eds., Plates, plumes and paradigms* (pp. 449–461). Geological Society of America Special Paper 388. <https://doi.org/10.1130/0-8137-2388-4.449>

- Elkins-Tanton, L. T., & Hager, B. H. (2000). Melt intrusion as a trigger for lithospheric foundering and the eruption of the Siberian flood basalts. *Geophysical Research Letters*, 27(23), 3937–3940. <https://doi.org/10.1029/2000GL011751>
- Engebretson, D. C., Cox, A., & Thompson, A. (1985). Relative motions between oceanic and continental plates in the Pacific basin. *Relative Motions between Oceanic and Continental Plates in the Pacific Basin*, 59.
- Enkelmann, E., Zeitler, P. K., Pavlis, T. L., Garver, J. I., & Ridgway, K. D. (2009). Intense localized rock uplift and erosion in the St Elias orogen of Alaska. *Nature Geoscience*, 2(5), 360–363. <https://doi.org/10.1038/ngeo502>
- Enkelmann, E., Finzel, E., & Arkle, J. (2019). Deformation at the eastern margin of the Northern Canadian Cordillera: Potentially related to opening of the North Atlantic. *Terra Nova*, 31(3), 151–158. <https://doi.org/10.1111/ter.12374>
- Enkin, R. J., Johnston, S. T., Larson, K. P., & Baker, J. (2006). Paleomagnetism of the 70 Ma Carmacks Group at Solitary Mountain, Yukon, confirms and extends controversial results: Further evidence for the Baja British Columbia model. *Geological Association of Canada, Special Paper*, 46, 221–232.
- Estève, C., Gosselin, J. M., Audet, P., Schaeffer, A. J., Schutt, D. L., & Aster, R. C. (2021). Surface-wave tomography of the Northern Canadian Cordillera using earthquake Rayleigh wave group velocities. *Journal of Geophysical Research: Solid Earth*, 126(8), e2021JB021960. <https://doi.org/10.1029/2021JB021960>
- Faccenda, M., Minelli, G., & Gerya, T. V. (2009). Coupled and decoupled regimes of continental collision: Numerical modeling. *Earth and Planetary Science Letters*, 278(3–4), 337–349. <https://doi.org/10.1016/j.epsl.2008.12.021>
- Faul, U., & Jackson, I. (2005). The seismological signature of temperature and grain size variations in the upper mantle. *Earth and Planetary Science Letters*, 234(1–2), 119–134. <https://doi.org/10.1016/j.epsl.2005.02.008>
- Finzel, E. S., Flesch, L. M., & Ridgway, K. D. (2014). Present-day geodynamics of the northern North American Cordillera. *Earth and Planetary Science Letters*, 404, 111–123. <https://doi.org/10.1016/j.epsl.2014.07.024>

- Flück, P., Hyndman, R. D., & Lowe, C. (2003). Effective elastic thickness  $T_e$  of the lithosphere in western Canada. *Journal of Geophysical Research: Solid Earth*, 108, 2430. <https://doi.org/10.1029/2002JB002201>
- Francis, D., Minarik, W., Proenza, Y., & Shi, L. (2010). An overview of the Canadian Cordilleran lithospheric mantle. *Canadian Journal of Earth Sciences*, 47(4), 353–368. <https://doi.org/10.1139/E09-072>
- Freeburn, R., Bouilhol, P., Maunder, B., Magni, V., & van Hunen, J. (2017). Numerical models of the magmatic processes induced by slab breakoff. *Earth and Planetary Science Letters*, 478, 203–213. <https://doi.org/10.1016/j.epsl.2017.09.008>
- French, S. W., & Romanowicz, B. A. (2014). Whole-mantle radially anisotropic shear velocity structure from spectral-element waveform tomography. *Geophysical Journal International*, 199(3), 1303–1327. <https://doi.org/10.1093/gji/ggu334>
- Fullsack, P. (1995). An arbitrary Lagrangian-Eulerian formulation for creeping flows and its application in tectonic models. *Geophysical Journal International*, 120(1), 1–23. <https://doi.org/10.1111/j.1365-246X.1995.tb05908.x>
- Fuston, S., & Wu, J. (2021). Raising the Resurrection plate from an unfolded-slab plate tectonic reconstruction of northwestern North America since early Cenozoic time. *GSA Bulletin*, 133(5–6), 1128–1140. <https://doi.org/10.1130/B35677.1>
- Gabrielse, H., & Yorath, C. J. (1991). *The geology of the Cordilleran Orogen in Canada* (Vol. G2). Geological Survey of Canada.
- Gabrielse, H., Murphy, D. C., & Mortensen, J. K. (2006). Cretaceous and Cenozoic dextral orogen-parallel displacements, magmatism, and paleogeography, north-central Canadian Cordillera. In Haggart, J.W., Enkin, R.J. and Monger, J.W.H., Eds., *Paleogeography of the North American Cordillera: Evidence For and Against Large-Scale Displacements: Geological Association of Canada, Special paper 46*, 255–276.
- Garber, J. M., Maurya, S., Hernandez, J., Duncan, M. S., Zeng, L., Zhang, H. L., et al. (2018). Multidisciplinary constraints on the abundance of diamond and eclogite in the cratonic lithosphere. *Geochemistry, Geophysics, Geosystems*, 19(7), 2062–2086. <https://doi.org/10.1029/2018GC007534>

- Gardés, E., Gaillard, F., & Tarits, P. (2014). Toward a unified hydrous olivine electrical conductivity law. *Geochemistry, Geophysics, Geosystems*, 15(12), 4984–5000. <https://doi.org/10.1002/2014GC005496>
- Gerya, T. (2009). *Introduction to Numerical Geodynamic Modelling - 2nd edition*. Cambridge University Press. Retrieved from <https://doi.org/10.1017/CBO9780511809101>
- Gilbert, H., Yang, Y., Forsyth, D. W., Jones, C. H., Owens, T. J., Zandt, G., & Stachnik, J. C. (2012). Imaging lithospheric foundering in the structure of the Sierra Nevada. *Geosphere*, 8(6), 1310–1330. <https://doi.org/10.1130/GES00790.1>
- Gleason, G. C., & Tullis, J. (1995). A flow law for dislocation creep of quartz aggregates determined with the molten salt cell. *Tectonophysics*, 247(1–4), 1–23. [https://doi.org/10.1016/0040-1951\(95\)00011-B](https://doi.org/10.1016/0040-1951(95)00011-B)
- Goes, S., & van der Lee, S. (2002). Thermal structure of the North American uppermost mantle inferred from seismic tomography. *Journal of Geophysical Research*, 107(B3), 2050. <https://doi.org/10.1029/2000JB000049>
- Goes, S., Armitage, J., Harmon, N., Smith, H., & Huisman, R. (2012). Low seismic velocities below mid-ocean ridges: Attenuation versus melt retention. *Journal of Geophysical Research: Solid Earth*, 117(B12), B12403. <https://doi.org/10.1029/2012JB009637>
- Göğüş, O. H., & Pysklywec, R. N. (2008a). Near-surface diagnostics of dripping or delaminating lithosphere. *Journal of Geophysical Research*, 113(B11), B11404. <https://doi.org/10.1029/2007JB005123>
- Göğüş, O. H., & Pysklywec, R. N. (2008b). Mantle lithosphere delamination driving plateau uplift and synconvergent extension in eastern Anatolia. *Geology*, 36(9), 723. <https://doi.org/10.1130/G24982A.1>
- Göğüş, O. H., & Ueda, K. (2018). Peeling back the lithosphere: Controlling parameters, surface expressions and the future directions in delamination modeling. *Journal of Geodynamics*, 117, 21–40. <https://doi.org/10.1016/j.jog.2018.03.003>
- Göğüş, O. H., Pysklywec, R. N., Corbi, F., & Faccenna, C. (2011). The surface tectonics of mantle lithosphere delamination following ocean lithosphere subduction: Insights from physical-

- scaled analogue experiments. *Geochemistry, Geophysics, Geosystems*, 12(5), n/a-n/a. <https://doi.org/10.1029/2010GC003430>
- Göğüş, O. H., Pysklywec, R. N., & Faccenna, C. (2016). Postcollisional lithospheric evolution of the Southeast Carpathians: Comparison of geodynamical models and observations. *Tectonics*, 35(5), 1205–1224. <https://doi.org/10.1002/2015TC004096>
- Gorczyk, W., Hobbs, B., & Gerya, T. (2012). Initiation of Rayleigh–Taylor instabilities in intracratonic settings. *Tectonophysics*, 514–517, 146–155. <https://doi.org/10.1016/j.tecto.2011.10.016>
- Gordon, S. M., Whitney, D. L., Teyssier, C., & Fossen, H. (2013). U–Pb dates and trace-element geochemistry of zircon from migmatite, Western Gneiss Region, Norway: Significance for history of partial melting in continental subduction. *Lithos*, 170–171, 35–53. <https://doi.org/10.1016/j.lithos.2013.02.003>
- Gough, D. I. (1986). Mantle upflow tectonics in the Canadian Cordillera. *Journal of Geophysical Research*, 91(B2), 1909. <https://doi.org/10.1029/JB091iB02p01909>
- Gray, R., & Pysklywec, R. N. (2012). Geodynamic models of mature continental collision: Evolution of an orogen from lithospheric subduction to continental retreat/delamination. *Journal of Geophysical Research: Solid Earth*, 117(B3), B03408. <https://doi.org/10.1029/2011JB008692>
- Greenfield, A. M. R., Ghent, E. D., & Russell, J. K. (2013). Geothermobarometry of spinel peridotites from southern British Columbia: implications for the thermal conditions in the upper mantle. *Canadian Journal of Earth Sciences*, 50(10), 1019–1032. <https://doi.org/10.1139/cjes-2013-0037>
- Griffin, W. L., O'Reilly, S. Y., Abe, N., Aulbach, S., Davies, R. M., Pearson, N. J., et al. (2003). The origin and evolution of Archean lithospheric mantle. *Precambrian Research*, 127(1–3), 19–41. [https://doi.org/10.1016/S0301-9268\(03\)00180-3](https://doi.org/10.1016/S0301-9268(03)00180-3)
- Griffin, W. L., O'Reilly, S. Y., Afonso, J. C., & Begg, G. C. (2009). The composition and evolution of lithospheric mantle: a re-evaluation and its tectonic implications. *Journal of Petrology*, 50(7), 1185–1204. <https://doi.org/10.1093/petrology/egn033>

- Grose, C. J., & Afonso, J. C. (2013). Comprehensive plate models for the thermal evolution of oceanic lithosphere. *Geochemistry, Geophysics, Geosystems*, *14*(9), 3751–3778. <https://doi.org/10.1002/ggge.20232>
- Gu, Y. J., Okeler, A., Shen, L., & Contenti, S. (2011). The Canadian Rockies and Alberta Network (CRANE): New constraints on the Rockies and Western Canada Sedimentary Basin. *Seismological Research Letters*, *82*(4), 575–588.
- Gu, Y. J., Chen, Y., Dokht, R. M. H., & Wang, R. (2018). Precambrian Tectonic Discontinuities in Western Laurentia: Broadband Seismological Perspectives on the Snowbird and Great Falls Tectonic Zones. *Tectonics*, *37*(5), 1411–1434. <https://doi.org/10.1029/2017TC004843>
- Gutiérrez-Alonso, G., Fernández-Suárez, J., Jeffries, T. E., Johnston, S. T., Pastor-Galán, D., Murphy, J. B., et al. (2011). Diachronous post-orogenic magmatism within a developing orocline in Iberia, European Variscides. *Tectonics*, *30*(5), n/a-n/a. <https://doi.org/10.1029/2010TC002845>
- Hacker, B. R., Abers, G. A., & Peacock, S. M. (2003). Subduction factory 1. Theoretical mineralogy, densities, seismic wave speeds, and H<sub>2</sub>O contents. *Journal of Geophysical Research*, *108*(B1), 2029.
- Hammer, P. T. C., & Clowes, R. M. (2004). Accreted terranes of northwestern British Columbia, Canada: Lithospheric velocity structure and tectonics. *Journal of Geophysical Research: Solid Earth*, *109*(B6), B06305. <https://doi.org/10.1029/2003JB002749>
- Hammer, P. T. C., Clowes, R. M., & Ellis, R. M. (2000). Crustal structure of NW British Columbia and SE Alaska from seismic wide-angle studies: Coast Plutonic Complex to Stikinia. *Journal of Geophysical Research: Solid Earth*, *105*(B4), 7961–7981. <https://doi.org/10.1029/1999JB900378>
- Handy, M. R., Ustaszewski, K., & Kissling, E. (2015). Reconstructing the Alps–Carpathians–Dinarides as a key to understanding switches in subduction polarity, slab gaps and surface motion. *International Journal of Earth Sciences*, *104*(1), 1–26. <https://doi.org/10.1007/s00531-014-1060-3>

- Hardebol, N. J., Pysklywec, R. N., & Stephenson, R. (2012). Small-scale convection at a continental back-arc to craton transition: Application to the southern Canadian Cordillera. *Journal of Geophysical Research: Solid Earth*, *117*(B1), n/a-n/a. <https://doi.org/10.1029/2011JB008431>
- Harder, M., & Russell, J. K. (2006). Thermal state of the upper mantle beneath the Northern Cordilleran Volcanic Province (NCVP), British Columbia, Canada. *Lithos*, *87*(1–2), 1–22. <https://doi.org/10.1016/j.lithos.2005.05.002>
- Hieronymus, C., Shomali, Z., & Pedersen, L. (2007). A dynamical model for generating sharp seismic velocity contrasts underneath continents: Application to the Sorgenfrei–Tornquist Zone. *Earth and Planetary Science Letters*, *262*(1–2), 77–91. <https://doi.org/10.1016/j.epsl.2007.07.043>
- Hirschmann, M. M. (2000). Mantle solidus: Experimental constraints and the effects of peridotite composition. *Geochemistry, Geophysics, Geosystems*, *1*(10), 2000GC000070. <https://doi.org/10.1029/2000GC000070>
- Hirschmann, M. M., Aubaud, C., & Withers, A. C. (2005). Storage capacity of H<sub>2</sub>O in nominally anhydrous minerals in the upper mantle. *Earth and Planetary Science Letters*, *236*, 167–181. <https://doi.org/10.1016/j.epsl.2005.04.022>
- Hirschmann, M. M., Tenner, T., Aubaud, C., & Withers, A. C. (2009). Dehydration melting of nominally anhydrous mantle: The primacy of partitioning. *Physics of the Earth and Planetary Interiors*, *176*, 54–68. <https://doi.org/10.1016/j.pepi.2009.04.001>
- Hirth, G., & Kohlstedt, D. L. (1996). Water in the oceanic upper mantle: implications for rheology, melt extraction and the evolution of the lithosphere. *Earth and Planetary Science Letters*, *144*(1–2), 93–108. [https://doi.org/10.1016/0012-821X\(96\)00154-9](https://doi.org/10.1016/0012-821X(96)00154-9)
- Hirth, G., & Kohlstedt, D. L. (2003). Rheology of the upper mantle and the mantle wedge: A view from the experimentalists. *Inside the Subduction Factory, 2004, Geophysical Monograph Series, 138*(Blackwell Publishing Ltd.), 83–105. <https://doi.org/10.1029/138GM06>
- Hoffman, P. F. (1988). United Plates of America, The Birth of a Craton: Early Proterozoic Assembly and Growth of Laurentia. *Ann. Rev. Earth Planet. Sci.*, *16*, 543–603.

- Houseman, G. A., & Molnar, P. (1997). Gravitational (Rayleigh-Taylor) instability of a layer with non-linear viscosity and convective thinning of continental lithosphere. *Geophysical Journal International*, 128(1), 125–150. <https://doi.org/10.1111/j.1365-246X.1997.tb04075.x>
- Huisman, R. S., & Beaumont, C. (2003). Symmetric and asymmetric lithospheric extension: Relative effects of frictional-plastic and viscous strain softening. *Journal of Geophysical Research: Solid Earth*, 108(B10). <https://doi.org/10.1029/2002JB002026>
- Humphreys, E. D., & Coblenz, D. D. (2007). North American dynamics and western U.S. tectonics. *Reviews of Geophysics*, 45(3), RG3001. <https://doi.org/10.1029/2005RG000181>
- Hyndman, R. D., Currie, C. A., & Mazzotti, S. P. (2005). Subduction zone backarcs, mobile belts, and orogenic heat. *GSA TODAY*, 15(2), 4–10. [https://doi.org/10.1130/1052-5173\(2005\)015<4:SZBMBA>2.0.CO;2](https://doi.org/10.1130/1052-5173(2005)015<4:SZBMBA>2.0.CO;2)
- Hyndman, R.D., & Currie, C. A. (2011). Why is the North America Cordillera high? Hot backarcs, thermal isostasy, and mountain belts. *Geology*, 39(8), 783–786. <https://doi.org/10.1130/G31998.1>
- Hyndman, R.D., & Lewis, T. J. (1999). Geophysical consequences of the Cordillera–Craton thermal transition in southwestern Canada. *Tectonophysics*, 306(3–4), 397–422. [https://doi.org/10.1016/S0040-1951\(99\)00068-2](https://doi.org/10.1016/S0040-1951(99)00068-2)
- Hyndman, R.D., Currie, C. A., Mazzotti, S., & Frederiksen, A. (2009). Temperature control of continental lithosphere elastic thickness,  $T_e$  vs  $V_s$ . *Earth and Planetary Science Letters*, 277(3–4), 539–548. <https://doi.org/10.1016/j.epsl.2008.11.023>
- Hyndman, R. D., & Canil, D. (2021). Geophysical and geochemical constraints on Neogene-recent volcanism in the North American Cordillera. *Geochemistry, Geophysics, Geosystems*, 22(5). <https://doi.org/10.1029/2021GC009637>
- Irving, E., Thorkelson, D. J., Wheadon, P. M., & Enkin, R. J. (1995). Paleomagnetism of the Spences Bridge Group and northward displacement of the Intermontane Belt, British Columbia: A second look. *J. Geophys. Res. Solid Earth*, 100, 6057–6071. <https://doi.org/10.1029/94JB03012>

- Jackson, I., & Faul, U. H. (2010). Grainsize-sensitive viscoelastic relaxation in olivine: Towards a robust laboratory-based model for seismological application. *Physics of the Earth and Planetary Interiors*, 183(1–2), 151–163. <https://doi.org/10.1016/j.pepi.2010.09.005>
- Jackson, J. A., Austrheim, H., McKenzie, D., & Priestley, K. (2004). Metastability, mechanical strength, and the support of mountain belts. *Geology*, 32(7), 625. <https://doi.org/10.1130/G20397.1>
- James, T. S., Clague, J. J., Wang, K., & Hutchinson, I. (2000). Postglacial rebound at the northern Cascadia subduction zone. *Quaternary Science Reviews*, 19(14–15), 1527–1541. [https://doi.org/10.1016/S0277-3791\(00\)00076-7](https://doi.org/10.1016/S0277-3791(00)00076-7)
- Jamieson, R. A., & Beaumont, C. (2013). On the origin of orogens. *Geological Society of America Bulletin*, 125(11–12), 1671–1702. <https://doi.org/10.1130/B30855.1>
- Jin, Z.-M., Zhang, J., Green, H. W., & Jin, S. (2001). Eclogite rheology: Implications for subducted lithosphere. *Geology*, 29(8), 667–670.
- Johnston, S. T. (2001). The Great Alaskan Terrane Wreck: reconciliation of paleomagnetic and geological data in the northern Cordillera. *Earth Planet. Sci. Lett.*, 193, 259–272. [https://doi.org/10.1016/S0012-821X\(01\)00516-7](https://doi.org/10.1016/S0012-821X(01)00516-7)
- Johnston, S. T. (2008). The Cordilleran Ribbon Continent of North America. *Ann. Rev. Earth Planet. Sci.*, 36, 495–530. <https://doi.org/10.1146/annurev.earth.36.031207.124331>
- Jones, A. G., Fullea, J., Evans, R. L., & Muller, M. R. (2012). Water in cratonic lithosphere: Calibrating laboratory-determined models of electrical conductivity of mantle minerals using geophysical and petrological observations. *Geochemistry, Geophysics, Geosystems*, 13(6), Q06010. <https://doi.org/10.1029/2012GC004055>
- Jones, A. G., Afonso, J. C., & Fullea, J. (2017). Geochemical and geophysical constraints on the dynamic topography of the Southern African Plateau. *Geochemistry, Geophysics, Geosystems*, 18(10), 3556–3575. <https://doi.org/10.1002/2017GC006908>
- Jull, M., & Kelemen, P. B. (2001). On the conditions for lower crustal convective instability. *Journal of Geophysical Research: Solid Earth*, 106(B4), 6423–6446. <https://doi.org/10.1029/2000JB900357>

- Karato, S.-I., & Wang, D. (2013). Electrical Conductivity of Minerals and Rocks. In Shun-Ichiro Karato (Ed.), *Physics and Chemistry of the Deep Earth* (pp. 145–182). Chichester, UK: John Wiley & Sons, Ltd. <https://doi.org/10.1002/9781118529492.ch5>
- Karato, S.-I. (1990). The role of hydrogen in the electrical conductivity of the upper mantle. *Nature*, *347*(6290), 272–273. <https://doi.org/10.1038/347272a0>
- Karato, S.-I. (1993). Importance of anelasticity in the interpretation of seismic tomography. *Geophysical Research Letters*, *20*, 1623–1626. <https://doi.org/10.1029/93GL01767>
- Karato, S.-I. (2003). Mapping water content in the upper mantle. In J. Eiler (Ed.), *Geophysical Monograph Series* (Vol. 138, pp. 135–152). Washington, D. C.: American Geophysical Union. <https://doi.org/10.1029/138GM08>
- Karato, S.-I., & Wu, P. (1993). Rheology of the upper mantle: A synthesis. *Science*, *260*(5109), 771–778. <https://doi.org/10.1126/science.260.5109.771>
- Karlstrom, K. E., Crow, R., Crossey, L. J., Coblenz, D., & Van Wijk, J. W. (2008). Model for tectonically driven incision of the younger than 6 Ma Grand Canyon. *Geology*, *36*(11), 835. <https://doi.org/10.1130/G25032A.1>
- Katz, R. F., Spiegelman, M., & Langmuir, C. H. (2003). A new parameterization of hydrous mantle melting. *Geochemistry, Geophysics, Geosystems*, *4*(9), 1073. <https://doi.org/10.1029/2002GC000433>
- Kay, R. W., & Kay, S. M. (1993). Delamination and delamination magmatism. *Tectonophysics*, *219*(1–3), 177–189. [https://doi.org/10.1016/0040-1951\(93\)90295-U](https://doi.org/10.1016/0040-1951(93)90295-U)
- Kelley, K. A., Plank, T., Newman, S., Stolper, E. M., Grove, T. L., Parman, S., & Hauri, E. H. (2010). Mantle melting as a function of water content beneath the Mariana Arc. *Journal of Petrology*, *51*(8), 1711–1738. <https://doi.org/10.1093/petrology/egq036>
- Kilgore, M. L., Peslier, A. H., Brandon, A. D., Schaffer, L. A., Morris, R. V., Graff, T. G., et al. (2020). Metasomatic control of hydrogen contents in the layered cratonic mantle lithosphere sampled by Lac de Gras xenoliths in the central Slave craton, Canada. *Geochimica et Cosmochimica Acta*, *286*, 29–53. <https://doi.org/10.1016/j.gca.2020.07.013>

- King, S. D., & Anderson, D. L. (1998). Edge-driven convection. *Earth and Planetary Science Letters*, *160*(3–4), 289–296. [https://doi.org/10.1016/S0012-821X\(98\)00089-2](https://doi.org/10.1016/S0012-821X(98)00089-2)
- Király, Á., Portner, D. E., Haynie, K. L., Chilson-Parks, B. H., Ghosh, T., Jadamec, M., et al. (2020). The effect of slab gaps on subduction dynamics and mantle upwelling. *Tectonophysics*, *785*, 228458. <https://doi.org/10.1016/j.tecto.2020.228458>
- Klöcking, M., White, N. J., Maclennan, J., McKenzie, D., & Fitton, J. G. (2018). Quantitative relationships between basalt geochemistry, shear wave velocity, and asthenospheric temperature beneath western North America. *Geochemistry, Geophysics, Geosystems*, *19*(9), 3376–3404. <https://doi.org/10.1029/2018GC007559>
- Kopylova, M. G., & Russell, J. K. (2000). Chemical stratification of cratonic lithosphere: constraints from the Northern Slave craton, Canada. *Earth and Planetary Science Letters*, *181*, 71–87.
- Kovács, I., Green, D. H., Rosenthal, A., Hermann, J., O'Neill, H. St. C., Hibberson, W. O., & Udvardi, B. (2012). An experimental study of water in nominally anhydrous minerals in the upper mantle near the water-saturated solidus. *Journal of Petrology*, *53*(10), 2067–2093. <https://doi.org/10.1093/petrology/egs044>
- Krystopowicz, N. J., & Currie, C. A. (2013). Crustal eclogitization and lithosphere delamination in orogens. *Earth and Planetary Science Letters*, *361*, 195–207. <https://doi.org/10.1016/j.epsl.2012.09.056>
- Langmuir, C. H., Bézou, A., Escrig, S., & Parman, S. W. (2006). Chemical systematics and hydrous melting of the mantle in back-arc basins. In D. M. Christie, C. R. Fisher, S.-M. Lee, & S. Givens (Eds.), *Geophysical Monograph Series* (Vol. 166, pp. 87–146). Washington, D. C.: American Geophysical Union. <https://doi.org/10.1029/166GM07>
- Le Pourhiet, L., Gurnis, M., & Saleeby, J. (2006). Mantle instability beneath the Sierra Nevada Mountains in California and Death Valley extension. *Earth and Planetary Science Letters*, *251*(1–2), 104–119. <https://doi.org/10.1016/j.epsl.2006.08.028>
- Lebedev, S., Boonen, J., & Trampert, J. (2009). Seismic structure of Precambrian lithosphere: New constraints from broad-band surface-wave dispersion. *Lithos*, *109*(1–2), 96–111. <https://doi.org/10.1016/j.lithos.2008.06.010>

- Ledo, J., & Jones, A. G. (2005). Upper mantle temperature determined from combining mineral composition, electrical conductivity laboratory studies and magnetotelluric field observations: Application to the intermontane belt, Northern Canadian Cordillera. *Earth and Planetary Science Letters*, 236(1–2), 258–268. <https://doi.org/10.1016/j.epsl.2005.01.044>
- Lee, C.-T. A., Cheng, X., & Horodyskyj, U. (2006). The development and refinement of continental arcs by primary basaltic magmatism, garnet pyroxenite accumulation, basaltic recharge and delamination: insights from the Sierra Nevada, California. *Contributions to Mineralogy and Petrology*, 151(2), 222–242. <https://doi.org/10.1007/s00410-005-0056-1>
- Leech, M. L. (2001). Arrested orogenic development: eclogitization, delamination, and tectonic collapse. *Earth and Planetary Science Letters*, 185(1–2), 149–159. [https://doi.org/10.1016/S0012-821X\(00\)00374-5](https://doi.org/10.1016/S0012-821X(00)00374-5)
- Lei, T., Li, Z.-H., & Liu, M. (2019). Removing mantle lithosphere under orogens: delamination versus convective thinning. *Geophysical Journal International*, 219(2), 877–896. <https://doi.org/10.1093/gji/ggz329>
- Leonard, L. J., Mazzotti, S., & Hyndman, R. D. (2008). Deformation rates estimated from earthquakes in the northern Cordillera of Canada and eastern Alaska. *Journal of Geophysical Research: Solid Earth*, 113(B8), B08406. <https://doi.org/10.1029/2007JB005456>
- Levander, A., Schmandt, B., Miller, M. S., Liu, K., Karlstrom, K. E., Crow, R. S., et al. (2011). Continuing Colorado plateau uplift by delamination-style convective lithospheric downwelling. *Nature*, 472(7344), 461–465. <https://doi.org/10.1038/nature10001>
- Lewis, T. J., Hyndman, R. D., & Flück, P. (2003). Heat flow, heat generation, and crustal temperatures in the northern Canadian Cordillera: Thermal control of tectonics. *Journal of Geophysical Research: Solid Earth*, 108(B6), 2316. <https://doi.org/10.1029/2002JB002090>
- Li, Y., Yang, X., Yu, J.-H., & Cai, Y.-F. (2016). Unusually high electrical conductivity of phlogopite: the possible role of fluorine and geophysical implications. *Contributions to Mineralogy and Petrology*, 171(4), 37. <https://doi.org/10.1007/s00410-016-1252-x>

- Li, Z.-H., Liu, M., & Gerya, T. (2016). Lithosphere delamination in continental collisional orogens: A systematic numerical study. *Journal of Geophysical Research: Solid Earth*, *121*(7), 5186–5211. <https://doi.org/10.1002/2016JB013106>
- Lowe, C., & Ranalli, G. (1993). Density, temperature, and rheological models for the southeastern Canadian Cordillera: implications for its geodynamic evolution. *Canadian Journal of Earth Sciences*, *30*(1), 77–93. <https://doi.org/10.1139/e93-007>
- Mallyon, D. (2017). *The Evolution of Craton Margin Geometry Through Time* (Master's thesis). University of Alberta.
- Mazzotti, S., & Hyndman, R. D. (2002). Yakutat collision and strain transfer across the northern Canadian Cordillera. *Geology*, *30*(6), 495–498. [https://doi.org/10.1130/0091-7613\(2002\)030<0495:YCASTA>2.0.CO;2](https://doi.org/10.1130/0091-7613(2002)030<0495:YCASTA>2.0.CO;2)
- McCarthy, C., Takei, Y., & Hiraga, T. (2011). Experimental study of attenuation and dispersion over a broad frequency range: 2. The universal scaling of polycrystalline materials. *Journal of Geophysical Research*, *116*(B9), B09207. <https://doi.org/10.1029/2011JB008384>
- Memiş, C., Göğüş, O. H., Uluocak, E. Ş., Pysklywec, R., Keskin, M., Şengör, A. M. C., & Topuz, G. (2020). Long wavelength progressive plateau uplift in eastern Anatolia since 20 Ma: Implications for the role of slab peel-back and break-off. *Geochemistry, Geophysics, Geosystems*, *21*(2). <https://doi.org/10.1029/2019GC008726>
- Mitchell, B. J. (1995). Anelastic structure and evolution of the continental crust and upper mantle from seismic surface wave attenuation. *Reviews of Geophysics*, *33*(4), 441. <https://doi.org/10.1029/95RG02074>
- Molnar, P., & Jones, C. H. (2004). A test of laboratory based rheological parameters of olivine from an analysis of late Cenozoic convective removal of mantle lithosphere beneath the Sierra Nevada, California, USA. *Geophysical Journal International*, *156*(3), 555–564. <https://doi.org/10.1111/j.1365-246X.2004.02138.x>
- Monger, J., & Price, R. (2002). The Canadian Cordillera: geology and tectonic evolution. *CSEG Recorder*, *27*, 17–36.

- Morency, C., & Doin, M.-P. (2004). Numerical simulations of the mantle lithosphere delamination. *Journal of Geophysical Research*, 109(B3), B03410. <https://doi.org/10.1029/2003JB002414>
- Mulch, A., Teyssier, C., Cosca, M. A., & Chamberlain, C. P. (2007). Stable isotope paleoaltimetry of Eocene core complexes in the North American Cordillera: CORE COMPLEX PALEOALTIMETRY. *Tectonics*, 26(4), n/a-n/a. <https://doi.org/10.1029/2006TC001995>
- Nelson, J., & Colpron, M. (2007). Tectonics and metallogeny of the British Columbia, Yukon and Alaskan Cordillera, 1.8 Ga to the present. In: *Mineral Deposits of Canada: A Synthesis of Major Deposit-Types, District Metallogeny, the Evolution of Geological Provinces, and Exploration Methods*, W.D. Goodfellow (Ed.), GAC Special Publication No. 5, 755–791.
- Özaydın, S., & Selway, K. (2020). MATE: An Analysis Tool for the Interpretation of Magnetotelluric Models of the Mantle. *Geochemistry, Geophysics, Geosystems*, 21(9). <https://doi.org/10.1029/2020GC009126>
- Özaydın, S., Selway, K., & Griffin, W. L. (2021). Are xenoliths from southwestern Kaapvaal Craton representative of the broader mantle? Constraints from magnetotelluric modeling. *Geophysical Research Letters*, 48(11). <https://doi.org/10.1029/2021GL092570>
- Padrón-Navarta, J. A., & Hermann, J. (2017). A Subsolidus Olivine Water Solubility Equation for the Earth's Upper Mantle. *Journal of Geophysical Research: Solid Earth*, 122(12), 9862–9880. <https://doi.org/10.1002/2017JB014510>
- Pavlis, T. L., Enkelmann, E., Gulick, S. P. S., & Pavlis, G. L. (2014). Introduction: Neogene tectonics and climate-tectonic interactions in the southern Alaskan orogen themed issue. *Geosphere*, 10(3), 424–427. <https://doi.org/10.1130/GES01023.1>
- Peslier, A. H., Woodland, A. B., Bell, D. R., & Lazarov, M. (2010). Olivine water contents in the continental lithosphere and the longevity of cratons. *Nature*, 467(7311), 78–81. <https://doi.org/10.1038/nature09317>
- Pinet, N., Lavoie, D., Dietrich, J., Hu, K., & Keating, P. (2013). Architecture and subsidence history of the intracratonic Hudson Bay Basin, northern Canada. *Earth-Science Reviews*, 125, 1–23. <https://doi.org/10.1016/j.earscirev.2013.05.010>

- Poudjom Djomani, Y. H., O'Reilly, S. Y., Griffin, W. L., & Morgan, P. (2001). The density structure of subcontinental lithosphere through time. *Earth and Planetary Science Letters*, 184(3–4), 605–621. [https://doi.org/10.1016/S0012-821X\(00\)00362-9](https://doi.org/10.1016/S0012-821X(00)00362-9)
- Powell, J. W., Issler, D. R., Schneider, D. A., Fallas, K. M., & Stockli, D. F. (2019). Thermal history of the Mackenzie Plain, Northwest Territories, Canada: Insights from low-temperature thermochronology of the Devonian Imperial Formation. *GSA Bulletin*, 132(3–4), 767–783. <https://doi.org/10.1130/B35089.1>
- Price, R. A. (1994). Cordilleran Tectonics and the Evolution of the Western Canada Sedimentary Basin. *Canadian Society of Petroleum Geologists and Alberta Research Council*, Chapter 2 in G.D. Mossop and I. Shetsen, compilers, Geological atlas of the Western Canada Sedimentary Basin: Calgary.
- Priestley, K., & McKenzie, D. (2006). The thermal structure of the lithosphere from shear wave velocities. *Earth and Planetary Science Letters*, 244(1–2), 285–301. <https://doi.org/10.1016/j.epsl.2006.01.008>
- Priestley, K., & McKenzie, D. (2013). The relationship between shear wave velocity, temperature, attenuation and viscosity in the shallow part of the mantle. *Earth and Planetary Science Letters*, 381, 78–91. <https://doi.org/10.1016/j.epsl.2013.08.022>
- Pysklywec, R. N., Beaumont, C., & Fullsack, P. (2002). Lithospheric deformation during the early stages of continental collision: Numerical experiments and comparison with South Island, New Zealand. *Journal of Geophysical Research: Solid Earth*, 107(B7), ETG 3-1-ETG 3-19. <https://doi.org/10.1029/2001JB000252>
- Pysklywec, R. N., & Beaumont, C. (2004). Intraplate tectonics: feedback between radioactive thermal weakening and crustal deformation driven by mantle lithosphere instabilities. *Earth and Planetary Science Letters*, 221(1–4), 275–292. [https://doi.org/10.1016/S0012-821X\(04\)00098-6](https://doi.org/10.1016/S0012-821X(04)00098-6)
- Rippe, D. (2012). *Magnetotelluric constraints on the role of fluids in convergent plate boundaries* (Doctoral dissertation). University of Alberta. Retrieved from <https://doi.org/10.7939/R3P94P>

- Rippe, D., Unsworth, M. J., & Currie, C. A. (2013). Magnetotelluric constraints on the fluid content in the upper mantle beneath the southern Canadian Cordillera: Implications for rheology: Fluid Content In the Canadian Cordillera. *Journal of Geophysical Research: Solid Earth*, *118*(10), 5601–5624. <https://doi.org/10.1002/jgrb.50255>
- Ross, J. V. (1983). The nature and rheology of the Cordilleran upper mantle of British Columbia: Inferences from peridotite xenoliths. *Tectonophysics*, *100*, 321–357.
- Russell, J. K., & Kopylova, M. G. (1999). A steady state conductive geotherm for the north central Slave, Canada: Inversion of petrological data from the Jericho Kimberlite pipe. *Journal of Geophysical Research*, *104*, 7089–7101.
- Saleeby, J., Le Pourhiet, L., Saleeby, Z., & Gurnis, M. (2012). Epeirogenic transients related to mantle lithosphere removal in the southern Sierra Nevada region, California, part I: Implications of thermomechanical modeling. *Geosphere*, *8*(6), 1286–1309. <https://doi.org/10.1130/GES00746.1>
- Saleeby, J., Saleeby, Z., & Le Pourhiet, L. (2013). Epeirogenic transients related to mantle lithosphere removal in the southern Sierra Nevada region, California: Part II. Implications of rock uplift and basin subsidence relations. *Geosphere*, *9*(3), 394–425. <https://doi.org/10.1130/GES00816.1>
- Saruwatari, K., Ji, S., Long, C., & Salisbury, M. H. (2001). Seismic anisotropy of mantle xenoliths and constraints on upper mantle structure beneath the southern Canadian Cordillera. *Tectonophysics*, *339*(3–4), 403–426. [https://doi.org/10.1016/S0040-1951\(01\)00136-6](https://doi.org/10.1016/S0040-1951(01)00136-6)
- Schaeffer, A. J., & Lebedev, S. (2014). Imaging the North American continent using waveform inversion of global and USArray data. *Earth and Planetary Science Letters*, *402*, 26–41. <https://doi.org/10.1016/j.epsl.2014.05.014>
- Schott, B., & Schmeling, H. (1998). Delamination and detachment of a lithospheric root. *Tectonophysics*, *296*(3–4), 225–247. [https://doi.org/10.1016/S0040-1951\(98\)00154-1](https://doi.org/10.1016/S0040-1951(98)00154-1)
- Schurr, B., Rietbrock, A., Asch, G., Kind, R., & Oncken, O. (2006). Evidence for lithospheric detachment in the central Andes from local earthquake tomography. *Tectonophysics*, *415*(1–4), 203–223. <https://doi.org/10.1016/j.tecto.2005.12.007>

- Schutt, D. L., & Leshner, C. E. (2006). Effects of melt depletion on the density and seismic velocity of garnet and spinel lherzolite. *Journal of Geophysical Research: Solid Earth*, *111*(B5), n/a-n/a. <https://doi.org/10.1029/2003JB002950>
- Schutt, D. L., Lowry, A. R., & Buehler, J. S. (2018). Moho temperature and mobility of lower crust in the western United States. *Geology*, *46*(3), 219–222. <https://doi.org/10.1130/G39507.1>
- Sifré, D., Gardés, E., Massuyeau, M., Hashim, L., Hier-Majumder, S., & Gaillard, F. (2014). Electrical conductivity during incipient melting in the oceanic low-velocity zone. *Nature*, *509*(7498), 81–85. <https://doi.org/10.1038/nature13245>
- Soyer, W., & Unsworth, M. (2006). Deep electrical structure of the northern Cascadia (British Columbia, Canada) subduction zone: Implications for the distribution of fluids. *Geology*, *34*(1), 53. <https://doi.org/10.1130/G21951.1>
- Stein, C., Comeau, M. J., Becken, M., & Hansen, U. (2022). Numerical study on the style of delamination. *Tectonophysics*, *827*, 229276. <https://doi.org/10.1016/j.tecto.2022.229276>
- Stern, T., Houseman, G., Salmon, M., & Evans, L. (2013). Instability of a lithospheric step beneath western North Island, New Zealand. *Geology*, *41*(4), 423–426. <https://doi.org/10.1130/G34028.1>
- Stewart, J. H. (1972). Initial deposits in the Cordillera geosyncline. Evidence of a late Precambrian (<850 Ma) continental separation. *GSA Bulletin*, *83*, 1345–1360.
- Stewart, J. H. (1976). Late Precambrian evolution of North America: Plate tectonics implication. *Geology*, *4*, 11–15.
- Stixrude, L., & Lithgow-Bertelloni, C. (2011). Thermodynamics of mantle minerals - II. Phase equilibria. *Geophysical Journal International*, *184*(3), 1180–1213. <https://doi.org/10.1111/j.1365-246X.2010.04890.x>
- Takei, Y. (2017). Effects of partial melting on seismic velocity and attenuation: A new insight from experiments. *Annual Review of Earth and Planetary Sciences*, *45*(1), 447–470. <https://doi.org/10.1146/annurev-earth-063016-015820>

- Tesauro, M., Kaban, M. K., Mooney, W. D., & Cloetingh, S. A. P. L. (2014). Density, temperature, and composition of the North American lithosphere-New insights from a joint analysis of seismic, gravity, and mineral physics data: 2. Thermal and compositional model of the upper mantle. *Geochemistry, Geophysics, Geosystems*, *15*(12), 4808–4830. <https://doi.org/10.1002/2014GC005484>
- Tesauro, M., Kaban, M. K., & Mooney, W. D. (2015). Variations of the lithospheric strength and elastic thickness in North America. *Geochemistry, Geophysics, Geosystems*, *16*(7), 2197–2220. <https://doi.org/10.1002/2015GC005937>
- Thorkelson, D. J., Madsen, J. K., & Sluggett, C. L. (2011). Mantle flow through the Northern Cordilleran slab window revealed by volcanic geochemistry. *Geology*, *39*(3), 267–270. <https://doi.org/10.1130/G31522.1>
- Trop, J. M., Benowitz, J., Cole, R. B., & O’Sullivan, P. (2019). Cretaceous to Miocene magmatism, sedimentation, and exhumation within the Alaska Range suture zone: A polyphase reactivated terrane boundary. *Geosphere*, *15*(4), 1066–1101. <https://doi.org/10.1130/GES02014.1>
- Ueda, K., Gerya, T. V., & Burg, J.-P. (2012). Delamination in collisional orogens: Thermomechanical modeling. *Journal of Geophysical Research: Solid Earth*, *117*(B8), n/a-n/a. <https://doi.org/10.1029/2012JB009144>
- Unsworth, M., & Rondenay, S. (2013). Mapping the distribution of fluids in the crust and lithospheric mantle utilizing geophysical methods. In D. E. Harlov & H. Austrheim, *Metasomatism and the Chemical Transformation of Rock* (pp. 535–598). Berlin, Heidelberg: Springer Berlin Heidelberg. [https://doi.org/10.1007/978-3-642-28394-9\\_13](https://doi.org/10.1007/978-3-642-28394-9_13)
- Valera, J. L., Negrodo, A. M., & Villaseñor, A. (2008). Asymmetric Delamination and Convective Removal Numerical Modeling: Comparison with Evolutionary Models for the Alboran Sea Region. *Pure and Applied Geophysics*, *165*(8), 1683–1706. <https://doi.org/10.1007/s00024-008-0395-8>
- Valera, J. L., Negrodo, A. M., Billen, M. I., & Jiménez-Munt, I. (2014). Lateral migration of a foundering high-density root: Insights from numerical modeling applied to the southern Sierra Nevada. *Lithos*, *189*, 77–88. <https://doi.org/10.1016/j.lithos.2013.08.021>

- van der Lee, S., & Frederiksen, A. (2005). Surface wave tomography applied to the North American upper mantle. In Alan Levander & G. Nolet (Eds.), *Geophysical Monograph Series* (Vol. 157, pp. 67–80). Washington, D. C.: American Geophysical Union. <https://doi.org/10.1029/157GM05>
- van Wijk, J. W., Baldrige, W. S., van Hunen, J., Goes, S., Aster, R., Coblenz, D. D., et al. (2010). Small-scale convection at the edge of the Colorado Plateau: Implications for topography, magmatism, and evolution of Proterozoic lithosphere, 38, 611–614. <https://doi.org/10.1130/G31031.1; 2>
- Wang, D., Mookherjee, M., Xu, Y., & Karato, S. (2006). The effect of water on the electrical conductivity of olivine. *Nature*, 443(7114), 977–980. <https://doi.org/10.1038/nature05256>
- Wang, H., & Currie, C. A. (2015). Magmatic expressions of continental lithosphere removal. *Journal of Geophysical Research*, 120, 7239–7260. <https://doi.org/10.1002/2015JB012112>
- Wang, H., & Currie, C. A. (2017). Crustal deformation induced by mantle dynamics: Insights from models of gravitational lithosphere removal. *Geophysical Journal International*, 210(2), 1070–1091. <https://doi.org/10.1093/gji/ggx209>
- Wang, H., Currie, C. A., & DeCelles, P. G. (2015). Hinterland basin formation and gravitational instabilities in the central Andes: Constraints from gravity data and geodynamic models. In P. G. DeCelles, M. N. Ducea, B. Carrapa, & P. A. Kapp, *Geodynamics of a Cordilleran Orogenic System: The Central Andes of Argentina and Northern Chile*. Geological Society of America. [https://doi.org/10.1130/2015.1212\(19\)](https://doi.org/10.1130/2015.1212(19))
- Wang, H., Currie, C. A., & DeCelles, P. G. (2021). Coupling between lithosphere removal and mantle flow in the central Andes. *Geophysical Research Letters*, 48(16), e2021GL095075. <https://doi.org/10.1029/2021GL095075>
- Wang, J., Gu, Y. J., & Chen, Y. (2020). Shear velocity and radial anisotropy beneath southwestern Canada: evidence for crustal extension and thick-skinned tectonics. *Journal of Geophysical Research: Solid Earth*, 125(2). <https://doi.org/10.1029/2019JB018310>
- Wang, Y. F., Zhang, J. F., Jin, Z. M., & Green, H. W. (2012). Mafic granulite rheology: Implications for a weak continental lower crust. *Earth and Planetary Science Letters*, 353–354, 99–107. <https://doi.org/10.1016/j.epsl.2012.08.004>

- Warren, C. J., Beaumont, C., & Jamieson, R. A. (2008). Formation and exhumation of ultra-high-pressure rocks during continental collision: Role of detachment in the subduction channel. *Geochemistry, Geophysics, Geosystems*, 9(4), n/a-n/a. <https://doi.org/10.1029/2007GC001839>
- Willett, S. D. (1999). Rheological dependence of extension in wedge models of convergent orogens. *Tectonophysics*, 305(4), 419–435. [https://doi.org/10.1016/S0040-1951\(99\)00034-7](https://doi.org/10.1016/S0040-1951(99)00034-7)
- Withers, A. C., Bureau, H., Raepsaet, C., & Hirschmann, M. M. (2012). Calibration of infrared spectroscopy by elastic recoil detection analysis of H in synthetic olivine. *Chemical Geology*, 334, 92–98. <https://doi.org/10.1016/j.chemgeo.2012.10.002>
- Wu, L., Gu, Y. J., Chen, Y., & Liang, H. (2019). Shear wave splitting discloses two episodes of collision-related convergence in western North America. *Journal of Geophysical Research: Solid Earth*, 124(3), 2990–3010. <https://doi.org/10.1029/2018JB016352>
- Xu, W., Lithgow-Bertelloni, C., Stixrude, L., & Ritsema, J. (2008). The effect of bulk composition and temperature on mantle seismic structure. *Earth and Planetary Science Letters*, 275(1–2), 70–79. <https://doi.org/10.1016/j.epsl.2008.08.012>
- Yamauchi, H., & Takei, Y. (2016). Polycrystal anelasticity at near-solidus temperatures. *Journal of Geophysical Research: Solid Earth*, 121(11), 7790–7820. <https://doi.org/10.1002/2016JB013316>
- Zandt, G., Gilbert, H., Owens, T. J., Ducea, M., Saleeby, J., & Jones, C. H. (2004). Active foundering of a continental arc root beneath the southern Sierra Nevada in California. *Nature*, 431(7004), 41–46. <https://doi.org/10.1038/nature02847>
- Zaporozan, T., Frederiksen, A. W., Bryksin, A., & Darbyshire, F. (2018). Surface-wave images of western Canada: lithospheric variations across the Cordillera–craton boundary. *Canadian Journal of Earth Sciences*, 55(8), 887–896. <https://doi.org/10.1139/cjes-2017-0277>
- Zhang, F., Dai, R., & Liu, H. (2014). Seismic inversion based on L1-norm misfit function and total variation regularization. *Journal of Applied Geophysics*, 109, 111–118. <https://doi.org/10.1016/j.jappgeo.2014.07.024>

Zhang, J., & Green, H. W. (2007). Experimental investigation of eclogite rheology and its fabrics at high temperature and pressure. *Journal of Metamorphic Geology*, 25(2), 97–115.  
<https://doi.org/10.1111/j.1525-1314.2006.00684.x>

Zhu, R., Xu, Y., Zhu, G., Zhang, H., Xia, Q., & Zheng, T. (2012). Destruction of the North China Craton. *Science China Earth Sciences*, 55(10), 1565–1587.  
<https://doi.org/10.1007/s11430-012-4516-y>